

Geodätisch-geophysikalische Arbeiten in der Schweiz

(Fortsetzung der Publikationsreihe
«Astronomisch-geodätische Arbeiten in der Schweiz»)

herausgegeben von der

Schweizerischen Geodätischen Kommission
(Organ der Schweizerischen Akademie der Naturwissenschaften)

Dreiundsechzigster Band
Volume 63

**Analysis of refraction influences
in geodesy using image processing
and turbulence models**

Philipp Flach

2001

Adresse der Schweizerischen Geodätischen Kommission:

Institut für Geodäsie und Photogrammetrie
Eidg. Technische Hochschule Zürich
ETH Hönggerberg
CH-8093 Zürich, Switzerland

Internet: <http://www.sanw.ch/exthp/geodet/>

ISBN 3-908440-05-X

Redaktion des 63. Bandes:
Dr. Ph. Flach, Dr. B. Bürki

Druck: Print-Atelier E. Zingg, Zürich

VORWORT

Bei nahezu allen optischen geodätischen Präzisionsmessverfahren stellt die Refraktion immer mehr den genauigkeitslimitierenden Faktor dar. Bisher versuchte man für hochgenaue Messungen im Bereich der Ingenieurgeodäsie und Industrievermessung, den Zustand der Atmosphäre durch Messung der Temperaturgradienten im Bereich des Zielstrahles zu bestimmen.

Mit der vorliegenden Arbeit von Herrn Dr. Philipp Flach wurde ein neuer Weg beschritten, indem die in modernen Messinstrumenten eingebauten CCD Flächen- oder Zeilensensoren entsprechende Atmosphärenparameter erfassen und daraus direkt Richtungskorrekturen für das Messverfahren ermitteln. So wurde untersucht, ob aus der zeitlichen Veränderung und der räumlichen Verzerrung von definierten Zielzeichen, z.B. Codemustern, wie sie beim digitalen Nivellierverfahren eingesetzt werden, sowie aus den Intensitätsfluktuationen, sich die Strukturparameter C_n^2 und die innere Skalenlänge l_0 bestimmen lassen. Diese Grössen sind charakteristisch für die Energie des Aufwärmungs- und Abstrahlungsprozesses des Bodens. Mit Hilfe der Monin-Obukov-Similarität kann daraus der Temperaturgradient und damit eine Richtungs-Refraktionskorrektur abgeleitet werden. Um die gesuchten Atmosphärenparameter überhaupt sichtbar werden zu lassen, wurden verschiedene digitale Kantendetektionsverfahren programmiert sowie adaptive Filterverfahren implementiert.

In mehreren ausführlichen Feldkampagnen, u. a. im Rahmen des Schweizerischen MAP (Mesoscale Alpine Programme) Projektes, wurde diese neu entwickelte, CCD basierende Mess- und Auswertetechnik der sogenannten Szintillometrie gegenübergestellt. Im Vergleich zum szintillometrischen Messverfahren zeigten sich nahezu identische Messergebnisse. Ebenso wurden Vergleiche mit dem am Institut für Geodäsie und Photogrammetrie entwickelte Temperaturgradientenmesssystem gemacht. Dabei konnte ebenso eine hohe Übereinstimmung zwischen der indirekten und direkten Messmethode festgestellt werden. Im Gegensatz zu dem an einem diskreten Punkt aufgestellten Temperaturgradientenmesssystem konnte das neu entwickelte System den Vorteil einer integralen Temperaturerfassung und damit die Repräsentativität der Messungen über den gesamten Zielstrahl verdeutlichen.

Herr Flach hat die anspruchsvollen Modellierungen im Zusammenhang mit der Monin Obukov Similarität weiter verbessert. Zudem konnte der Beweis erbracht werden, dass in Zukunft mit den eingebauten CCD Sensoren und einer entsprechenden Software das Problem der terrestrischen Refraktion unmittelbar im Messinstrument gelöst werden kann. Mit den erzielten Ergebnissen und den potentiellen Anwendungsmöglichkeiten in der optisch geodätischen Messtechnik hat er eine wichtige wissenschaftliche Grundlage geschaffen.

Die Schweizerische Geodätische Kommission dankt Herrn Flach für diese gebietsübergreifende wichtige Publikation. Der Schweizerischen Akademie für Naturwissenschaften (SANW) sind wir für die Übernahme der Druckkosten zu grossem Dank verpflichtet.

Prof. Dr. H. Ingensand
Institut für Geodäsie und
Photogrammetrie, ETH Zürich

Prof. Dr. H.-G. Kahle
ETH Zürich
Präsident der SGK

Dr. h.c. E. Gubler, Direktor
Bundesamt für Landestopographie
Vizepräsident der SGK

PREFACE

Pratiquement toutes les méthodes optiques de mesure en géodésie sont faussées par la réfraction qui constitue de plus en plus le véritable facteur de limitation de la précision. Jusqu'à maintenant pour les mesures de haute précision effectuées par les ingénieurs dans le domaine de la géodésie et des mesures industrielles, on essayait donc de déterminer l'état de l'atmosphère par des mesures ciblées de la température, respectivement du gradient de température, dans la zone du rayon de visée. Cette méthode pose toutefois d'énormes exigences quant à la technique de mesure de température.

Dans le présent travail Monsieur Philipp Flach suit une voie nouvelle pour la détermination des paramètres atmosphériques. Il utilise des instruments de mesure modernes qui sont équipés de détecteurs optogéométriques, tels que capteurs de surface ou de ligne CCD à haute résolution ; ceux-ci enregistrent les paramètres atmosphériques et prennent directement en compte la correction de direction pour la méthode de mesure. On a donc cherché à savoir si les paramètres de structure C_n^2 et la longueur d'échelle interne l_0 pouvaient être déterminés à partir des fluctuations d'intensité ainsi qu'à partir de la variation temporelle et de la déformation spatiale d'indices cibles définis, par exemple le code barre, également utilisés dans les procédés électroniques de nivellement. Ces grandeurs se trouvent être caractéristiques de l'énergie du processus de réchauffement et du rayonnement du sol. A l'aide de la similitude de Monin-Obukov, on peut en déduire ensuite le gradient de température, et de là une correction de direction de réfraction. Pour rendre généralement visibles les paramètres atmosphériques recherchés, diverses méthodes numériques de détection de bords ont été programmées, et des procédés de filtres adaptatifs ont été mis en œuvre.

Au cours de plusieurs campagnes d'essai détaillées sur le terrain, entre autres dans le cadre du programme suisse MAP (Mesoscale Alpine Programme), cette nouvelle technique de mesure et de dépouillement basée sur le CCD a été comparée avec la scintillométrie, et les résultats obtenus pour C_n^2 et l_0 se sont avérés presque identiques. Pour la détermination du gradient de température, objectif final de l'étude, un système de mesure développé à l'Institut de géodésie et de photogrammétrie a également été mis en œuvre durant différentes campagnes de mesures. On a pu constater là aussi une grande concordance entre la méthode de mesure indirecte et directe de ce nouveau système de mesure du gradient de température. Au contraire du système installé en un point discret, le nouveau système a mis en évidence l'avantage d'une méthode intégrale de saisie de température, et ainsi la représentativité des mesures sur la totalité du rayon de visée.

Monsieur Flach a significativement amélioré la modélisation en relation avec la similarité de Monin-Obukhov. Avec les résultats obtenus et les applications potentielles dans le domaine de la métrologie optique en géodésie il a apporté un important fondement scientifique à la méthode. Ce travail a aussi permis de prouver qu'il sera possible de résoudre le problème de la réfraction terrestre à l'aide des détecteurs CCD intégrés et d'un logiciel approprié dans l'instrument même.

La Commission Suisse de Géodésie remercie vivement Monsieur Flach pour cette importante contribution. Nous remercions l'Académie Suisse des Sciences Naturelles (ASSN) pour avoir pris à sa charge les frais d'impression du présent fascicule.

Prof. Dr. H. Ingensand
Institut de Géodésie et
Photogrammétrie, ETH Zurich

Prof. Dr. H.-G. Kahle
ETH Zürich
Président de la CGS

Dr. h.c. E. Gubler, Directeur
de l'Office fédéral de topographie
Vice-président de la CGS

FOREWORD

For almost all optical geodetic precision measuring procedures, refraction represents the actual limiting factor. The present work making part of the ETH research project PEARL (Precise Elevation Angle Measurement for Real-time Leveling) gives one possible solution to the problem. Up to now, for high-precision measurements in engineering geodesy and industrial surveying tasks it has been aimed at the determination of the atmospheric conditions near to the line of sight by measuring temperature and temperature gradients, respectively, in a well-directed procedure.

In this work Dr. Philipp Flach has followed a new approach by determining atmospheric parameters using optic-geometrical sensors which are built into modern measuring systems - such as high-resolution area or line CCD sensors - in order to directly obtain corrections of the raw data. Therefore, investigations were made whether temporal displacements, intensity fluctuations, and spatial distortions of defined targets such as code patterns in digital leveling procedures can be used to determine the structure parameters C_n^2 and the inner scale l_0 . These quantities are characteristic of the energy of the warming-up and irradiation processes of the ground. Based on the Monin-Obukhov similarity relation, temperature gradients can be derived to correct refraction-influenced direction measurements. In order to make the required atmospheric parameters visible, various digital edge detection algorithms have been designed, and adaptive filtering methods have been implemented.

During several elaborate field experiments, such as in the scope of the Swiss Mesoscale Alpine Programme (MAP), the newly developed CCD-based measuring and evaluation technique was focused on atmospheric parameters derived from scintillometric metrology. In comparison to the results obtained by the scintillometer, almost identical measuring results were revealed. Further various comparative measuring experiments were made with a temperature gradient measuring system which had been developed at the Institute of Geodesy and Photogrammetry. Thereby, an equivalent correlation between the indirect and the direct measuring method based on the temperature gradient measuring system could be asserted. Unlike the temperature gradient measuring system which was positioned on a discrete point, the newly developed system could point up the advantage of an integral temperature measurement and the representativeness of measurements integrated over the whole line of sight.

Ph. Flach has demonstrated in this volume that modeling in connection with the Monin-Obukhov similarity could be substantially improved. Built-in CCD sensors and a corresponding evaluation software will be able to solve the problem of terrestrial refraction in future with the measuring instrument. With the results obtained potential applications in the field of optical geodetic metrology have been outlined. This contribution forms a highly valuable scientific basis for future research activities.

The Swiss Geodetic Commission (SGC) thanks Ph. Flach for his interdisciplinary and important contribution to geodesy in Switzerland. Thanks are also due to the Swiss Academy of Sciences (SAS) for providing funds for printing this volume.

Prof. Dr. H. Ingensand
Institute of Geodesy and
Photogrammetry, ETH Zurich

Prof. Dr. H.-G. Kahle
ETH Zurich
President of SGC

Dr. h.c. E. Gubler, Director
Federal Office of Topography
Vice President of SGC

Abstract

The propagation path of light in the atmosphere is influenced by inhomogeneities of the refractive index. These refraction effects deteriorate the accuracy of the direction and distance measurements in geodetic applications. As illustrated by two examples in this report, the refraction effects cannot be accurately corrected up to now and, therefore, solutions must be provided which can be implemented into geodetic instruments. The presented approach is based on the determination of the temperature gradient being the decisive influential parameter for angular refraction effects.

In the atmosphere, temperature gradients are related to turbulent thermal exchange processes such as the turbulent sensible heat flux. In order to describe atmospheric turbulence, the applied statistical approach uses the method of spectral analysis which states that the atmospheric turbulent velocity field can be thought to consist of many eddies of different densities. This energy spectrum of turbulence can be modelled using the structure constant of refractive index C_n^2 and the inner scale l_0 of turbulence. If these two structure parameters are measured, the temperature gradient is derived from dimensionless profile functions using the so-called Monin-Obukhov similarity description. Hereby, the fact should be kept in mind, that the Monin-Obukhov similarity description and the energy spectrum of turbulence are only valid for vertical temperature gradient profiles in the atmospheric boundary layer.

This research work investigates the determination of the required structure parameter C_n^2 and l_0 by means of image sensors which can be built into geodetic instruments. To derive the structure parameters C_n^2 and l_0 from the acquired image data, the application of appropriate image processing techniques is examined. The evaluation concept is based on angle-of-arrival fluctuations and intensity fluctuations. Angle-of-arrival fluctuations are perceived as high-frequency motions of image patterns grabbed by the sensor, and intensity fluctuations are related to the temporal variation of the gray values of the pixels. As presented in this report, these two effects of optical turbulence can be used to determine the structure parameter C_n^2 and l_0 . For this purpose, image processing techniques must parameterize both angle-of-arrival fluctuations and intensity fluctuations. Within this research work, the angle-of-arrival fluctuations are modelled by the variance σ_X^2 characterizing the shifting of image patterns which are located using edge detection algorithms. The intensity fluctuations are modelled by the variance σ_V^2 characterizing the temporal intensity spectrum of the incoming light beam. In the scope of this research work, the variance σ_V^2 is provided using digital filter techniques such as the Wiener filter or least-squares template matching.

In order to validate this concept, the video theodolite Leica TM3000V and a digital line scan camera Basler L120 are used as two different imaging systems to acquire image data during various practical field experiments. These field experiments revealed a partial good agreement between the structure parameter C_n^2 and l_0 obtained by the image sensors and the ones obtained by a reference system (scintillometer). Basically, the method presented here is appropriate to reduce the refraction influence. A decisive advantage of this method is based on the fact that additional sensors are not necessary (except for the image sensors which are built into the instrument). However, as the exemplary comparison of temperature gradients shows at the end of the report, further research work in the scope of the atmospheric boundary layer is still necessary.

Zusammenfassung

Die Ausbreitung von Licht in der Atmosphäre wird durch Inhomogenitäten des Brechungsindex beeinflusst. Diese Refraktionseinflüsse verschlechtern die Genauigkeit von Richtungs- und Distanzmessungen in geodätischen Anwendungen. Wie in zwei Beispielen dieses Berichts dargelegt wird, können Refraktionseinflüsse bis heute nicht vollständig korrigiert werden, und deshalb müssen Lösungen gefunden werden, welche in den geodätischen Instrumenten implementiert werden können. Der vorgelegte Ansatz basiert auf der Bestimmung des Temperaturgradienten, da dieser den entscheidenden Einflussparameter des Refraktionseinflusses auf Winkelmessungen darstellt.

In der Atmosphäre stehen Temperaturgradienten in Beziehung mit turbulenten Wärmeaustauschprozessen wie zum Beispiel dem turbulenten Fluss der fühlbaren Wärme. Um die atmosphärische Turbulenz beschreiben zu können, verwendet der untersuchte Ansatz die Methode der Spektralanalyse, welche auf der Vorstellung beruht, dass das turbulente atmosphärische Geschwindigkeitsfeld aus vielen Wirbeln unterschiedlicher Größe besteht. Dieses turbulente Energiespektrum kann mit Hilfe der Strukturkonstante C_n^2 des Brechungsindex und der inneren Skalenlänge l_0 modelliert werden. Sind C_n^2 und l_0 gemessen, so lässt sich der Temperaturgradient von dimensionslosen Profilkfunktionen unter Berücksichtigung der sogenannten Monin-Obukhov Similarität ableiten, wobei beachtet werden muss, dass diese Theorie nur für vertikale Temperaturgradienten in der atmosphärischen Grenzschicht gültig ist

Diese Forschungsarbeit untersucht die Bestimmung der erforderlichen Strukturparameter C_n^2 und l_0 mittels Bildsensoren, welche in geodätischen Instrumenten eingebaut werden können. Um diese Strukturparameter von den erfassten Bilddaten ableiten zu können, wird die Anwendung von Bildverarbeitungstechniken untersucht. Dazu benützt das Auswertekonzept Winkel- und Intensitätsfluktuationen. Winkelfluktuationen können als hochfrequente Bewegungen von Bildmustern, die der Bildsensor erfasst, wahrgenommen werden, und Intensitätsfluktuationen stehen in Beziehung mit der zeitlichen Grauwert-Variation der Pixel. Wie in diesem Bericht dargelegt, können diese zwei Effekte der optischen Turbulenz für die Bestimmung der Strukturparameter C_n^2 und l_0 verwendet werden. Zu diesem Zweck müssen Bildverarbeitungstechniken sowohl die Winkel- als auch die Intensitätsfluktuationen mit Parametern beschreiben. Im Rahmen dieser Forschungsarbeit werden die Winkelfluktuationen mittels der Varianz σ_X^2 modelliert, welche das Verschieben von Bildmustern charakterisiert, die mit Hilfe von Kantendetektionsalgorithmen lokalisiert werden. Die Modellierung der Intensitätsfluktuationen erfolgt durch die Varianz σ_V^2 , welche mittels digitaler Filtertechniken wie das Wiener Filter oder das Least-squares template matching Verfahren berechnet wird.

Um diese Konzept zu validieren, werden als zwei unterschiedliche Bilderfassungssysteme der Videotheodolit Leica TM3000V und die digitale Zeilenkamera Basler L120 verwendet, um Bilder während verschiedener praktischer Feldexperimente zu erfassen. Diese Feldexperimente ergaben zum Teil eine gute Übereinstimmung zwischen den aus den Bildsensoren gewonnen Strukturparametern und denjenigen, die aus einem Referenzmesssystem (Scintillometer) erhalten wurden. Grundsätzlich ermöglicht die vorgestellte Methode eine Reduktion der Refraktionseinflüsse. Ihr entscheidender Vorteil besteht darin, dass nebst den im Instrument vorhandenen Bildsensoren keine zusätzliche Sensoren benötigt werden. Wie jedoch am Ende des Berichts anhand der exemplarischen Berechnung von Temperaturgradienten gezeigt wird, sind noch weitere Forschungsarbeiten im Bereich der atmosphärischen Grenzschicht notwendig.

Contents

1	Introduction	1
1.1	Correction methods	1
1.2	Previous research work on turbulence models and refraction.....	2
1.3	New developments and concepts of the presented research work	3
2	Wave propagation in refractive media	6
2.1	Refractive index	6
2.2	Refraction influence on propagation path	7
2.3	Refraction angle	11
2.4	Energy fluxes causing refractive index gradients in the atmosphere	13
2.4.1	Energy balance and stratification	13
2.4.2	Sensible heat flux and temperature gradient	14
2.5	Relevance of refraction influences for geodetic applications	16
2.5.1	Refraction influences in the context of other thermal influences.....	16
2.5.2	Precise levelling	16
2.5.3	Vertical angle measurements.....	18
2.6	Conclusions.....	20
3	Atmospheric turbulence model	21
3.1	Introduction.....	21
3.2	Energy spectrum	23
3.2.1	Energy density function of turbulent kinetic energy	23
3.2.2	Viscous subrange and dissipation rate.....	26
3.2.3	Inertial subrange.....	26
3.2.4	Energy input range	28
3.2.5	Stationarity of energy spectrum	28
3.2.6	Inner scale	28
3.2.7	Structure constants of velocity and temperature	30
3.3	Monin-Obukhov similarity	31
3.3.1	Scaling parameters	31
3.3.2	Dimensionless profile functions for structure parameters and temperature	34
3.4	Calculation of refraction angle using Monin-Obukhov similarity	35
3.5	Footprint considerations.....	37
3.6	Conclusions.....	39
4	Optical turbulence.....	41
4.1	Phenomena of optical turbulence	41
4.2	Modelling optical turbulence	43
4.2.1	Refractive index spectrum.....	43
4.2.2	Light propagation in turbulent media.....	45

4.3	Angle-of-arrival fluctuations for determination of C_n^2	48
4.3.1	Phenomenon	48
4.3.2	Modelling	49
4.4	Intensity fluctuations for determination of inner scale	52
4.4.1	Phenomena	52
4.4.2	Modelling	52
4.5	Analysis of accuracy	56
4.5.1	Random deviations	56
4.5.2	Systematic deviations	57
4.6	Conclusions	61
5	Measuring systems.....	63
5.1	Introduction	63
5.2	Imaging systems	64
5.2.1	CCD sensors	64
5.2.2	Criteria for the imaging systems	65
5.2.3	Video theodolite	65
5.2.4	Line scan camera	66
5.3	Reference measuring systems	71
5.3.1	Scintillometer	71
5.3.2	Temperature gradient measuring system	73
5.4	Calibration of image sensors	74
5.4.1	Video theodolite	75
5.4.2	Line scan camera	77
5.4.3	Radiometric calibration	78
5.5	Target	79
5.5.1	Reflectors.....	79
5.5.2	Coded levelling staffs	81
5.6	Data recording	83
6	Image processing.....	85
6.1	Introduction	85
6.2	Spectral analysis	86
6.2.1	Introduction	86
6.2.2	Stochastic model for the image signal	87
6.2.3	Estimation of power spectral density	88
6.2.4	Outlook: Wavelet transformation	91
6.3	Wiener filter for determination of intensity fluctuation	94
6.3.1	Introduction	94
6.3.2	Noncausal Wiener filter	96
6.3.3	Model of the power spectral density used for the Wiener filter	98
6.3.4	Implementation using adaptive Wiener filter	100
6.3.5	Conclusions and outlook	104
6.4	Edge detection for determination of angle-of-arrival fluctuation.....	105
6.4.1	Introduction	105
6.4.2	Edge operators	107

6.4.3	Comparison and evaluation	113
6.4.4	Implementation of least squares template matching (LSM).....	115
6.4.5	Implementation of Canny operator.....	118
6.4.6	Accuracy of edge detection	124
6.4.7	Conclusions	125
7	Measurements and results	127
7.1	Video theodolite.....	127
7.1.1	Field experiment.....	127
7.1.2	Results and conclusions.....	129
7.2	Line scan camera.....	133
7.2.1	Field experiment.....	133
7.2.2	Results and conclusions.....	137
7.3	Temperature measurements	143
7.4	Temperature gradient profile	147
7.5	Accuracy of temperature gradient and refraction angle	148
7.5.1	Derivation.....	148
7.5.2	Conclusions	150
8	Conclusions and outlook	152
8.1	Determination of C_n^2	152
8.2	Inner scale	153
8.3	Field experiments.....	154
8.4	Disturbing influences on imaging systems	155
8.5	Outlook	155
	Appendix A: Fractals.....	157
	Appendix B: List of symbols	161
	References	165

1 Introduction

For the last two hundred years, the precision of geodetic instruments has made enormous progress. Although advancing instrument technology allows a high degree of precision and automation, the accuracy and reliability of geodetic measurements is still limited due to atmospheric influences, especially refraction. Up-to-now, refraction is still one of the unsolved problems in numerous applications of surveying. Though refractive effects arise in several fields of surveying such as photogrammetry and satellite based positioning, the following investigations concentrate on applications of close-range photogrammetry and terrestrial geodesy, especially on direction transfer and levelling since the refractive influences of the atmosphere are especially crucial for these applications, e.g., [WITTE, 1990].

As shown below (section 1.1), various approaches using additional measuring equipment have been investigated to correct the refractive influences. In contrast to these approaches, the approach of this work investigates the direct analysis of the measured signal of the geodetic instruments needed for the 1D-, 2D-, or 3D-positioning. This approach is particularly suitable for geodetic applications using image signals, since these signals contain additional information which is not required for the positioning.

Due to progress in instrument technology, imaging sensors are widely applied in numerous geodetic instruments. For instance, tracking tacheometers and digital levels use CCD sensors in order to automate tasks in terrestrial geodesy. Using image processing techniques which estimate the amount of refraction influences, an improvement of accuracy can be expected. Therefore, the following research work investigates the potential of imaging techniques to achieve refraction-reduced measurements.

1.1 Correction methods

When considering direction transfer and levelling in terrestrial geodesy, correction methods for refraction aim at the determination of the refraction angle. The refraction angle is caused by the curvature of the light ray due to varying density of the air and is defined as the angular deviation between the refracted incident ray and the undisturbed ray. Several correction methods can be applied:

- i. Measurement of the temperature gradient of air layers since this gradient is the main influential factor for the refraction angle, using high-precision temperature sensors, e.g., [GOTTWALD, 1985], [WILHELM, 1993], [HENNES *et al.*, 1999]. This method can provide accurate results if the selected measuring points are representative for the refraction influences on the geodetic observations. However, the instrumental equipment is extensive and the setup for field measurements is demanding (e.g., time-consuming on-site calibrations are required).
- ii. Special measuring procedures such as mutual-simultaneous observations or symmetrical observation configurations in order to reduce the effects of refraction, e.g., [JORDAN *et al.*, 1956], [BAHNERT, 1986]. The drawback of this method is that the real conditions do not always agree with the assumptions underlying this method such as uniform stratification of air layers.

- iii. Incorporation of atmospheric effects into the adjustment process of geodetic networks, e.g., [ELMIGER, WUNDERLICH, 1983], [BRUNNER, 1984].

This method is reasonable if the number of measurements is high enough and allows a confident estimation of the additional parameters. But as in method ii., errors may occur if the parameters and the model are not representative for the real conditions.

- iv. Dual-wavelength methods utilizing atmospheric dispersion to derive the refraction angle from the dispersion angle: This method was investigated in the scope of astronomy by [HERTZSPRUNG, 1912]. A first feasibility study about the dispersion effect for applications in geodesy was presented by [HUISER, GAECHTER 1989]. Further experiments using the dispersion effect were done for a rapid precision levelling system as reported in [INGENSAND, 1990a]. These experiments revealed various difficulties in respect of measuring the dispersion angle, but they were the starting-point for the further development of a dispersometer theodolite. In this regard, the updated concept was presented in [INGENSAND, BOECKEM, 1997]; furthermore, first results of system tests and new technological aspects are discussed in [BOECKEM, 2000].

The method using the dispersion effect is the most accurate method since it allows the determination of integral corrections holding for the whole line of sight. However, up to now it also needs a considerable instrumental effort.

- v. Turbulent transfer model using the upward sensible heat flux for derivation of the temperature gradient [BRUNNER, FRASER, 1977]. The required parameters follow from the measurement of scintillation effects such as amplitude fluctuations or phase fluctuations of the incoming waves [HILL, OCHS, 1978], [BRUNNER 1979].

The following investigations focus on this method because it determines the temperature gradient as an integral value along the whole optical path and, therefore, can be effectively utilized to model correction values for refraction influences. In doing so, the structure parameter needed for the Monin-Obukhov similarity model (section 3.3) and for the determination of the temperature gradient are derived directly from the measured signal. As an advantage to other approaches, the turbulent transfer model in combination with image processing techniques needs less instrumental efforts than other methods such as dual-wavelength methods.

1.2 Previous research work on turbulence models and refraction

The significance of the atmospheric turbulence for the determination of refraction influences has already been investigated in previous research work. In the field of geometric levelling, the phenomena caused by refraction influences can be visualized as the movements of scale lines of the leveling rods as seen through the level telescope. A practical experiment during 48 hours showed quite a good correlation between these movements and the temperature gradient [KUKKAMÄKI, 1950]. But quantitative formulae for the correction of refraction influences basing on turbulence models were not available at that time. Only the research work of MONIN and OBUKHOV [1954] proposing a new model for the turbulent exchange processes in the atmospheric boundary layer enabled the determination of temperature gradients basing on similarity relations.

In order to use the Monin-Obukhov similarity theory for geodetic applications such as levelling or direction transfer, information must be derived from the behavior of the light waves propagating through air layers of randomly varying refractive indices. In this regard, the fundamental theories of optical propagation in a turbulent medium were mainly developed in Russia [TATARSKII, 1961]. Practical experiments for geodetic applications were reported from [GURVICH *et al.*, 1974] and [VINOGRADOV *et al.*, 1985]. Despite the simple visual methods, they achieved a reduction of the systematic distortions up to about 80%. In doing so, the theoretical formulations were not applied rigorously but were partially replaced by semi-empirical modeling. As a drawback, these methods need experienced operators and are not suited for automation.

In respect of geodetic refraction problems, a theory for the determination of the vertical refraction angle using the variance of the angle-of-arrival fluctuations and profile shape functions has been presented by BRUNNER [1979]. In this regard, the vertical temperature profile along the line of sight is combined with the movements of the target as seen through the telescope and this model can be used for instance to determine the refraction effects in geodetic levelling [BRUNNER, 1980]. This mostly theoretical research work showed that refraction detection using image fluctuations is possible in principle. For the last twenty years, several research work aiming at the derivation of turbulence parameters from geodetic observations have been carried out thanks to the progressing developments of geodetic systems in terrestrial geodesy. In doing so, several experimental setups have been developed using a modified distance meter [HENNES, 1995] or a CCD area scan camera with 100 x 100 pixels as described in [CASOTT, 1999] and [DEUSSEN, 2000].

Although the experiments using an area scan camera are quite promising, the application of area scan camera make great demands on the hardware such as data transfer and data storage. Therefore, the following research work investigates both area scan cameras (built into video theodolites) and line scan sensors. The hardware requirements of line scan sensors are less demanding than the ones of area scan camera. Line scan sensors are especially suited for digital levelling whereby refraction influences can cause systematic deviations which still cannot be eliminated by other methods. Additionally, alternative methods are presented to derive the turbulence parameters reliably using adapted image processing algorithms (cf. section 6.3.4).

1.3 New developments and concepts of the presented research work

The following research work aims at the development of a precise elevation angle measurement system using image processing techniques and turbulence models. As mentioned at the beginning of section 1, the concept states that the analysis of the measured signal (image signal) is sufficient and no additional measuring system is required except image sensors. In this regard several innovations are introduced:

- Determination of inner scale l_0 by means of intensity fluctuations derived from image processing techniques.
- Development and experimental validation of an image acquisition system which is capable of determining refraction influences using a CCD line scan sensor and image processing techniques.

- Practical field experiments comparing the results of the levelling system with those of a reference system (scintillometer) providing the parameters of optical turbulence (C_n^2 and l_0) and with the results of a temperature gradient measurement system. Additionally, the results are compared with a field experiment using a video theodolite as a representative of a commercially available geodetic instrument.
- Optimization of image processing techniques in respect of refraction analysis for geodetic applications.

Figure 1.1 presents an overview of the research work and the structure of the report: Obviously, the report is mainly focused on the investigation and development of image processing algorithms which can be used for processing the image data provided by the imaging systems, which are presented in section 5.

In section 5, other systems are also described which provide measuring data for comparison with the data obtained by image processing. The image processing techniques make available quantities which determine the intensity fluctuations and angle-of-arrival fluctuations of the incoming wave fronts and intensity variations. Consequently, the intensity fluctuations and angle-of-arrival fluctuations can be used to determine the structure constant C_n^2 (section 4.1) and the inner scale l_0 (section 3.4) as described in section 4.

These two structure parameter C_n^2 and l_0 obtained by image processing can be compared with the parameters C_n^2 and l_0 derived from the measurements using a scintillometer. The comparison is shown in section 7.1 and 7.2. Furthermore, the parameters C_n^2 and l_0 provide the temperature gradient by means of turbulence models, Monin-Obukhov similarity, and dimensionless profile functions as presented in section 3. The modelled gradient is compared with measurements obtained by temperature sensors in section 7.3. Furthermore, section 2 presents the fundamentals used to derive the refraction angle from the temperature gradient. Finally, conclusions and a brief outlook are given in section 8.

As mentioned above, the investigations are primary restricted to refraction influences on vertical angle measurements and precise levelling since the vertical temperature gradient is dominant in the normal case.

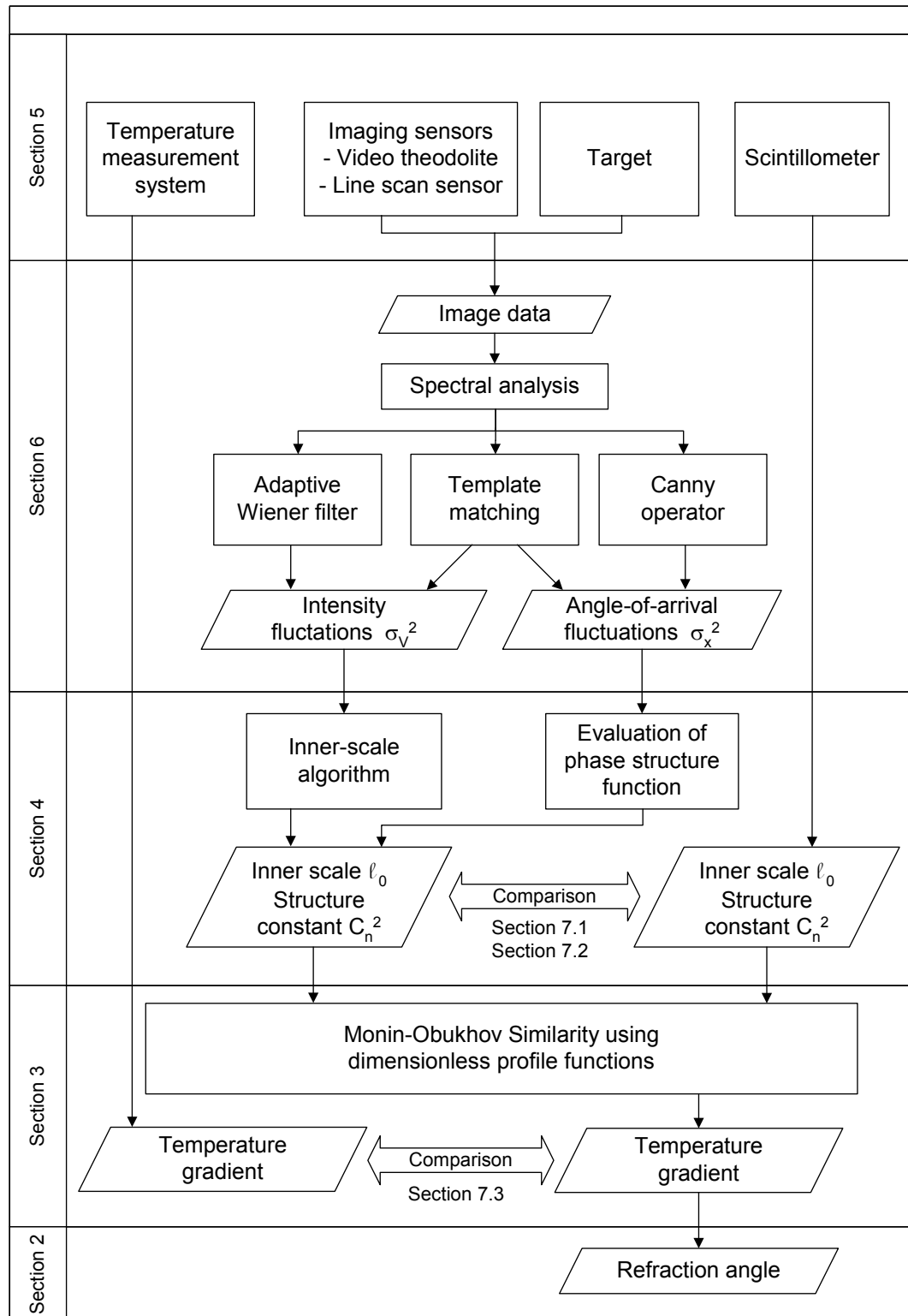


Figure 1.1: Scope of presented research work: Overview

2 Wave propagation in refractive media

2.1 Refractive index

The refractive index is a physical property of the medium and is defined as the ratio of the wave propagation velocity in the medium and the wave propagation velocity in a vacuum.

If the electromagnetic conductivity of the medium can be neglected, the refractive index n and its spatial distribution in the medium describe the propagation of the wave which propagates through the medium. The refractive index for the atmosphere can be expressed for optical and infrared wavelengths as [OWENS, 1967]:

$$n - 1 = \alpha_\lambda \frac{p_d}{T} + \alpha_{\lambda,w} \frac{p_w}{T} \quad (2.1)$$

with

- α_λ Dry-air wavelength-dependence function for wavelength λ
- $\alpha_{\lambda,w}$ Water vapor wavelength-dependence function for wavelength λ
- p_d Partial pressure for dry air [hPa]
- p_w Partial pressure for water vapor [hPa]
- T Temperature [K]

For most applications in the atmosphere, the dry-air term dominates [BELAND, 1993], thus, moisture effects of the air are neglected and the refractive index n of air can be expressed as a function of the wavelength λ , the temperature T and the pressure p [GOTTWALD 1985]:

$$n - 1 = \alpha_\lambda \frac{p}{T} \quad (2.2)$$

with

- α_λ Dry-air wavelength-dependence function for wavelength λ
 $\alpha_\lambda = 78.83 \cdot 10^{-6} \text{ K/hPa}$ for $\lambda = 590 \text{ nm}$, cf. e.g., [BELAND, 1993]
- p Total pressure ($p = p_d + p_w$) [hPa]
- T Temperature [K]

The refractive index of air is subject to spatial variations depending on the temperature, pressure and moisture. Due to the influence of, e.g., energy fluxes and thermal gradients, the distribution of the refractive index changes decisively in the atmospheric air layers.

The spatial inhomogeneity of the distribution of the refractive index leads to refractive index gradients. Assuming a constant pressure gradient and neglecting moisture effects, the refractive index gradient is given by [GOTTWALD 1985]:

$$\frac{dn}{dz} = -\frac{78.83 \cdot 10^{-6}}{T^2} p \left(0.0342 + \frac{dT}{dz} \right) \quad (2.3)$$

with dn/dz Refractive index gradient [m^{-1}]
 z Height [m]
 dT/dz Temperature gradient [K/m]

(2.3) is valid for visible light ($\lambda = 590$ nm). The refractive index gradient is subject to considerable changes in the atmosphere due to the spatial variations of temperature, temperature gradient and pressure which are the main influence parameters.

2.2 Refraction influence on propagation path

The refractive index gradient as introduced in (2.3) is the dominant parameter for the calculation of refraction influences on the propagation path of electromagnetic waves. In general, the path of electromagnetic waves propagating through a medium of varying refractive index is curved because the wave seeks a propagation path which leads to a minimal transit time. This so-called Fermat principle can be interpreted geometrically as follows. If the wave passes a boundary between a medium of refractive index n and another medium of refractive index $n+dn$ the angle of incidence β is bent according to the Snellius law:

$$\frac{n + dn}{n} = \frac{\sin(\vartheta + d\beta)}{\sin(\vartheta)} \quad (2.4)$$

with dn Infinitesimal change of refractive index
 ϑ Angle between refractive index gradient and propagation path

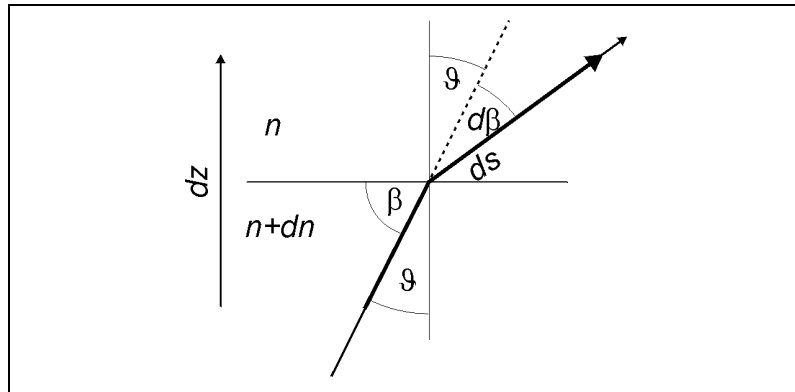


Figure 2.1: Refraction of wave according the SNELLIUS law

Using the trigonometrical addition theorem

$$\sin(\vartheta + d\beta) = \sin(\vartheta) \cos(d\beta) + \cos(\vartheta) \sin(d\beta) \quad (2.5)$$

and

$$\frac{dz}{ds} = \cos(\vartheta) \quad (2.6)$$

$$\sin(d\beta) = d\beta ; \cos(d\beta) = 1 \quad (2.7a,b)$$

with ds Infinitesimal change of path length

equation (2.4) can be written as:

$$\frac{1}{n} \frac{dn}{dz} \sin(\vartheta) = \frac{d\beta}{ds} = \kappa_{ref} \quad (\text{for } \gamma_n = 0) \quad (2.8)$$

with κ_{ref} Curvature of propagation path
 γ_n Angle between the refractive index gradient and vertical z -axis (see below in Figure 2.2)

Instead of κ_{ref} , the traditional geodetic derivation of refraction influences often uses the coefficient of refraction κ_{ref}' , which is introduced as follows:

$$\kappa_{ref}' = R_E \cdot \kappa_{ref} \quad (2.9)$$

with R_E Radius of earth

The application of κ_{ref}' is an alternative way to express the refraction influences but gives no further information when dealing with refraction influences in geodesy. The following derivation uses the curvature κ_{ref} to describe the wave propagation in refractive media. Assuming that the curvature of the propagation path is given by (2.8), the computation of the propagation path $z = z(x)$ is possible in principle. This computation is briefly explained in the following.

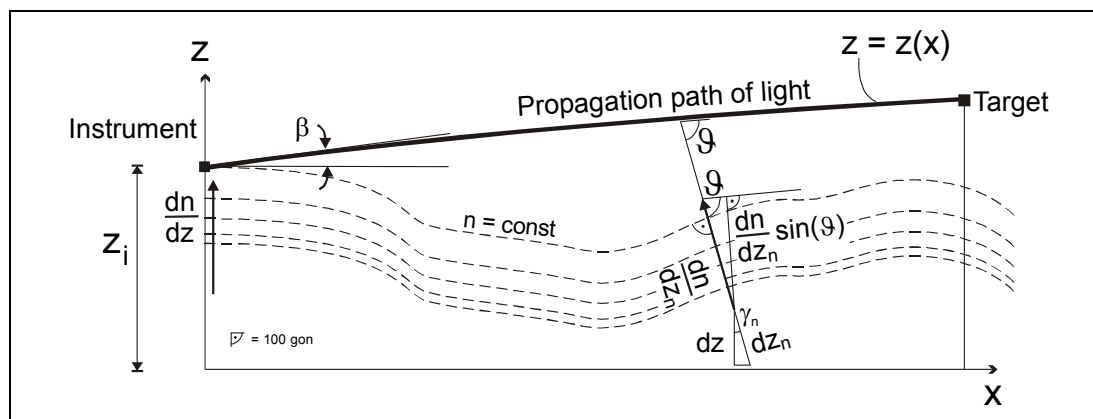


Figure 2.2: Coordinate system

To facilitate the explanation without loss of universality, the computation can be performed in a Cartesian coordinate system where the z -axis runs vertically through the instrument point with the foot-point of the instrument as zero point (Figure 2.2). The propagation path starts at the height of instrument z_i . The x -axis is perpendicular to the z -axis and runs in the direction of the target. The result of the computation is a function $z = z(x)$ which expresses the position z of the light ray for each coordinate x of the axis defined by the instrument and target (Figure 2.2).

It is possible that the refractive index gradient is not parallel to the z -axis at every point along the propagation path. In this case, the angle γ_n between the refractive index gradi-

ent and vertical z -axis is not zero and dn/dz has to be replaced by dn/dz_n where z_n runs parallel to the refractive index gradient:

$$\kappa_{ref} = \kappa_{ref}(x, z) = \frac{1}{n} \frac{dn}{dz_n}(x, z) \cdot \sin(\vartheta) = \frac{d\beta}{ds} \quad (2.10)$$

For a computation using (2.8) [or (2.10), respectively] it is necessary to relate the curvature $d\beta/ds$ to the Cartesian coordinate system as introduced in Figure 2.2. Since the angle of incidence β at the instrument is given by

$$\tan(\beta) = \frac{dz}{dx} = z' \quad (2.11)$$

it follows

$$\beta = \arctan(z') \quad (2.12)$$

$$d\beta = \frac{z''}{1+z'^2} dx \quad (2.13)$$

Using the relation

$$ds = \sqrt{dx^2 + dz^2} = \sqrt{1+z'^2} dx \quad (2.14)$$

equation (2.8) yields to the following second-order differential equation:

$$\frac{d^2z}{dx^2} = z'' = \kappa_{ref} (1+z'^2)^{3/2} \quad (2.15)$$

If the height of instrument z_i and the angle of incidence β of the wave at the instrument are inserted as the initial values, the solution of the ordinary second-order differential equation (2.15) is determined, i.e., the solution is the propagation path $z(x)$ as a function of x . An analytical solution for (2.15) is not possible since the differential equation is not linear and since κ_{ref} depends also on the position (x, z) of the light ray in space.

But a numerical solution for (2.15) can be achieved if the second-order differential equation is transformed into a system of two first-order differential equations as follows:

$$\begin{cases} z' = z_2 \\ z_2' = \kappa_{ref} (1+z_2^2)^{3/2} \end{cases} \quad (2.16)$$

The variable z_2 substitutes for the first derivation of $z(x)$.

With the initial values

$z(0)$: Height of instrument z_i

$z_2(0)$: Angle of incidence β

the system of differential equations (2.16) can be solved. In doing so, the algorithm applied in the following calculations uses the explicit Runge-Kutta (4,5) formula as published in [DORMAND, PRINCE, 1980]. This algorithm is a one-step solver, that means it needs only the solution at the immediately preceding space point $z(x_{k-1})$ for the solution of $z(x_k)$. The advantage of this algorithm is its high accuracy under the assumption that the problem is non-stiff. This assumption is normally fulfilled in (2.16).

Depending on the kind of refraction problem which will be simulated either the angle of incidence β is known (e.g., in the case of levelling where $\beta = 0$) or the height $z(x_{Target})$ of the target must be given. In the latter case, the angle of incidence β is not known exactly and the propagation path must be calculated by means of iterations. In this case, a first approximation for β is derived from the refraction-free direction $\beta_{(0)}$ which is determined using the coordinates of the instrument and the target (Figure 2.3).

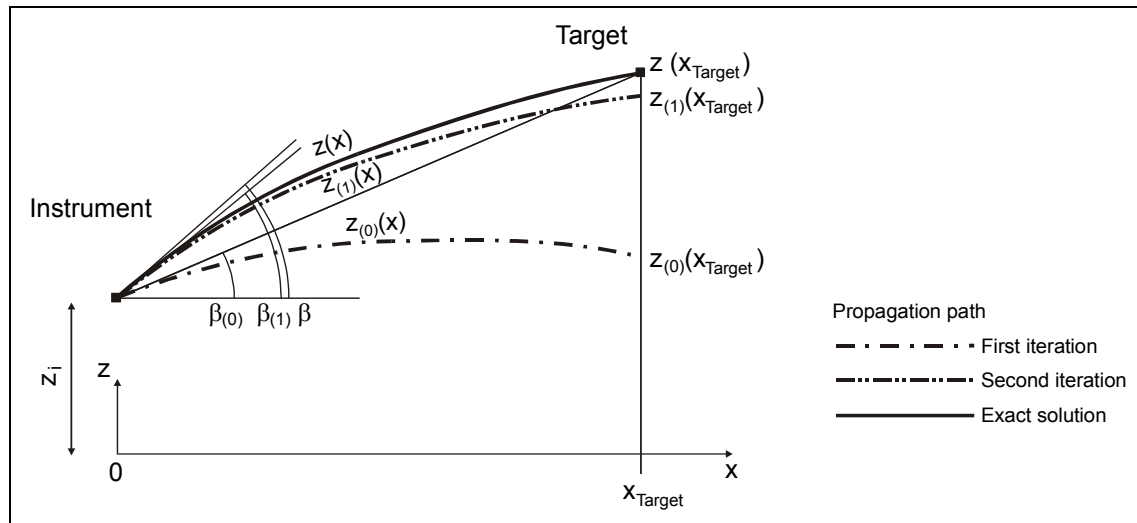


Figure 2.3: Iterative calculation of the propagation path

As illustrated in Figure 2.3, the exact solution of the propagation path $z(x)$ is calculated using iterations $z_{(0)}(x)$, $z_{(1)}(x)$, ... as follows:

$$1. \quad \beta_{(0)} = \arctan\left(\frac{z(x_{Target}) - z_i}{x_{Target}}\right) \quad (2.17)$$

$$2. \quad \text{Solving (2.16) using } z(0) = z_i \text{ and } z_2(0) = \beta_{(0)} \quad \Rightarrow \quad z_{(0)}(x)$$

$$3. \quad \beta_{(1)} = \beta_{(0)} + \arctan\left(\frac{z(x_{Target}) - z_{(0)}(x_{Target})}{x_{Target}}\right) \quad (2.18)$$

4. Solving (2.16) using $z(0) = z_i$ and $z_2(0) = \beta_{(0)} \Rightarrow z_{(1)}(x)$

$$5. \quad \beta = \beta_{(1)} + \arctan\left(\frac{z(x_{Target}) - z_{(1)}(x_{Target})}{x_{Target}}\right) \quad (2.19)$$

6. Solving (2.16) using $z(0) = z_i$ and $z_2(0) = \beta \Rightarrow z_{(2)}(x)$

The algorithm terminates as soon as the absolute error of convergence $|z_{(j)}(x) - z(x)|$ can be neglected.

2.3 Refraction angle

In most of the applications in geodesy, not all of the information about the run of the propagation path is required. Instead, the refraction influences are characterized by a few parameters such as the refraction angle δ or the deviation d_q between the real position of the target and the apparent position. δ and d_q are defined as shown in Figure 2.4 and are related by

$$d_q \approx R \sin(\delta) \approx R\delta \quad (2.20)$$

with R Length of propagation path

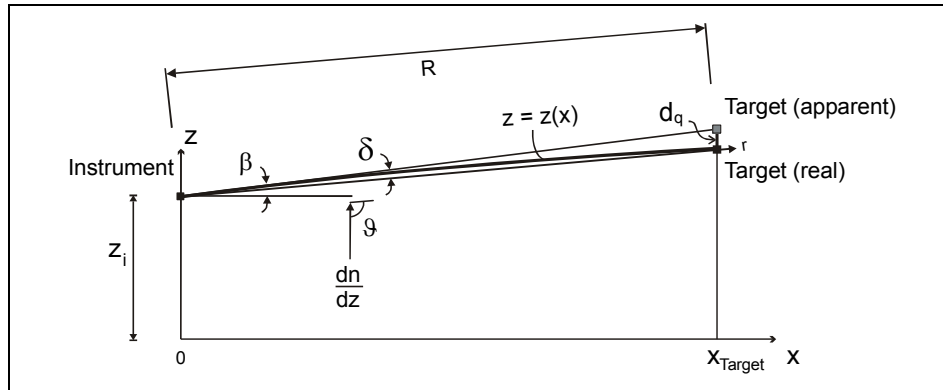


Figure 2.4: Refraction angle

A simple method to calculate the refraction angle is the direct derivation of this angle from the propagation path of the light. If the function $z = z(x)$ of the propagation path is given, the refraction angle δ follows from:

$$\delta = \arctan\left[\frac{dz(x)}{dx}\bigg|_{x=0}\right] - \arctan\left[\frac{z(x_{Target}) - z(0)}{x_{Target}}\right] \quad (2.21)$$

Alternatively to the calculation of δ using (2.21) and the second-order differential equation (2.15), it is also possible to derive the refraction angle by means of integration

along the propagation path of the light ray. In doing so, the r -axis is introduced which connects the instrument with the target (Figure 2.4).

The refraction angle which is defined by the angle between the r -axis and the incoming light beam at the instrument is very small (normally < 1 mgon). Hence, the refraction angle can be calculated using the integration as given by [MORITZ, 1962]:

$$\delta \approx \frac{d_q}{R} = \frac{1}{R} \int_{Instrument}^{Target} (r - R) d\beta = \frac{1}{R} \int_0^R (r - R) \kappa_{ref} dr = \frac{1}{R} \int_0^R \frac{1}{n} \frac{dn}{dz} (r - R) dr \quad (2.22)$$

with R Length of propagation path

Hereby, the propagation path is assumed approximately perpendicular to the *refractive index gradient*, i.e., $\sin(\vartheta) \approx 1$.

In the publication of MORITZ [1962], the factor r instead of $(r-R)$ is used in the integral. The factor $(r-R)$ is correct if the refraction angle is defined at the instrument point (e.g., theodolite, level). If the refractive index gradient is symmetrically distributed along the propagation path, the different formulae yield the same results. If the refractive index gradient is constant along the propagation path, the refraction angle is given by

$$\delta = -\frac{1}{2n} \cdot \frac{dn}{dz} R \quad \text{for } dn/dz = \text{const.} \quad (2.23)$$

Since the refraction angle is proportional to the length of propagation path, the deviation between the real position of the target and the apparent position is quadratic to the length of propagation path:

$$d_q = -\frac{1}{n} \frac{dn}{dz} \int_0^R (r - R) dr = \frac{1}{2n} \cdot \frac{dn}{dz} R^2 \quad \text{for } dn/dz = \text{const.} \quad (2.24)$$

These formulae allow a useful interpretation of the refractive index gradient dn/dz by means of the geometrical elements (δ or d_q) and, therefore, a quantification of refraction influences in geodesy. But (2.23) and (2.24) only work under the assumption of a constant refractive index gradient. However, this assumption does not strictly hold in practical field measurements, with other words, the refractive index gradient must be determined as a function of the propagation path whereby dn/dz is mainly influenced by the temperature gradient as mentioned in (2.3).

In order to obtain an overview over the relevant parameters influencing the temperature gradient and, consequently, the refractive index gradient, the following section presents some basics on modelling the thermal exchange processes which are responsible for these gradients in nature.

2.4 Energy fluxes causing refractive index gradients in the atmosphere

2.4.1 Energy balance and stratification

As shown in (2.3), the refractive index gradient mainly depends on the temperature gradient, temperature, and pressure. When considering geodetic field measurements, these quantities are related to thermal energy fluxes in the atmospheric boundary layer. These energy fluxes fulfill the following equation according to the law of conservation of energy, e.g., [GEIGER *et al.*, 1995]:

$$R_n + L_{ET} + H + G_s = 0 \quad (2.25)$$

with R_n Net radiation [$\text{Jm}^{-2}\text{s}^{-1}$]
 L_{ET} Latent heat flux [$\text{Jm}^{-2}\text{s}^{-1}$]
 H Sensible heat flux [$\text{Jm}^{-2}\text{s}^{-1}$]
 G_s Geothermal heat flux of the soil [$\text{Jm}^{-2}\text{s}^{-1}$]

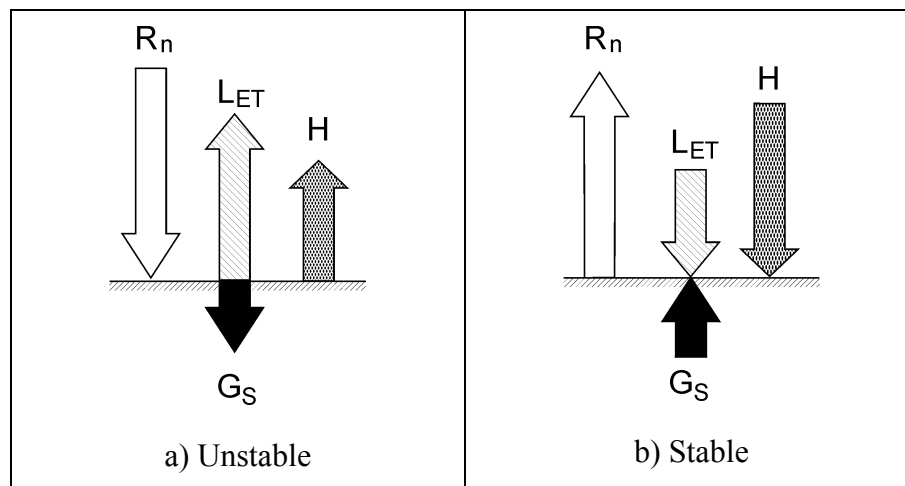


Figure 2.5: Energy balance at the ground surface (schematically)

The energy flux of net radiation can be modelled as follows: During a sunny day, the short-wave radiation from the sun reaches the ground surface. A part of the incoming radiation R_{Down} is reflected but the most of the incoming radiation is absorbed by the ground surface. Due to Kirchoff's law, the ground surface sends out its own long-wave radiation R_{Up} which warms up the air of the atmospheric boundary layer. Thus, the net radiation R_n is given by, e.g., [GEIGER *et al.*, 1995]:

$$R_n = R_{Down}(1 - \alpha_{Alb}) - R_{Up} \quad (2.26)$$

with α_{Alb} Albedo
 R_{Down} Incoming radiation (short-wave)
 R_{Up} Radiation emitted by the ground (long-wave)

According to the circumstances (such as daytime, sunset, clouds, exposition of the ground, material properties of the soil, water content of the soil, vegetation) the value of

the fluxes R_n , L_{ET} , H , and G_S can change considerably. In this regard, three relevant cases must be distinguished, e.g., [STULL, 1991]:

$$\begin{aligned} H > 0 &\Leftrightarrow \text{Unstable stratification (usually during daytime, Figure 2.5a)} \\ H < 0 &\Leftrightarrow \text{Stable stratification (inversion, night time, Figure 2.5b)} \\ H = 0 &\Leftrightarrow \text{Neutral stratification (transition)} \end{aligned} \quad (2.27)$$

During sunshine (cf. Figure 2.5a), the energy of R_n is consumed by the evaporation, i.e., the latent heat flux L_{ET} on the one hand. On the other hand, energy of R_n is also put into mass convection, which is expressed by the sensible heat flux H . In the atmosphere, the sensible heat flux transports heat and energy by air parcels.

During daytime, these air parcels arise due to buoyancy. A minor part of the energy of net radiation R_n leads to the geothermal flux G_S which warms up the ground surface and the underlying layers of the soil.

As shown schematically in Figure 2.5b, the net radiation is inverted during the nighttime and G_S transports heat to the surface from the underlying layers of the soil. The latent flux L_{ET} becomes smaller since less energy is available for evaporation during nighttime. Often, the latent flux L_{ET} is inverted which means that water is condensed. Additional, the nighttime is characterized by a descent of air parcels, i.e., the sensible heat flux points in the direction of the soil.

At least, the neutral stratification implies a specific situation where no convection exists and the sensible heat flux is zero. Normally, this stratification is present during the transition from unstable to stable stratification or vice versa.

2.4.2 Sensible heat flux and temperature gradient

During adiabatic processes, the temperature of the air changes only by pressure changes. It is thus convenient to reference temperature to a given pressure by defining the potential temperature which does not change during adiabatic processes, including those having large pressure changes. The temperature gradient dT/dz which is used to calculate the refractive index gradient (2.3) is related to the potential temperature gradient $d\theta/dz$ as follows, e.g., [STULL, 1991]:

$$\frac{dT}{dz} = \frac{d\theta}{dz} - \Gamma_d \quad (2.28)$$

with Γ_d Dry-adiabatic temperature gradient: $\Gamma_d = 0.0098 \text{ K/m}$

The sensible heat flux is a decisive parameter for determination of the (dry-air) potential temperature θ . This relationship becomes evident if the gradient of the sensible heat flux is investigated: The gradient of the sensible heat flux H causes a loss or gain of potential temperature. The correspondent continuity equation is given by, e.g., [BLACKADAR, 1996]:

$$c_p \rho \frac{d\theta}{dt} = -\frac{dH}{dz} \quad (2.29)$$

with c_p Constant-pressure heat capacity of air [J/kg/K]
 ρ Density [kg/m³]
 θ Potential temperature [K]
 t Time [s]

The sensible heat flux can be measured using methods of scintillometry or sonic-anemometry. When measuring H , the question may arise whether the latent heat flux L_{ET} affects the measured value of H . The Bowen ratio is an appropriate criterion to decide if the influence of moisture is relevant or not. This ratio is defined by, e.g., [BRUNNER, 1982]:

$$B = \frac{H}{L_{ET}} \quad (2.30)$$

Field measurements as reported in [WEISS *et al.*, 1999] showed that the relative error due to moisture is less than 10% if the measurements base on optical scintillation (infrared or visible waves) and the Bowen ratio is not smaller than 0.4. Further considerations about the influence of moisture are made in [WESELY, DERZKO, 1975].

Back again, besides the gradient of sensible heat flux dH/dz , additional information is required to derive the potential temperature since the problem (2.29) is under-determined. The Monin-Obukhov similarity theory which will be introduced in section 3.4 is a possible method to overcome this problem and allows the determination of the potential temperature and its gradient $d\theta/dz$.

As a consequence of these thermal exchange processes which are presented above, the temperature gradient is subject to vast temporal and spatial changes. In order to analyze the temperature profile in the lowest 100 m of the atmosphere, extensive temperature measurements have been performed such as those documented in [BROCKS, 1948]. These measurements are valid for the unstable stratification and took place at different locations and times. As a result of the investigations of [BROCKS, 1948], the parameters a_T and b_T have been determined which are part of the empirical formula modelling the temperature gradient:

$$\frac{dT}{dz} = a_T z^{-b_T} \quad (2.31)$$

with a_T, b_T Parameters of temperature gradient model

This model is used in the following section where the influence of refraction on typical geodetic measurements is quantified by means of mathematical simulations.

2.5 Relevance of refraction influences for geodetic applications

2.5.1 Refraction influences in the context of other thermal influences

The influence of refraction deteriorating the accuracy of geodetic measurements is still a crucial point for the positioning in geodesy. In particular, refraction influences direction measurements, distance measurements, height differences, GPS measurements and measurements using photogrammetry.

As shown in section 2.4, the refraction influences are always a function of the temperature gradient. Unfortunately, other systematic deviations of geodetic measuring procedures also depend on the temperature, thus, these systematic deviations can combine with refraction influences.

For example, variations of temperature can influence the line of vision of levels equipped with an integrated compensator in the order of $0.15 \text{ mgon}/^\circ\text{C}$ [INGENSAND, MEISSL, 1995]. Assuming that the variation of temperature is large enough (more than 5°C) and the resulting deviation is not compensated otherwise, the systematic deviations of geodetic instruments can exceed the refraction influences. As a further example, changes of temperature can also produce systematic deviations by shifting and inclining of measuring pillars on which the geodetic instrument is positioned.

But the considerations in this section assume that these non-refractive effects are compensated by adapted accompanying measures (e.g., by means of calibration functions, adapted design of the instruments and measurement configurations) and therefore can be neglected in the following.

In order to demonstrate the effects and relevance of refraction, the following two examples of geodetic applications are calculated in the next subsections:

1. Precision levelling
2. Vertical angle measurements

These two applications are chosen for the following reasons: On the one hand, they are applications which often make high demands on accuracy (sub-millimeter range). On the other hand, the system and algorithms developed within the scope of this research work are expected to increase the accuracy for those two applications, i.e., the following simulation illustrates the requirements which must be met by any method correcting refraction influences.

2.5.2 Precise levelling

The following simulation deals with refraction influences in precise levelling neglecting other systematic deviations such as stability of the staffs. With a central position of the levelling instrument between staff 1 and staff 2 (Figure 2.6), the total refraction effect from one levelling setup will always be the difference of the refraction influences between the foresight measurement and the backsight measurement.

Thus, isothermal air layers which do not run parallel to the line of sight cause systematic deviations due to unsymmetrical refraction effects. In other words, these circumstances cause a systematic deviation k_r , which mounts up with increasing length of the

levelling line. For example, the problem occurs when the levelling line consists of an extensive slope. This situation is displayed in Figure 2.6 which characterizes the following simulation.

In this simulation, a temperature of 300 K and a pressure of 1000 hPa are assumed and the temperature gradient is a function of the height of the line of sight above ground. Hereby, the temperature gradient model of (2.31) is applied with parameters $a_T = 0.34$ and $b_T = 0.99$ [BROCKS, 1948]. Thereby, these parameters represent the temperature profile of the first 100 m of the atmospheric boundary layer in the morning of a clear day in summer.

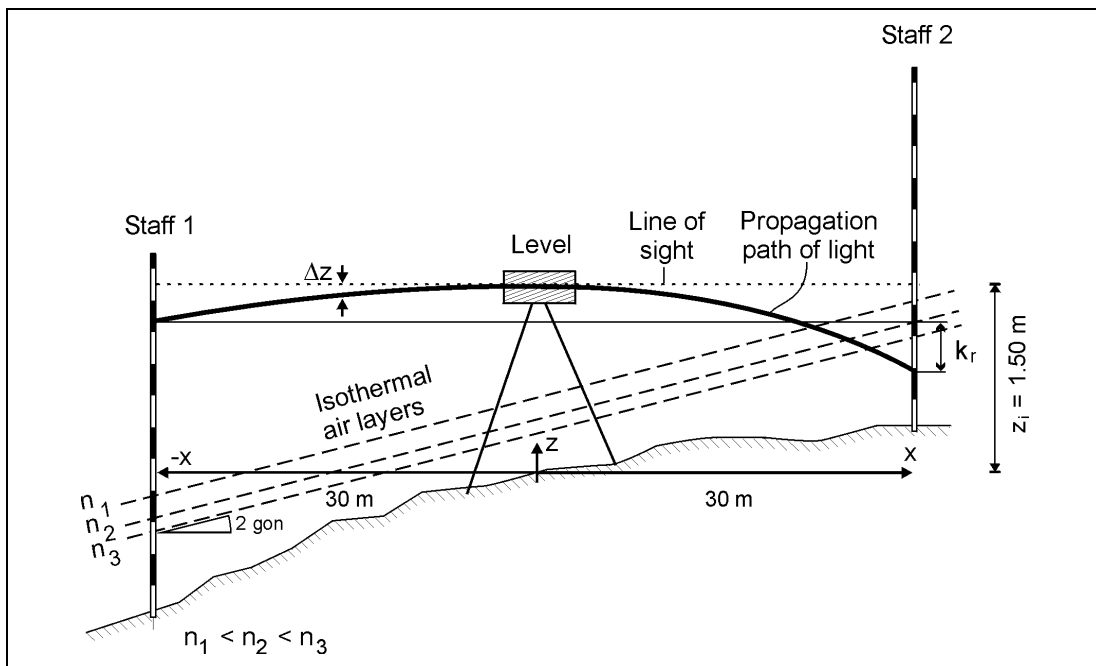


Figure 2.6: Refraction influences in precise levelling: Configuration of simulation

By using the differential equation (2.15), the propagation path of light $z(x)$ can be determined. The results are shown in Figure 2.7 wherein the difference $\Delta z(x)$ between the calculated value $z(x)$ and the initial value z_i are plotted. As shown in Figure 2.7, the systematic deviation k_r is about 0.044 mm for the stated input parameters.

Assuming 17 levelling setups along a levelling line of 1 km, the total systematic deviation caused by refraction is 0.75 mm/km. For comparison: the standard deviation of height differences obtained by precise levelling using digital levels is about 0.3 to 0.4 mm/km (double run levelling) as reported, e.g., in [INGENSAND, 1995]. Therefore, the refraction influences should be taken into consideration.

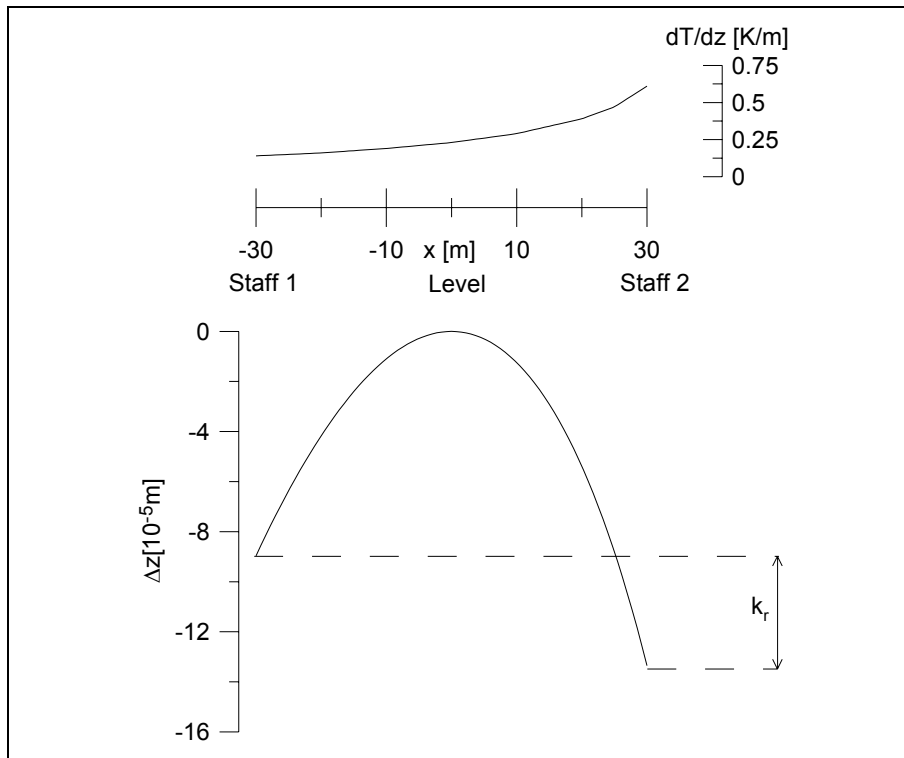


Figure 2.7: Precise levelling: Simulation of propagation path $z(x)$

2.5.3 Vertical angle measurements

The second example investigates refraction influences on vertical angle measurements used for trigonometric height determination. The instrument points to a target which is positioned 60 m away. Target and instrument are assumed to be at the same height z . The simulation includes two cases characterized by different temperature gradient fields. In both cases, a temperature of 300 K and a pressure of 1000 hPa are assumed.

- In case (a) the temperature gradient is assumed to be constant ($dT/dz = 0.25$ K/m) along the line of sight. This case is typical, e.g., for homogeneous ground surfaces which are heated uniformly by the sun radiation.
- Case (b) investigates the wave propagation through the air wherein 3/4 of the propagation path is not influenced by temperature gradients and 1/4 is strongly affected by a temperature gradient of 1 K/m. This situation may occur, e.g., when the wave propagates near a heat source such as a warmed asphalt road.

The results of the simulations are displayed in Figure 2.8 for both cases.

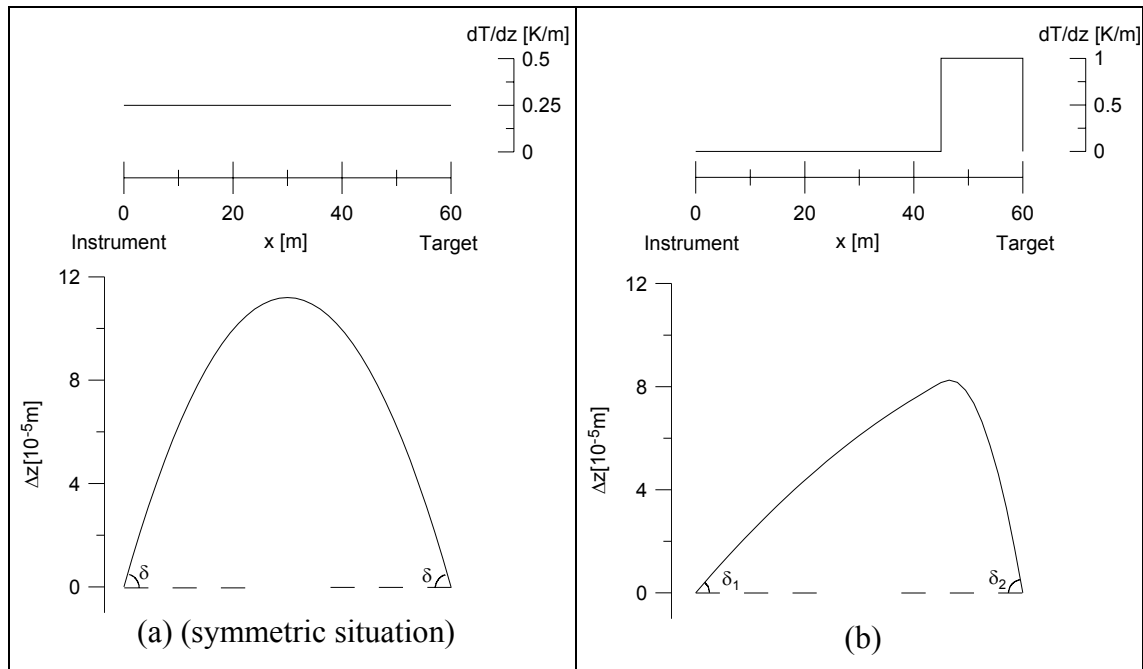


Figure 2.8: Direction measurement: Simulation of propagation path $z(x)$

The integrated contribution of the temperature gradient is equal in both cases, but the distribution of the temperature gradient is different. As a consequence of the different distribution of the temperature gradient, the angle of refraction is subject to considerable variations as shown in Table 2.1.

Case	Refraction angle [mgon]	
	δ_1	δ_2
(a): $\delta_1 = \delta_2 = \delta$	0.48	0.48
(b): $\delta_1 \neq \delta_2$	0.16	0.73

Table 2.1: Amount of refraction angle

These numerical examples and equations show that large temperature gradients are especially critical if they arise close to the instrument. Temperature gradients arising near the target are less critical.

For example, if the measurements are performed as depicted in case (b), i.e., if the instrument is in the range where no gradients occur, the refraction angle is only 20 % of the refraction angle obtained by measurements where the instrument and the target are positioned vice versa.

In case (a) the refraction angle causes a height deviation d_q of about 0.45 mm. This deviation can be eliminated if

- the vertical angle is measured reciprocally whereby the instrument and the target are exchanged (reciprocal-simultaneous observations)
- the temperature gradients do not change between the two measurements
- the temperature gradient field is symmetrical

Obviously, the last condition is not fulfilled in case (b). Although the instrument and the target are exchanged, a considerable part of the refraction influence still remains. The difference in case (b) is about 0.57 mgon which causes a deviation d_q of 0.54 mm for a propagation path length of 60 m. Thus, d_q does not disappear when measuring using reciprocal-simultaneous configurations.

2.6 Conclusions

Refraction influences are a limiting factor in the accuracy of high-precision geodetic measurement. As demonstrated by the example of precise levelling in section 2.5.2, the amount of refraction influences is about twice the standard deviation of double run levelling. The contribution of refraction influences depends to a large extent on the temperature gradient and its spatial distribution. For example, the influence of the spatial distribution is illustrated by the simulated case (b) in section 2.5.3. This example shows that an appropriate choice of the place for the instrument can reduce the refraction angle by more than 80%.

As it is shown in section 2.4.2, the temperature gradient is correlated with the sensible heat flux. This flux can be described using the energy balance presented in section 2.4.1. The fluxes of this energy balance are subject to considerable temporal and spatial changes according to a variety of influence parameters as mentioned in section 2.4.1. Hereby, the temperature gradient is the dominating influential parameter for the refraction effects when dealing with IR and light-wave. Up to now, the temperature gradient needed for refraction analysis must be obtained by additional measurements and cannot be derived from general thumb rules.

Refraction may occur simultaneously with other temperature-induced deviations of the measuring setup as mentioned in section 2.5.1 which makes it difficult to separate refraction influences from other influences. Traditional approaches in geodesy (such as symmetrical observation configurations, reciprocal-simultaneous observation or redundant observations by multiple aiming at targets positioned one above the other or at reference height marks) often eliminate refraction influences simultaneously together with other systematic deviations. Hereby, these approaches base on certain assumptions concerning the propagation path of light such as symmetry or circular shape which usually are not strictly fulfilled when performing geodetic field measurements.

In order to obtain a hypothesis-free reduction of refraction influences, it is necessary to determine the refraction influences integrally along the propagation path. In the scope of this research work, the evaluation of the measured signal only is assumed to provide a satisfying estimation of the refraction influences. This estimation is based on image processing techniques which use the image data from built-in geodetic image sensors. Additionally, to estimate the refraction influences, the image processing techniques must be combined with atmospheric turbulence models as presented in the following sections.

3 Atmospheric turbulence model

3.1 Introduction

The goal of the atmospheric turbulence model presented in the following sections is to model the turbulent exchange processes of momentum and sensible heat in the atmospheric boundary layer. From the turbulent fluxes of momentum and sensible heat, the temperature gradients can be derived, which are used to estimate refraction influences as modelled by (2.3).

Turbulence is characterized by irregular fluctuations of the parameters (velocity, temperature, concentration, etc.) of a gas or a fluid. The nature of turbulence is irregular and rather unpredictable. The Navier-Stokes equation is regarded as a deterministic answer to fluid dynamic and turbulence problems, e.g., [TRITTON, 1977]. Assuming a constant density, the conservation of momentum leads to the Navier-Stokes equation as given by, e.g., [DRACOS, 1990]:

$$\rho \frac{\partial \mathbf{u}}{\partial t} = \underbrace{-\rho \mathbf{u} \cdot \nabla \mathbf{u}}_{\text{Inertia force}} - \underbrace{\nabla p}_{\text{Pressure force}} + \underbrace{\nu \rho \cdot \nabla^2 \mathbf{u}}_{\text{Viscous force}} \quad [\text{N/m}^3] \quad (3.1)$$

with \mathbf{u} Velocity vector [m/s]
 ρ Density [kg/m³]
 p Pressure [hPa]
 ν Kinematic viscosity [m²/s]
 ∇ Nabla operator (gradient)

The Navier-Stokes equation describes the motion of all kinds of flows passing any surface. They also describe the sensible heat flux H which is characterized by convective mass transfer in the atmospheric boundary layers and which is related to the temperature gradient as shown in (2.29). In order to distinguish turbulent flows from laminar (non-turbulent) flows, the Reynolds number Re is the appropriate measure because turbulence effects only arise when the inertia force exceeds a threshold given by the viscous properties of the fluid or gas. Thus, the Reynolds number defines the ratio of the inertia force and the viscous force and is related to the Navier-Stokes equation as follows, e.g., [DRACOS, 1990]:

$$Re = \frac{F_{inertia}}{F_{viscous}} = \frac{|\mathbf{u} \cdot \nabla \mathbf{u}|}{|\nu \nabla^2 \mathbf{u}|} \approx \frac{UL}{\nu} \quad (3.2)$$

with U Characteristic velocity [m/s] of the fluid or of the gas
 L Characteristic length [m]

Flows described by the same Reynolds number are similar in physical sense, where this property can be utilized for experimental setups such as wind tunnels.

In laminar flows (i.e., absence of turbulence effects), the Navier-Stokes equation is approximately linear since $|\mathbf{u} \cdot \nabla \mathbf{u}| \ll |\nu \nabla^2 \mathbf{u}|$. A turbulent flow is defined as a flow where the Reynolds number exceeds a defined value (in general: > 2300). For turbulence oc-

curing in atmospheric boundary layers, the Reynolds number is very large and lies in the range of 10^6 to 10^7 . The choice for the characteristic length L used in (2.4) depends on the application. For example, in hydraulic engineering the characteristic length L may be the diameter of a tube. In the atmospheric boundary, the Obukhov length which will be introduced in section 3.3.1 is an appropriate choice for the characteristic length.

Under turbulent conditions, the term $\rho \mathbf{u} \cdot \nabla \mathbf{u}$ cannot be neglected, therefore, the Navier-Stokes equation becomes non-linear. Small perturbations draw energy from the laminar trajectories of the flow. As a consequence of non-linearity, the energy is redistributed into an increasing number of perturbations which become smaller and smaller. This effect yields eddies building a cascade of the turbulent flow.

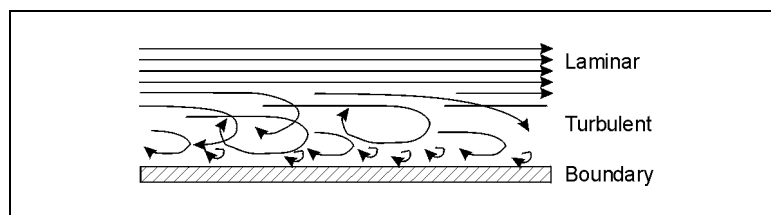


Figure 3.1: Cascade of turbulence

The perturbations of the turbulent flow have a transient chaotic behavior and therefore cannot be described in a deterministic way. There are several approaches to deal with turbulence. Hereby, the approach using fractal theory has to be mentioned which states that several facets of fully developed turbulent flows are fractals, e.g., [MANDELBROT, 1977]. Previous research work shows that several aspects of turbulence can be described roughly by fractals, and that their fractal dimensions can be measured [GROSSMANN, 1990]. These relationships are presented in Appendix A. However, it is not clear how, given the dimensions for several of the facets of turbulence, one can solve up to a useful accuracy the inverse problem of reconstructing the original turbulent flow itself [SREENIVASAN, MENEVEAU, 1996].

For this reason, the following turbulence model uses the statistical properties of turbulence as introduced by KOLMOGOROV [1941]. His approach advances a hypothesis for high ($Re > 10^6$ - 10^7) Reynolds numbers. This model explains why the scale size of the finest turbulence structures becomes smaller and smaller with increasing Re , and should allow the treatment the finest details in a homogeneous way. It cannot explain why certain structures form and not others, but it describes the average flow of energy across the scale sizes of turbulence.

The spectrum of kinetic energy as introduced in section 3.2 is a key point of the statistical approach by Kolmogorov. As will be explained in greater detail in section 3.2, kinetic energy enters the medium on large scales, in the form of convection or friction on an obstacle (energy range). The energy is transferred towards smaller scale sizes over eddy fragmentation, while the Reynolds number decreases (inertia range). The smallest eddies have sub-critical Reynolds numbers, they dissipate heat, and are stable (viscous range).

The energy spectrum (section 3.2) mainly depends on the following two parameters: the structure constant of temperature C_T^2 (cf. (3.62)) and the inner scale l_0 (cf. (3.19)). Both

parameters can be determined using appropriate methods such as methods of scintillometry, sonic-anemometry, or image processing. Hereby, the applied measurement methods and algorithms are described in sections 4 to 6.

C_T^2 and l_0 can be used to determine the temperature gradient since they allow the determination of the sensible heat flux by means of dimensionless profile functions as presented in section 3.3.2. This procedure is valid so long as the quantities described by the profile function are Monin-Obukhov similar as postulated in section 3.3.

In the following, a more detailed explanation of the relevant elements of this procedure is given, which allows the determination of temperature gradients by means of atmospheric turbulence.

3.2 Energy spectrum

3.2.1 Energy density function of turbulent kinetic energy

Turbulence can only be maintained by continuous inflow of kinetic energy because viscous forces dissipate the kinetic energy into thermal energy. Therefore, the kinetic energy production and dissipation characterize the turbulent flow.

The determination of the kinetic energy and the dissipation energy requires the knowledge of the velocity u of the molecules of the fluid or gas which obeys the Navier-Stokes equation. Because this equation is non-linear, the Navier-Stokes equation still cannot be solved exactly [FEFFERMAN, 2000].

As a trade-off, the Reynolds approach to turbulence implicates that modelled parameters such as the velocity u ($= |\mathbf{u}|$), the turbulent kinetic energy E_{kin} , the density ρ , etc., can be split into

- an average part denoted by an overline, e.g., \bar{u} , \bar{E}_{kin} , etc., and
- a random fluctuation part denoted by an apostrophe, e.g., u' , E' , etc. whereby the random fluctuations are much smaller than the average part:

Consequently, the Reynolds approach can be written as:

$$u(t) = \bar{u} + u'(t) \quad (3.3)$$

$$E_{kin}(t) = \bar{E}_{kin} + E'(t) \quad (3.4)$$

In (3.4), E' represents the turbulent kinetic energy of the turbulent motion per unit mass. E' is related to the random fluctuations of the velocity by:

$$E' = \frac{1}{2} \overline{u'^2} \quad [\text{m}^2 \text{s}^{-2}] \quad (3.5)$$

The apostrophe indicates that the turbulent kinetic energy is the total kinetic energy (time-averaged) minus the kinetic energy of the mean motion. E' is generated by imposed shear, transported by various mechanisms, and dissipated by viscosity [PANOF-SKY, DUTTON, 1984].

In turbulent flows, a direct measurement of u' is possible by means of high-resolution anemometers, e.g., [OHMURA, ROTACH, 1997]. However, due to the random fluctuations of $E'(t)$ the direct interpretation of the time series $E'(t)$ does not reveal the parameters C_T^2 and l_0 which are needed for refraction detection. For this purpose, the spectral analysis of the time series of $E'(t)$ is brought into play. Hereby, the Fourier transform of $E'(t)$ characterizes the turbulent kinetic energy by means of energy density distribution $E'(\omega)$ which is a function of the frequency ω [TATARSKII, 1971]:

$$E'(\omega) = \int_{-\infty}^{\infty} e^{-i\omega t} E'(t) dt \quad (3.6)$$

The energy density distribution described by (3.6) can be measured as a (temporal) spectrum. Whereas the temporal spectrum is measured during a given length of time, the application of the energy density distribution for the determination of the inner scale (which is a spatial quantity as shown in section 3.2.6) requires the determination of the spatial structure of turbulence at a specified point of time. In order to obtain a relationship between temporal and spatial structure of turbulence, Taylor's frozen turbulence hypothesis can be used. This hypothesis states that the temporal series of turbulent movements can be converted to the spatial one whereby the temporal and the spatial series are related by the covariance tensor R_{ij} as follows, e.g., [PANOFSKY, DUTTON, 1984]:

$$R_{ij}(t) = R_{ij}(2\pi / \kappa) \quad \text{for } i = 1, 2, \dots; j = 1, 2, \dots \quad (3.7)$$

$$\text{with } \kappa = \frac{2\pi}{u_q \cdot t} \quad (3.8)$$

κ Spatial wave number of the turbulence [m^{-1}]
 u_q Velocity of crosswind [m/s]

The frozen turbulence hypothesis can only be applied to those cases where the turbulent eddies evolve with a timescale longer than the time it takes the eddy to be advected past a sensor. In other words, the frozen turbulence hypothesis holds if the local wind velocity is high in comparison to the change of the shape of the turbulent eddies. When considering scintillation measurements using imaging sensors or scintillometers, only the wind component which is perpendicular to the line of sight is relevant because the wind parallel to the line of sight does not deliver a relevant contribution to the temporal statistics, e.g., [HUFNAGEL, 1978].

Measurements presented by POWELL and ELDERKIN [1974] show that the frozen turbulence hypothesis is valid in the atmospheric boundary layer and under near-neutral conditions if the crosswind u_q and the wave number κ fulfill the following equation:

$$\kappa \cdot u_q \geq 4 \frac{du_q}{dz} \quad (3.9)$$

Thus, the energy spectrum makes it possible to describe the scales of the eddies in the turbulent continuum. This means the spectral analysis allows the description of the

transport of energy from large eddies (low frequency) to small eddies (high frequency). Using the spatial frequency spectrum, the density distribution of turbulent energy $E'(\kappa)$ is a function of the wave number κ instead of the frequency ω . This energy density distribution is also known as turbulence spectrum describing the amount of turbulent kinetic energy which is contributed by eddies of the correspondent wave number $\kappa = 2\pi/\ell$ (ℓ : Eddy size). The eddy sizes L_0 and l_0 denote the limits of the ranges of energy injection, energy transfer and energy dissipation as schematically shown in Figure 3.2.

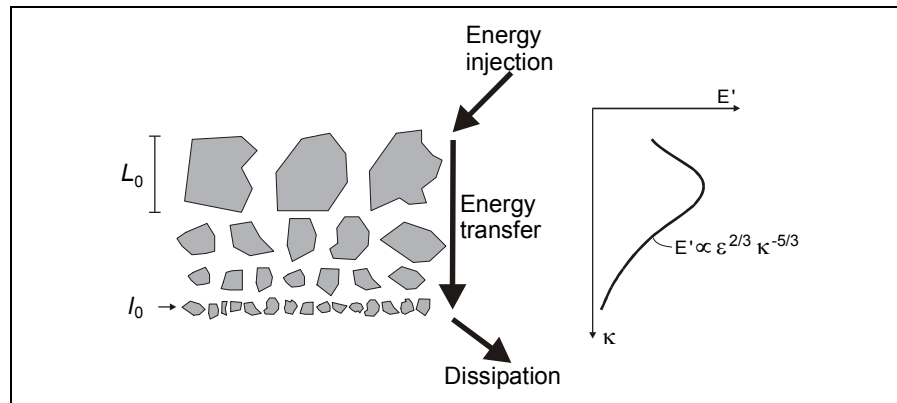


Figure 3.2: Energy transfer and turbulence spectrum $E'(\kappa)$, see also (3.16)

Herein, turbulent kinetic energy is generated and injected at the lower wave numbers, i.e., at large eddy sizes. Then, a process of eddy fragmentation transfers the energy through the spectrum. Hence, the energy put in at low wave numbers is transformed to the higher wave numbers and, therefore, the eddies lose their anisotropic configuration form and become more and more isotropic and smaller until they are dissipated.

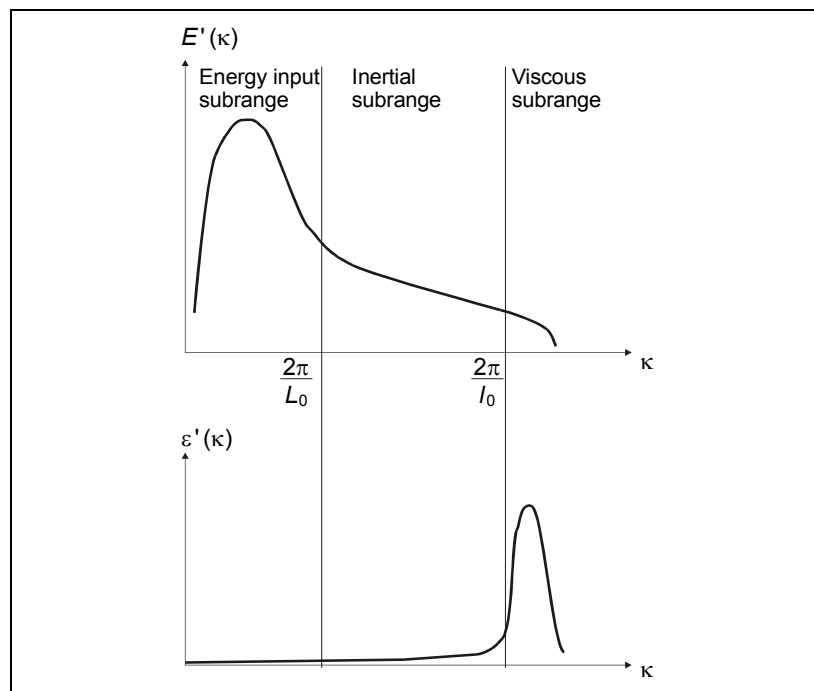


Figure 3.3: Energy spectrum E' and spectral density of dissipation rate ε' , adapted from [TATARSKII, 1971]

Based on this energy transfer process, the spectral energy density of the kinetic energy $E'(\kappa)$ and the corresponding spectral density of the energy dissipation rate $\varepsilon'(\kappa)$ is shown schematically in Figure 3.3. Figure 3.3 shows that the run of the function of $E'(\kappa)$ can be split into an energy input subrange, an inertial subrange and a viscous subrange whereby these ranges are separated by the parameters L_0 (outer scale) and l_0 (inner scale). The properties of $E'(\kappa)$ in these subranges are presented in the following sections.

3.2.2 Viscous subrange and dissipation rate

As plotted in Figure 3.3, the spectral density of the energy dissipation rate $\varepsilon'(\kappa)$ is dominant in the viscous subrange. $\varepsilon'(\kappa)$ can be derived from the viscous force term of the Navier-Stokes equation (3.1) using the definition of the turbulent energy E' (3.5) and Taylor's frozen turbulence hypothesis. Thus the spectral density of the dissipation rate is given by [TATARSKII, 1971]:

$$\varepsilon'(\kappa) = 2\nu\kappa^2 E'(\kappa) \quad [\text{m}^3/\text{s}^3] \quad (3.10)$$

When $\varepsilon'(\kappa)$ is integrated over all scales, the rate of loss of turbulent energy, denoted by the dissipation rate ε is calculated by

$$\varepsilon = 2\nu \int_0^{\infty} \kappa^2 E'(\kappa) d\kappa \quad [\text{m}^2/\text{s}^3] \quad (3.11)$$

The kinematic viscosity ν used in (3.11) is specific to each medium. Moreover, in the case of the air, the kinematic viscosity can also be influenced slightly by the density and the temperature of the air [PRUPPACHER, KLETT, 1978]:

$$\nu = \frac{1.718 + 0.0049 (T - 273.15)}{\rho} \cdot 10^{-5} \quad [\text{m}^2/\text{s}] \quad (3.12)$$

with T Temperature [K]
 ρ Density [kg/m^3]

The κ^2 -term of equation (3.10) causes a peak of $\varepsilon'(k)$ in the regions of high frequency κ (Figure 3.3). In other words, the dissipation of kinetic energy takes place mainly at high frequencies, i.e., in the viscous subrange. Thus, the viscous forces dominate the inertia forces of (3.1) and turbulence effects only arises in the range where $\kappa < 2\pi/l_0$. This criterion gives the limit between the viscous subrange and the inertial subrange which is described in section 3.2.3.

3.2.3 Inertial subrange

In the inertial range, the kinetic energy associated with the large anisotropic eddies is transformed without loss of energy $\varepsilon'(\kappa)$ to successively smaller and smaller eddies until finally the diameter is smaller than l_0 . As shown in Figure 3.3, the inertial subrange is a nearly dissipationless subrange of the spectrum. This subrange corresponds to spatial

dimensions of some meters to 2-3 kilometers in the atmospheric boundary, e.g., [BREMER, 1999].

The energy distribution function characterizing the inertial subrange is part of classical turbulence theory [KOLMOGOROV, 1941]. This theory is based on the assumption that on the convection scales denoted as inertial subrange, the constant mean dissipation rate ε is the only relevant parameter. In comparison with the viscous subrange, the spectrum $E'(\kappa)$ of turbulent energy is independent of the viscosity parameter ν in the inertial subrange.

Using Buckingham's Pi theorem which states that physical laws are independent of the form of the units, the energy density spectrum E' is given by

$$E' = E'(\varepsilon, \kappa) = \varepsilon^{\alpha_1} \kappa^{\alpha_2} \Pi_E \quad (3.13)$$

The factor Π_E is a dimensionless numerical coefficient which must be determined by the use of physical experiments. The unknown parameters α_1 and α_2 can be derived from (3.13) by use of the analysis of the dimensions:

$$[\text{m}^3 \text{s}^{-2}]^1 = [\text{m}^2 \text{s}^{-3}]^{\alpha_1} \cdot [\text{m}^{-1}]^{\alpha_2} \quad (3.14)$$

$$\begin{aligned} [\text{m}]: \quad & 3 = -\alpha_2 + 2\alpha_1 \\ [\text{s}]: \quad & -2 = \quad -3\alpha_1 \end{aligned} \quad (3.15)$$

The unknown parameters can be calculated from (3.15). From the solution $\alpha_2 = -5/3$ and $\alpha_1 = 2/3$ it follows:

$$E' = \varepsilon^{2/3} \kappa^{-5/3} \Pi_E \quad \text{for } 2\pi/L_0 < \kappa < 2\pi/l_0 \quad (3.16)$$

The 2/3-relation which was first introduced by KOLMOGOROV [1941] has been confirmed by numerous investigations. An overview is given in [GROSSMANN, 1990] and [BATCHELOR, 1993]. Hereby, the dimensionless constant Π_E in (3.16) appears to be a universal constant with a value close to 1.5 [MONIN, YAGLOM, 1975].

In order to obtain a function of $E'(\kappa)$ which is valid for both viscous subrange and inertial subrange, an additional term $f_\Phi(\kappa)$ is introduced which describes the decay of the upper end of the turbulent energy spectrum:

$$E'(\kappa) = \Pi_E \varepsilon^{2/3} \kappa^{-5/3} f_\Phi(\kappa) \quad \text{for } \kappa > 2\pi/L_0 \quad (3.17)$$

A number of authors have given forms of the spectrum with these properties, such as

$$f_\Phi(\kappa) = \exp\left(-\frac{3\Pi_E}{2} \kappa^{1/3}\right) \quad [\text{PAO, 1965}] \quad (3.18)$$

Further forms of $f_\Phi(\kappa)$ are discussed in section 4.2.

3.2.4 Energy input range

A turbulent medium can be maintained in the turbulent state only if energy is continuously fed into the system so that the energy injection rate equals the rate of dissipation. The energy input occurs at the low frequency end of the curve with size scales on the order of 10 to 10,000 m, e.g., [PANOFSKY, DUTTON, 1984]. The largest eddies are therefore several orders of magnitude larger than the smallest, energy containing eddies. This fundamental physical property of turbulent flow makes it extremely difficult to describe a turbulent flow completely. Additionally, large eddies become more and more anisotropic since obstacles in the boundary layer such as hills, wood, etc., have an increasing influence on the shape of the large eddies. Therefore, the run of $E'(\kappa)$ is uncertain in the range where $\kappa < 2\pi/L_0$. For that reason, the definition of structure constants which are derived from the turbulent energy spectrum must be limited to the inertial subrange (cf. section 3.2.7).

3.2.5 Stationarity of energy spectrum

The studies of the energy transfer process described in the preceding sections is based on the assumption that production and dissipation are often slightly out of balance and the energy spectrum is either statistically stationary or the decay of the energy spectrum is only slow during the observation time. This implies a so-called "equilibrium of turbulence". The equilibrium of turbulence requires that the dissipated energy is compensated by the same amount of energy which the undisturbed laminar flow supplies to the turbulent flow at the limits between laminar and turbulent flow.

If nearly stationary turbulence can be assumed, the classical turbulence theory of Kolmogorov is valid, otherwise the energy transfer process changes. Up to now, little is known about non-equilibrium energy transfer, but further investigations [LUND *et al.* 1998] have shown that the energy transfer process is not fundamentally changed under non-equilibrium conditions. Therefore, the assumption that the energy spectrum closely follows the $\kappa^{-5/3}$ scaling is quite reasonable within the range of $2\pi/L_0 < \kappa < 2\pi/l_0$.

3.2.6 Inner scale

As mentioned in section 3.2.1, the crossover from the inertial subrange to the dissipation range is expected to happen at a scale denoted as l_0 . On smaller scales (i.e., on higher spatial frequencies) of the energy density spectrum, viscosity is effective explicitly. In order to separate the inertial subrange from the viscous range, the Reynolds number is the decisive criterion because turbulence does not occur in the dissipation subrange. The Reynolds number in the inertial subrange is in practice in the range of $Re > 10^6 - 10^7$, whereas the dissipation range yields a Reynolds number smaller than 1.

Hence, the Reynolds number is used to separate the inertial subrange from the dissipation range whereby $Re = 1$ at the crossover. The characteristic length of Re at which the Reynolds number is about 1 defines the inner scale l_0 :

$$Re = \frac{U_{l_0} l_0}{\nu} = 1 \Leftrightarrow \text{Crossover inertial subrange to dissipation range} \quad (3.19)$$

The characteristic velocity U_{l_0} can be obtained as a function of the kinematic viscosity $[\text{m}^2/\text{s}]$ and the dissipation rate $[\text{m}^2\text{s}^{-3}]$. By applying the Pi theorem again, the desired function of the characteristic velocity is given by

$$U_{l_0} = f(\nu, \varepsilon) = \nu^{\alpha_1} \varepsilon^{\alpha_2} \Pi_{l_0} \quad (3.20)$$

The unknown parameters α_1 and α_2 can be obtained by the analysis of the dimensions:

$$[\text{m s}^{-1}]^1 = [\text{m}^2\text{s}^{-1}]^{\alpha_1} [\text{m}^2\text{s}^{-3}]^{\alpha_2} \quad (3.21)$$

$$\begin{aligned} [\text{m}]: \quad & 1 = 2\alpha_1 + 2\alpha_2 \\ [\text{s}]: \quad & -1 = -\alpha_1 - 3\alpha_2 \end{aligned} \quad (3.22)$$

From (3.22) it follows $\alpha_1 = \alpha_2 = 1/4$ and

$$U_{l_0} = \sqrt[4]{\nu\varepsilon} \cdot \Pi_{l_0} \quad (3.23)$$

If (3.23) is applied to (3.19), the inner scale l_0 can be written as

$$l_0 = \Pi_{l_0}^{-1} \cdot \sqrt[4]{\nu^3\varepsilon^{-1}} \quad (3.24)$$

The constant Π_{l_0} is derived in [OBUHKOV, 1949], [TATASRKII, 1971] and [HILL, CLIFFORD, 1978]:

$$\Pi_{l_0}^{-1} = \left[\frac{9\beta_1\Gamma(1/3)}{\text{Pr}} \right]^{3/4} \approx 7.4 \quad (3.25)$$

with Pr Prandtl's number for air: $\text{Pr} = 0.72$
 β_1 Obukhov-Corrsin constant of one-dimensional scalar spectrum:
 $\beta_1 = 0.43$
 Γ Gamma function: $\Gamma(1/3) = 2.679$

The Obukhov-Corrsin constant was first derived by CORRSIN [1951]. Measurements for this constant are given in, e.g., [HILL, 1978]. (There are two definitions of β_1 depending on the definition of the dissipation rate (3.11). These definitions deviate by the factor 2 from each other. Following the formulae of, e.g., [THIERMANN, GRASSL, 1992], $\beta_1 = 0.86$ is applied, cf. (3.65)).

Hence, the inner scale follows from (3.24) and (3.25), thus, l_0 is given by:

$$l_0 = 7.4 \cdot \sqrt[4]{\nu^3\varepsilon^{-1}} = 7.4\eta \quad (3.26)$$

where η Kolmogorov microscale

Regarding the turbulent motions of eddies, the inner scale l_0 has the following meaning: Eddies the scale of which is shorter than l_0 are dissipated by viscosity. For the atmospheric boundary layer, the inner scale is typically $l_0 = 3 \text{ mm} - 10 \text{ mm}$ [THIERMANN, 1990].

3.2.7 Structure constants of velocity and temperature

Besides the inner scale l_0 , the 2/3 power law of (3.16) can also be used to define so-called structure constants such as the structure constant of temperature C_T^2 which are needed to determine the temperature gradient by means of dimensionless profile functions (cf. section 3.4). Whereas the turbulent energy spectrum $E'(\kappa)$ describes the behavior of the velocity fluctuations in the one-dimensional Fourier space, the calculations using the structure constants are performed in real space (cf. section 3.4). Thus, the inverse Fourier transform must be applied whereby this transform provides the structure function of velocity fluctuations $D_u(r)$ as follows, e.g., [CLIFFORD, 1978]:

$$D_u(r) = 2[R_u(0) - R_u(r)] \quad (3.27)$$

$$\text{with } R_u(r) = \int_{-\infty}^{\infty} E'(\kappa) \exp(-i\kappa r) d\kappa = E[u(x) \cdot u(x+r)] \quad (3.28)$$

R_u Autocorrelation of u
 x Coordinate
 r Distance (lag)

(3.27) and (3.28) introduce $D_u(r)$ which is defined by the following statistical quantity:

$$D_u(r) = \left\langle |u(x) - u(x+r)|^2 \right\rangle \quad [\text{m}^2 \text{ s}^{-2}] \quad (3.29)$$

The angular brackets in (3.29) denote a time average. The definition of $D_u(r)$ as presented in (3.29) is based on the assumption of a homogeneous and locally isotropic, random process whereby $D_u(r)$ is independent of x .

Within the inertial subrange (section 3.2.3), the dissipation rate ε is the only influence coefficient on $E'(\kappa)$. Therefore, due to the integration in (3.28), the structure function $D_u(r)$ of the velocity field only depends on ε and r . Thus, (3.31) can be derived by means of the following dimensional analysis:

$$[\text{m}^2 \text{ s}^{-2}]^1 = [\text{m}^2 \text{ s}^{-3}]^{\alpha_1} \cdot [\text{m}^1]^{\alpha_2} \quad (3.30)$$

$$D_u(r) = \Pi_u \varepsilon^{2/3} r^{2/3} \quad (3.31)$$

The structure constant C_u^2 resumes the constant coefficients of (3.31), thus the structure function and the structure constant can be expressed as

$$D_u(r) = C_u^2 r^{2/3} \quad \text{for } L_0 > r > l_0 \quad (3.32)$$

$$C_u^2 = \Pi_u \varepsilon^{2/3} = D_u(r) \cdot r^{-2/3} \quad (3.33)$$

The structure constant of temperature C_T^2 can be derived in a similar manner. Hereby, the power spectrum Φ_T with the property

$$\Phi_T(\kappa) \propto \kappa^{-5/3} \quad \text{for } 2\pi/L_0 < \kappa < 2\pi/l_0 \quad (3.34)$$

is introduced which states that fluctuations of the temperature associated with the same turbulent flow as used in (3.16) inherit also the same power spectrum. Therefore, the structure constant of temperature C_T^2 can be obtained from (3.34) and yields:

$$C_T^2 = D_T(r) \cdot r^{-2/3} \quad \text{for } L_0 > r > l_0 \quad (3.35)$$

with C_T^2 Structure constant of temperature $[\text{K}^2 \cdot \text{m}^{-2/3}]$

$$D_T(r) = \left\langle |\theta(x) - \theta(x+r)|^2 \right\rangle \quad [\text{K}^2] \quad (3.36)$$

θ Potential temperature [K]

As presented in the following sections, the structure constant of temperature C_T^2 is Monin-Obukhov similar and is applied therefore to the determination of temperature gradients by means of the Monin-Obukhov similarity.

3.3 Monin-Obukhov similarity

3.3.1 Scaling parameters

As mentioned in section 2.4, the description of turbulent transport processes is important for refraction detection since these processes are related to gradients of temperatures, pressures and moistures wherein the gradient of temperature is predominant. As described in section 2.4.2, the temperature gradient is mainly determined by the sensible heat flux, cf. equation (2.29). However, (2.29) is not sufficient for the determination of the temperature gradient. In order to overcome this problem, the theory of Monin-Obukhov similarity can be utilized which was introduced by MONIN and OBUKHOV [1954]. This similarity theory uses scaling quantities such as the Obukhov length to determine the temperature gradient and to characterize stable, unstable and neutral stratification whereby these types of stratification have already been introduced in section 2.4.1.

The Obukhov length is related to the turbulent energy transport, which is modelled as follows: Atmospheric turbulence consists of mechanical turbulence, driven by vertical shear and the wind, dissipation, and thermal turbulence such as heat convection, generally driven by sensible heat flux. Thus, an equilibrium of energy is given by [e.g., OHMURA, ROTACH, 1997]:

$$\frac{dE'}{dt} = \underbrace{\tau_s \frac{d\bar{u}}{dz}}_{\text{Windshearing}} - \underbrace{\varepsilon}_{\text{Dissipation}} - \underbrace{\frac{d\varphi_g}{dt}}_{\text{Gravitation}} \quad (3.37)$$

$$\text{with } \tau_s = -\overline{\rho u'w'} \quad (3.38)$$

$$\frac{d\phi_g}{dt} = -g\overline{\rho'w'} = -g\frac{H}{Tc_p} \tag{3.39}$$

- with
- τ_s Shearing stress or momentum flux [N/m^2]
 - u' Randomly fluctuating wind component in horizontal direction [m/s]
 - w' Randomly fluctuating wind component in vertical direction [m/s]
 - ϕ_g Gravitation potential [J]
 - ρ' Randomly fluctuating density [kg/m^3]
 - H Sensible heat flux [$\text{Jm}^{-2}\text{s}^{-1}$]
 - c_p Constant-pressure heat capacity of air [$\text{J kg}^{-1} \text{K}^{-1}$]

The solution of (3.39) requires an approximate model of the vertical distribution of mean wind. The phenomenological theory of PRANDTL [1932] assumes a logarithmic profile given by:

$$\frac{d\bar{u}}{dz} = \frac{u_*}{k_k z} \tag{3.40}$$

with $u_* = \sqrt{\frac{\tau_s}{\rho}} = \sqrt{-\langle u'w' \rangle}$ (3.41)

- k_k Von Kàrmàn constant: $k_k = 0.4$
- u_* Friction velocity [m/s]

The product l_{Pr} with

$$l_{Pr} = k_k Z \tag{3.42}$$

is known as the Prandtl "mixing length" which can be interpreted as follows: The mean velocity of a gas molecule is assumed to run in the horizontal direction. However, when a random fluctuation of velocity displaces the gas molecule in the z -direction, the molecule covers the mixing length l_{Pr} until it has been mixed within its neighborhood, i.e., the molecule has delivered the impulse in z -direction to neighboring molecules. The concept of the Prandtl mixing length assumes that the turbulence is stationary (section 3.2.5). Moreover it assumes the ground to be horizontal and flat which can only be fulfilled approximately in geodetic practice.

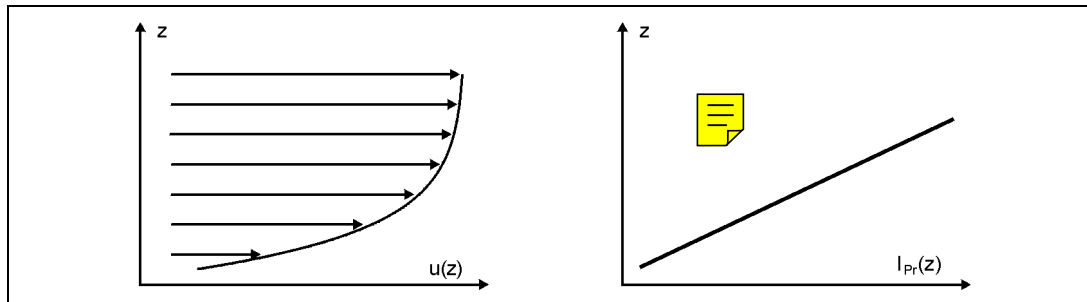


Figure 3.4: Logarithmic velocity profile and the Prandtl mixing length (schematically)

The logarithmic profile defined by (3.40) is only valid under neutral conditions of the atmospheric boundary layer, i.e., the sensible heat flux H is zero. Moreover, (3.40) assumes that turbulence is generated mechanically and the gradients of wind are linear to the friction velocity. Thus, equation (3.40) must be generalized with the use of (3.37). From (3.37), (3.39), and (3.40) follows

$$\frac{dE'}{dt} = \tau_s \frac{u_*}{k_k z} - \underset{\approx 0}{\varepsilon} + g \frac{H}{T c_p} \quad (3.43)$$

(3.43) depends on the height z . The Obukhov length L_{MO} is defined as $L_{MO} = z$ if the equilibrium of (3.43) is in steady state, i.e., $dE'/dt = 0$ [OBUKHOV, 1941]. Neglecting the dissipation rate ε , the Obukhov length can be derived from (3.41) and (3.43), thus L_{MO} is given by:

$$L_{MO} = - \frac{u_*^3 \overline{\rho T} c_p}{k_k g H} \quad (3.44)$$

The sensible heat flux H depends on the difference between surface temperature and temperature aloft. If the effects of humidity on buoyancy are neglected, the Obukhov length becomes:

$$L_{MO} = - \frac{u_*^2 \overline{T}}{k_k g T_*} \quad (3.45)$$

$$\text{with } T_* = \frac{\langle T'w' \rangle}{u_*} \approx \frac{H}{u_* \overline{\rho} c_p} \quad (3.46)$$

T_* Temperature scale

The Obukhov length is independent of height and is therefore suited for a length scale to model turbulent structures in a way similar the scale factor Λ used in fractal theory (cf. Appendix A). As presented in (3.44), the Obukhov length depends on the sensible heat flow H which defines the stratification of the atmospheric boundary layer (section 2.4.1). For this reason, the Obukhov length is also used as a criterion to distinguish stable stratification from unstable stratification:

$$\begin{aligned} L_{MO} < 0 & \Leftrightarrow \text{Unstable stratification (usually during daytime)} \\ L_{MO} > 0 & \Leftrightarrow \text{Stable stratification (inversion, night time)} \\ L_{MO} = 0 & \Leftrightarrow \text{Neutral stratification (transition)} \end{aligned} \quad (3.47)$$

But the classification of (3.47) should be applied with caution because the original definition of stratification used to classify atmospheric boundary layers is characterized by the sensible heat flux H as described in (2.27).

The derivation of the Obukhov length neglects the influence of dissipation as shown in (3.43). Moreover, the assumption of (3.40) is only an approximation valid for neutral stratification. For these reasons, [WYNGAARD *et al.*, 1971] introduced the flux-

Richardson number R_f as a more suitable stability criterion for flux-profile relationships in the atmospheric surface layer. The flux-Richardson number R_f is defined by [RICHARDSON, 1920]:

$$R_f = -g \frac{H}{\bar{T} u_*^2 c_p \left(\frac{du}{dz} \right)} \approx g \frac{\frac{d\bar{T}}{dz} + \Gamma_d}{\bar{T} u_*^2 \left(\frac{du}{dz} \right)^2} \quad (3.48)$$

Thus the stability criterion using the flux-Richardson number R_f is given by:

$$\begin{aligned} R_f < 0 & \Leftrightarrow \text{Unstable stratification (day time)} \\ R_f > 0 & \Leftrightarrow \text{Stable stratification (inversion, night time)} \\ R_f = 0 & \Leftrightarrow \text{Neutral stratification (transition)} \end{aligned} \quad (3.49)$$

For example, during day time the temperature gradient $d\bar{T}/dz$ is normally negative. Thus, the flux-Richardson number is also negative. Normally, the exact value of the flux-Richardson number R_f has no importance to the user in geodesy with the exception discussed in section 3.6. The decisive criterion is only the sign of R_f . The reason is that, depending on the stratification (unstable or stable), different dimensionless profile functions for structure parameters and temperature must be applied (cf. section 3.3.2). Using the Obukhov length as a scale factor, these profile functions allow the determination of the effective temperature gradient and therefore a correction of refraction influences.

3.3.2 Dimensionless profile functions for structure parameters and temperature
MONIN and OBUKHOV [1954] based the Monin-Obukhov similarity theory on the assumption that the dimensionless ratio ζ given by

$$\zeta = \frac{z}{L_{MO}} \quad (3.50)$$

defines the surface-layer stability, which expresses the relative efficacy of buoyancy and shear in producing turbulence. In this case, Monin-Obukhov similarity theory implies that the wind shear du/dz becomes a universal function $\varphi_M(\zeta)$ of ζ , if the momentum flux is scaled with a typical scale parameter u_* :

$$\frac{k_k z}{u_*} \cdot \frac{du}{dz} = \varphi_M(\zeta) \quad (3.51)$$

with φ_M Dimensionless profile function of wind shearing

With respect to (3.40), the dimensionless profile function for neutral stratification is defined by:

$$\varphi_M(0) = 1 \quad (3.52)$$

The Monin-Obukhov similarity theory can be extended to other quantities under the assumption that a dimensionless profile function $\varphi(\zeta)$ is determinable and sufficiently models the quantity. In doing so, the similarity theory offers a description of the common-behavior of the desired quantity (e.g., temperature gradient) by an universal function which is empirically determined. This function is universally valid, if the quantity is properly scaled. In the scope of refraction detection, the mean potential temperature gradient $d\theta/dz$ can be derived using the dimensionless function for the sensible heat flux [MONIN, OBUKHOV, 1954]:

$$\frac{k_k z}{T_*} \cdot \frac{d\theta}{dz} = \varphi_h(\zeta) \quad (3.53)$$

With φ_h Dimensionless profile function of sensible heat flux

In order to obtain φ_h , it is common to expand the universal function in powers of ζ and fitting the results to observations. Since the direction of the flux depends on the stratification (stable / unstable), different profile functions are usually given and are distinguished into the two cases $L_{MO} < 0$ and $L_{MO} > 0$. BUSINGER *et al.* [1971] suggested for the wind profile similarity:

$$\begin{aligned} \varphi_M &= (1-16\zeta)^{-1/4} & L_{MO} < 0 \\ \varphi_M &= 1+5\zeta & L_{MO} > 0 \end{aligned} \quad (3.54)$$

DYER [1974] and BRUNNER [1979] suggested for the temperature profile similarity:

$$\begin{aligned} \varphi_h &= \varphi_M^2 = (1-16\zeta)^{-1/2} & L_{MO} < 0 \\ \varphi_h &= \varphi_M = 1+5\zeta & L_{MO} > 0 \end{aligned} \quad (3.55)$$

The investigation on the profile functions is not yet finished. The re-evaluation of HÖGSTRÖM [1988] showed that φ_h should be slightly modified as follows:

$$\begin{aligned} \varphi_h &= (1-12\zeta)^{-1/2} & L_{MO} < 0 \\ \varphi_h &= 1+7.8\zeta & L_{MO} > 0 \end{aligned} \quad (3.56)$$

The differences of the profile functions arose because the amount of the von Kàrmàn constant k_k was not known exactly. Using $k_k = 0.4$, (3.56) can be expected to confidentially determine the temperature gradient in the scope of this research work. In order to validate this statement, a comparison between (3.55) and (3.56) is discussed in section 7.3, whereby this comparison is based on the temperature gradient measurements in the field experiments of section 7.2. If the temperature profile function and the Obukhov length L_{MO} are given, the corresponding gradient $d\theta/dz$ of potential temperature can be calculated using (3.45) and (3.53) (cf. section 3.4). In this regard, the determination of L_{MO} is required using the dimensionless profile functions of the dissipation rate $\varphi_\epsilon(\zeta)$ (3.60) and the temperature structure constant $\varphi_{CT}(\zeta)$ (3.65) as explained in section 3.4.

3.4 Calculation of refraction angle using Monin-Obukhov similarity

As presented in section 2.1 the temperature gradient dT/dz is the decisive parameter for the calculation of the refractive index gradient and the refraction angle. Assuming the

Monin-Obukhov similarity theory is valid, the mean temperature gradient follows from (2.28), (3.45), (3.46), (3.51), and (3.53) as follows:

$$\frac{d\bar{T}}{dz} = \frac{T_*}{k_k z} \varphi_h \left(\frac{z}{L_{MO}} \right) - \Gamma_d \quad (3.57)$$

$$\text{with } T_* = -\frac{u_*^2 \bar{T}}{k_k g L_{MO}} \quad (3.58)$$

The friction velocity u_* and the Obukhov length L_{MO} must be derived from quantities which can be measured using field instruments. Hereby, u_* (3.41) and the temperature scale T_* (3.46) can be determined, e.g., by use of a sonic-anemometer which determines the variances of the wind components and of the temperature. Thus, L_{MO} can be calculated using (3.45) if the temperature scale T_* is determined. But in geodetic practice, neither values for u_* nor L_{MO} are available. In order to express the friction velocity by another equation, the dissipation rate is used, because the dissipation rate can be determined by means of the inner scale (3.26) which can be derived from image processing algorithms (section 4 and 6). Assuming the dissipation rate is Monin-Obukhov similar, the dimensionless profile function of the dissipation rate φ_ε is given by [WYNGAARD, CLIFFORD, 1978]:

$$\varphi_\varepsilon(\zeta) = \frac{k_k z}{u_*^3} \cdot \varepsilon \quad (3.59)$$

In (3.59) the dimensionless profile function is scaled by the friction velocity u_* . In other words, φ_ε only depends on the ratio $\zeta = z/L_{MO}$. In doing so, φ_ε can be expressed by a semi-empirical profile function $\varphi_\varepsilon(\zeta)$ whereby numerous profile functions differing slightly from each other are known in the literature. In this research work, the following functions are applied which have been determined from tower measurements and scintillation data [THIERMANN, GRASSL, 1992]:

$$\begin{aligned} \varphi_\varepsilon &= (1-3\zeta)^{-1} - \zeta & L_{MO} < 0 \\ \varphi_\varepsilon &= (1+4\zeta+16\zeta^2)^{1/2} & L_{MO} > 0 \end{aligned} \quad (3.60)$$

The dissipation rate derived from (3.26) is given by

$$\varepsilon = 7.4^4 \cdot v^3 l_0^{-4} \quad (3.61)$$

where the inner scale is assumed as known with use of a scintillometer (cf. section 5.2) or of other methods based on optical turbulence (cf. section 4).

Thus the problem of calculation of refraction angle is reduced to the determination of the Obukhov length needed as scale parameter in (3.57). Since the Obukhov length depends on the temperature scale T_* as shown in (3.45), an additional profile function is required which contains T_* . For this reason, the structure constant of temperature C_T^2 can be used which is defined by:

$$D_T(r) = C_T^2 r^{2/3} \quad \text{for } L_0 > r > l_0 \quad (3.62)$$

$$\text{with } D_T(r) = \left\langle |\theta(x) - \theta(x+r)|^2 \right\rangle \quad (3.63)$$

D_T Structure function of temperature [K²]
 θ Potential temperature [K]

Here, the structure function of (3.62) is considered in the inertial subrange and the temperature field $\theta(x)$ of (3.63) is assumed to be locally isotropic and homogeneous. Since the structure constant of temperature C_T^2 can be assumed to be Monin-Obukhov similar, the following profile function can be used [WYNGAARD *et al.*, 1971]:

$$\Phi_{CT}(\zeta) = \frac{(k_k z)^{2/3}}{T_*^2} \cdot C_T^2 \quad (3.64)$$

The same experimental investigations as in (3.60) yield the following semi-empirical scaling functions [THIERMANN, GRASSL, 1992]:

$$\begin{aligned} \Phi_{CT} &= 4\beta_1(1-7\zeta+75\zeta^2)^{-1/3} & L_{MO} < 0 \\ \Phi_{CT} &= 4\beta_1(1+2.5\zeta^{3/5})^{1/3} & L_{MO} > 0 \end{aligned} \quad (3.65)$$

with β_1 Obukhov-Corrsin constant with $\beta_1 = 0.86$

Using (3.58), (3.59), (3.61), and (3.64), the following nonlinear equation for $\zeta = z/L_{MO}$ can be formulated [WEISS, 1998]:

$$\frac{(k_k z)^{4/3}}{v^4 T^2 \left(\frac{7.4}{l_0} \right)^{16/3}} \cdot g^2 C_T^2 - \zeta^2 \Phi_{CT}(\zeta) \Phi_\varepsilon(\zeta)^{-4/3} = 0 \quad (3.66)$$

The inner scale l_0 and the structure constant of temperature C_T^2 are determined using measurements of optical turbulence as described in sections 4 where the measuring path runs horizontally in a height of z above ground. If an approximation of L_{MO} is provided, (3.66) can be solved, e.g., with use of the method of generalized reduced gradients (GRG).

Attention should be paid to the sign of L_{MO} since the profile functions are different for $L_{MO} > 0$ (stable stratification) and $L_{MO} < 0$ (unstable stratification). If the Monin-Obukhov length is determined after a few iterations of (3.66), the scale is known for all profile functions based on Monin-Obukhov similarity theory and, thus, the temperature gradient needed for calculation of refraction angle can be determined using (3.57).

3.5 Footprint considerations

The determination of temperature gradients using Monin-Obukhov similarity theory should be interpreted by a quantitative criterion for the representativeness of the flux measurements since the dimensionless profile functions are only valid for locally homogeneous areas. Footprint considerations can provide this criterion. In doing so, foot-

print considerations assume that measurements at a given height in the surface layer are related to the spatial distribution of surface sources which is defined by the source area of the influence of the sensor. This so-called footprint includes an area which is responsible for a specified contribution to the value measured by the sensor. The determination of footprints is useful if the surface is inhomogeneous since footprints allow an indication of the spatial resolution of meteorological observations above inhomogeneous surfaces.

The footprint can be modelled for relatively large-scale and geometrically simple surface inhomogeneities. There are various models of footprint, but, in the following, the description is restricted to a model as presented by [SCHMID, 1994] because it allows practical and descriptive conclusions about the spatial representativeness and the localness of the field measurements. In this regard, this model used for footprints assumes that the surface consists of an infinite array of unit point sources. These sources are weighted in respect to the influence to the sensor. The source weight is small for small separation distances because of the wind moving the meteorological quantities (e.g., fluxes or temperature) away from the sensor. With increasing distance, the source weight increases too and reaches a maximum. If the separation distance to the sensors continues to increase, the source weight falls off again and tends to zero for large distances due to diffusion effects. The equipotential curve of the described source weight function bounds the area of the footprint. The shape is displayed schematically in Figure 3.5.

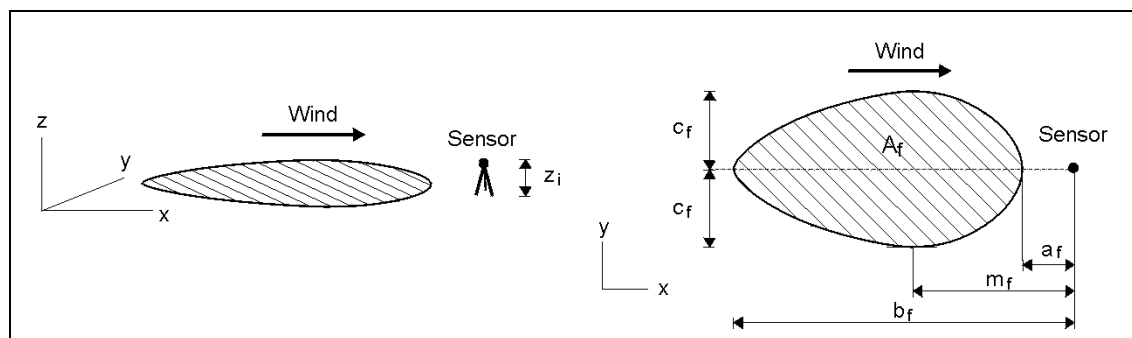


Figure 3.5: Shape of footprint (adapted from [SCHMID, 1994])

Assuming the diffusion perpendicular to the wind direction is Gaussian, the shape of the footprint is axial-symmetric and can be described by the area A_f , the upwind distance a_f between near end of footprint and the sensor, the distance b_f between far end of footprint and the sensor, the distance m_f of maximum source weight of the footprint and the lateral half-width c_f of the footprint. Algorithms and models for the determination of these parameters are given in [SCHMID, 1994]. The decisive quantity for the determination of footprints is the height of the sensor above ground z_i . The area A_f and the lateral half-width c_f linearly increase with an increasing height of instrument. Moreover, the Obukhov length L_{MO} , the surface roughness, the wind direction, the wind speed and the fluctuation of wind also affect the size of the footprint and its position.

In section 7, an estimation of the footprints is integrated into the description of the experiments. The position and size of the footprint enable a decision as to whether the site conditions can be assumed to be homogeneous or inhomogeneous.

3.6 Conclusions

The introduction of the turbulent energy spectrum, structure functions, and the Monin-Obukhov similarity theory represent an efficient method to model the turbulent exchange processes in the atmospheric boundary layer because the similarity relations link scintillation statistics obtained from field measurements to the desired meteorological variables used for refraction correction. Although, it should be emphasized that the structure functions as introduced in (3.29) and (3.63) are only valid if the velocity fields (or the temperature fields, respectively) are locally isotropic and homogeneous.

In order to characterize geometrically the equilibrium of turbulent kinetic energy in the atmospheric boundary layer, the Obukhov length can be applied. This length provides a scale which uses averaged quantities such as T_* and u_* and, thus, operates with a statistical approach to describe turbulence. Since this statistical approach requires that T_* and u_* are stationary during the integral time, the validity of the data available from field experiments can be limited because of the continuous change of the meteorological conditions.

Under the condition that L_{MO} , T_* , and u_* are not zero, these quantities are used as scaling parameters for dimensionless profile functions which determine the momentum flux and sensible heat flux. These dimensionless profile functions based on the Monin-Obukhov similarity theory are only valid in the atmospheric boundary layer where all fluxes being at the same height z are assumed to be constant and independent of the position, e.g., [STULL, 1991]. This assumption is plausible if the source area of the influence of the sensor (footprint) is approximately homogeneous.

The presented algorithm to determine the temperature gradient only holds if the sensible heat flux, the dissipation rate, and the structure constant of temperature are a function of z/L_{MO} , i.e., Monin-Obukhov similar. This similarity theory has been proved in several experiments [BUSINGER *et al.*, 1971] and [DYER *et al.*, 1982]. But in general, many quantities of boundary layer meteorology such as temperature and pressure are not Monin-Obukhov similar.

Since the dimensionless profile functions depend on the Prandtl mixing length, the presented derivation of the Obukhov length can cause the following contradiction. On the one hand, the Monin-Obukhov similarity theory uses the Prandtl's logarithmic velocity profile in the calculation of kinetic energy and, at the same time, this similarity theory generates a velocity profile which differs from logarithmic profile. The contradiction only disappears in the case of neutral stratification, i.e., $\phi_M(0) = 1$.

Herein, the flux-Richardson number quantifies the deviation of the actual stratification (i.e., $R_f > 0$ or $R_f < 0$) from the neutral stratification ($R_f = 0$). For this reason, it would be sensible to replace $\zeta = z/L_{MO}$ by $\zeta' = R_f$ using the relation

$$R_f = \frac{z}{L_{MO}\phi_M(\zeta)} \quad (3.67)$$

The derivation of (3.67) is given by definitions provided in (3.45), (3.46), (3.48), and (3.55). The influence of this correction (3.67) on the results evaluated from field meas-

urements is discussed in section 7.3. As is mentioned there, a comparison between the data processed using R_f with those processed using L_{MO} does not yield more accurate results.

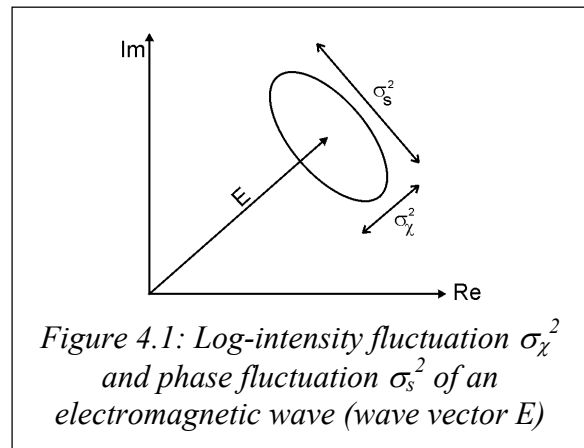
The dimensionless profile function φ_h (3.53) for the determination of temperature gradients is based on the sensible heat flux H . However, in addition to H , the latent heat flux L_{ET} is also part of the energy transfer processes as presented in section 2.4.1, i.e., moisture effects can affect the determination of temperature gradients. Further investigations are still in process to check if additional moisture measurements are needed [WEISS *et al.*, 1999].

4 Optical turbulence

4.1 Phenomena of optical turbulence

The determination of refraction angles using temperature gradients and Monin-Obukhov similarity theory requires the calculation of the structure constant C_T^2 and the inner scale l_0 , cf. (3.66). These quantities can be determined using the effects of optical turbulence. Optical turbulence is a phenomena of waves propagating through turbulent media. The following paragraphs summarize essential elements of this theory [CLIFFORD, 1978] needed for refraction analysis.

Optical waves traversing a turbulent propagation medium develop spatial patterns of irradiance and phase fluctuations since turbulent exchange processes such as convection induces random irregularities in the atmosphere's index of refraction. Optical turbulence is usually understood as a regime of the light propagation medium characterized by intense refractive index fluctuations in both time and space over a large range of scales. The phenomena of optical turbulence can be classified into phase fluctuations and fluctuations of the intensity of light beams (Figure 4.1).



Phase fluctuations σ_s^2 are perceived in the plane of the receiver as follows: Random distortions of the incoming wave front cause slight image motion and image blurring in the plane of the imaging sensor (Figure 4.2).

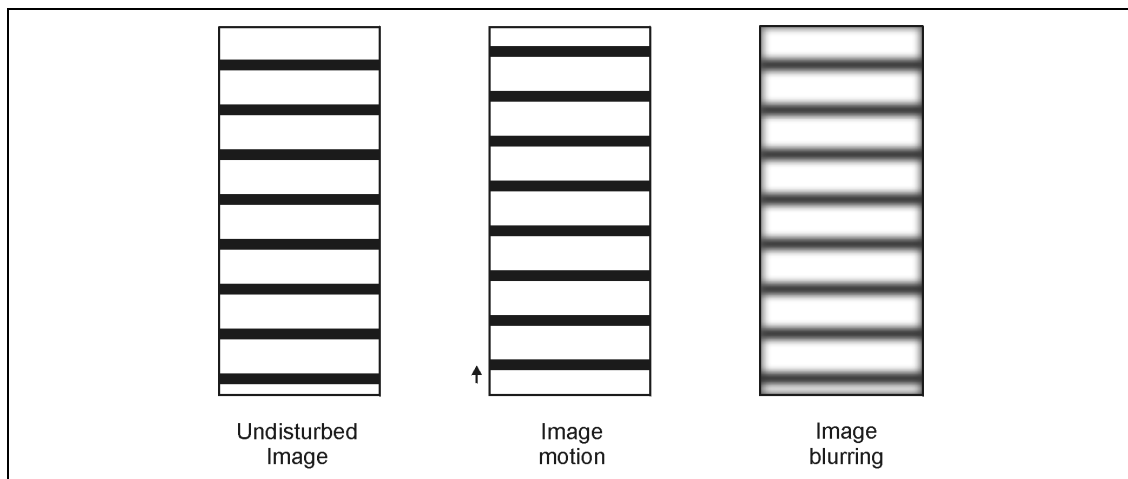


Figure 4.2: Effects of optical turbulence on one-dimensional pattern grabbed by an imaging system (schematically)

Intensity fluctuations can be perceived as temporal variations of the received irradiance of the light beam. Phenomena of intensity fluctuations are the twinkling of stars or the

irregular change of brightness of pixels in optical imaging systems. Scintillometers (cf. section 5) also utilize intensity fluctuations: These instruments send out laser beams and measure the intensity fluctuations of these beams after propagating through a turbulent medium.

Both phase fluctuations and intensity fluctuations result from refractive index fluctuations. These refractive-index fluctuations are caused by turbulent eddy motions along the propagation path. These eddy motions are generated by temperature and humidity fluctuations. The eddies of these motions act as a collection of converging and diverging lenses which affect the propagation of the light beams.

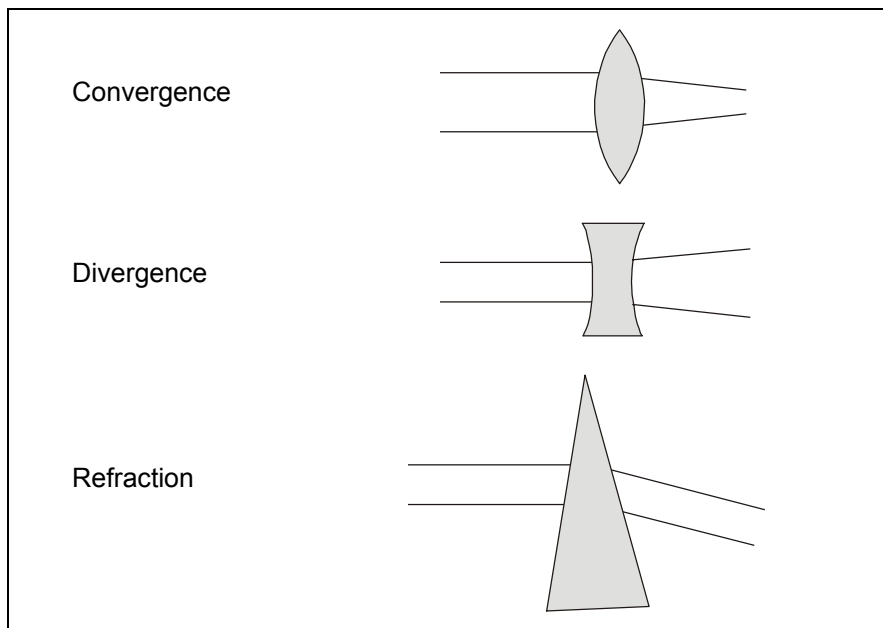


Figure 4.3: Effects of eddies (gray) on light beams

The refractive-index fluctuations are known as optical turbulence and can be characterized by the refractive-index structure constant C_n^2 . As presented in (2.2), the refractive index is mainly influenced by the temperature and pressure. Thus, the refractive-index structure constant C_n^2 can be derived from the structure constant of temperature C_T^2 and from (2.2) as follows:

$$C_n^2 = \left(\frac{\alpha_\lambda p}{T^2} \right)^2 C_T^2 \quad (4.1)$$

(4.1) neglects moisture effects. This neglect is adequate if the wavelength of the measured waves is in the range of visible light [WEISS *et al.*, 1999].

The refractive-index structure constant C_n^2 is not a constant in the mathematical sense. In fact, the structure constant C_n^2 varies in dependence of the turbulent regime of temperature and buoyancy. As the sun rises, convection causes hot turbulent air eddies to rise. The rising turbulent air has a large refractive structure constant in contrast to down-moving, cool air, which is characterized to a very small refractive structure constant [HILL, 1992].

The refractive-index structure constant can be assumed to be constant along the propagation path if the optical path runs parallel to the locally homogeneous ground. When the propagation path is not parallel the refractive-index structure constant may vary because of the altitude dependence of C_n^2 . In general, the refractive-index structure constant decreases with increasing height above the ground [HUFNAGEL 1978].

4.2 Modelling optical turbulence

4.2.1 Refractive index spectrum

Due to the relation (4.1) between the structure constant of temperature C_T^2 and that of refractive index C_n^2 , the properties of C_n^2 follow the same statistical approach as C_T^2 . Analogous to (3.35), the structure constant refractive index spectra can be related to the structure function of refractive index D_n as presented in (3.62) and (3.63):

$$C_n^2 = D_n(r)r^{-2/3} \quad [\text{m}^{-2/3}] \quad \text{for } L_0 > r > l_0 \quad (4.2)$$

$$\text{with } D_n(r) = \langle |n(x) - n(x+r)|^2 \rangle \quad (4.3)$$

D_n Structure function of refractive index

The exponent "-2/3" in (3.62) is a consequence of a dimensional analysis (cf. section 3.2.7). This analysis uses the one-dimensional spectrum of Kolmogorov $\Phi_n(\kappa)$, which describes the fluctuations of the refractive index:

$$\Phi_n(\kappa) \propto \kappa^{-5/3} \quad \text{for } 2\pi/L_0 < \kappa < 2\pi/l_0 \quad (4.4)$$

$$\text{with } \kappa = \frac{2\pi}{\ell} \quad (4.5)$$

ℓ Diameter of turbulent eddy

Hereby, the structure function of the refractive index is related to the Fourier transform of the spectrum $\Phi_n(\kappa)$, e.g., [BELAND, 1993]:

$$D_n(r) = 2[R_n(0) - R_n(r)] \quad (4.6)$$

$$\text{with } R_n(r) = \int_{-\infty}^{\infty} \Phi_n(\kappa) \exp(-i\kappa r) d\kappa \quad (4.7)$$

$$R_n(r) = E[n(x) \cdot n(x+r)] \quad (4.8)$$

These relations reveal that the refractive index spectrum is an essential element to describe the phenomena of optical turbulence. For further investigations in three-dimensional space, the refractive index spectrum $\Phi_n(\kappa)$ must be extended by the introduction of the three-dimensional frequency $\mathbf{\kappa}$. Thus, the three-dimensional refractive index spectrum is given by [CLIFFORD, 1978]:

$$\Phi_n(\mathbf{\kappa}) = \frac{1}{(2\pi)^3} \int_{-\infty}^{\infty} R_n(\mathbf{r}) \exp(-i\mathbf{\kappa} \cdot \mathbf{r}) d^3\mathbf{r} \quad (4.9)$$

Assuming that the random medium is statistically homogeneous and isotropic in each transverse plane of the wave, the autocorrelation function $R_n(\mathbf{r})$ and the refractive index spectrum $\Phi_n(\boldsymbol{\kappa})$ only depend on the magnitude of the vectors $r = |\mathbf{r}|$ and $\kappa = |\boldsymbol{\kappa}|$, respectively. Using (3.62), (4.6), and (4.9), the relationship between the refractive-index structure constant C_n^2 and the refractive index spectrum is principally given under the condition that the Fourier transform in (4.9) converges. Hence, the refractive index spectrum in the inertial range is given by, e.g., [CLIFFORD, 1978]:

$$\Phi_n(\boldsymbol{\kappa}) = 0.033 \cdot C_n^2 \kappa^{-11/3} \quad \text{for } 2\pi/L_0 < \kappa < 2\pi/l_0 \quad (4.10)$$

This equation is theoretically derived and can be applied to other quantities the corresponding spectrum obeys the "2/3"-law of Kolmogorov (3.16) such as the turbulence spectrum of temperature Φ_T , e.g., [HILL, *et al.*, 1980]:

$$\Phi_T(\boldsymbol{\kappa}) = 0.033 \cdot C_T^2 \kappa^{-11/3} \quad \text{for } 2\pi/L_0 < \kappa < 2\pi/l_0 \quad (4.11)$$

Since (4.10) and (4.11) are only valid in the inertial range, the following equation provides a cut-off for the dissipation range and, thus, introduces the inner scale into the function of the refractive index spectrum [TATARSKII, 1961]:

$$\Phi_n(\boldsymbol{\kappa}) = 0.033 \cdot C_n^2 \kappa^{-11/3} \exp\left(-\frac{\kappa^2}{\kappa_m^2}\right) \quad \text{for } 2\pi/L_0 < \kappa \quad (4.12)$$

with $\kappa_m = 5.92/l_0$

Due to the mathematical structure of (4.12), this spectrum can be applied in the whole frequency domain of $\kappa > 2\pi/L_0$. Various authors have extended the Tatarskii-model in respect of the outer scale which limits the inertial subrange at the large-eddy scale L_0 , such as [GARDNER, PLONUS, 1975]:

$$\Phi_n(\boldsymbol{\kappa}) = 0.033 \cdot C_n^2 \left(1 + \kappa^2 L_0^2\right)^{-11/6} \exp\left(-\frac{\kappa^2}{\kappa_m^2}\right) \quad (4.13)$$

The refractive index spectrum has been experimentally determined in field experiments, e.g., in Boulder (CA) [HILL, CLIFFORD, 1978] and [PRIESTLEY, HILL, 1985]. These measurements confirmed the spectra of (4.12) and (4.13) in general, but it is recommended that the decay from the inertial range to the dissipation range be modelled by a more sophisticated model:

$$\Phi_n(\boldsymbol{\kappa}) = 0.033 \cdot C_n^2 \left(1 + \kappa^2 L_0^2\right)^{-11/6} f_\Phi(\boldsymbol{\kappa}, l_0) \quad (4.14)$$

with f_Φ Decay of refractive index fluctuations in dissipation subrange

The function f_Φ is introduced by HILL [1978] in order to model the refractive index spectrum in the range of high Reynolds numbers more precisely. He proposed to derive f_Φ from a second-order, linear, homogeneous differential equation. To avoid solving the

differential equation, a good analytical approximation for f_Φ is given in [CHURNSIDE, 1990]:

$$f_\Phi = \exp(-70.5\kappa^2\eta^2) + 1.45 \cdot \exp(-0.97 \cdot [\ln(\kappa\eta) + 1.55]^2) \quad (4.15)$$

with η Kolmogorov microscale: $\eta = 0.135 l_0$, cf. (3.26)

With regard to the mathematical integration, the approach (4.15) is quite problematical for calculation. Therefore, ANDREWS [1992] suggested a more simplified approach:

$$f_\Phi = 1 + 1.08 \cdot (\kappa/\kappa_l) - 0.254 \cdot (\kappa/\kappa_l)^{7/6} \quad (4.16)$$

with $\kappa_l = \frac{3.3}{l_0}$ (4.17)

Unless otherwise mentioned, the Hill spectrum introduced in (4.14) with the simplification of (4.16) is used for further calculations because of the conformity with results of practical experiments [HILL, CLIFFORD, 1978]. The good conformity of the Hill spectrum bases an a slight bump for κ near the inner scale. This bump is shown in Figure 4.4 where the refractive index spectrum of Hill is compared with the Tatarskii spectrum.

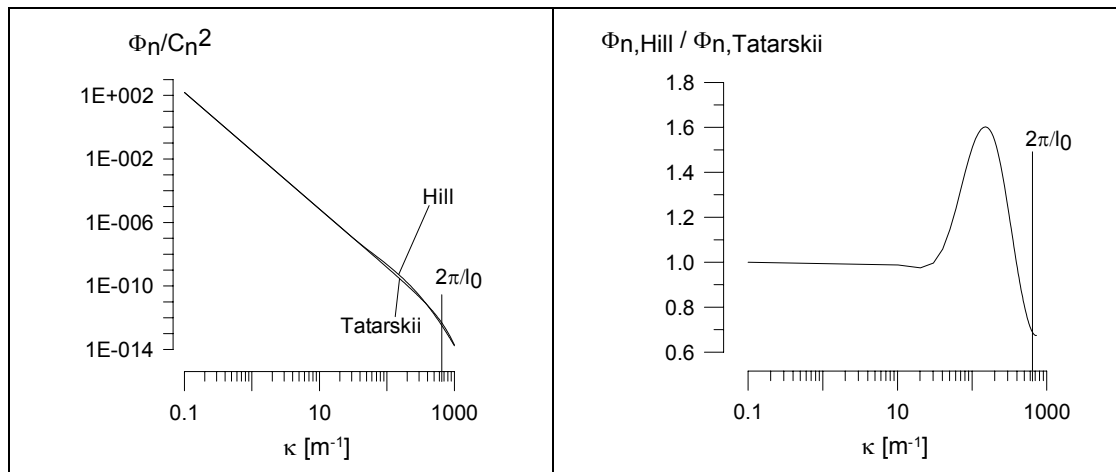


Figure 4.4: Comparison between Hill spectrum and Tatarskii spectrum

4.2.2 Light propagation in turbulent media

The refractive index spectrum obtained in section 4.2.1 provides information about the energy transfer processes in the turbulent medium through which the light beams are propagating. However, the relation between the phenomena of optical turbulence as introduced in section 4.1 and the refractive index spectrum must still be formulated. This relation is given by the Helmholtz equation

$$\nabla^2 \mathbf{E} + k^2 n^2 \mathbf{E} = 0 \quad (4.18)$$

with \mathbf{E} Electric field vector
 k Wave number: $k = 2\pi/\lambda$ (λ : Wavelength)

(4.18) assumes that depolarization terms are negligible for the propagation of optical waves in the earth's atmosphere, e.g., [CLIFFORD, 1978]. The refractive index n used in the Helmholtz equation is a space-variant random variable. Assuming the Reynolds approach of section 3.2.1 is valid for space-variant random variables, n becomes:

$$n = n(\mathbf{r}_T, R) = \bar{n} + n'(\mathbf{r}_T, R) \quad (4.19)$$

with \mathbf{r}_T Transverse vector of the spreading light beam

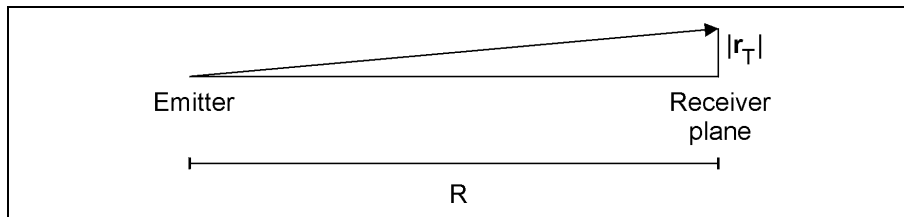


Figure 4.5: Transverse vector of the spreading light beam, adapted from [ANDREWS, PHILLIPS, 1998]

The spectrum of n is given by Φ_n (section 4.2.1). Thus, the Helmholtz equation (4.18) principally provides a relationship between the refractive index spectrum Φ_n and the random amplitude and phase fluctuations of the electric field of the wave propagating through a random medium. However, (4.18) cannot be solved in close form. Therefore, further simplifying approaches must be formulated which then yield only approximate solutions of the Helmholtz equation. Some of these heuristic approaches are summarized in a brief overview presented in Figure 4.6.

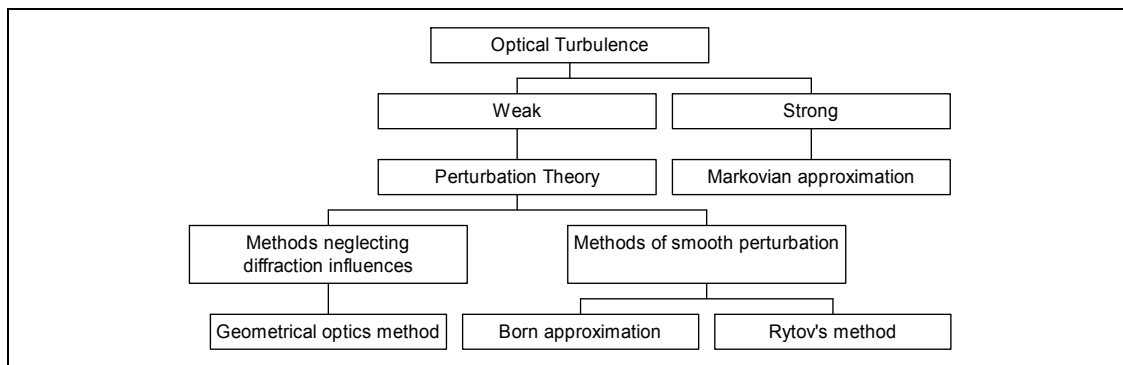


Figure 4.6: Approaches for modelling of light propagation in turbulent media

The approaches of Figure 4.2 mostly treat the optical wave propagation by means of simple models of waves such as an unbounded plane wave or a spherical wave.

The model of plane waves assumes equiphase phase fronts which form parallel planes. Plane waves are mostly applied in astronomy when the scintillations of stars are evaluated.

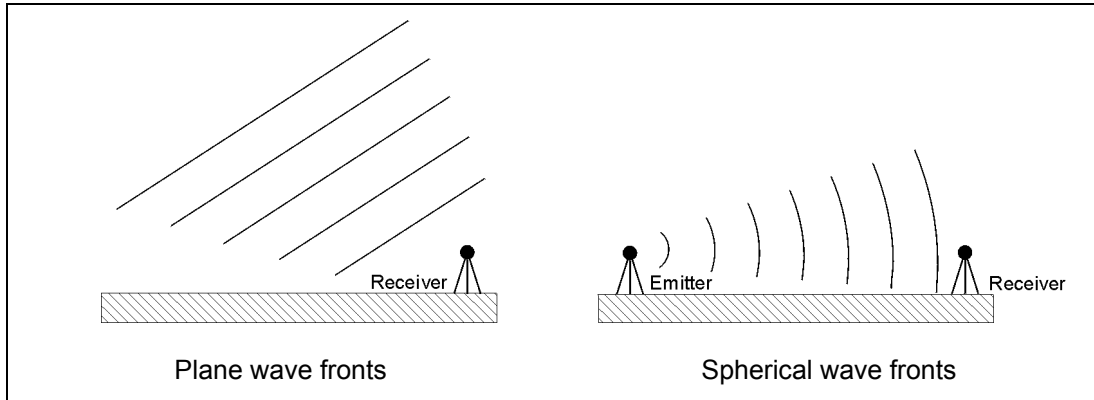


Figure 4.7: Plane waves and spherical waves

In contrast to plane waves, spherical waves consist of equiphase surfaces which are characterized by concentric spheres. The spherical wave model is valid for point emitters of light where the wave spherically emanates from the origin (emitter).

Assuming the propagation path is limited to a few hundred meters, the regime of the so-called weak turbulence prevails (cf. section 4.5.2a). Under these conditions, the Rytov method was found to give good agreement with scintillation data and, therefore, is the standard method used today under these conditions, e.g., [TATARSKII, 1992].

As a method of smooth perturbation (MSP), the Rytov approximation models the propagation of a scalar wave through a medium with large-scale inhomogeneities, i.e., $l_0 \gg \lambda$ where λ is the wavelength. Unlike other methods such as the geometrical-optics method, the Rytov approximation takes into account diffraction effects which arise when the Fresnel radius $(\lambda R)^{1/2}$ is larger than the inner scale l_0 ; e.g., for the propagation path $R = 100$ m and $\lambda = 550$ nm, the Fresnel radius is about 7 mm. Since the inner scale l_0 can fall below 7 mm, e.g., under windy conditions, diffraction effects cannot be neglected in this example.

The Rytov method uses the following approach to provide an approximate solution of the Helmholtz equation (4.18), e.g., [TATARSKII, 1971; ISHIMARU, 1978]:

$$E = A_0 \cdot \exp[\psi(\mathbf{r}_T, R)] \quad (4.20)$$

$$\psi(\mathbf{r}_T, R) = \chi(\mathbf{r}_T, R) + i \cdot S(\mathbf{r}_T, R) \quad (4.21)$$

$$\chi(\mathbf{r}_T, R) = \ln \frac{A(\mathbf{r}_T, R)}{A_0} \quad (4.22)$$

with A_0 Electromagnetic amplitude of incident wave
 $\psi(\mathbf{r}_T, R)$ Complex phase perturbation
 $\chi(\mathbf{r}_T, R)$ Logarithm of amplitude (Log-amplitude)
 $S(\mathbf{r}_T, R)$ Phase
 R Length of propagation path

Considering diffraction effects, the Rytov method introduces the total complex phase perturbation of the electromagnetic wave which is influenced by inhomogeneities of the

refractive index. The Rytov approximation is an acceptable solution of the Helmholtz equation (4.18) under the assumption that the turbulence regime is weak (section 4.5.2a) and backscatter effects are negligible, e.g., [STROHBEHN, 1978].

If these assumptions hold, the Rytov method enables the calculation of the angle-of-arrival fluctuations and intensity fluctuations as presented in the following sections 4.3 and 4.4. The calculations are based on the spectral representation of ψ and depends on the refractive index spectrum and on the assumed wave model (e.g., spherical or plane waves). The spectral representation of ψ leads to complicated integrals, therefore, the following sections only presents the results. A more detailed reference for the derivation of the angle-of-arrival fluctuations and intensity fluctuations is given, e.g., in [ANDREWS, PHILLIPS, 1998] and [LAWRENCE, STROHBEHN, 1970].

4.3 Angle-of-arrival fluctuations for determination of C_n^2

4.3.1 Phenomenon

Angle-of-arrival fluctuations are perceived as, e.g., image blurring and image motions. These fluctuations are related to the wave front of a propagating wave which is a surface of constant phase. Angle-of-arrival fluctuations occur when optical wave fronts passing through irregularities of the refractive index field become distorted.

As radiation with a distorted wave front continues to propagate, its local irradiance also must vary under the focusing and spreading effects of that wave front. These degradation effects cause image blurring and image motions where image motion comes from the influences of large eddies moving across the aperture and image blur arises from the combination of small-scale effects and large-scale effects produced by eddies of different size.

The angle-of-arrival which is a measure for these effects is defined by the angle between the normal to the perturbed phase front and the normal to the unperturbed wave front, i.e., to the tangent of the direction of light propagation. This configuration is displayed in Figure 4.8 where the wave is assumed to be propagating horizontally.

For plane and spherical waves propagating through a statistically homogeneous isotropic medium, the fluctuations in the plane normal to the ray are also isotropic. With regard to the vertical angle-of-arrival α_V and horizontal angle-of-arrival α_H , the random fluctuations become [RYTOV *et al.*, 1987]:

$$\sigma_{\alpha_H}^2 \approx \sigma_{\alpha_V}^2 =: \sigma_\alpha^2 \quad (4.23)$$

This result has also been confirmed as a result of field measurements in Claro / Switzerland [TROLLER, 2000]. As a conclusion for geodetic practice, the measurements are only needed for either the horizontal or the vertical component of the angle-of-arrival, i.e., the use of line scan sensors is possible.

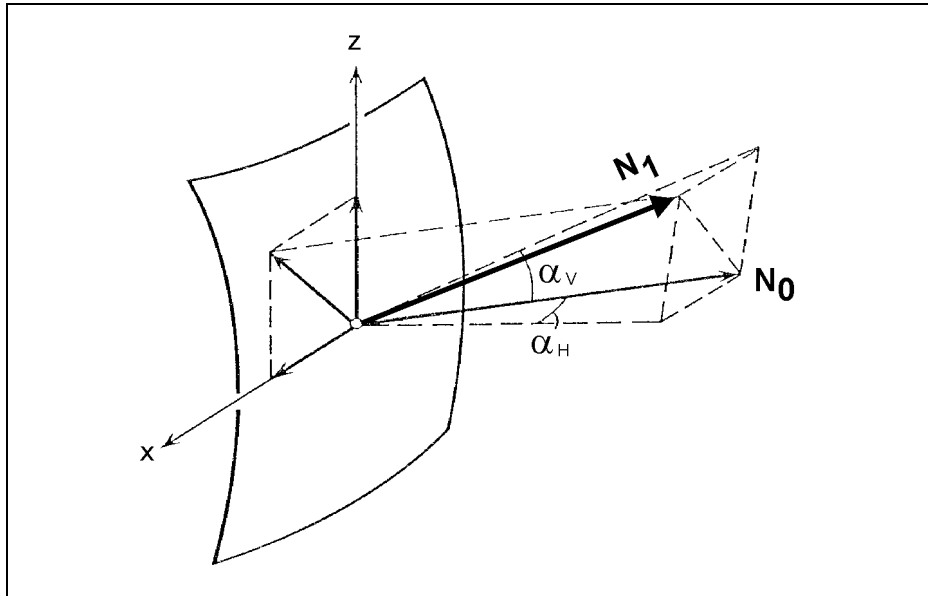


Figure 4.8: Normal vectors of unperturbed (N_0) and perturbed (N_1) wave fronts, adapted from [RYTOV et al., 1978]

4.3.2 Modelling

The modelling of angle-of-arrival fluctuations uses the phase front and its deviation from the unperturbed state. Referring to Figure 4.8, angle-of-arrival fluctuations are caused by random phase shifts whereby these phase shifts are interpreted as the random distortion of the phase front of the wave. Assuming a statistically homogeneous and isotropic random medium, the fluctuation of the phase can be described by means of the following phase structure function $D_S(a)$ defined by:

$$D_S(a) = \langle |S(r) - S(r+a)|^2 \rangle \quad (4.24)$$

with a Diameter of receiver aperture

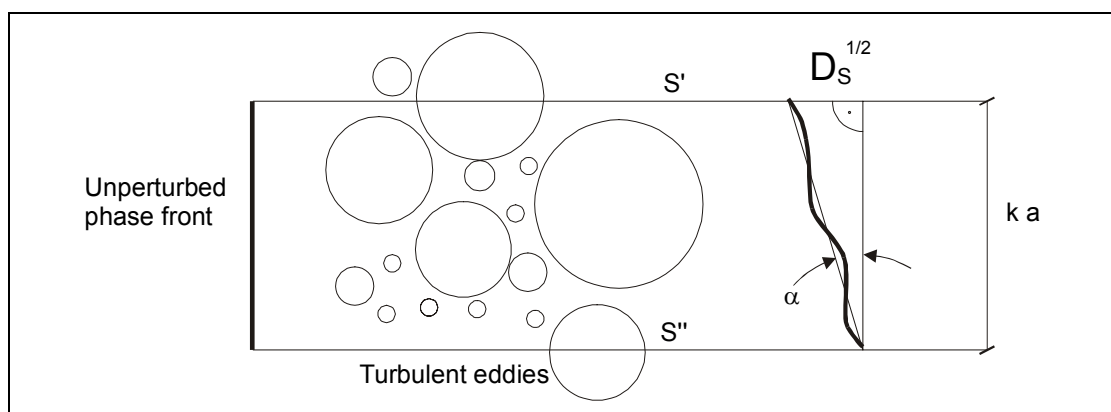


Figure 4.9: Relation between angle-of-arrival α and phase structure function D_S
 S' and S'' denote the phase of the lower and upper end of the wave front

Using the geometrical-optics approximation as shown in Figure 4.9, the angle-of-arrival fluctuations can be expressed by the phase structure function as follows:

$$\sigma_\alpha^2 = \frac{D_s(a)}{k^2 a^2} \quad (4.25)$$

where (4.25) assumes the angle-of-arrival to be small, i.e., $\tan(\alpha) \approx \alpha$. (4.25) implies that the angle-of-arrival is given if the phase structure function is known.

Using the spectral representation of the complex phase perturbation of the Rytov method, TATARSKII [1961] expressed the phase structure function by means of the refractive index spectrum. The following representation of the phase structure function is given by [LAWRENCE, STROHBEHN, 1970]:

$$D_s(a) = 8\pi^2 k^2 \int_0^R \int_0^\infty \kappa \cdot \Phi_n(\kappa) \left[1 - J_0\left(\frac{a\kappa r}{R}\right) \right] \cos^2\left[\frac{\kappa^2 r(R-r)}{2kR}\right] d\kappa dr \quad \text{for spherical waves} \quad (4.26)$$

with J_0 Bessel function of the first kind (order = 0)

and

$$D_s(a) = 4\pi^2 k^2 \int_0^R \int_0^\infty \kappa \cdot \Phi_n(\kappa) [1 - J_0(a\kappa)] \cdot \left[1 + \frac{k}{\kappa^2 R} \sin\left(\frac{\kappa^2 R}{k}\right) \right] d\kappa dr \quad \text{for plane waves} \quad (4.27)$$

The phase structure function as given in (4.26) and (4.27) is valid for statistically homogeneous isotropic media. If the Hill spectrum $\Phi_n(\kappa)$ (4.14) is used, the phase structure function becomes approximately [ANDREWS, PHILIPPS, 1998]:

$$D_s(a) = 1.093 \cdot C_n^2 k^2 R a^{5/3} \left(1 - 0.715 \left(\frac{a}{L_0} \right)^{1/3} \right) \quad \text{for } a \gg l_0 \text{ and spherical waves} \quad (4.28)$$

$$D_s(a) = 2.914 \cdot C_n^2 k^2 R a^{5/3} \left(1 - 0.805 \left(\frac{a}{L_0} \right)^{1/3} \right) \quad \text{for } a \gg l_0 \text{ and plane waves} \quad (4.29)$$

A comparison between (4.28) and (4.29) reveals that the angle-of-arrival fluctuations of spherical waves are about three times smaller than those for the plane wave. This rule holds under the assumption that the source of the spherical wave lies within the randomly inhomogeneous medium and both spherical and plane waves propagate through the same medium and with the same propagation path length R .

Since angle-of arrival fluctuations of an optical wave in the plane of the receiver aperture can be measured as slight motions of image structures, the angle-of-arrival fluctuation can be determined using the focal length f of the imaging system as illustrated in Figure 4.10.

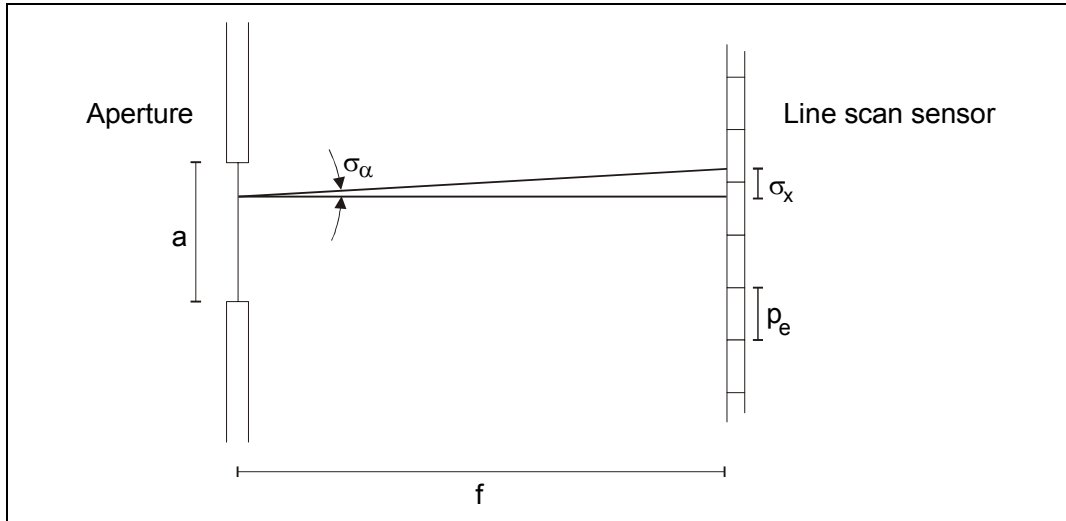


Figure 4.10: Angle-of-arrival fluctuation σ_α^2 and fluctuation of image structures σ_x^2

Using the geometrical relations depicted in Figure 4.10, it follows that:

$$\sigma_\alpha^2 = \frac{p_e^2 \cdot \sigma_x^2}{f^2} \quad (4.30)$$

with f Focal length [m]
 p_e Size of quadratic pixel element [m/pixel]
 σ_x^2 Variance of the motion of image structures [pixel]

The determination of σ_x^2 will be discussed in section 6.4, where edge detection algorithms are described in order to determine σ_x^2 . Using (4.25), (4.28), (4.30), and neglecting the influence of the outer scale L_0 , the structure constant of refractive index follows from [BRUNNER, 1979]:

$$C_n^2 = \frac{\sigma_\alpha^2 a^{1/3}}{1.09R} = \frac{p_e^2 \cdot \sigma_x^2 a^{1/3}}{1.09 f^2 R} \quad (4.31)$$

(4.31) allows a direct determination of C_n^2 without any knowledge about the inner scale l_0 and the outer scale L_0 . The application of (4.31) is only valid if the outer scale is assumed to be very large (i.e., $L_0 \rightarrow \infty$). This assumption concerning the outer scale L_0 and the effect on the determination of C_n^2 will be investigated in section 4.5.2.

(4.31) in combination with (4.1) allows the determination of the structure constant of the temperature fluctuations which is assumed to be Monin-Obukhov similar and which can be used to calculate the temperature gradient as presented in section 3.4. However, as shown in section 3.4, the determination of temperature gradients requires also the knowledge of the inner scale l_0 . Thus, the determination of l_0 is investigated in the following section.

4.4 Intensity fluctuations for determination of inner scale

4.4.1 Phenomena

Intensity fluctuations are perceived as temporal changes of the irradiance of the incoming light beams, e.g., as twinkling of a target or as temporal changes of the brightness of an image. Using CCD sensors, these changes can be measured by the temporal variation of the voltage which is accumulated on each pixel element during the integration time. The intensity fluctuations of a light ray propagating through turbulence can be expressed using the log-amplitude variance σ_χ^2

$$\sigma_\chi^2 = \frac{1}{4} \ln \left(\frac{\sigma_I^2}{\langle I \rangle^2} + 1 \right) \quad (4.32)$$

The normalized intensity fluctuation $\sigma_I^2 / \langle I \rangle^2$ is a measure and provided, e.g., with use of the detectors of a scintillometer as described, e.g., in [HILL, OCHS, 1978], [COULTER, WESELY, 1980], [HILL *et al.*, 1992], [THIERMANN, GRASSL, 1992]

Moreover, the normalized intensity fluctuation can also be determined using image processing algorithms as described in section 6.3 and 6.4.4.b), e.g., when the adaptive Wiener filter or least squares template matching algorithm are applied. These methods estimates the noise variance σ_V^2 of the image signal which yields the normalized intensity variance as follows:

$$\frac{\sigma_I^2}{\langle I \rangle^2} = \sigma_V^2 \quad (4.33)$$

(4.32) and (4.33) yields the log-normal amplitude influenced by the inner scale and by other parameters such as C_n^2 and length of the propagation path. Thus, the determination of the inner scale is based on the measurement of intensity fluctuations and log-normal amplitudes needs a sophisticated model as described in the following section.

4.4.2 Modelling

Intensity fluctuations are associated with a redistribution of the ray energy which arises as a consequence of the focus effects of the turbulent eddies.

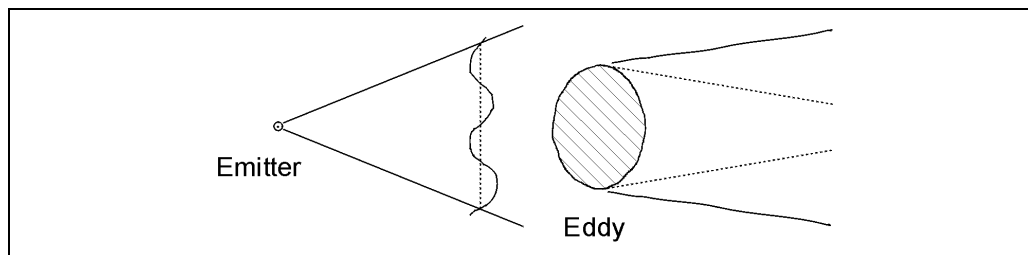


Figure 4.11: Focus effects of eddy on an emitted wave

Since the focus effects are related to the diameter of the turbulent eddies, the intensity fluctuations depend on the spectrum of the refractive index fluctuations Φ_n and, hence,

on the inner scale l_0 . This dependence allows the calculation of the inner scale using the intensity fluctuations and the Rytov approach which provides an approximate solution to the Helmholtz equation as presented in section 4.2.2 under the assumption that log-amplitude fluctuations are small, i.e.,

$$\overline{\chi^2} \ll 1 \quad (4.34)$$

First, a relation between the refractive index fluctuations Φ_n and the log-amplitude variance σ_χ^2 is derived from the second-order spectral representation of the Rytov approximation. Including the refractive index spectrum, these fluctuations can be written with the integral representation as follows [LAWRENCE, STROHBEHN, 1970]

$$\sigma_\chi^2 = 2\pi k^2 R \int_{\kappa=0}^{\infty} \kappa \Phi_n(\kappa) \left(1 - \frac{k}{\kappa^2 R} \sin \left[\frac{\kappa^2 R}{k} \right] \right) d\kappa \quad \text{for plane waves} \quad (4.35)$$

$$\sigma_\chi^2 = 4\pi k^2 \int_{r=0}^R \int_{\kappa=0}^{\infty} \kappa \Phi_n(\kappa) \sin^2 \left[\frac{\kappa^2 r(R-r)}{2kR} \right] d\kappa dr \quad \text{for spherical waves} \quad (4.36)$$

Using the Hill Spectrum given by (4.14), (4.16), and (4.17) the fluctuations of log-amplitude are given by [ANDREWS, PHILLIPS, 1998]:

$$\begin{aligned} \sigma_\chi^2 = 0.965\beta_l^2 \left[\left(1 + \frac{1}{Q_l^2} \right)^{11/12} \left\{ \sin \left(\frac{11}{6} \arctan Q_l \right) + \frac{1.507}{(1+Q_l^2)^{1/4}} \sin \left(\frac{4}{3} \arctan Q_l \right) \right. \right. \\ \left. \left. - \frac{0.273}{(1+Q_l^2)^{7/24}} \sin \left(\frac{5}{4} \arctan Q_l \right) \right\} - \frac{3.50}{Q_l^{5/6}} \right] \quad \text{for plane waves} \end{aligned} \quad (4.37)$$

$$\begin{aligned} \sigma_\chi^2 = 0.965\beta_l^2 \left[0.40 \left(1 + \frac{9}{Q_l^2} \right)^{11/12} \left\{ \sin \left(\frac{11}{6} \arctan \frac{Q_l}{3} \right) + \frac{2.610}{(9+Q_l^2)^{1/4}} \sin \left(\frac{4}{3} \arctan \frac{Q_l}{3} \right) \right. \right. \\ \left. \left. - \frac{0.518}{(9+Q_l^2)^{7/24}} \sin \left(\frac{5}{4} \arctan \frac{Q_l}{3} \right) \right\} - \frac{3.50}{Q_l^{5/6}} \right] \quad \text{for spherical waves} \end{aligned} \quad (4.38)$$

$$\text{with } Q_l = \frac{R\kappa_l^2}{k} \quad (4.39)$$

$$\beta_l^2 = 1.23 \cdot C_n^2 k^{7/6} R^{11/6} \quad (4.40)$$

$$k = 2\pi/\lambda \quad (4.41)$$

In the following, the spherical wave case (4.38) which is assumed to be valid for geodetic applications is used. Basically, (4.38) provides a relation between the (measured) log-amplitude variance σ_χ^2 and the inner scale l_0 . Since this relation (4.38) is not suitable for the efficient computation of l_0 , (4.38) is simplified in the following by the introduction of the auxiliary variables x_c and y_c defined as follows:

$$x_c = \frac{\sigma_\chi^2}{C_n^2} \cdot 10^{12} \quad (4.42)$$

$$y_c = \frac{\sqrt{\lambda \cdot R}}{l_0} \quad (4.43)$$

If (4.38) is evaluated, a function graph can be plotted as shown in Figure 4.12.

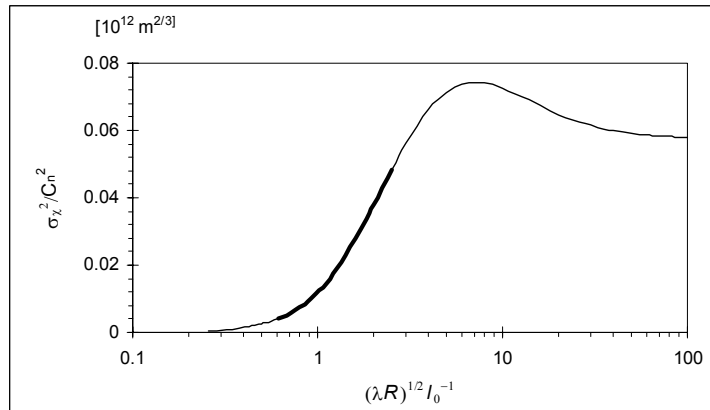


Figure 4.12: Relation between inner scale and log-amplitude fluctuations (spherical waves)

The bold subsection of the graph of Figure 4.12 denotes the range of $(\lambda R)^{1/2} l_0^{-1}$ which is typical for applications in geodesy. Within this range, one-to-one relation between $(\lambda R)^{1/2} l_0^{-1}$ and σ_χ^2 / C_n^2 is available.

The relation between x_c and y_c can be molded into an approximate formula which is valid for the bold range in Figure 4.12. With the assistance of a simulation program (SLS-OPS, Scintec Ltd, Tübingen) based on (4.38), σ_χ^2 can be calculated if λ , R , l_0^2 , and C_n^2 are specified [FLACH, HENNES, 1998]. The output of the simulation is a series of values (x_c, y_c) as shown in Figure 4.13.

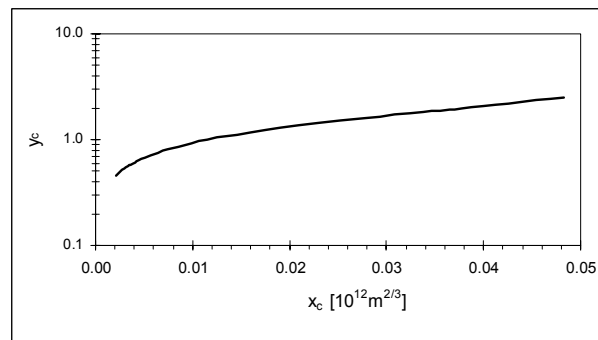


Figure 4.13: Results from simulation

The following empirical function gives a relation between x_c and y_c :

$$y_c = -2.692 - 140.5 x_c + 31.86 x_c^{1/2} + 377.8 x_c^{3/2} - 0.317 \ln(x_c) \quad (4.44)$$

(4.44) has been determined as follows: Assuming l_0 , λ , R , and C_n^2 are known, σ_χ^2 is calculated using (4.38) and the values x_c and y_c are determined using (4.42) and (4.43). These values are displayed in Figure 4.13. The curve in Figure 4.13 can be modelled using a least squares fit which yields the terms in Table 4.1.

Term	Value	Std. deviation
(Intercept)	-2.6919	0.4038
x_c	-140.4709	12.3855
$x_c^{3/2}$	31.8603	2.8071
$x_c^{3/2}$	377.7963	22.5371
$\ln(x_c)$	-0.3170	0.0488

Table 4.1: Estimated parameters and standard deviations

Besides the estimated values, the standard deviations of the parameters are also presented in Table 4.1 to illustrate the quality of the regression. The chosen function (4.44) is advantageous in comparison to high order polynomials since (4.44) is more stable than high order polynomials.

In order to compare the fitted function (4.44) with the original function (4.38) of σ_χ^2 , (4.44) and the corresponding values of (4.38) are presented in Figure 4.14.

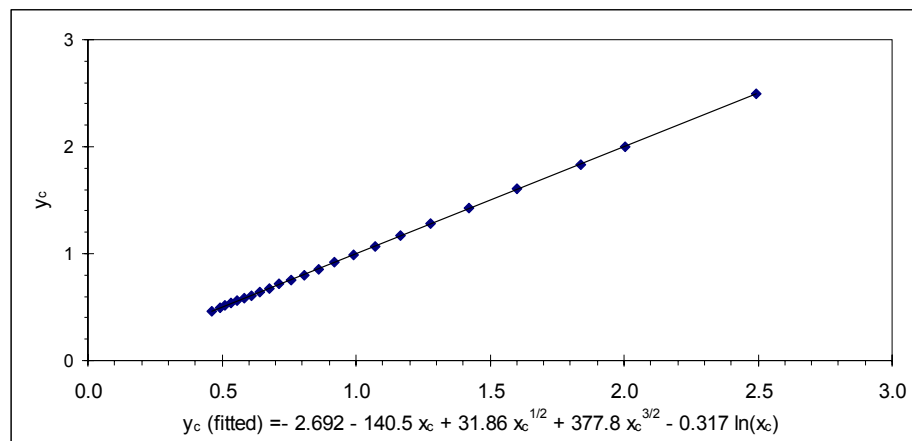


Figure 4.14: Comparison between simulated values y_c and approximation y_c (fitted)

Hence, (4.44) provides a sufficient relation between y_c and x_c in the bold range of Figure 4.12.

Summarizing this section, the inner scale l_0 is calculated as follows

1. Determine C_n^2 using angle-of-arrival fluctuations and (4.31)
2. Calculate the log-amplitude σ_χ^2 using the intensity fluctuation and (4.32)
3. Insert C_n^2 and σ_χ^2 into (4.42) and compute x_c
4. Determine y_c with use of x_c and (4.44)
5. Insert y_c , λ , and R into (4.43) and solve for l_0

From (4.42), (4.43), and (4.44) follows the observation equation for l_0 given by:

$$l_0 = \frac{\sqrt{\lambda \cdot R}}{y_c} = \sqrt{\lambda \cdot R} \cdot \left[-2.692 - 140.5 \cdot \frac{\sigma_\chi^2}{C_n^2} \cdot 10^{12} + 31.86 \cdot \left(\frac{\sigma_\chi^2}{C_n^2} \cdot 10^{12} \right)^{1/2} + 377.8 \cdot \left(\frac{\sigma_\chi^2}{C_n^2} \cdot 10^{12} \right)^{3/2} - 0.317 \cdot \ln \left(\frac{\sigma_\chi^2}{C_n^2} \cdot 10^{12} \right) \right]^{-1} \quad (4.45)$$

Thus, the inner scale can be calculated using the relationship shown in Figure 4.12 if the remaining parameters (λ , R , σ_χ^2 , C_n^2) are known or measured. This procedure is called "inner-scale algorithm" in the following. The inner-scale algorithm which approximates (4.38) is stable since the fitting function converges for all valid input values and, furthermore, this algorithm is advantageous since small deviations caused by the limited accuracy of measurements are not amplified in the algorithm.

4.5 Analysis of accuracy

In general, the quality of the estimation of parameters can be deteriorated by

- random deviations due to the measuring process and the imperfectness of the sensors.
- systematic deviations in cases where the applied model does not entirely hold.

The influence of random deviations can be decreased using sensors which provide results of an adequate accuracy. In this sense, the analysis of random deviations can yield some hints for selecting an appropriate measuring system (section 5). In order to avoid or reduce systematic deviations, the applied model must be refined. However, the refinement often involves the measurement of additional quantities. Both random and systematic deviations are discussed in the following analysis.

4.5.1 Random deviations

In sections 4.3 and 4.4, the structure constant of refractive index C_n^2 and inner scale l_0 are derived from the angle-of-arrival fluctuations and the intensity fluctuations whereby these fluctuations must be determined using imaging sensors and image processing techniques (section 6). In order to analyze the required accuracy of the system, assumptions about the planned experiments and the meteorological conditions are necessary. For this purpose, $R = 75$ m, $\lambda = 550$ nm, $C_n^2 = 0.32$, and $l_0 = 4.6$ mm are assumed whereby C_n^2 and l_0 represent conditions of a sunny summer day. Further, assumptions about the desired accuracy of C_n^2 and l_0 are required. Investigations about the accuracy of C_n^2 and l_0 and their influence on the temperature gradient are presented in [DEUSSEN, 2000]. It was found that the accuracy of C_n^2 and l_0 which is required for the determination of the temperature gradient depends on the actual turbulent conditions.

Since general rules do not exist, the following analysis assumes a required standard deviation of $\sigma_{Cn^2} = 0.032 \cdot 10^{-12} \text{ m}^{-2/3}$ and $\sigma_{l_0} = 0.46$ mm which means a relative accuracy of 10%. Using the law of propagation of variances, the standard deviation of the structure constant C_n^2 follows from (4.31) and is given by:

$$\sigma_{C_n^2} = \frac{a^{1/3}}{1.09R} \sigma_{\sigma_a^2} \quad [10^{-12} \text{ m}^{-2/3}] \quad (4.46)$$

If an aperture of $a = 0.065$ m is assumed, the required accuracy for the angle-of-arrival fluctuations is $6.5 \cdot 10^{-12} \text{ rad}^2$. Therefore, an imaging system with a focal length $f = 500$ mm and a size $p_e = 10^{-5}$ m/pixel of pixel elements must determine the standard deviation of σ_x^2 with an required accuracy of $\sigma_{\sigma_x^2} = 0.016 \text{ pixel}^2$.

The accuracy of the estimation of the inner scale is influenced both by the accuracy of the log-amplitude fluctuations $\sigma_{\sigma_{\chi^2}}$ and of the structure constant $\sigma_{C_n^2}$. Using (4.45) and the values for R , λ , C_n^2 , and l_0 which are assumed above, the standard deviation of the inner scale follows from the law of propagation of variances and is given by:

$$\sigma_{l_0} = \sqrt{(8.4 \cdot 10^{12} \cdot \sigma_{C_n^2})^2 + (2.8 \cdot \sigma_{\sigma_{\chi^2}})^2} \quad [\text{mm}] \quad (4.47)$$

If an accuracy $\sigma_{l_0} = 0.46$ mm is necessary, an accuracy of the log-amplitude fluctuations $\sigma_{\sigma_{\chi^2}} = 13\%$ is required as follows from (4.47). This demand is equivalent to a signal-to-noise ratio (SNR) of 8.8 dB. The SNR and the standard deviation of σ_x^2 can be considered as criteria for the suitability of the imaging systems and the image processing techniques presented in section 5 and 6.

4.5.2 Systematic deviations

a) *Weak turbulence and saturation effects*

Systematic deviations may occur when modelling optical turbulence by Rytov's method of small perturbations as presented in section 4.2. As shown, e.g., in [CLIFFORD, *et al.*, 1973], modelling optical turbulence requires the distinction of weak and strong turbulence. This distinction is essential since, within the range of weak turbulence, the intensity fluctuations increases with the path length and with the strength of turbulence until it reaches the "saturation" range and, thus, the beginning of the regime of strong turbulence.

This description of intensity fluctuations is illustrated in Figure 4.15. The abscissa shows the Rytov variance β_0^2 defined by, e.g., [TATARSKII, 1992], [ANDREWS, *et al.*, 1998] or [AZOULAY *et al.*, 1988]

$$\beta_0^2 = 1.23 \cdot C_n^2 k^{7/6} R^{11/6} \quad \text{for plane waves} \quad (4.48)$$

$$\beta_0^2 = 0.496 \cdot C_n^2 k^{7/6} R^{11/6} \quad \text{for spherical waves} \quad (4.49)$$

$$\text{with } k = 2\pi/\lambda \quad (4.50)$$

λ Wavelength of light

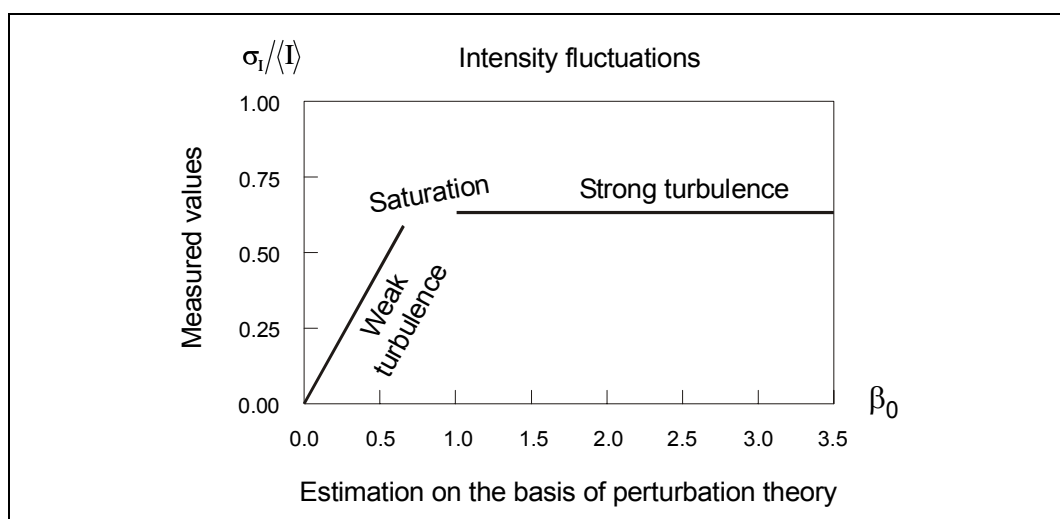


Figure 4.15: Comparison between measured intensity fluctuations and estimated values (Data: [TATARSKII, 1992])

The ordinate of Figure 4.15 displays the normalized intensity fluctuations. The graph of Figure 4.15 is interrupted at the transition from weak turbulence to strong turbulence because there is still a lack of an accepted theoretical description of the saturation phenomenon. Nevertheless, the Rytov variance is a measure of the strength of fluctuations by the medium in this type of wave propagation and allows the distinction between weak and strong turbulence. If $\beta_0^2 < 0.6$, the criterion of weak turbulence is fulfilled as given in Figure 4.15 and the methods presented in section 4.3 and 4.4 can be applied.

The saturation phenomenon as described above is especially important for the determination of the inner scale using the intensity fluctuations since the measured intensity fluctuations lose their significance if the range of weak turbulence is exceeded. During day-time (i.e., $C_n^2 < 10^{-12} \text{ m}^{-2/3}$), the assumption of weak turbulence is normally valid for a maximal length of propagation path $R_{max} = 170 \text{ m}$ as follows from (4.49). For spherical waves, the relation between C_n^2 and R_{max} is plotted in Figure 4.16.

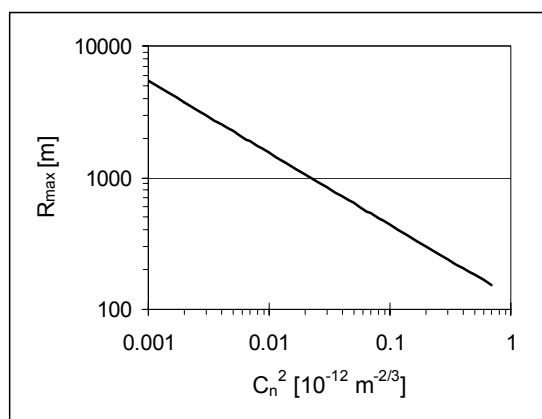


Figure 4.16: Maximal length of propagation path R_{max} for weak turbulence

As shown in Figure 4.16, an increase of C_n^2 requires a decrease of the measuring path. Practical field experiments should take account of this limitation due to saturation. In contrast to intensity fluctuations, phase fluctuations continue to increase with increasing path length, although, the theoretical propagation of phase fluctuations in the strong turbulence range has not been fully investigated yet [GARDNER, PLONUS, 1975]. But this is not relevant, since, as mentioned above, the measurement technique is more restricted by the saturation of the intensity fluctuations than by the phase fluctuations.

b) Aperture averaging

In the atmosphere, the light beams are subject to multiple scattering and the propagation path varies randomly. Strictly speaking, the spherical-waves equations as given, e.g., in (4.36) assume a point source and a point receiver which collects the radiation. But dealing with practical applications, the entrance aperture of the receiver has a finite effective diameter d_e . Whether a receiver can be approximated by a point receiver depends on its lateral dimension relative to the lateral dimensions of the intensity fluctuations of the corresponding light beams. In other words, aperture averaging may arise if the aperture is not relatively small to the Fresnel radius $(\lambda R)^{1/2}$ since the effective diameter d_e acts as a lowpass filter [FRIED, 1967].

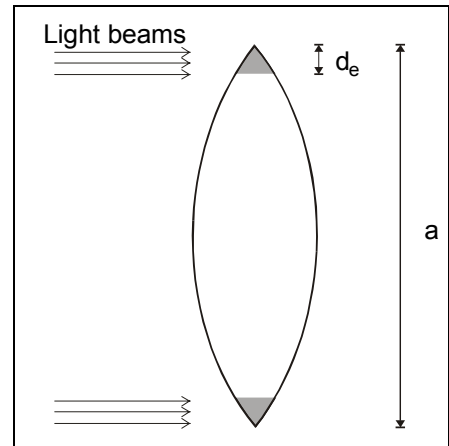


Figure 4.17: Effective diameter

Aperture averaging causes a spatial average of the incident irradiance over the aperture and, thus, weakens the scintillation effects. These effects can be modelled by the attenuation coefficient for aperture averaging A_{sph} which is introduced for spherical waves by ANDREWS [1992] as follows:

$$A_{sph} = \left[1 + 0.333 \left(\frac{k \cdot d_e^2}{4R} \right)^{5/6} \right]^{-7/5} \quad (4.51)$$

with d_e Effective diameter of detector

The attenuation coefficient is to be multiplied with the log-amplitude fluctuations obtained by (4.38). Hence, the log-amplitude attenuates as illustrated in Figure 4.18.

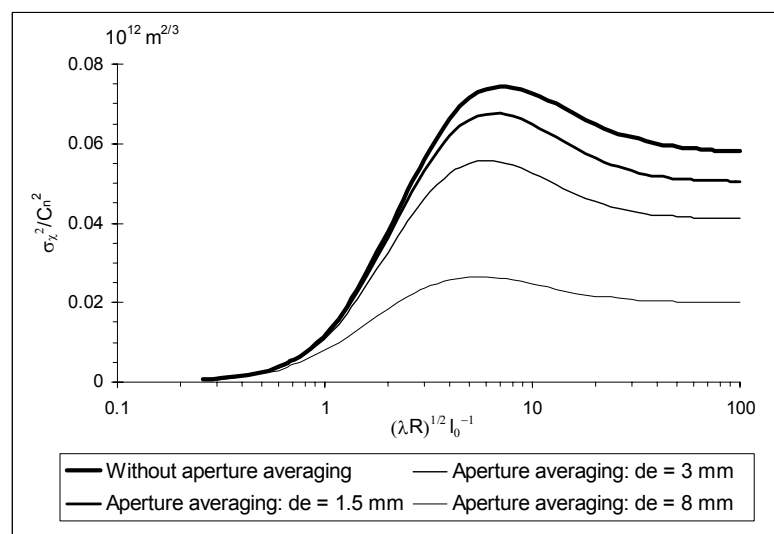


Figure 4.18: Influence of aperture averaging on log-amplitude fluctuations

For this research work, aperture averaging effects are neglected because of the absence of an exact model which estimates the effective diameter d_e . In order to reduce aperture averaging effects, image sensors were selected in section 5 which provides a considerably higher sensitivity than the required SNR of 8.8 dB (section 4.5.1), such as, e.g., the video theodolite TM3000V with SNR = 46 dB (CCD camera). Due to the higher sensitivity, the determination of σ_χ^2 as the input for the determination of l_0 is expected to be still possible. Further research work should investigate the aperture averaging problem in more detail.

c) Outer scale

The outer scale L_0 bounds the anisotropic turbulence range and the upper end of the inertial subrange, i.e., the inertial subrange copes with eddies the diameter of which is larger than L_0 . As mentioned in section 4.3.2, the outer scale L_0 is assumed to influence the angle-of-arrival fluctuations (4.26) and (4.27) since L_0 appears in the refractive index spectrum $\Phi_n(\kappa)$ as given by (4.14) and, therefore, L_0 is also included in (4.28) and (4.29). Thus, the influence coefficient for outer scale c_L is introduced in order to model this influence whereby c_L is defined by

$$c_L = \frac{\sigma_\alpha^2 a^{1/3}}{C_n^2 R} \quad (4.52)$$

Assuming L_0 to be negligible, the influence coefficient for outer scale c_L is 1.09. The value 1.09 follows from (4.31). In the literature, other factors are reported, too, e.g., GURVICH *et al.* [1968] introduced $c_L = 1.05$. The relation between c_L and L_0 can be determined using (4.28) and (4.29) and is shown in Figure 4.19 and Figure 4.20 (plots are determined with $a = 0.065$ m and $R = 75$ m).

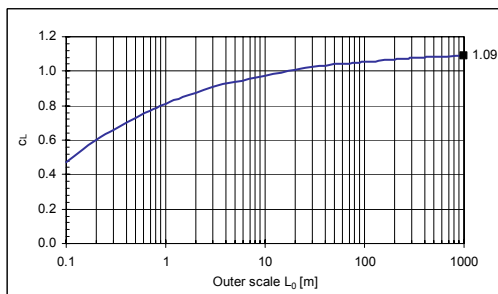


Figure 4.19: Influence coefficient for spherical waves

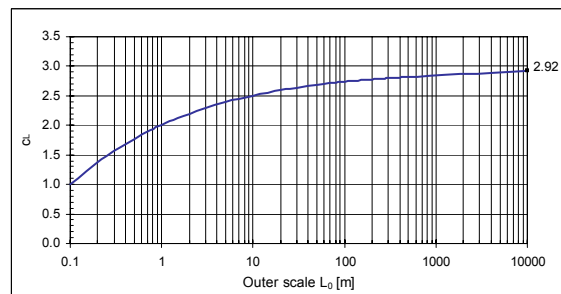


Figure 4.20: Influence coefficient for plane waves

Figure 4.19 and Figure 4.20 show a decrease of the influence coefficient c_L for a decreasing outer scale L_0 where the decrease is strong especially in the lower ranges of L_0 . For practical applications, the height above ground is sometimes used as a rough estimate of the outer scale for the atmospheric surface layer, e.g., [HUFNAGEL, 1978].

But the outer scale L_0 is uncertain since the boundary between the anisotropic turbulence range where energy is injected and the inertial subrange cannot be determined exactly, cf. section 3.2.4. The reason is that, in an anisotropic regime, the eddies are not spherical yet but have different extensions in horizontal and vertical direction. There-

fore, the outer scale can be assumed to extend more than 100 meters in horizontal direction and a few meters in vertical direction [STROHBEHN, 1968].

Hence, the outer scale is thought to be on the order of some 100 meters and the value $c_L = 1.09$ for the influence coefficient of spherical waves seems to be a good approximation. In this case, the systematic deviation is at the most about 5 %, if L_0 is not smaller than 100 m.

4.6 Conclusions

It is shown that the angle-of-arrival fluctuations and the log-amplitude fluctuations are meaningful for the determination of the inner scale l_0 and structure constant C_n^2 . Both parameters are needed to calculate the refraction angle (cf. section 3.4). For this purpose, the method of smooth perturbation (Rytov method) can be introduced to derive a relation between the wave parameters and l_0 and C_n^2 .

In the scope of this research work, the angle-of-arrival fluctuations based on (4.31) are applied to determine C_n^2 . Basically, this relation was already used in previous geodetic research work, such as [BRUNNER, 1979], [CASOTT, 1999], [DEUSSEN, 2000]. In addition to those publications, the analysis presented in section 4.5.2c) also investigates the influence of the outer scale L_0 . This mostly theoretical analysis shows that the influence of L_0 causing systematic deviations for the determination of C_n^2 can be neglected if L_0 is larger than 100 m.

The inner-scale algorithm presented in section 4.4.2 is a new method to determine l_0 . In contrast to [CASOTT, 1999] which uses the balance point of the full intensity spectrum of the incoming ray to estimate l_0 by means of an empirical function, the inner-scale algorithm is based on the variance of the log-amplitude variance σ_χ^2 of the incoming ray. The analysis of accuracy in section 4.5 reveals that l_0 can be accurately determined in this way.

A still unsolved problem is a general rule for the measuring time needed to determine σ_χ^2 . Basically, the measuring time is important since the refraction correction is based on the average of the temperature gradients (cf. section 3.4). A general rule for the measuring time can not be derived from the theoretical formulae of section 4.4.2. Thus, further investigations are required which take the auto-correlation function of the turbulent regime into account. With respect to the capability characteristics of current geodetic instruments, a measuring time in the range of 1 to 10 seconds was chosen for the measurements of section 7.

The disadvantage of the Rytov method is its sensitivity to saturation on longer path lengths since the determination of inner scale is based on the measurement of intensity fluctuations. Due to saturation influences, the evaluation of these fluctuations is not valid yet if the propagation path and the optical turbulence exceed the limit defined by the Rytov variance (Figure 4.16). However, the determination of C_n^2 suffers less from this restriction which requires the presence of weak turbulence. In fact, the evaluation of the angle-of-arrival fluctuations is considered valid under strong turbulent conditions, also [ISHIMARU, 1978].

The presented algorithms are designed for imaging systems and propagation path lengths of less than 200 m. The analysis of accuracy provides some hints for choosing appropriate sensors and image processing algorithms (section 4.5.1). Uncertainties still exist about aperture averaging (section 4.5.2b) which attenuates the log-amplitude fluctuations. This attenuation caused by aperture averaging should be compensated by high-sensitivity imaging sensors and by optimizing the lens system. But further investigations are required.

The theory of optical turbulence as outlined above is based on the principles of statistical radiophysics describing the wave propagation in turbulent media. The experimental data which are used to verify this theory are based on measurements in the atmospheric boundary layer. Since it is very difficult to measure atmospheric turbulence by adequate reference systems, the experimental results based on the introduced modelling tools such as the refractive index spectrum and the turbulent eddies are very difficult to verify and should be discussed carefully. Practical measurements as discussed, e.g., in [VINOGRADOV *et al.*, 1985], [THIERMANN, 1990], [CASOTT, 1999], and [TROLLER, 2000] often show quite a good agreement between the experimental data and the theoretical predictions or the data obtained by a reference system, however. Therefore, the application of optical turbulence for refraction analysis seems to be quite promising.

5 Measuring systems

5.1 Introduction

In order to analyze the refraction influences using atmospheric turbulence, the experiments presented in section 7 use the following types of measuring systems:

- Imaging systems which determine the structure parameter C_n^2 and l_0 by means of image processing (section 6) and the model of optical turbulence as presented in section 4.

Under turbulent conditions, the image sensors are applied to grab the image of a target such as a coded levelling staff. Due to the turbulence cells (eddies) along the propagation path, the light propagation through the turbulent medium is disturbed (Figure 5.1) since these eddies are characterized by a slightly varying refractive index.

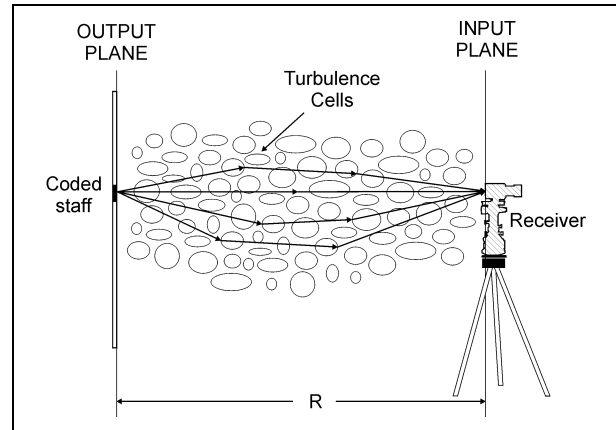


Figure 5.1: Model of light propagation through turbulent medium used for the measurements of image sensors (receiver) and a coded staff (target).

Hence, the recorded images such as the code pattern of a digital staff (cf. section 5.5.2) are subject to intensity fluctuations and angle-of-arrival fluctuations. These fluctuations are evaluated in order to determine the structure parameter C_n^2 and l_0 as discussed in section 4.

- Reference systems providing data for a comparison of the results obtained by the image sensors. Hereby, two different reference systems are utilized:
 - A scintillometer which provides the structure parameter C_n^2 and l_0 .
The measurement principle of the scintillometer is based on relative evaluations of the intensity statistics as presented in section 5.3.1.
 - A temperature gradient measurement system determining the gradient dT/dz .
This temperature gradient can be compared with the gradient calculated using the atmospheric turbulence model (section 3.4) and the structure parameter C_n^2 and l_0 .

In the following sections, the measuring systems are explained in more detail. The explanations concentrate on the imaging systems than on the others, since these imaging systems are applied for the first time in the field of refraction analysis.

5.2 Imaging systems

5.2.1 CCD sensors

Within this research work, charge-coupled devices (CCD) are used as image sensors. CCD sensors were first developed in the AT & Bell laboratories, New York in the 1970s. They measure the light intensity by accumulating charges and transferring the charge to the gate of the sensor (bucket-principle). The concept of the CCD sensor is given in [SEQUIN, TOMPSETT, 1975], [BOYLE, SMITH, 1980], [BEYNON, LAMB, 1980]. The advantage of CCD sensors is the linear relationship between the strength of the incident radiation and the charge which is measured at the gate, e.g., [LENZ 1991]. Additionally, CCD sensors allow a high-frequency sampling of image data.

The general procedure of the image acquisition is illustrated in Figure 5.2. The accumulated charges of the CCD sensor are sampled and yield an analog signal. In order to avoid aliasing effects, this signal is filtered using lowpass filters which have been directly mounted on the CCD chip by the manufacturer. Then, the analog signal is converted into digital gray values with 8-bit resolution (0...255) using a frame grabber. Hereby, modern CCD chips (such as the chip of the line scan camera presented in section 5.2.4) have a AD-converter which is also mounted on the chip and, therefore, the AD-conversion by an external frame grabber is not necessary.

Software drivers control the data transfer of the digitized data which are stored on storage media for post-processing (see also section 5.6). The image acquisition of the sensor as presented in Figure 5.2 can be controlled by means of external signals such as pixel clock and reference voltage.

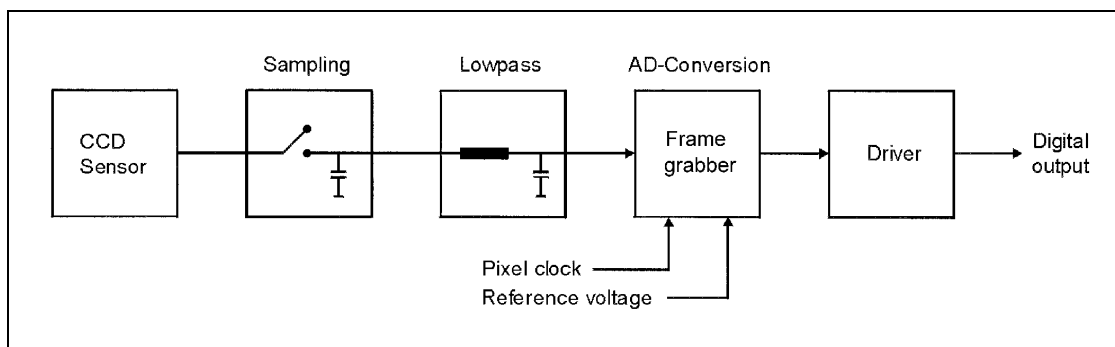


Figure 5.2: Image acquisition using CCD image sensors

In future, it is possible that CMOS (Complementary Metal-Oxide-Silicon) sensors will substitute CCD sensors in imaging systems. CMOS sensors are based on photosensitive diodes which are connected to resistors in series. As a result, the photocurrent is continuously converted into an output voltage. The manufacturing process of CMOS devices is considerably simpler than that of CCD devices. Therefore, industrial oriented CMOS cameras, including an interface for PCs, are cheaper than a classic system as shown in Figure 5.2. But up to now, today's CMOS cameras have a signal-to-noise ratio which is about 1 to 2 decades lower than that of CCD cameras.

5.2.2 Criteria for the imaging systems

The imaging system must be able to measure the angle-of-arrival fluctuations and the intensity fluctuations with an acceptable accuracy. As investigated in section 4.5.1, the required relative accuracy for the angle-of-arrival fluctuations should be at least 10 % and the sensor should have a signal-to-noise ratio (SNR) of at the most 9 dB. Since the SNR of the applied CCD sensors is in the range from 46 dB to 75 dB (cf. SNR of video theodolite and line scan camera, see below), this criterion is unproblematic.

However, the desired accuracy of the angle-of-arrival fluctuations is demanding, and, therefore, the following considerations are presented with regard to the accuracy of the angle-of-arrival fluctuations. In this regard, it is necessary to take the accuracy of the image processing techniques (edge detection) into account. Practical investigations (section 6.4.6) show that the accuracy of the edge detection σ_{single} using the Canny operator or least squares template matching is about 0.05 pixel. As investigated further in section 6.4.6, the desired accuracy of the angle-of-arrival fluctuations can be achieved if the focal length f of the imaging system is at least about 300 mm, the aperture a is about 65 mm and the size of the pixel element p_e is about 10 μm .

Basically, the accuracy of the angle-of-arrival fluctuations and of the intensity fluctuations can be improved if the aperture is as small as possible and the focal length as large as possible. However, diffraction effects limit the resolution p_{res} as follows:

$$p_{res} = 1.22 \cdot \lambda \frac{f}{a} \quad (\text{Size of the Airy disk, Rayleigh criterion}) \quad (5.1)$$

Assuming a focal length $f = 500$ mm, a wavelength $\lambda = 550$ nm (visible light) and an aperture $a = 65$ mm, p_{res} is 5 μm as follows from (5.1). In this case, $p_{res} < p_e = 10$ μm , thus, the specifications ($300 \text{ mm} \leq f \leq 500 \text{ mm}$), $p_e \approx 10$ μm , and ($34 \text{ mm} \leq a \leq 65 \text{ mm}$) seem to be reasonable.

5.2.3 Video theodolite

The video theodolite TM 3000V (Leica Ltd., Switzerland) displayed in Figure 5.3 is a motorized theodolite including a CCD camera. The following technical data are gathered from internal technical documents of Leica Ltd [LEICA, 1989].

The CCD camera is coupled into the optical ray as shown in Figure 5.4: Behind the lenses (A), an optical coupler (B) turns the ray round to the CCD camera. Instead of the optical coupler, an ocular can also be mounted in order to aim the target by eye. The telescope has panfocal properties, and the focus lens is driven by a servomotor. The aperture of the video theodolite is $a = 52$ mm and the focal length is $f = 295$ mm (cf. section 5.4.1).

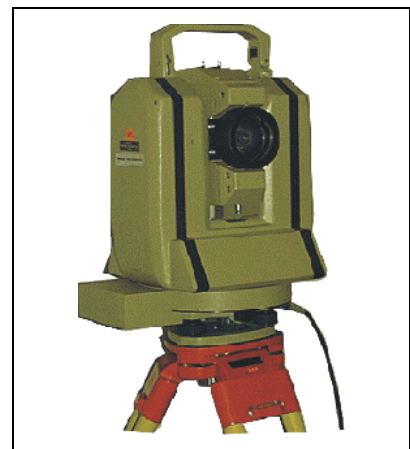


Figure 5.3: Video theodolite

The focal length $f = 295$ mm does not exactly fulfill the corresponding criterion $f = 300$ mm as discussed in section 5.2.2 but the deviation of 1.7 % is assumed to be acceptable. The aperture of the video theodolite is in the specified range ($34 \text{ mm} \leq a \leq 65 \text{ mm}$), thus, this criterion is met.

Instead of a crosshair, the video theodolite has an internal reference frame which defines the reference system for the two-dimensional image data. This reference frame is combined with the optical coupler in such a way as to display the frame on the CCD camera. The CCD camera consists of a sensor array of 500×582 pixels (H x V) and its pixel size is $17 \times 11 \text{ }\mu\text{m}$ (H x V). The minimal required luminous intensity of the CCD camera is 5 lux at F1.4. The signal-to-noise ratio is 46 dB [LEICA, 1989].

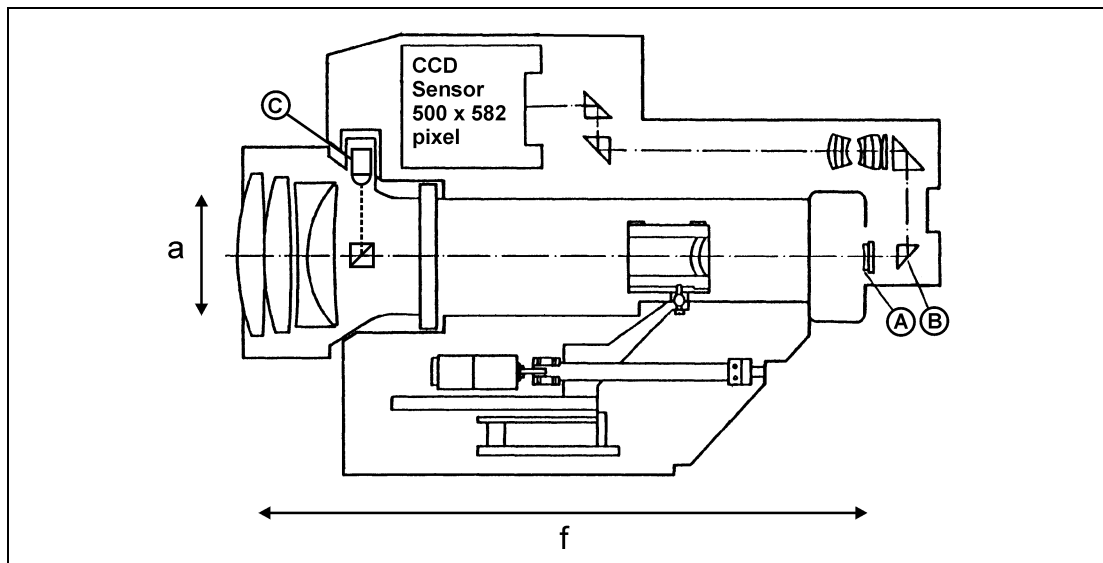


Figure 5.4: Video theodolite with integrated CCD sensor (500 x 582 pixel):
 (A): Internal reference frame, (B): Optical coupler,
 (C): Infrared emitting diode for target illumination (cf. section 5.5)

The video output signal of the video theodolite is a standardized CCIR-PAL video signal, e.g., [CCIR, 1990]. The video signal is AD-converted by the frame grabber which grabs the image sequences with a frequency of 25 Hz. Since the video signal is standardized the output frequency cannot be altered.

5.2.4 Line scan camera

a) Instrumental setup

The line scan camera (BASLER L120, manufactured by Basler Ltd., Highland, Illinois) includes a CCD line sensor with 1024 pixels (pixel size: $10 \times 10 \text{ }\mu\text{m}$). The camera is mounted behind an objective (Nikkor 500 mm, Nikon) and both are fixed on an optical theodolite (Wild T2, Leica, Heerbrugg) as shown in Figure 5.5. The telescope of this theodolite is utilized to aim the target by eye. The following information is provided by the technical documentation of the Basler line scan camera L120 [BASLER, 1998].

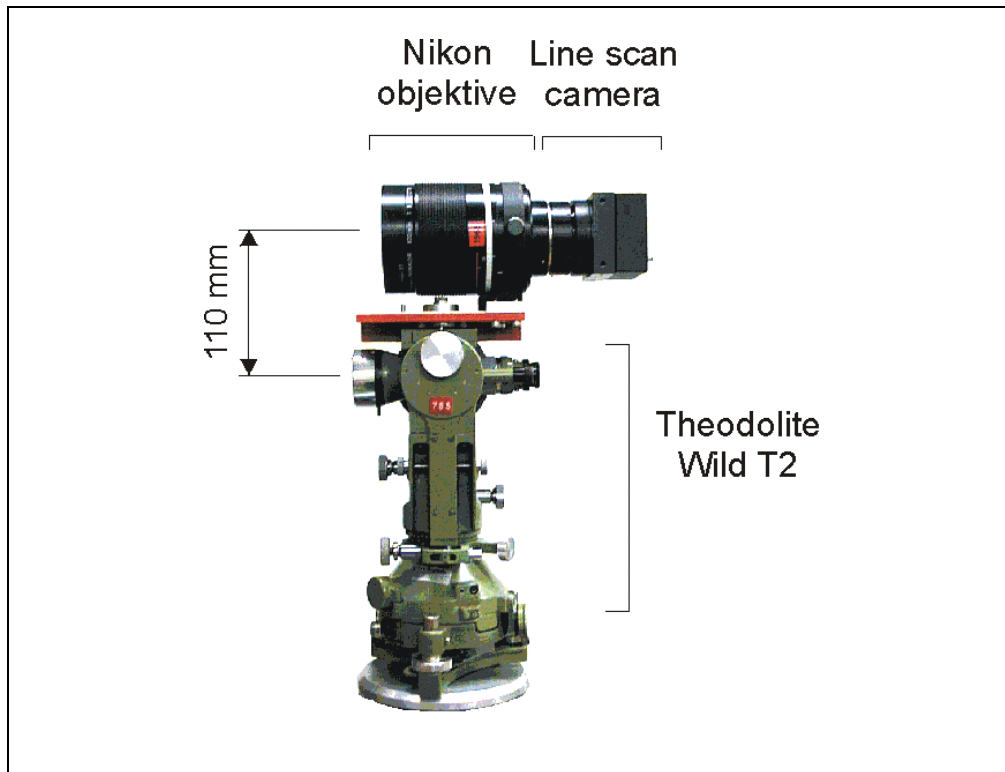


Figure 5.5: Mounting of line scan camera

The camera displayed above is a digital line scan camera in the sense that the CCD chip (SNR = 75 dB) is directly combined with an A/D converter within the camera. This means the accumulated charges are digitized by the camera itself and not by an external A/D converter as is the case when dealing with the video theodolite TM3000V. The line scan camera outputs the values of the digitized charges to the external circuitry via three connectors located at the back of the camera.

The cross section in Figure 5.6 presents the Cassegrain type objective (1) which is connected with the theodolite by an adapter (3) and which has a focal length of $f = 500$ mm and a fixed aperture ($a = 1/8 f = 63$ mm). The field of view of the objective is 5° . The line scan camera (2) is mounted on the objective by a Nikon bayonet fixing (6).

The sensor chip (7) is positioned according to the specifications of Nikon C mount, i.e., the backflange-to-CCD distance is 17.526 mm with an accuracy of 0.002 mm [NIKON, 2000]. The positioning tolerance of the sensor chip in the horizontal and vertical direction is 0.3 mm and the rotational positioning tolerance is 0.3° .

The connector of the female D-Sub HD 44 pin (4) interfaces the video data and the signals which are needed for synchronization (EXSYNC, LVAL, PVAL, see below). The pin connector (5) of the male D-Sub 9 is a RS-232 interface which controls the settings of the line scan camera such as exposure time and clamping.

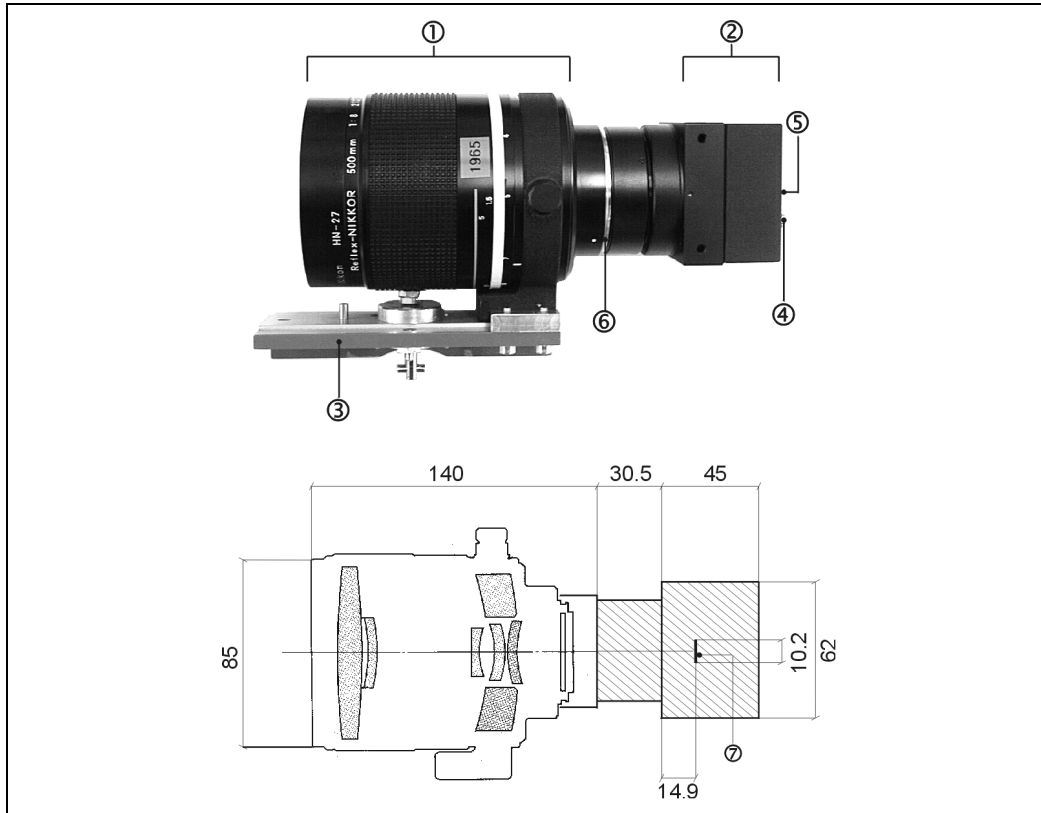


*Figure 5.6: Cross section of objective and line scan sensor.
The unit of the presented quantities is the millimeter*

b) Video data and control

The analog digital converter (ADC) in the line scan camera converts the accumulated charges into video data. The digitized video data have a resolution of 8 bit and are, thus, transferred to the digital interface connector of the frame grabber (section 5.6) by 2 x 8 separated wires.

Additionally, the so-called LVAL and PVAL signals are generated to indicate a valid line (LVAL) and a valid pixel of data (PVAL). Both signals are used to synchronize the digital video output data into external circuitry.

The PVAL signal of the Basler line scan camera L120 has a frequency of 20 MHz (pixel clock). In other words, this pixel clock implies that the charge transfer of a pixel takes about 0.05 μ s. The pixel clock is displayed schematically at the top of Figure 5.7. The camera line scan rate is controlled by the synchronization signal EXSYNC (Figure 5.7) provided by the external frame grabber. The line is read out and output with the rising edge of EXSYNC.

The exposure time is controlled by a programmable internal counter which is included in the CCD chip and can be addressed by the serial interface RS-232 mentioned above. The exposure time of a line being read out is determined using the time between the rising edge and the following falling edge of the signal of the programmable counter. The exposure time may vary 2 pixel clocks due to the requirement that the external syn-

chronization signal must be internally synchronized. The line read out starts about $2.5 \mu\text{s}$ after the exposure time is finished. As shown in Figure 5.7, the exposure time which is chosen as $2900 \mu\text{s}$ cannot be enlarged arbitrarily since the time needed for line read out and the line scan rate (e.g., 333 Hz in Figure 5.7) limits the exposure time.

Besides exposure time and line scan rate, the gain and the offset of the A/D-conversion can also be optimized. As presented in Figure 5.8 and Figure 5.9, the CCD sensor signal can be shaped to optimally match input voltage of the ADC range for a given application.

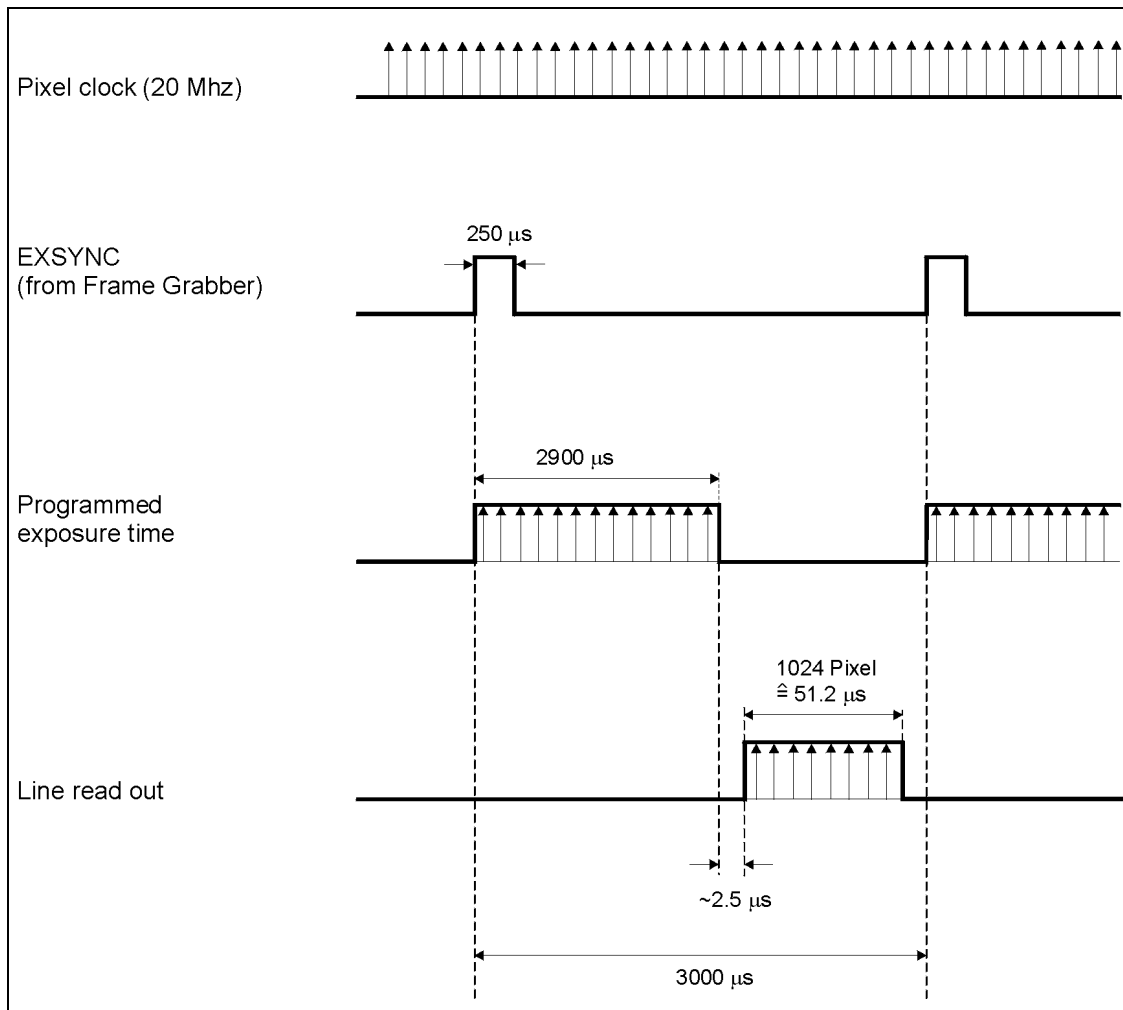


Figure 5.7: Signals and exposure control of line scan camera

For most applications gain and offset settings are advantageous if black has a gray value of just above 0 and white a gray value of just below 255. Settings should usually not be 0 and 255 to ensure optimal exposure conditions.

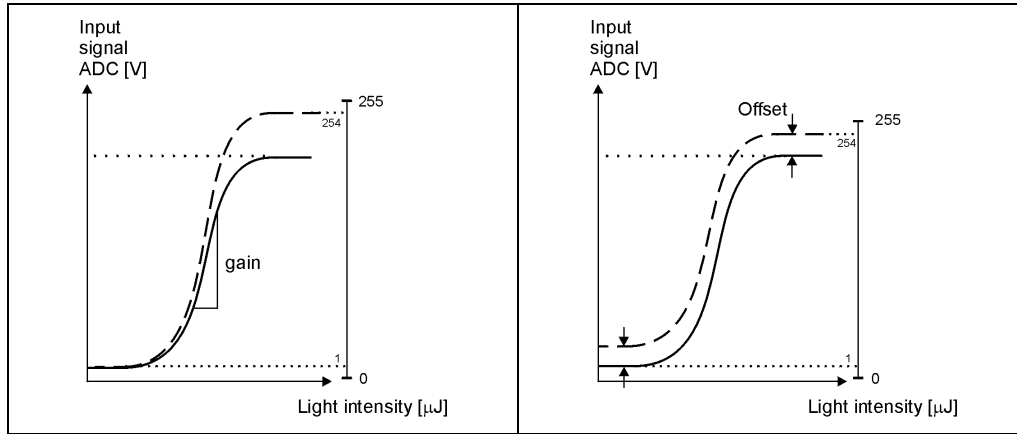


Figure 5.8: Gain

Figure 5.9: Offset

c) **Optical filter**

The CCD sensor of the Basler line scan camera is sensitive for wavelengths in the range from 400 nm to 1100 nm. Plants (grass, leaves etc.) emit infrared radiation which fluctuates and, therefore, can also deteriorate the measurement of the refraction-induced intensity fluctuations. Hereby, the reflectance spectra of grass is shown as thin line in Figure 5.10 [USGS, 1998].

For these reasons, an UV-IR-cut filter is mounted on the objective where the bold line in Figure 5.10 specifies the spectral transmission of this filter. The filter reduces the disturbing frequencies and, at the same time, transmits the remaining radiation in a range where the CCD sensor is still responsive.

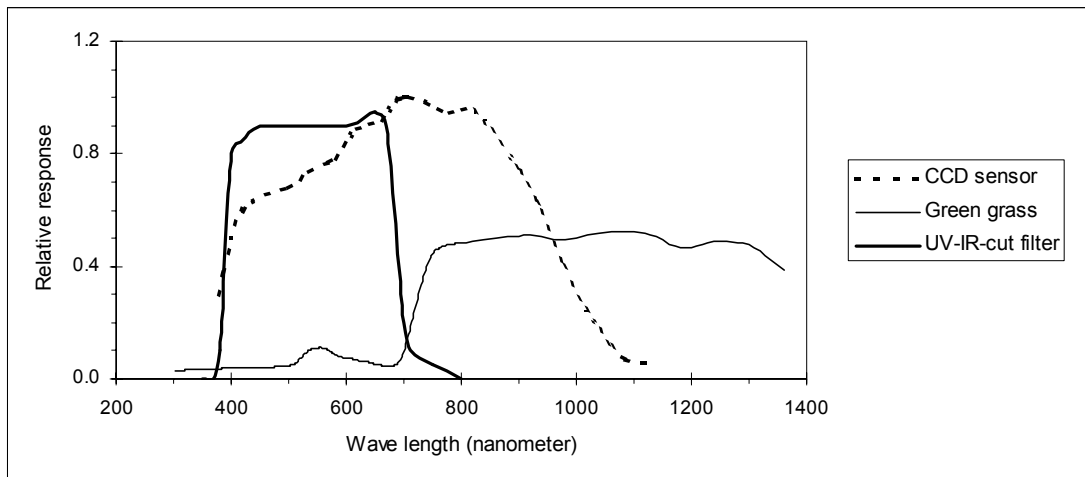


Figure 5.10: Dimensioning of UV-IR-cut filter taking into account spectral responsivity of CCD sensor and reflectance spectrum of green grass

5.3 Reference measuring systems

5.3.1 Scintillometer

A scintillometer determines the structure parameter of optical turbulence using a laser beam. Scintillometers have been developed based on different concepts and specifications. Depending on the concept which is applied, the scintillometer is able to determine both C_n^2 and l_0 or C_n^2 only. More details are presented in [GRAY, WATERMAN, 1970], [HILL, OCHS, 1978], [WANG *et al.*, 1978], [AZOULAY *et al.*, 1988] and [HILL *et al.*, 1992].

The displaced-beam scintillometer SLS 20 which is used in the scope of this research work can determine both structure parameter C_n^2 and l_0 and was developed by THIERMANN [1992]. This system only needs one laser source and one receiver since the laser beam is split into two parallel beam rays which have different polarization and are displaced by the amount a .

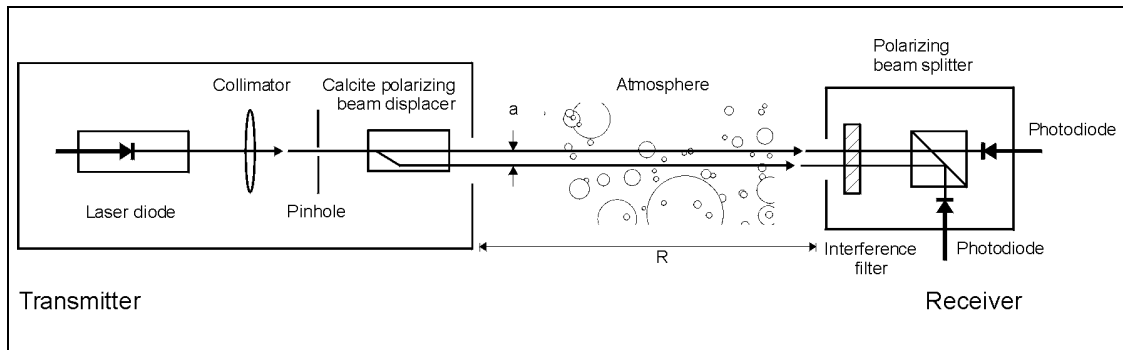


Figure 5.11: Transmitter and receiver of a displaced-beam scintillometer

The two photodiodes of the receiver detect the incoming radiation of the laser beams and generate an analog signal which is transferred to an analog digital converter (ADC) board of a portable computer where the inner scale l_0 and the structure constant of refractive index C_n^2 are determined.

While the determination of the inner scale l_0 according to the procedures of section 4.4.2 assumes that the structure constant of refractive index C_n^2 is known, the displaced-beam scintillometer provides the inner scale directly. This determination makes use of the correlation of the displaced beams given by the logarithm of the amplitude of the received radiation. In doing so, the correlation of the log-amplitude r_χ is introduced as follows [THIERMANN, 1992]:

$$r_\chi = \frac{Cov_\chi}{\sigma_\chi^2} = f(l_0, a, d, R) \quad (5.2)$$

$$\text{with } Cov_\chi = 4\pi k^2 \int_{r=0}^R \int_{\kappa=0}^{\infty} \kappa \Phi_n(\kappa) J_0(\kappa a) \sin^2 \left[\frac{\kappa^2 r (R-r)}{2kR} \right] \cdot \frac{4J_1^2 \left(\frac{\kappa dr}{2R} \right)}{\left(\frac{\kappa dr}{2R} \right)^2} d\kappa dr \quad (5.3)$$

$$\sigma_\chi^2 = 4\pi k^2 \int_{r=0}^R \int_{\kappa=0}^{\infty} \kappa \Phi_n(\kappa) \sin^2 \left[\frac{\kappa^2 r (R-r)}{2kR} \right] d\kappa dr \quad (5.4)$$

J_1 Bessel function of the first kind

The correlation coefficient r_χ applied in the displaced-beam scintillometer is independent of the structure constant C_n^2 because of the division in (5.2). Therefore, the correlation coefficient r_χ only depends on the receiver separation a , the diameter d of the detector, and, besides these instrumental quantities a and d , on the inner scale and the propagation path length which is assumed to be known. Thus, the comparison of the two measured scintillation statistics Cov_χ and σ_χ enables the direct determination of the inner scale since the correlation allows a non-ambiguous relation to the inner scale.

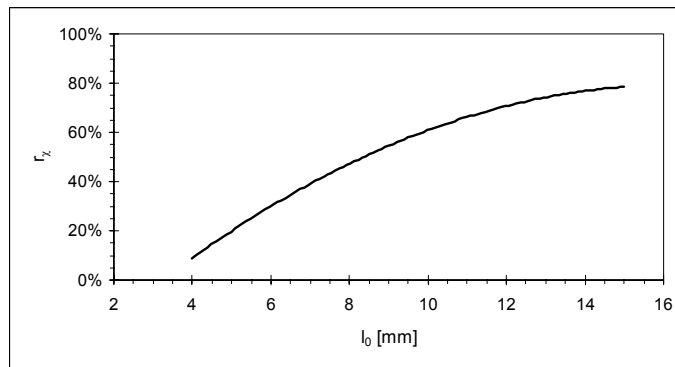


Figure 5.12: Correlation and inner scale (for $a = d = 3$ mm, $R = 75$ m)

The graph of Figure 5.12 is generated by means of (5.2) and shows that l_0 can be derived from the correlation coefficient r_χ .

The determination the structure constant C_n^2 uses the following equation derived from (5.3):

$$\sigma_\chi^2 = 0.124 C_n^2 k^{7/6} R^{11/6} f_\Phi(l_0) \quad (5.5)$$

where f_Φ Decay of Hill spectrum, cf. (4.16)

Besides C_n^2 , all quantities of (5.5) are measured or known, i.e., (5.5) can be solved for C_n^2 . The commercially available scintillometer SLS 20 uses a wavelength of 670 nm and operates over a distance of 50 to 200 m. The measuring range for C_n^2 is from $3 \cdot 10^{-16}$ to $3 \cdot 10^{-12} \text{ m}^{-2/3}$ and the range for the inner scale l_0 is from 2 to 15 mm [THIERMANN, 1997]. The accuracy of the structure parameter C_n^2 and l_0 determined using the scintillometer SLS 20 is not specified by the manufacturer. Investigations of the accuracy and the capabilities of the scintillometer SLS 20 are presented in [DEUSSEN, 2000] and [SCHWIZER, STÄHLI, 1998]. Hereby, the relative accuracy seems to be about 5 % to 10 % under the assumption that the sensor and the detector are aligned exactly. Therefore, at the beginning of the measurements, the alignment must be checked each time by means of a special calibration procedure as documented in [THIERMANN, 1997].

5.3.2 Temperature gradient measuring system

The determination of the temperature gradient using scintillometers is based on the hypothesis of the Monin-Obukhov similarity (section 3.3) whereas temperature gradient measuring systems including several high-precision temperature sensors allow the direct measurement of temperature gradients if the distance between the temperature sensors is known. Thus, they can be used as a reference system in comparison with the results obtained by means of turbulence models.

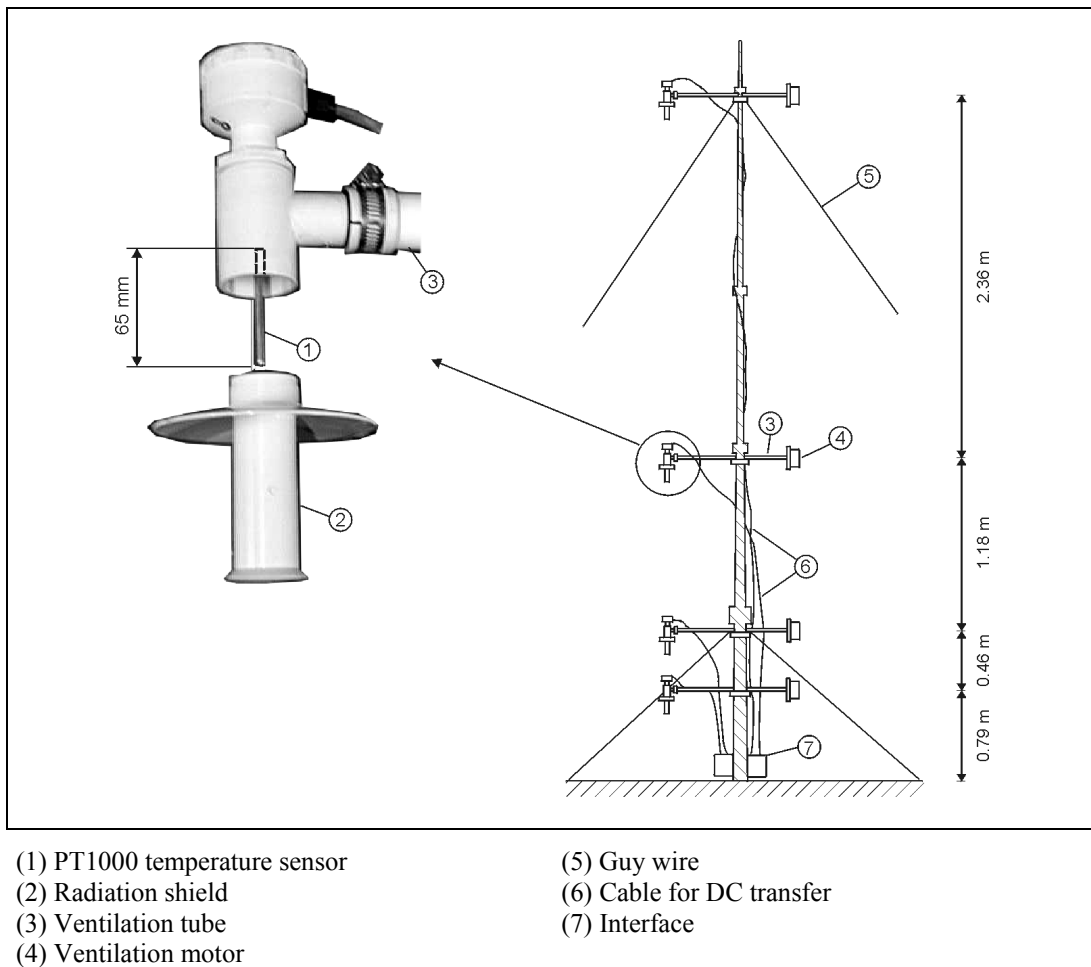


Figure 5.13: Mast with temperature measuring system

The temperature gradient measuring system presented in the following consists of resistive sensors (Pt1000), radiation protection, ventilation, interface, and data acquisition unit. The sensors can be configured according to the requirements of the application. In order to measure vertical temperature gradients, four temperature sensors are mounted on a mast as illustrated in Figure 5.13. Assuming a non-linear temperature gradient profile as modelled in (2.31), the distances between the sensors allow a good approximation of the profile since the curvature of the profile (2.31) decreases with increasing height.

The resistance of PT1000 temperature sensor (1) depends linearly on the temperature where the nominal resistance at $T = 0^\circ$ is 1000Ω . The interface (7) supplies the sensors with constant current (DC) so that, according to the Ohm's law, the voltage drop is a

measure for the resistance of the temperature sensor and, thus, a measure for the temperature.

The output voltages of each sensor are amplified using the amplifier of the interface. In order to measure temperature fields as a function of time, the amplified signals are simultaneously fed into the ADC board of a portable computer. The ADC board digitizes the analog input signals and subsequent program procedures correct the raw data using constants of the calibration.

The accuracy of the temperature measuring sensor can be undermined by various interfering influences, e.g., heating by sun radiation. Thus, the sensors are positioned within the housing of the radiation shield (2) protecting the sensors from sun. Each sensor is equipped with a ventilation tube (3) supplying the sensors with the air of the environment in order to grant representative results. The ventilation motor (4) is opposite of the temperature sensor to avoid troublesome influences.

As only temperature differences among the sensors are of interest, the temperature sensors do not need to be calibrated absolutely in relation to the international temperature normal. However, the sensors must be accurate relative to each other. In order to determine the offset between the sensors, they are calibrated in a climatic chamber where the sensors are put together at the same position and, therefore, should yield the same results. The accuracy of the system can be improved, if it is also calibrated in the same way at the beginning of the experiments for about 40 min [HENNES *et al.*, 1999]. Several calibrations reveal that the relative accuracy (standard deviation) of the described system is about 0.02 K [HENNES *et al.*, 1999].

5.4 Calibration of image sensors

The calibration discussed in the following establishes the relationship between values grabbed by means of image systems and the corresponding values realized by a reference standard. Dealing with image sensors, geometrical calibration and radiometric calibration are applied. The geometrical calibration seeks to define the inner orientation of the camera or video theodolite, i.e., the position of the center point within the focal plane and the focal length. The radiometric calibration considers the irregularities of the grabbed pixel intensity which is influenced by the transfer function of each pixel of the sensor (section 5.4.3).

In sections 5.4.1 and 5.4.2, the geometrical calibration is investigated. Basically, the procedure can be compared with the camera constant calibration used in applications of photogrammetry.

Since the geometrical measurands required for refraction detection are standard deviations, the position of the center point does not have to be calibrated. Therefore, the calibration only seeks to confirm the focal length f which is used for the conversion from the measured pixel values to the angle-of-arrival.

5.4.1 Video theodolite

In order to calibrate the video theodolite in the calibration laboratory, the instrument aims at a target positioned in a distance R . In Figure 5.14, the field of view is plotted by continuous lines and the line of vision by dashed line. During the calibration, the line of vision is rotated slightly in vertical direction at each step (about 10 mgon). Hereby, the vertical angle $\Delta\beta$ denotes the angular deviation between the actual line of vision and the line of vision of the sensor at the beginning of the calibration.

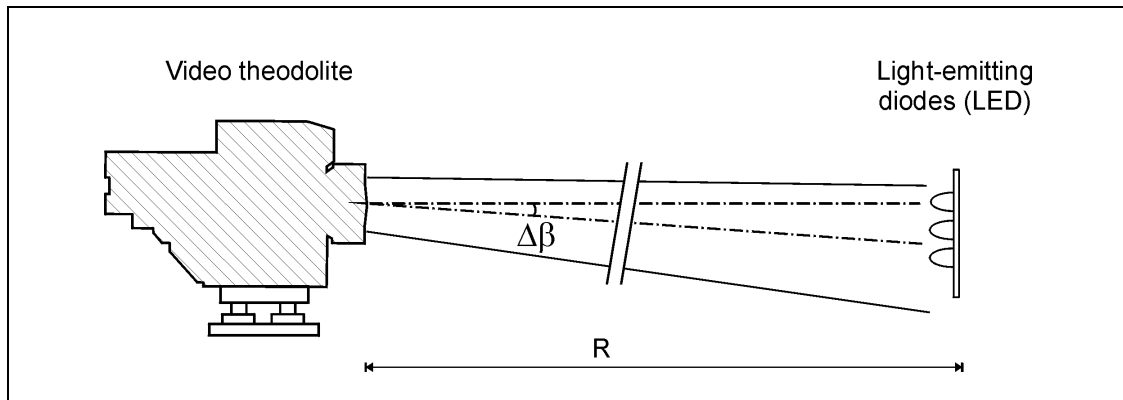


Figure 5.14: Calibration setup of video theodolite

Because of the absence of daylight in the calibration laboratory, the target consists of three light-emitting diodes (LED). The LED are mapped as patterns in the images grabbed by the video theodolite (Figure 5.15). The position of the patterns (no 7 – 9) relative to the reference frame (no 1 – 4) can be measured using least squares template matching (section 6.4.4).

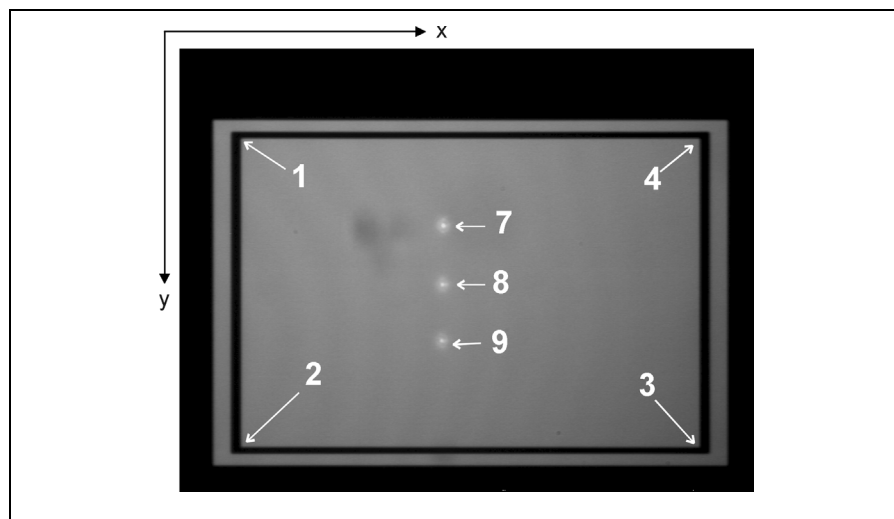


Figure 5.15: Video image of three LED (no 7 – 9).
The vertices of the reference frame are denoted by no 1 – 4

As mentioned above, the position of the telescope is moved in vertical direction during the calibration. Since the position of the LED pattern on the image depends on the position of the telescope the vertical angle $\Delta\beta$ can be measured and correlated to the vertical displacement Δy of the pattern in the grabbed image.

The correlation for the distance $R = 49.4$ m is shown in Figure 5.16. The range of $\Delta\beta$ is relatively small since the field of view of the theodolite is only about 100 mgon.

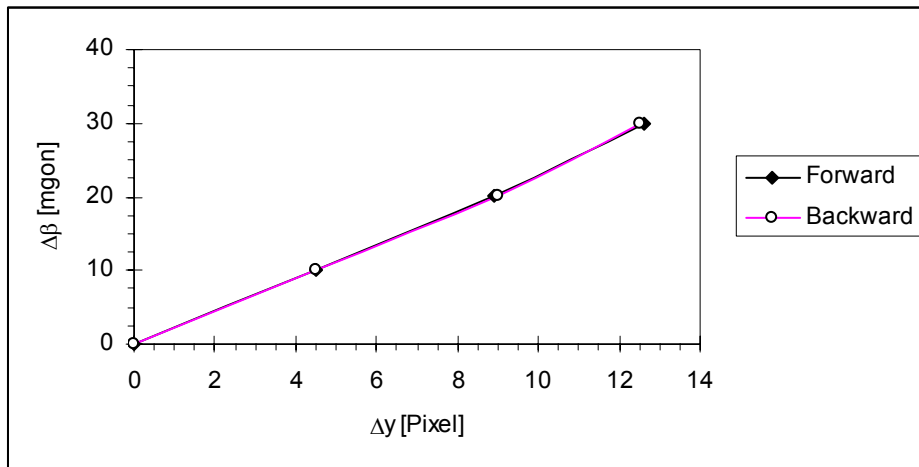


Figure 5.16: Relative displacement of vertical angle and position of pattern (average of the three diodes). Slope $a_1 = 2.37$ mgon/pixel

In general, the lens equation models the focal length as follows:

$$\frac{1}{f} = \frac{1}{b} + \frac{1}{R} \quad (5.6)$$

with R Object distance
 b Image distance

Since the calibration described above uses an object distance $R = 49.4$ m, the focal length can be approximated by the image distance b . Theoretically, this approximation is only valid for $R = \infty$ but the relative error is only 0.6% if R is not smaller than 49.4 m. Using linear regression, the slope a_1 of the curve in Figure 5.16 can be determined and inserted into the following equation to calculate the focal length f :

$$f \approx b = \frac{P_e}{\tan\left(a_1 \cdot \frac{\pi}{200000}\right)} \quad [\text{m}] \quad (5.7)$$

with a_1 Slope (from linear regression) [mgon/pixel]
 p_e Vertical size of pixel elements [m/pixel]

Based on the data obtained by the calibration of the video theodolite (cf. Figure 5.16) and using (5.7), the focal length f amounts to 0.295 m (with $a_1 = 2.37$ mgon/pixel and $p_e = 11$ μm /pixel). This result is assumed to be valid for $R > 49.4$ m.

Since the video theodolite has a panfocal telescope, the determination of the focal length is demanding for shorter distances, [BRANDSTAETTER, 1989].

5.4.2 Line scan camera

Basically, the line scan camera is calibrated in the same manner as the video theodolite and seeks to confirm the focal length with regard to the conversion from pixel to angle. In contrast to the video theodolite, the objective is mounted eccentrically to the telescope of the theodolite. However, the vertical angle $\Delta\beta$ is related to the telescope of the theodolite and to the optical axis of the line scan camera and can be directly used for calibration if the influence of the eccentricity can be neglected.

This eccentricity denoted by e_c in Figure 5.17 causes a vertical deviation Δz which is approximately given by:

$$\Delta z = \frac{1}{2} e_c \sin^2(\Delta\beta) \quad (5.8)$$

with e_c Eccentricity: $e_c = 110$ mm (Figure 5.5)

Assuming a distance $R = 50$ m and $\Delta\beta = 1$ gon, from (5.8) follows $\Delta z = 0.014$ mm and the error of $\Delta\beta = 0.017$ mgon, thus, the influence of the eccentricity can be neglected for distances $R > 50$ m.

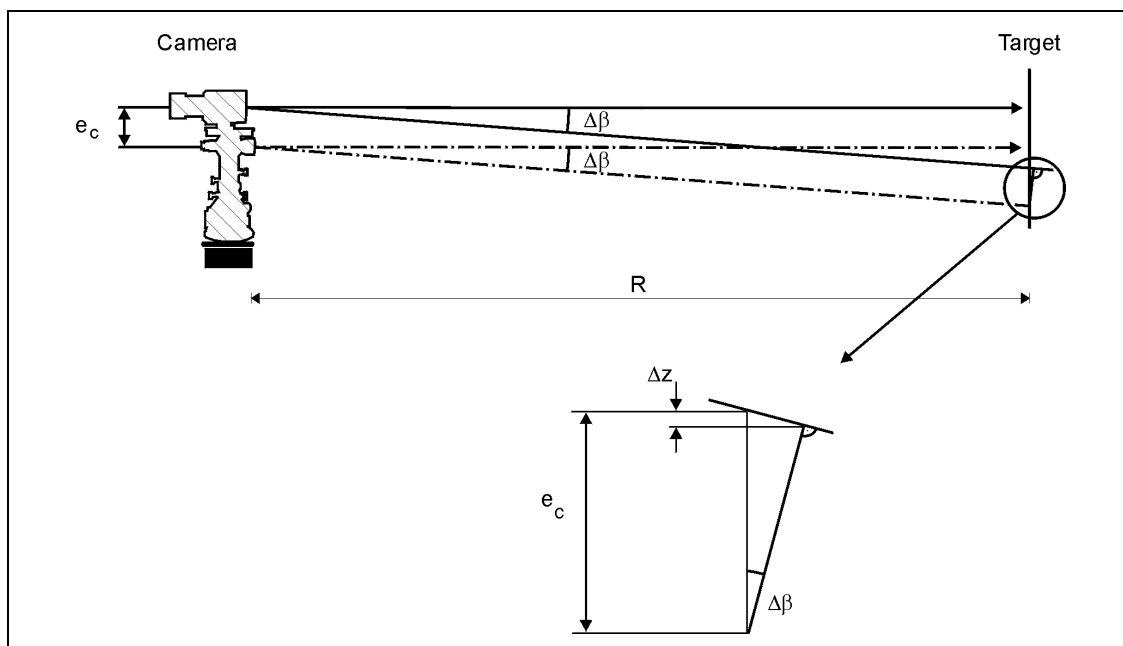


Figure 5.17: Calibration setup of line scan camera

As in the case of the video theodolite, the same light-emitting diodes (LED) operate as targets in the calibration laboratory. Since the sensor permanently grabs one line only, readouts of each line are put together into an image (see also section 5.6). In other words, images grabbed by line scan sensor map the LED (no 7 – 9) as stripes (Figure 5.18). In that image, the n_1 -axis denotes the index of the pixel of the line scan camera and the n_2 -axis of the image stands for the time, i.e., n_2 is the index number of the line readout of the line scan sensor.

The positions of the pattern in Figure 5.18 are measured using the Canny operator as an appropriated edge detection method (section 6.4.5).

In order to calibrate the system, the telescope is moved in vertical direction in regular steps and the change of the vertical angle $\Delta\beta$ is measured using the vertical circle of the WILD T2 theodolite.

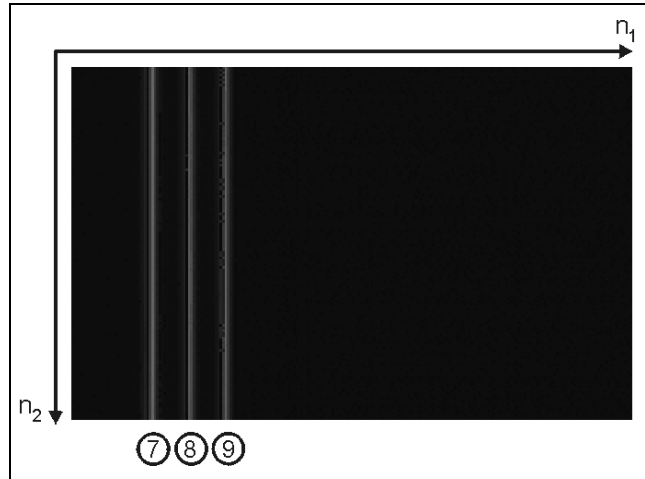


Figure 5.18: Line scan image of three LED (no 7 – 9)

Since the n_1 -coordinate of the LED stripes in the image depends on the position of the telescope, it is a function the change of the vertical angle $\Delta\beta$. The correlation for the distance $R = 50$ m is again shown in Figure 5.19. The range of $\Delta\beta$ is considerably larger than in the calibration of the video-theodolite since the field of view of the line scan camera is about 5° .

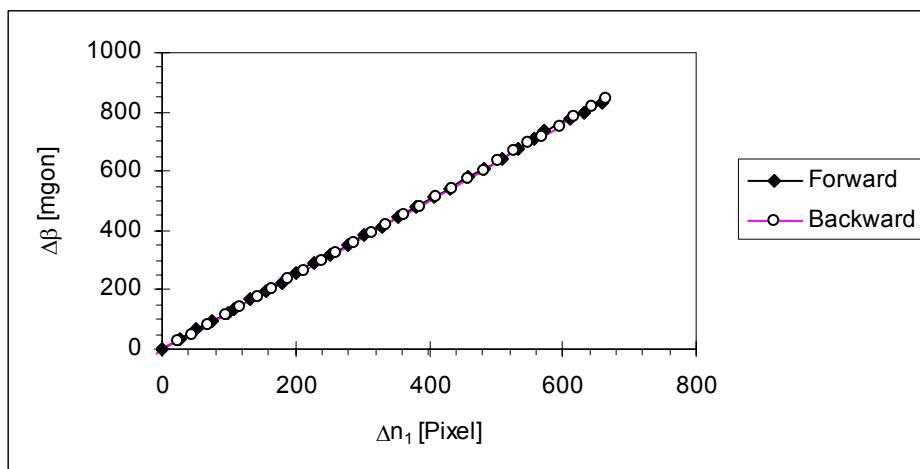


Figure 5.19: Relative displacement of vertical angle and position of pattern (average of the three diodes)

Using linear regression, the slope a_1 can be determined and yields $a_1 = 1.27$ mgon/pixel. From (5.7) follows the focal length $f = 0.500$ m. This value confirms the specifications as given by the manufacturer.

5.4.3 Radiometric calibration

Radiometric calibration can be essential if the output of the pixel array of the CCD sensor which is irradiated uniformly has irregularities in the intensity. If the sensor is illuminated uniformly by diffuse illumination, the gray values of each pixel should be same. In the calibration laboratory, the illumination is generated using a high-frequency Neon lamp and a diffuser which is mounted in front of the aperture of the unit under

test. The investigations show that this assumption holds when dealing with the line scan sensor but it fails when using the video theodolite (Figure 5.20).

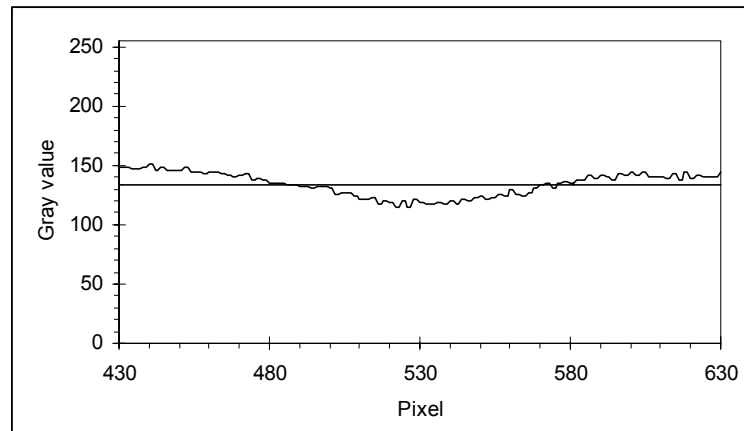


Figure 5.20: Radiometric defects in the output of the video theodolite

Figure 5.20 reveals that radiometric defects of the CCD sensor occur in selected ranges of the video theodolite. These defects are visualized as deviations from a line of constant gray value if the sensor is illuminated uniformly.

Principally, there are two trade-offs to compensate these radiometric defects. As a first option, the deviations can be determined in the calibration laboratory using a differing strength of illumination (dark, bright). Based on the measured deviations, a correction function can be fitted which is applied to each pixel [MAAS, 1993].

The second option is the application of image processing techniques which are not sensitive to the radiometric effects. Least squares template matching as presented in section 6.4.4 is suitable for this purpose since this technique uses the difference between a reference template and a corresponding image patch containing actual edge segments. In doing so, the differences are free from radiometric defects and the application of radiometric correction functions is not required any more.

5.5 Target

5.5.1 Reflectors

The target image should provide information which is subject to refraction influences arising along the light path between the target and the imaging sensor. With a suitable target structure, the intensity and the position of the elements of the target can be measured as time series from which the intensity fluctuations and angle-of-arrival fluctuations are derived by means of image processing (section 6). Optimal target structures should have enough detail (circles, bars etc.) since the image processing algorithms work the more precisely the more information content is in the image.

Since refraction detection should be integrated into geodetic instruments, the selection of an appropriated target is mainly focused on targets used in geodetic applications at present or targets which can be adapted easily. In doing so, the first investigations concentrate on reflectors which are applied in electronic distance measurement (EDM). In

order to provide 3D positioning, not only distance information is needed but also information about the vertical angle and the direction is required.

To obtain the vertical angle and the direction, tracking tacheometers (e.g., Leica TCA 2003) and video theodolites utilize the position of the image of a reflector on the internal CCD array sensor as presented, e.g., in [BAYER, 1992], [INGENSAND, BÖCKEM, 1997], or [FAVRE, HENNES, 2000]. Typical examples for this type of targets are 360° prism or retroreflecting prisms (Figure 5.21).

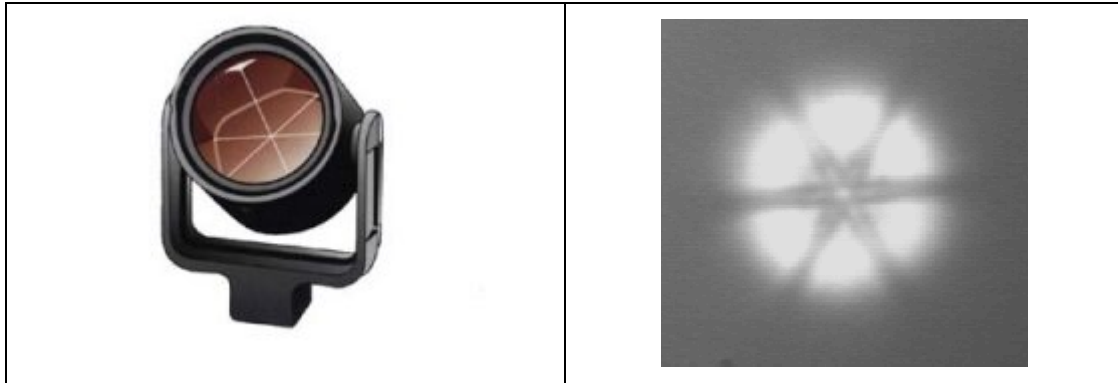


Figure 5.21: Leica GPR1 retroreflecting prism

Figure 5.22: Image of retroreflecting prism

Figure 5.22 shows the image of a retroreflecting prism positioned in the calibration laboratory at a distance of 46 m and grabbed using a video theodolite. Hereby, a (GaAl)As infrared emitting diode ($\lambda = 850$ nm, forward current: 100 mA) which is built into the video theodolite illuminates the reflector [WILD LEITZ, 1988] (The position of the diode is presented in Figure 5.4).

The retroreflecting prism of Figure 5.21 used as target for refraction detection is not advantageous since the structure is poor and the patterns are too large, especially for short distances.

A first attempt at creating a target image showing more details led to a modified reflector as shown in Figure 5.23. In doing so, a semi-circular perforated metal sheet is mounted in front of the reflector. The holes are countersunk using a regular grid (mesh size: 5 mm).

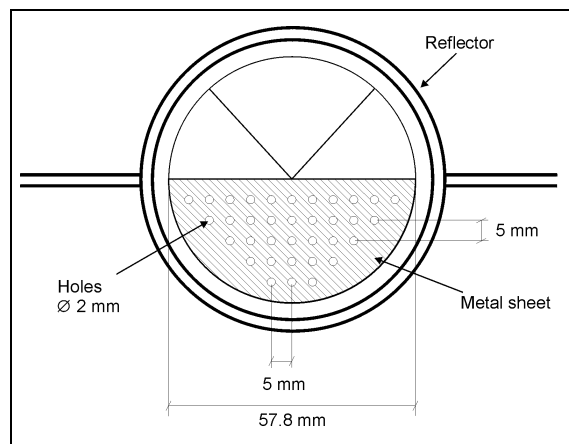


Figure 5.23: Modified reflector

If the video theodolite illuminates the modified reflector according to the mentioned configuration, it grabs a symmetrical image as shown in Figure 5.24. The symmetry is a consequence of the structure of retroreflecting prisms [MAURER, 1982]. Due to the modification, the structure of the image is more detailed.

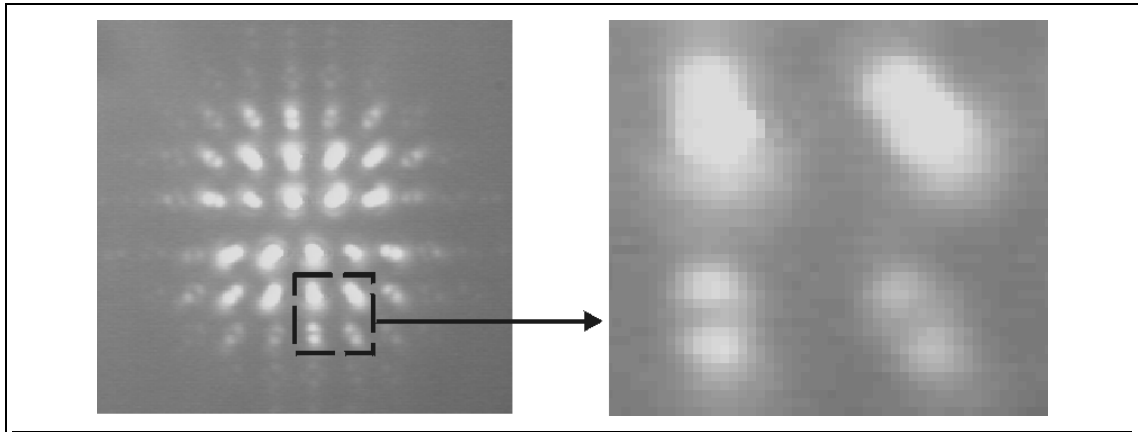


Figure 5.24: Image of the modified reflector acquired using a video theodolite (Distance: 46 m)

Figure 5.25: Sub-region of the grabbed image of the modified reflector

The cropped image region (Figure 5.25) reveals that the patches of the image have different shapes and intensities. For good localization, the image processing algorithms should utilize only the high-contrast patches in the center of the image.

Basically, the modified reflector is suitable for image processing techniques, but practical investigations reveal several difficulties:

- The image of the target is a function of the distance between the target and the sensor. If the target is far away from the sensor, the patches of neighboring holes merge, and a loss of information arises since the number of visible elements decreases.
- Thus, several types of metal sheet defined by various mesh sizes are required where the mesh size and the size of the holes must be adapted for the different distance ranges and for the properties of the geodetic instruments (optics, pixel size). Depending on the distance and the mentioned instrumental properties, it can be necessary to use a composed target consisting of several combined reflectors.
- Since the patches have circular shapes they are not appropriated for geodetic applications using line scan sensors such as digital levelling because the vertical signal information is highly influenced by the sector of the target which is grabbed by the line scan sensor.

In respect of applications in digital levelling, a one dimensional target (e.g., coded levelling staff) is preferred to the modified reflector. A coded levelling staff is especially advantageous since the structure of the code pattern is defined more precisely than that of the modified reflector.

5.5.2 Coded levelling staffs

Coded levelling staffs allow an automatic horizontal height reading of the staff using digital levels. For patent reasons different codes are applied in the digital levels which are commercially available. As the image of the codes varies not only in height but also in distance between level and staff, the code of the levelling staff should yield a unique image on the line scan sensor for each combination of distance and height reading. For the evaluation of an appropriated code with respect to the field experiments (section 7)

the pseudo-random code of the digital level Leica NA3003 is compared with the code of the digital level Zeiss DiNi 10 in the following.

One digit of the Leica code element has a length of 2.025 mm. As illustrated in Figure 5.26, the width of the code bars varies in the range between 2.025 mm (1 digit) and 28.35 mm (14 digits). For determination of height and scale, the digital level correlates the image of the CCD array with the internal reference code [INGENSAND, 1990b].

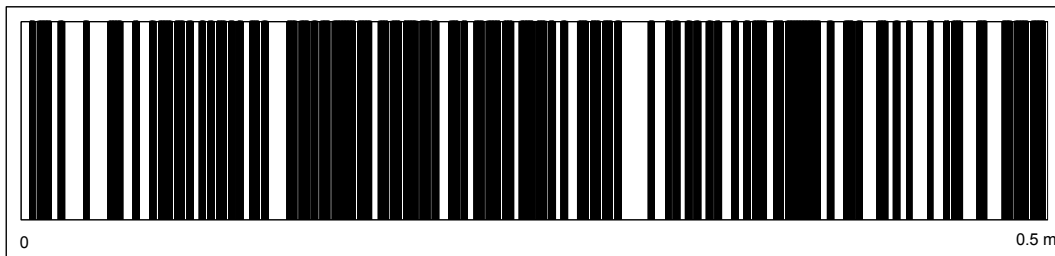


Figure 5.26: Section of pseudo-stochastic code (used in digital levels of Leica)

The Zeiss code has elements of 20 mm length. In contrast to the Leica code, the spacing of the Zeiss code is usually 10 mm or 20 mm and, therefore, more regular than the Leica code as shown in Figure 5.27. For height determination, 15 dark-light edges of the Zeiss code are normally measured by means of edge detection [FEIST *et al.* 1995].

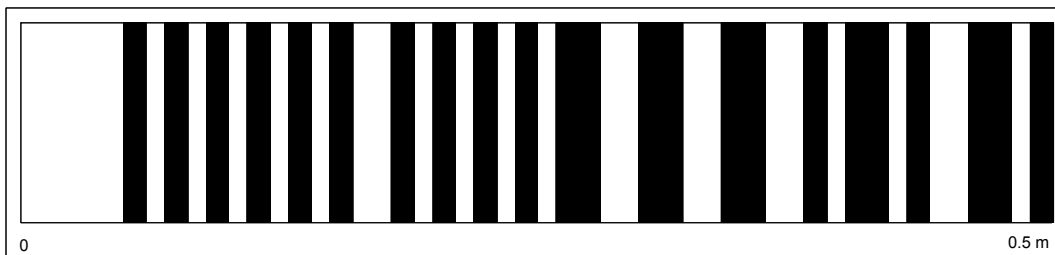


Figure 5.27: Section of Zeiss code

Depending on the code, the corresponding spatial spectrum of the code can vary considerably. In order to illustrate these relations, the Leica code and Zeiss code are sampled (sampling rate $f_s = 16 \text{ mm}^{-1}$) and analyzed using the algorithms of spectral density estimation as discussed in section 6.2. The spectrum of the Leica code reveals local maximums spaced at intervals of about 0.48 mm^{-1} whereas the spectrum of the Zeiss code decreases monotonously as shown in Figure 5.28. The spatial frequency depends on the distance and the focal length f . For example, assuming a distance of more than 30 m and $f = 240 \text{ mm}$, neighboring code elements of the Leica code coincide and yield an other code and an other spatial spectrum, respectively. This means that the analysis of the spatial spectrum for the purpose of refraction detection is principally possible but the mentioned distance sensitivity is a drawback. Thus, only the time-dependent displacement of code patterns is investigated in the scope of this research work but not the spatial spectrum.

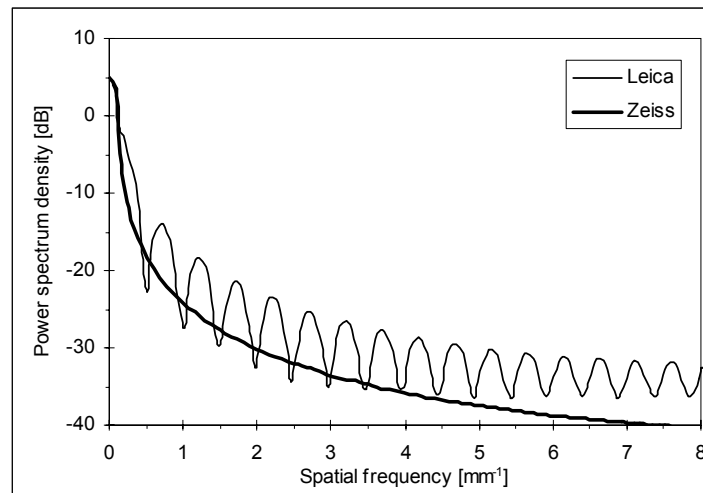


Figure 5.28: Spatial spectrum of Leica and Zeiss code

For the purpose of refraction detection, the determination of angle-of-arrival fluctuations does not require a very special code. The only requirement is that the code pattern provides enough image structures and a good contrast which can be detected reliably by image sensors over a distance up to 100 m. Therefore, a target consisting of strongly varying code bars seems promising because it allows the testing of image processing techniques using image patterns of strongly differing sizes. For this reason, the experiments presented in section 7 use staffs coded by the Leica code.

The influence of the code on the determination of the structure parameter C_n^2 and l_0 should be further investigated. As mentioned above, it is difficult to compare the spectra showed in Figure 5.28 with the spatial spectra of the same codes grabbed by imaging sensors in field experiments. The reason for the limited spectral analysis is the low spatial sampling rate in field experiments: Assuming a focal length $f = 500$ mm, a pixel size $p_e = 10$ μm , and a distance $R = 63$ m, the sampling rate is only $f_s = 0.8$ mm^{-1} . This means the spectrum can only be measured up to the Nyquist frequency of 0.4 mm^{-1} and, thus, special characteristics of the spectrum of the code such as the local maximums of the Leica code (cf. Figure 5.28) cannot be localized.

5.6 Data recording

The image data of the sensors are grabbed by a frame grabber (Matrox Pulsar) which is schematically described in Figure 5.29 and transfers the data to the peripheral component interconnect (PCI) bus of a portable computer. This frame grabber provides real-time CCIR or non-standard acquisition capabilities. The ADC of the board digitizes analog video input such as signals from the video theodolite with a resolution of 10 bit (at up to 30 MHz) or 8 bit (at up to 45 MHz). The programmable input lookup table (LUT) can transform data greater than 8 bits per pixel to 8 bits per pixel for transfer to the video-to-PCI bridge since the subsequent image processing units operate with 8-bit data.

Using an additional digital interface board, the frame grabber can also acquire RS-422 digital data such as provided by the Basler line scan camera. The maximum sampling rate of digital data is 30 MHz. This is high enough since the line scan camera is clocked with 20 MHz only (section 5.4.2).

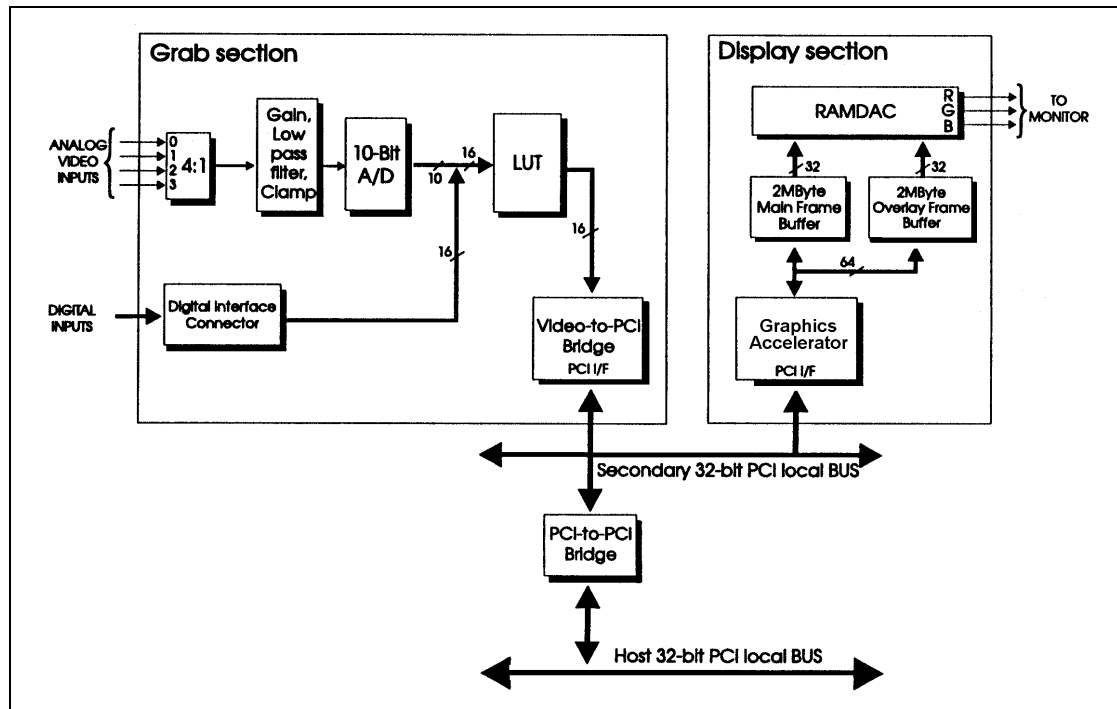


Figure 5.29: Block diagram of Matrox pulsar frame grabber

The PCI specification allows several PCI buses to run parallel within one computer, e.g., [SCHNURER, 1993]. Therefore a secondary 32-bit PCI bus can be used which connects the grab section with the display section which outputs the image data directly to the monitor. In doing so, the secondary PCI bus frees the host processor to perform other tasks. The introduction of a secondary bus requires a video-to-PCI bridge. This bridge acts as a router which sends data to the host memory, or to the frame buffers (external monitor) via the secondary PCI bus. The video-to-PCI bridge can also generate various interrupts towards the host processor such as grab events (grab-end) or video synchronization events (field-start). The PCI-to-PCI bridge sends the grabbed 8-bit image data to the host PCI bus. Hereby, the size of the image is limited because the internal memory of the frame grabber has 3 MB only.

Then, the image acquisition software stores the image data on the hard disc of the portable computer. Depending on the image data, the following two storage formats are applied:

- *1D image data (line scan sensor)*: All line readouts are composed to a single image where the rows of the image enclose the line readouts and the columns of the image contain the intensity value of each pixel of the line scan sensor (cf. section 6.2.1). Hence, several line readouts are stored in one image file only.
- *2D image data (video theodolite)*: The 2D images which are grabbed from the video theodolite are stored in separated image files. For example, if the video theodolite ($f_s = 25$ Hz) is in action during one second, 25 image files are generated automatically on the hard disc.

The image data files are now ready for post-processing using the image processing algorithms as introduced in section 6.

6 Image processing

6.1 Introduction

Within the last years, image processing techniques have been introduced which allows the analysis of optical turbulence in geodetic applications, e.g., [DEUSSEN, WITTE, 1997], [HENNES, FLACH, 1998], [CASOTT, 1999]. These publications deal with the derivation of appropriated parameters from image data to determine the turbulence parameters (l_0 , C_n^2) which have been discussed in section 3 and 4.

In the following section, a new approach is made by the introduction of the Wiener filter which aims to estimate appropriate parameters for the determination of intensity fluctuations and, thus, of the inner scale l_0 (cf. section 4.4.2). The (adaptive) Wiener filter was chosen since it is superior to conventional lowpass filters, especially in the range of low signal-to-noise ratio [KROSCHER, 1996]. The Wiener filter provides also filtered image data which can be used to estimate angle-of-arrival fluctuations by means of edge detection.

A brief overview of the approach is given in Figure 6.1. At the first step of Figure 6.1, the spectral analysis gives information about the frequency decomposition of the signal and indicates how the spectrum of the image data can be parameterized. The estimation of the power spectral density is described in section 6.2.

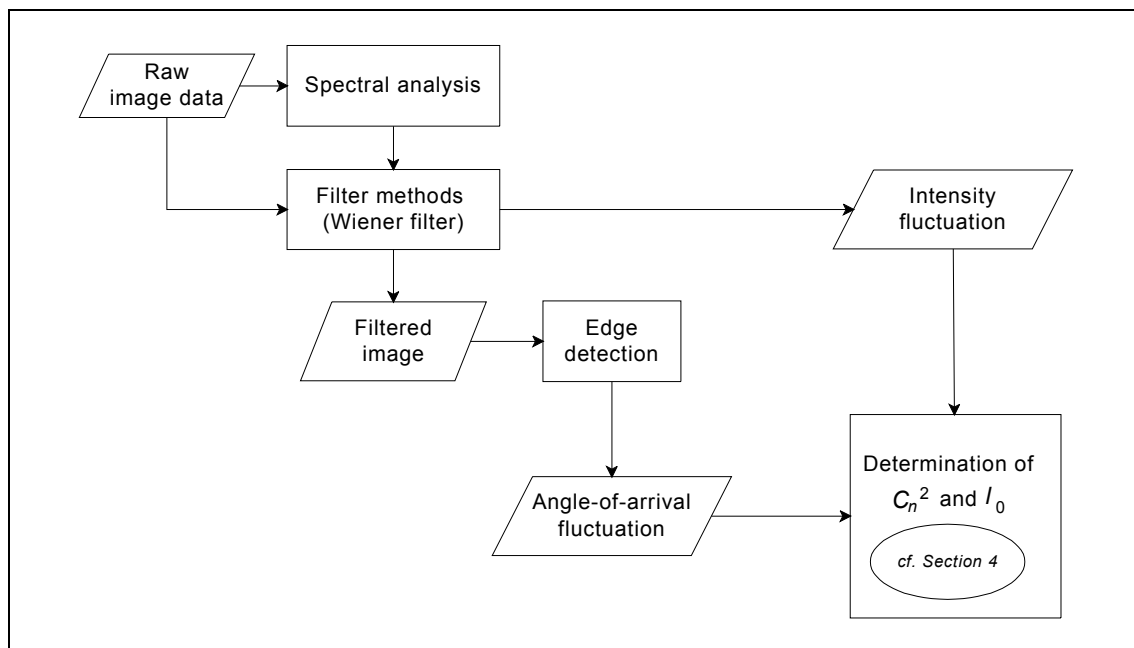


Figure 6.1: Structure of section 6

If a model for the spectrum is available, the Wiener filter can estimate the parameters of the model of the spectrum and, thus, determine the intensity fluctuation of the incoming waves.

Beside the parameter for intensity fluctuation, image processing has also to provide a suitable parameter for the angle-of-arrival fluctuation. This parameter can be obtained

by the standard deviation σ_X^2 of temporal displacement of edges whereby σ_X^2 is applied to (4.30) and (4.31). For the determination of σ_X^2 , the choice of an appropriate edge detection algorithm (edge operator) which provides the angle-of-arrival fluctuations is crucial since random noise caused also by optical turbulence diminishes the quality of image data. The investigated edge operators are described in section 6.4.2 where also an overview of actual methods is given (Figure 6.15). The evaluation and comparison of edge operators presented in section 6.4.2d use image data which were obtained by field experiments. The comparison of image processing algorithms shows that the least squares template matching and the Canny operator in combination with the adaptive Wiener filter are suited to analyze image data in consideration of turbulence effects. However, for this purpose, these techniques must be adapted as shown in sections 6.4.4, and 6.4.5 to provide good results.

6.2 Spectral analysis

6.2.1 Introduction

Spectral analysis discussed in this section tries to describe the frequency decomposition of an image signal $f(n_1, n_2)$ grabbed by imaging systems. The frequency decomposition provides a spectral model the parameters of which are determined by means of appropriate filtering methods such as the Wiener filter (cf. section 6.3.3).

In the scope of image processing using line scan sensors, the n_1 -axis of the analyzed image stands for the pixels of the line scan sensor and the n_2 -axis of the image stands for the time and determines the index number of the line readout of the line scan sensor (Figure 6.2).

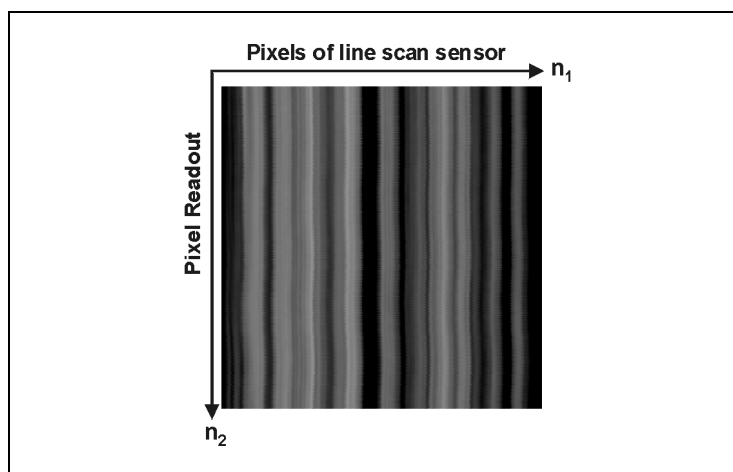


Figure 6.2: Example of two-dimensional signal grabbed by line scan sensor

However, spectral analysis can also be applied to series of current two-dimensional images as grabbed, e.g., using a video theodolite. In this case, a third index n_3 is necessary to indicate the time, but the further explanations are correspondingly valid.

In the following approach, only time series are evaluated to determinate intensity fluctuations. In other words, the spectrum which is relevant for the determination of the inner scale is assumed to depend on the temporal frequency corresponding to n_2 or n_3 , respectively. This assumption holds if the spatial spectrum of turbulence described by the distribution of eddies is equivalent to the temporal spectrum (cf. Taylor's frozen turbulence hypothesis, section 3.2.1).

The spectral analysis includes the estimation of the power spectral density. Hereby, the quality of the spectral analysis depends on capability characteristics of the estimator function which is applied to the power spectrum. Therefore, the crucial points of the estimation of power spectral density have to be observed in the following sections in order to obtain unbiased results.

6.2.2 Stochastic model for the image signal

The correct interpretation of a spectral analysis requires to know all assumptions which are implicitly included in the analysis. These assumptions are composed briefly in the following.

The first assumption is that the image signal can be described by means of time series consisting of pixel intensities recorded during the acquisition time, whereby these time series are modelled as a stochastic process. The basic features of a stochastic process in general are depicted schematically in Figure 6.3.

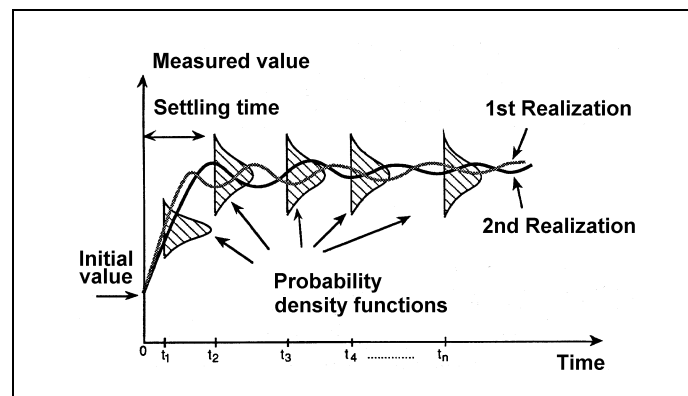


Figure 6.3: Stochastic process: General scheme

A stochastic process is a set of random variables described by their probability density function which implies that a measured time series is a realization of a stochastic process. Thus, the first realization of the stochastic process may generate another time series than the second realization in accordance with the probability density functions at each time t .

Figure 6.3 shows how the property density function can depend on time. This is the case, for instance, when the image sensor is settling (e.g. after the sensor is turned on).

After the settling time (see below) has passed, a second assumption states that average m_F and autocorrelation function $R_F(t_k)$ of the stochastic process are time-independent during the observation time. Hereby, the quantities m_F and $R_F(t_k)$ are defined as presented, e.g., in [OPPENHEIM, SCHAFER, 1992]:

$$m_F = E[f(t)] \quad (6.1)$$

$$R_F(t_k) = E[f(t) \cdot f(t + t_k)] \quad (6.2)$$

$$\text{with } t = n_2/f_s \quad \text{for line scan images} \quad (6.3)$$

$$t = n_3/f_s \quad \text{for 2D images} \quad (6.4)$$

$$t_k \quad \text{Lag}$$

$$f_s \quad \text{Sampling frequency} \quad [\text{Hz}]$$

$$E[\cdot] \quad \text{Expected value}$$

Referring to Figure 6.3, the second assumption is fulfilled for all $t \in [t_2 \dots t_n]$ where m_F and $R_F(t_k)$ are the time-independent. Stochastic processes where the second assumption is fulfilled are called wide-sense stationary, e.g., [KROSCHEL, 1996]. For wide-sense stationary processes, the power spectral density is related to the autocorrelation function by the Wiener-Khinchine relation given by:

$$S_F(\omega) = \sum_{k=-\infty}^{\infty} R_F(t_k) \cdot e^{-i\omega t_k} \quad (6.5)$$

If these two assumptions hold the power spectral density as defined in (6.5) is appropriate to analyze the image signals and can be estimated as described in section 6.2.3. Referring to a real imaging system, it is quite difficult to provide a stringent proof that the assumption of the mentioned weak-stationary stochastic process really holds.

In the calibration laboratory, practical investigations of the imaging systems presented in section 5 show that settling time of the systems is at the most 10 to 20 seconds and, after the settling time, a weak-stationary stochastic process seems at least plausible for a measuring time of the imaging sensors (< 1 min).

Further investigations about the settling time of CCD cameras are given, e.g., in [CA-SOTT, PRENTING, 1999] and [GÜLCH, 1984].

6.2.3 Estimation of power spectral density

In this section, the spectral analysis of a discrete line scan image signal $f(n_1, n_2)$ is investigated which is a realization of a stochastic process F (cf. section 6.2.2) and should be analyzed by its power spectral density S_F .

As mentioned above, the temporal frequencies ($\omega_2 = 2\pi/n_2$) are of interest only, i.e., the spectral estimation refers to a signal $f(n_2)$ for the pixel at the position n_1 . In general, the estimation of power spectra is demanding because no estimator function exists that is both consistent and unbiased at the same time, e.g., [KOCH, SCHMIDT, 1994]. In the following, the Welch method, which solves or at least reduces this difficult will be presented.

a) *Discrete Fourier transform*

The traditional estimator function for the power spectral density S_F uses the discrete Fourier transform (DFT) as described in (6.6), e.g., [PRATT, 1991]:

$$\hat{S}_F(\omega_2) = \frac{|\text{DFT}\{f(n_2)\}|^2}{N_2} \quad (6.6)$$

with $\omega_2 = \frac{2\pi}{n_2}$ (6.7)

N_2 Number of sampling points of the discrete signal $f(n_2)$

$$\text{DFT}\{f(n_2)\} = \sum_{n_2=0}^{N_2-1} f(n_2) \cdot e^{-i(\omega_2 \cdot n_2 / N_2)} \quad (6.8)$$

The hat $\hat{}$ in (6.6) denotes an estimated quantity. In equation (6.8), the discrete Fourier transform computes the one-dimensional Fourier transform of the column n_1 of image signal $f(n_1, n_2)$. The result of the estimation of power spectral density obtained by (6.6) is called periodogram.

Unfortunately, the estimation using the periodogram using (6.6) can fail because it is not a consistent estimator function. This means an increasing number N_2 of sampling points leads to an estimation of power spectral density which becomes more and more rough and inconsistent. Moreover, the spectrum has inconvenient side-lobes and the standard deviation of the periodogram increases in proportion to the amount of the spectrum. Thus, the standard deviation of the periodogram does not decrease with increasing number of samples, as it could be expected from a good estimation method.

b) *Improved estimation for power spectral density*

To decrease the standard deviation of the estimation method discussed above, WELCH [1967] suggested to average several periodograms. This method is illustrated schematically in Figure 6.4.

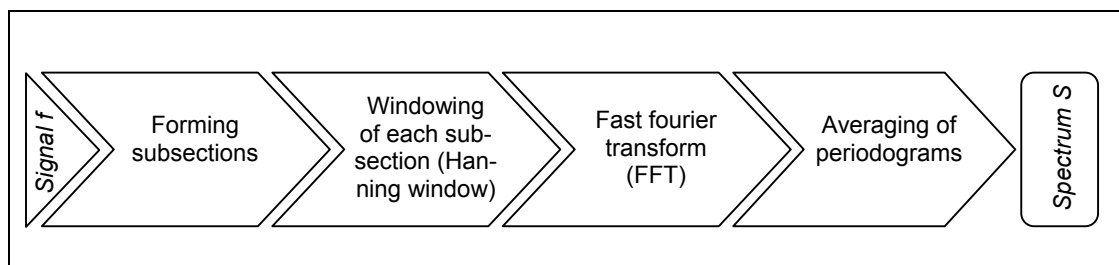


Figure 6.4: Welch method for estimation of power spectral density

When forming subsections, the signal f must be split into sub-signals or sections f_r which the corresponding periodogram is estimated with. Due to FFT algorithm, the length of the input sequence f_r must be a power of two.

In the next step, each subsection is windowed. That means the original signal values are not used directly. Instead the signal values are weighted with a windowing function. In

the scope of this research work, the Hanning window is used as windowing function (Figure 6.5) and which is defined by, e.g., [LIM, 1990]:

$$w(n_2) = \begin{cases} \frac{1}{2} \left[1 - \cos\left(\frac{2\pi n_2}{N_2}\right) \right] & \text{for } 0 \leq n_2 < N_2 \\ 0 & \text{else} \end{cases} \quad (6.9)$$

The choice of the Hanning window offers several advantages: The sides of the sub-signals f_r have less weight than the center of the signal and, additionally, the Hanning window can be computed fast and provides a smooth graph such as shown in Figure 6.5. This windowing technique avoids troublesome influences of the discrete Fourier transform such as side-lobes and, therefore, produces more reliable results.

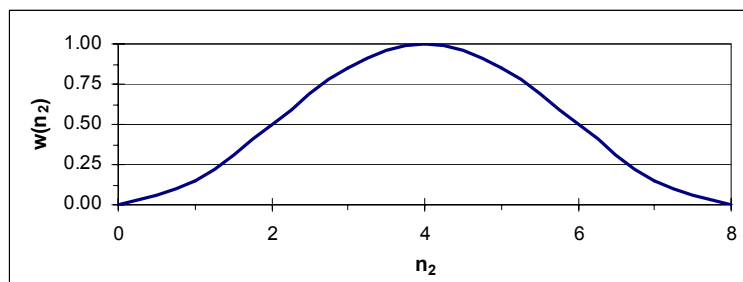


Figure 6.5: Hanning window with $N_2 = 8$

After the application of the Hanning window the periodogram is estimated from each windowed subsection whereby the estimated power spectral density is the average over all Fourier transformed windowed signal sections [WELCH, 1967]:

$$\hat{S}_X(\omega_2) = \frac{1}{\|w(n_2)\|^2} \cdot \frac{1}{K_S} \sum_{r=1}^{K_S} |\text{DFT}\{w(n_2) \cdot f_r(n_2)\}|^2 \quad (6.10)$$

$$\text{with } \text{DFT}\{w(n_2) \cdot f_r(n_2)\} = \sum_{n_2=0}^{N_2-1} w(n_2) \cdot f_r(n_2) \cdot e^{-i(\omega_2 \cdot n_2 / N_2)} \quad (6.11)$$

\hat{S}_X	Estimated power spectral density
$w(n_2)$	Windowing function, cf. (6.9)
$f_r(n_2)$	Signal section (sub-signal)
K_S	Number of windowed signal sections
N_2/f_s	Total measurement time

The factor $\|w(n_2)\|^2$ in (6.10) takes the choice of the windowing function into account. As a consequence of the averaging process in (6.10), the more sections are available for averaging, the lower the variance of the estimated power spectral density is, therefore, this method (which is length of section dependent) is consistent, e.g., [OPPENHEIM, SCHAFER, 1992].

In order to obtain more signal sections f_r from a given signal f , the sections f_r can overlap the adjoining section. A signal section is allowed to overlap an adjacent section up

to 50% overlap [WELCH, 1967]. To illustrate this technique, Figure 6.6 shows a discrete signal of 1024 values length, where the input for the calculation of the seven periodograms consists of seven overlapped signal sections.

With use of the Welch estimation method as discussed above, the power spectral density for the time series of the intensity of a single pixel can be estimated by (6.10). Thus, the power spectral density is available as an input variable for further image processing methods such as Wiener filter.

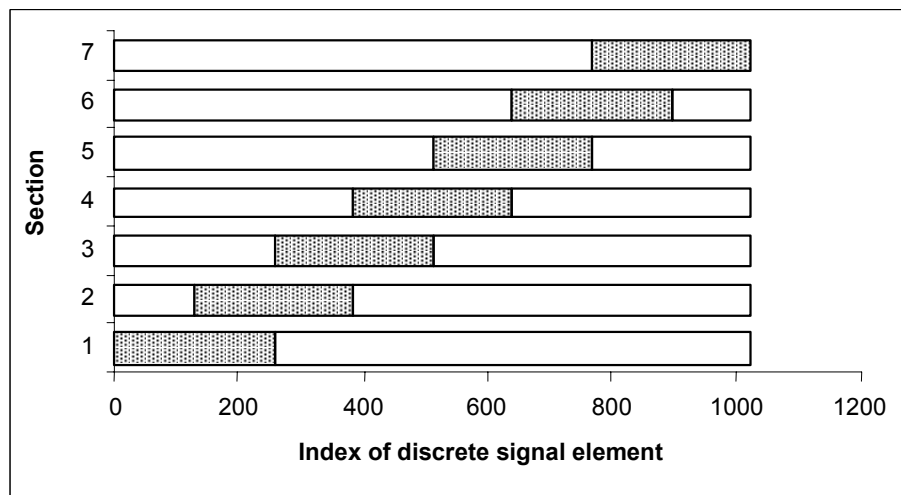


Figure 6.6: Example for the division of a discrete signal ($N=1024$ sampling points) into 7 signal sections (gray) which are used for the averaged periodogram

6.2.4 Outlook: Wavelet transformation

The question remains whether there are image processing methods which simultaneously perform the spectral analysis to calculate the variance σ_V^2 on the one hand and, on the other hand, locates the edges in the image to determine directly the structure constant C_n^2 . The wavelet transformation presented in this outlook is such a method which theoretically fulfills these requirements.

Wavelet analysis is an advancement of the spectral analysis: It uses a windowing technique with variable-sized regions. Wavelet analysis allows the use of long-time intervals where precise low frequency information is needed, and shorter regions where high frequency information is required, e.g., [CHUI, 1992].

A wavelet used in the wavelet transform is a waveform function Ψ of effectively limited duration which has an average value of zero. An example of the wavelet function is presented in Figure 6.7.

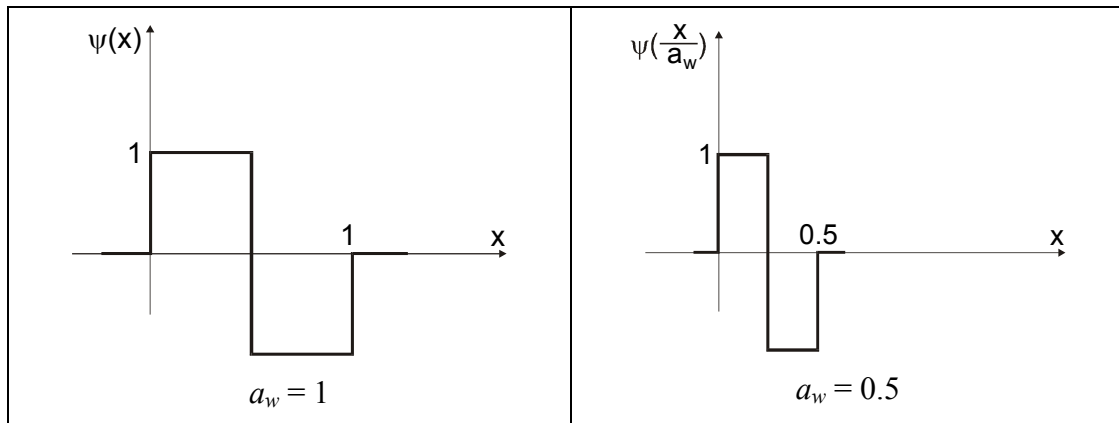


Figure 6.7: Example of waveform function: HAAR wavelet

The continuous wavelet transform CWT of the input function $f(x)$ is defined as the sum over all data of the signal multiplied by scaled and shifted versions of the waveform function Ψ :

$$CWT(a_w, b_w) = \int_{-\infty}^{\infty} f(x) \Psi\left(\frac{x-b_w}{a_w}\right) dx \quad (6.12)$$

with a_w Scale factor
 b_w Shift of position

As shown in Figure 6.7, a low scale a_w means a compressed wavelet, and, therefore, a signal with rapidly changing details, i.e., a high frequency of the signal. Thus, the inverse of the scale ($1/a_w$) is related to the frequency ω of the power spectral density. The decisive advantage of the wavelet transform is the ability to perform local analysis, in other words, to analyze a localized area of a larger signal. Hence, the wavelet transform can be used for both spectral analysis and edge detection in images. Evaluating the results of edge detection, the wavelet transform is a suitable method to determine the structure constant C_n^2 .

As an example of the wavelet transform using the Haar wavelet, Figure 6.8 shows the coefficients CWT in dependence of a_w and b_w . This wavelet transform is applied on a real grabbed one-dimensional image signal of the line scan sensor mentioned in section 5.2.4.

In this regard, the wavelet transform is implemented with use of the discrete wavelet transform algorithm developed by MALLAT [1988]. In contrast to the Welch method, the wavelet analysis simultaneously provides the spectral analysis of the signal and the positions of the edges. As illustrated in Figure 6.8, the bright stripes denotes the places of the edges. In other words, edges in the image signal represent a high value of the coefficients of the wavelet transform.

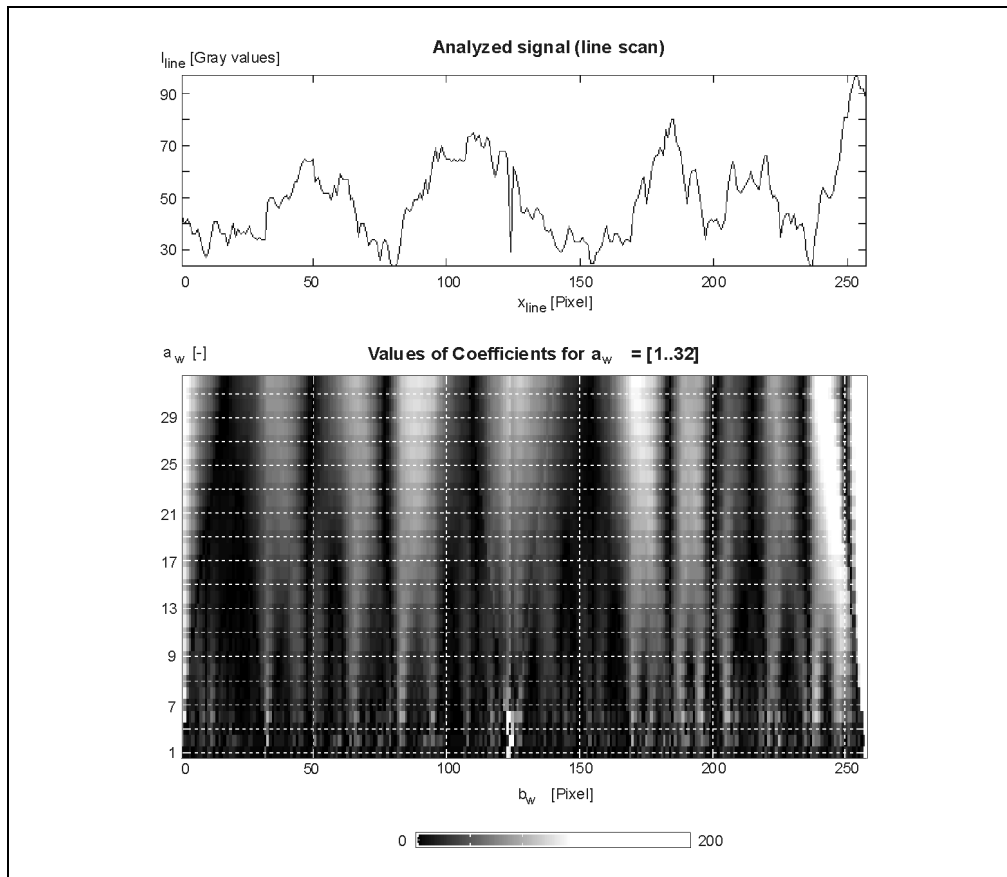


Figure 6.8: Wavelet transform of one-dimensional image signal

The connection between the wavelet transform and the structure constant is presented in [BETH, *et al.*, 1997] where the structure function of the phase $D_S(r)$ can be expressed by the wavelet transform:

$$D_S(a) = \left\langle [S(x_0 + a) - S(x_0)]^2 \right\rangle = \frac{1}{L_S} \int_0^{L_S} \left| S(x) \Psi \left(\frac{x - x_0}{a} \right) \right|^2 dx \quad (6.13)$$

with a Aperture
 x_0 Position of an edge in the image
 L_S Signal length

These relations are valid for each waveform function, but attention must be paid on the limited signal length L_S because (6.13) is only fulfilled if $L_S \gg a$. The structure function $D_S(a)$ is related to the structure constant C_n^2 as follows [DEUSSEN, WITTE, 1997]:

$$D_S(a) = \sigma_\alpha^2 \cdot (ka)^2 = c_L k^2 a^{5/3} C_n^2 R \quad (6.14)$$

with $c_L = 2.92$ (Plane waves)
 $= 1.09$ (Spherical waves)

The computational effort to perform a wavelet transform like in the example of Figure 6.8 is considerable. The example of Figure 6.8 (signal length: 256 pixels) requires 350,000 floating point operations, while other edge operators – e.g., the Canny operator

(cf. section 6.4) – only need about 24,000 floating point operations. In contrast to the Canny operator, the wavelet transform yields not only the position of the edge but also additional information about the spectrum. First results published in [BETH, *et al.*, 1997] show that the wavelet transform can be used for the determination of the structure constant C_n^2 .

However, a functional model connecting the wavelet transform $CWT(a_w, b_w)$ with the variance σ_V^2 necessary to determine the inner scale l_0 is not known up to now. For this reason, the additional computational effort of the wavelet transform is not accompanied by better results in comparison to other methods.

The edge operators presented in section 6.4 work more efficiently because no multiscale decomposition is needed. Since the artificial targets used in terrestrial geodesy do not have very different types of edges and other singularities, algorithms using the one-scale methods like Canny operator and Wiener filter reach sufficiently good results. Thus the latter technique will be investigated in the following.

6.3 Wiener filter for determination of intensity fluctuation

6.3.1 Introduction

As mentioned in section 6.1, the Wiener filter is applied for the following purposes:

1. Separation between signal and noise overlaying the signal. The spectrum of the noise is assumed to determine the intensity fluctuations necessary for the estimation of the inner scale l_0 .
2. Filtering the data to improve the edge detection which is used for estimation of the structure constant C_n^2 (cf. section 4.3.2).

Referring to point 1., the model of the Wiener filter supposes an undisturbed image signal $f(n_2)$ and additive noise signal $v(n_2)$. As given in (6.15), the signals f and v provide the (noisy) signal y which is measured:

$$y(n_2) = f(n_2) + v(n_2) \quad (6.15)$$

Herein, the time-dependent index variable n_2 is defined by (6.3). In general, a convolution filter estimates the filtered signal using the convolution of a linear discrete filter function $h(n_2)$ and the noisy signal $y(n_2)$ which is observed as given in (6.15).

$$\hat{f}(n_2) = h(n_2) \otimes y(n_2) \quad (6.16)$$

with \hat{f} Filtered signal (The hat $\hat{}$ denotes estimated quantities)

The discrete filter function $h(n_2)$ depends on the noise v which is influenced by intensity fluctuations. In other words, the filter function $h(n_2)$ is expected to provide information about the intensity fluctuations caused by turbulent processes. Thus, an appropriate digital filter must be found to describe optical turbulence. In the following approach, the Wiener filter is applied to provide the desired filter function $h(n_2)$ and the filtered signal.

The Wiener filter which was first described by WIENER [1950] was considered for image restoration in the 1960s and 1970s, e.g., [ANDREWS, HUNT, 1977]. In general, the Wiener filter uses minimum mean-square estimation to determine the filter function $h(n_2)$, e.g., [KROSCHEL, 1996]. Depending on the estimation algorithm, several sub-groups of Wiener filter exists. Figure 6.9 gives an overview of the classification of the Wiener filters. In Figure 6.9, the two criteria of classification are the filter type (causal or noncausal) and the application (global, image region) of the filter.

The first criterion of this classification is the filter type (causal or noncausal). Causal filters as mentioned in Figure 6.9 are defined by the following property:

$$f(n_2) = 0 \quad \text{for } n_2 < n_{2,0} \quad \Rightarrow \quad y(n_2) = h_{cau} \otimes f(n_2) = 0 \quad \text{for } n_2 < n_{2,0} \quad (6.17)$$

with $n_{2,0}$ Boundary value
 h_{caus} Point spread function of causal filter

The property of causal filters (6.17) implies that the effect y will not occur until the cause f has happened.

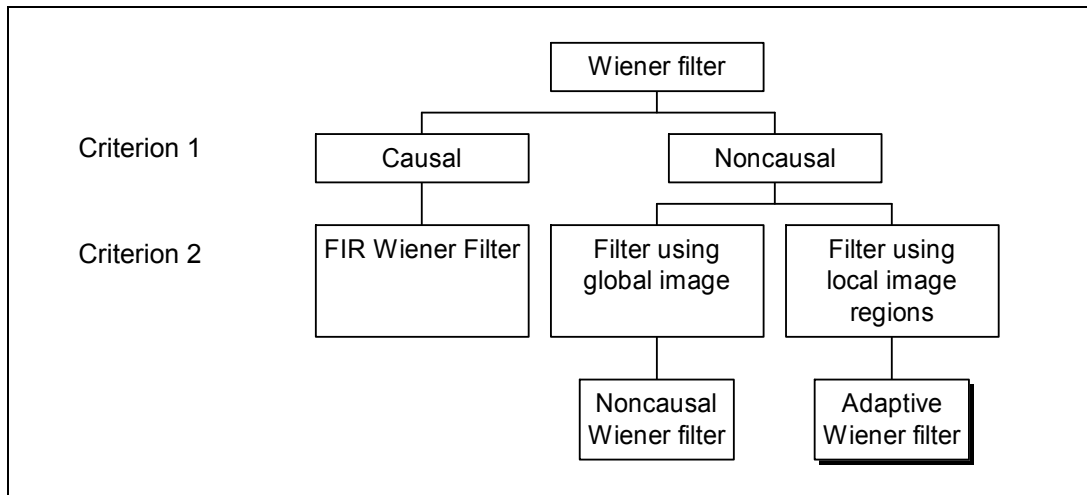


Figure 6.9: Classification of Wiener filter.

Highlighted: Type of Wiener filter applied in refraction analysis

Using the causal Wiener filter, the relation between the noisy observation y and the undisturbed image signal f is given by the Wiener-Hopf equations as follows, e.g., [KROSCHEL, 1996]:

$$\sum_{k_2=0}^{N_{Filt}} h(k_2) \cdot R_Y(n_2 - k_2) = R_{FY}(n_2) \quad 0 \leq n_2 \leq N_{Filt} \quad (6.18)$$

with N_{Filt} Length of the filter

where the autocorrelation function R_Y is defined by

$$R_Y(n_2) = E[y(k_2) \cdot y(k_2 + n_2)] \quad \text{for all } (k_2) \quad (6.19)$$

and the cross-correlation function R_{FY} by

$$R_{FY}(n_2) = E[f(k_2) \cdot y(k_2 + n_2)] \quad \text{for all } (k_2) \quad (6.20)$$

The Wiener-Hopf equations allow the computation of the filter coefficients $h(k_2)$ if the cross-correlation function and autocorrelation function of the input f and the output y are given or estimated by their power spectral densities. Solving the Wiener-Hopf (6.18) equations is demanding and can be simplified under the assumption that the Wiener filter is noncausal. Neglecting the requirement of causality (6.17) is feasible in applications of image processing, since the whole image signal information is available when the filter coefficients are computed, e.g., [PRATT, 1991]. The noncausal Wiener filter is presented in section 6.3.2. As shown there, a spectral model $S_V(\omega_2)$ of the noise signal $v(n_2)$ is necessary for the application of the Wiener filter. Based on the practical experiments, a spectral model $S_V(\omega_2)$ has been empirically derived which is presented in section 6.3.3.

The second criterion of the classification in Figure 6.9 emphasizes how the filter processes the given image signal. On the one hand, the (fixed) Wiener filter uses all pixels simultaneously to separate the signal from the noise overlaying the signal (Noncausal Wiener filter) and, on the other hand, the Wiener filter uses local regions of the image to estimate the signal f (adaptive Wiener filter). The adaptive Wiener filter as presented in section 6.3.4 is implemented to evaluate the measured image data obtained by the line scan camera (section 7.2).

6.3.2 Noncausal Wiener filter

As mentioned above, the noncausal Wiener filter assumes that, after the measuring time, all intensities $y(n_2)$ of the column n_1 of the image are available for the computation. A further requirement of the derivation of the noncausal Wiener filter is the stability of the filter, i.e., the impulse response must not be infinite:

$$\sum_{k_2=-\infty}^{\infty} |h(k_2)| < \infty \quad (6.21)$$

with k_2 Index variable of filter

Assuming that the stability criterion is fulfilled, the noncausal Wiener filter can be applied. From (6.16) follows that the signal f is related to the noisy observations y and the filter h using the discrete convolution:

$$\hat{f}(n_2) = \sum_{k_2=-\infty}^{\infty} h(k_2) \cdot y(n_2 - k_2) \quad (6.22)$$

If the filter function h is given, the discrete convolution (6.22) can be computed since all observations y are available (property of noncausal filter). In order to estimate the filter function h , the Wiener filter uses mean-squared-error estimation. This estimation uses the orthogonality principle which can be written as, e.g., [KROSCHER, 1996]:

$$E[\{f(n_2) - \hat{f}(n_2) \cdot y(n_2)\}] = 0 \quad (6.23)$$

If (6.23) is inserted into (6.22), the following so-called Wiener-Hopf equation for noncausal Wiener filtering is given by:

$$\sum_{k_2=-\infty}^{\infty} h(k_2)R_Y(n_2 - k_2) = R_{FY}(n_2) \quad \begin{array}{l} -\infty \leq n_1 \leq \infty \\ -\infty \leq n_2 \leq \infty \end{array} \quad (6.24)$$

Since equation (6.24) is fulfilled for all integer pixel coordinates n_2 , (6.24) can be rewritten using the convolution operator \otimes :

$$R_{FY}(n_2) = h(n_2) \otimes R_Y(n_2) \quad (6.25)$$

If the autocorrelation function and the cross-correlation functions are Fourier-transformed to the power spectral densities S_Y and S_{FY} as given in (6.28) and (6.29), the spectral filter function $H(\omega_2)$ can be solved from (6.25) and the noncausal Wiener filter is given by:

$$H(\omega_2) = \frac{S_{FY}(\omega_2)}{S_Y(\omega_2)} \quad (6.26)$$

$$\text{with } H(\omega_2) = \sum_{n_2=-\infty}^{\infty} h(n_2)e^{-i\omega_2 n_2} \quad (6.27)$$

$$S_{FY}(\omega_2) = \sum_{n_2=-\infty}^{\infty} R_{FY}(n_2)e^{-i\omega_2 n_2} \quad (6.28)$$

$$S_Y(\omega_2) = \sum_{n_2=-\infty}^{\infty} R_Y(n_2)e^{-i\omega_2 n_2} \quad (6.29)$$

On the assumption that the image signal $f(n_2)$ and the noise $v(n_2)$ are uncorrelated and zero-mean stochastic processes (i.e., $R_{FV} \equiv 0$), the autocovariance function R_{FY} in (6.25) can be written as:

$$\begin{aligned} R_{FY}(n_2) &= E[f(k_2+n_2) \cdot y(k_2)] \\ &= E[f(k_2+n_2) \cdot \{f(k_2)+v(k_2)\}] \\ &= R_F(n_2) + R_{FV}(n_2) \\ &= R_F(n_2) \end{aligned} \quad (6.30)$$

By using (6.15), the autocorrelation function R_Y can be obtained by

$$R_Y(n_2) = R_F(n_2) + R_V(n_2) \quad (6.31)$$

From (6.26), (6.30) and (6.31), the noncausal Wiener filter is given by

$$H(\omega_2) = \frac{S_F(\omega_2)}{S_F(\omega_2) + S_V(\omega_2)} \quad (6.32)$$

With the noncausal Wiener filter, the image signal f can be estimated using a linear estimator provided that the power spectral density of the undisturbed signal S_F and the power spectral density of the noise signal S_V are given or estimated. The noncausal

Wiener filter assumes that there is only one single power spectral density $S_F(\omega_2)$ which refers to the global image. In the case of adaptive Wiener filter discussed in 6.3.4, the power spectral density of the signal S_F is assumed to depend on the time, too, i.e., $S_F(\omega_2, n_2)$. Thus, the adaptive Wiener filter uses several power spectral densities in various image regions, i.e., one power spectral density S_F per image region (for details see section 6.3.4).

At first, the power spectral density of the noise signal $S_V(\omega_2)$ is unknown. Therefore, further investigations as presented in section 6.3.3 are necessary to model the noise signal $S_V(\omega_2)$ by means appropriate parameters (such as σ_V^2) whereby these parameters are expected to indicate the intensity fluctuations needed for the determination of l_0 .

The parameters of the spectrum $S_V(\omega_2)$ can be estimated by using the Welch method, (cf. section 6.2.3b) if the noise signal $v(n_2)$ is known. However, the noise signal $v(n_2)$ is not available before noisy observation signal y has been filtered. Thus, the estimation of $v(n_2)$ is given by:

$$\hat{v}(n_2) = y(n_2) - \hat{f}(n_2) \quad (6.33)$$

with $\hat{v}(n_2)$ Estimated noise signal

In (6.33), the filtered signal \hat{f} is assumed to be known. Since this is not the case, the noise signal $v(n_2)$ and the parameters of the spectrum $S_V(\omega_2)$ must be determined using iterative loops. In doing so, a first approximation of $S_{V,0}(\omega_2)$ is required which leads to a first approximation of the filtered signal \hat{f}_0 using (6.32) and (6.22). In the next steps, the succeeding approximations of $S_{V,j}(\omega_2)$ ($j = 1, 2, \dots$) can be calculated iteratively by estimating the power spectral density of the residuals $v(n_2)$ obtained by (6.33). At the end, this algorithm produces an estimation of the spectrum $S_V(\omega_2)$ the parameters of which can be used for the determination of intensity fluctuations. The model which describes the spectrum $S_V(\omega_2)$ and, thus, the intensity fluctuations is discussed in the following section.

6.3.3 Model of the power spectral density used for the Wiener filter

As presented in (6.32), the Wiener filter requires a function $S_V(\omega_2)$ for the power spectral density of the noise signal. Referring to the refractive index spectrum given by

$$\Phi_n(\kappa) \propto \cdot \kappa^{-11/3} \quad \text{for } 2\pi/L_0 < \kappa < 2\pi/l_0 \quad (6.34)$$

a plausible model of $S_V(\omega_2)$ can be suggested as follows

$$S_V(\omega_2) = a_\omega \omega_2^{-11/3} + \sigma_v^2 \quad (6.35)$$

This model is controlled by the parameters a_ω and σ_v^2 which must be estimated whereby σ_v^2 is assumed to be a measure for the intensity fluctuations and is used for the determination of the inner scale in section 4.4.

In order to validate the model (6.35), a line scan camera as introduced in section 5 grabbed images within the scope of the field experiments described in section 7, and a spectral analysis of these images was calculated. In doing so, the time series of the intensity of a selected pixel (fixed position of the pixel in the image = n_1) are analyzed by means of the Welch method as presented in section 6.2.3. Two representatives example of the spectral analysis are plotted in Figure 6.10

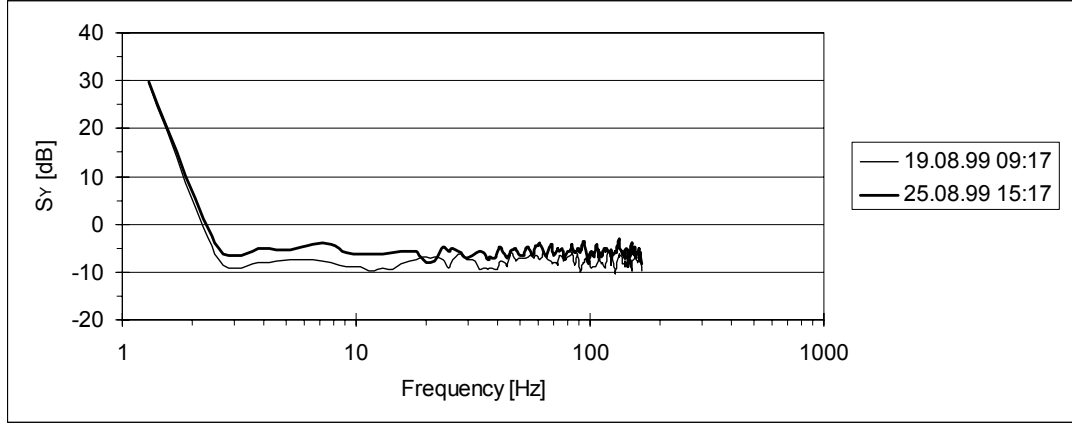


Figure 6.10 Spectral analysis of the time series of the pixel intensity
(Images recorded in Claro, cf. section 7.2)

The spectral analysis of Figure 6.10 is limited to a maximal frequency which is given by the Nyquist frequency $0.5f_s$. In other words, in order to recover all Fourier components of a periodic waveform, it is necessary to sample more than twice as fast as the highest waveform frequency. Hereby, the line scan camera grabbed with a sampling frequency $f_s = 333$ Hz, i.e., the maximal frequency which can be detected is at the most than 167 Hz. The peak in Figure 6.10 can be interpreted as DC-value and depends on the radiometric intensity of the grabbed target. Since the averaged intensity mainly depends on the exposure, the DC-value does not greatly matter for investigations of refraction influences. Thus, the investigation of refraction influences concentrates on the remaining Fourier components in the following.

From (6.15) and (6.35) follows the power spectral density of the measured signal y (intensities of a pixel) as

$$S_Y(\omega_2) = S_F(\omega_2) + S_V(\omega_2) = S_F(\omega_2) + a_\omega \omega_2^{-11/3} + \sigma_v^2 \quad (6.36)$$

As an approximation, this model of the power spectral density is modelled by

$$S_Y(\omega_2) = A_{DC} \cdot \delta(\omega_2) + \sigma_v^2 \quad (6.37)$$

with A_{DC} DC-value
 $\delta(\omega_2)$ Dirac function

and

$$S_V(\omega_2) = \sigma_v^2. \quad (6.38)$$

As an advantage, the modified spectrum of (6.38) facilitates the inverse Fourier transform of (6.32) which is required for the calculation of the Wiener filter.

The modified spectrum is depicted schematically in Figure 6.11. Besides the low frequencies, the modified spectrum parameterizes quite well with the measured spectrum.

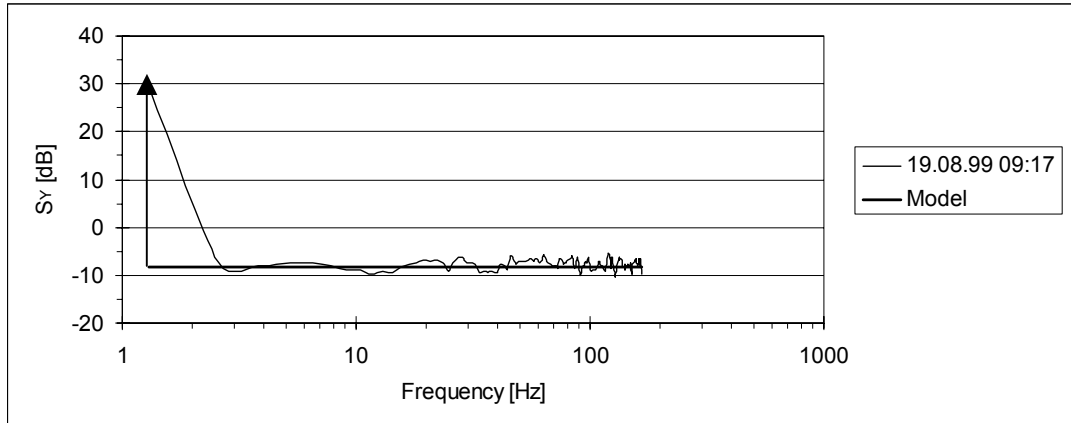


Figure 6.11: Spectrum of the modified model in comparison with the measured power spectral density

Thus, in the scope of the field experiments presented in section 7.2, the implemented Wiener-filter algorithm uses the modified model of (6.38) to determine the noise variance σ_V^2 which is required for the determination of the inner scale (section 4.4). Hereby, the implementation of the Wiener filter is discussed in the following section.

6.3.4 Implementation using adaptive Wiener filter

Although the noncausal Wiener filter can be efficiently implemented, this filter is usually not applied in image processing due to the following disadvantage: The use of a fixed filter such as the noncausal Wiener filter throughout the entire image signal $f(n_2)$ can cause systematic deviations of the estimated parameters since this filter is time-invariant.

This deviations can occur if the image patterns float (i.e. move slowly) in n_1 -direction with a slow frequency during the measuring time (e.g. due to vibrations of the instrument) whereby the Wiener filter is applied in n_2 -direction.

The influence of this floating process on the image signal $f(n_2)$ is depicted schematically in Figure 6.12.

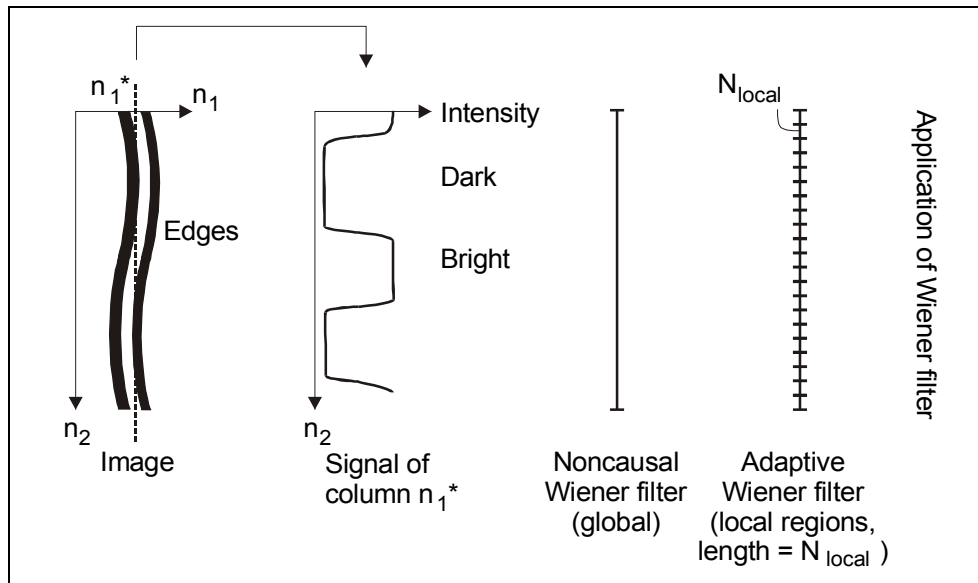


Figure 6.12: Intensity deviations in the signal $f(n_2)$ caused by Floating of image pattern (schematically)

Because the image characteristics (contrast, variance of intensities, etc.) may differ noticeably in parts of the image, adaptive image processing is recommended as is presented in the following [LIM, 1990]. Adaptive image processing involves that, at each pixel n_2 in a specified column n_1^* , the local characteristics are determined in the neighborhood of the pixel and are used as a-priori-knowledge to determine the presence of significant high-frequency details of the image signal.

In other words, instead of assuming a fixed spectral density S_F for the entire image, the adaptive Wiener filter locally estimates this spectral density: For each pixel, the algorithm extracts a part of the image, called local region. Since the adapted Wiener filter is applied in the direction of the n_2 -axis, the local regions have one pixel in n_1 -direction and N_{local} pixels in n_2 -direction whereby N_{local} must be defined by the user (cf. Figure 6.12). Within the local region corresponding to a pixel n_2 , the image signal f_{local} can be approximated by:

$$f_{local}(n_2) = m_{F, local}(n_2) + \sigma_{F, local}(n_2) \cdot N(0,1) \quad (6.39)$$

with $m_{F, local}$ Local mean of the (undisturbed) image signal F
 $\sigma_{F, local}$ Local standard deviation
 $N(0,1)$ Zero-mean Gaussian white noise with unit variance

This model is based on the assumption that the local mean and the local standard deviation of the image signal do not change in the local region and the random deviations can be described by zero-mean Gaussian white noise. Of course, this model will only hold if the size N_{local} of the local region is chosen correctly:

- If N_{local} is chosen too large, (6.39) is not fulfilled yet, since the signal is not stationary in a region which is too large.
- If N_{local} is chosen too small, practical investigations show that the estimation of the spectra is biased.

Based on the results of the field measurements (section 7.2) $N_{local} = 15$ pixel can be recommended. If N_{local} is chosen larger than 15 pixel, the results do not change significantly but a disadvantage is the increase of computational effort caused by the increase of the size of N_{local} , cf. (6.50) and (6.51).

Using the model of (6.37) and (6.39), the power spectral density of the local image signal $S_{F, local}$ leads to

$$S_{F, local} = S_{F, local}(\omega_2, n_2) = \sigma_{F, local}^2(n_2) \quad (6.40)$$

From (6.32), (6.38), and (6.40), the local filter function h_{local} for the adaptive Wiener filter is given by:

$$H_{local}(\omega_2, n_2) = \frac{S_{F, local}(\omega_2, n_2)}{S_{F, local}(\omega_2, n_2) + S_V(\omega_2)} = \frac{\sigma_{F, local}^2(n_2)}{\sigma_{F, local}^2(n_2) + \sigma_V^2} \quad (6.41)$$

$$h_{local}(n_2) = \text{DFT}^{-1}\{H_{local}\} = \frac{\sigma_{F, local}^2(n_2)}{\sigma_{F, local}^2(n_2) + \sigma_V^2} \delta(n_2) \quad (6.42)$$

with DFT^{-1} Inverse discrete Fourier Transform
 $\delta(n_2)$ Kronecker Delta function

As mentioned in the derivation of (6.32), the equations (6.32) and (6.41), respectively are only valid if the image signal $f(n_2)$ and the noise $v(n_2)$ are uncorrelated and zero-mean signals (i.e., $R_{FV} = 0$).

In order to obtain a zero-mean signal, a transformation with the shift variable $m_{F, local} = E[F(\cdot)]$ is required as illustrated in Figure 6.13. However, this transformation does not change the results of the estimation process.

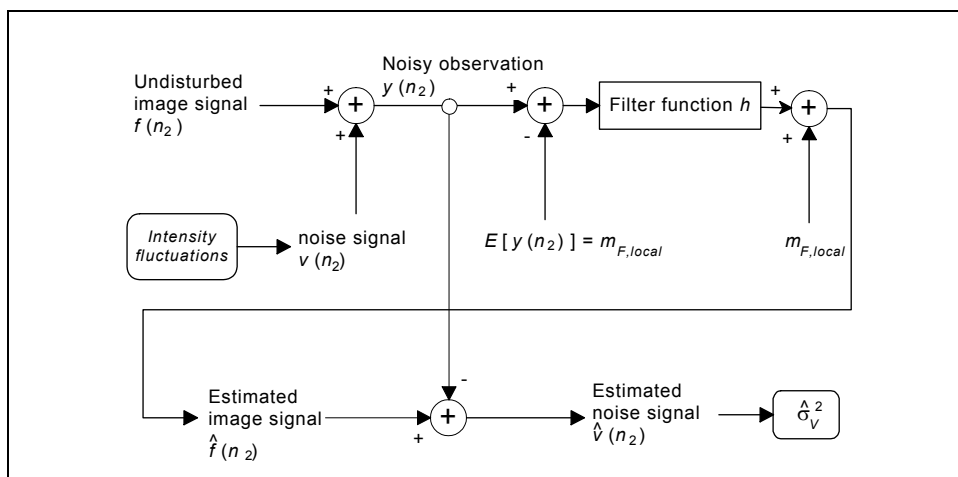


Figure 6.13: Model for signal estimation with Wiener filter h

From Figure 6.13 and (6.16), the filtered image signal \hat{f} is estimated by

$$\hat{f}(n_2) = \hat{m}_{F,local}(n_2) + [y(n_2) - \hat{m}_{F,local}(n_2)] \otimes h_{local}(n_2) \quad (6.43)$$

$$\text{with } \hat{m}_{F,local} = \frac{1}{N_{local}} \cdot \sum_{n_2 \in L_{reg}} y(n_2) \quad (6.44)$$

N_{local} Number of rows of the local image region

L_{reg} Set of pixels in the local region

Using the local filter function (6.42), equation (6.43) yields:

$$\hat{f}(n_2) = \hat{m}_{F,local}(n_2) + \frac{\hat{\sigma}_{F,local}^2(n_2)}{\hat{\sigma}_{F,local}^2(n_2) + \sigma_V^2} [y(n_2) - \hat{m}_{F,local}(n_2)] \quad (6.45)$$

$$\text{with } \hat{\sigma}_{F,local}^2 = \sigma_Y^2 - \sigma_V^2 = \frac{1}{N_{local} - 1} \cdot \sum_{n_2 \in L_{reg}} [y(n_2) - \hat{m}_{F,local}]^2 - \sigma_V^2 \quad (6.46)$$

Equation (6.45) provides the filtered image using the adaptive Wiener filter. In (6.45) and (6.46), the noise variance σ_V^2 as a parameter the spectrum of the noise signal S_V is assumed to be constant throughout the whole image and is assumed to be known. But in the scope of determination of intensity fluctuations, the noise variance σ_V^2 is unknown and, therefore, has to be estimated by means of iteration loops. At the beginning of the iteration loop, the first approximation for the variance $\sigma_{V,0}^2$ is calculated by:

$$\sigma_{V,0}^2 = E[(E(y) - y)^2] \quad (6.47)$$

Using $\sigma_{V,0}^2$, the adaptive Wiener filter provides the filtered signal \hat{f}_0 as a result of the first iteration loop. In the following step, the next iteration of σ_V^2 is given by

$$\sigma_{V,1}^2 = E[(\hat{f}_0 - y)^2] \quad (6.48)$$

Then, the filtered signal \hat{f}_1 of the next iteration loop is estimated by means of $\sigma_{V,1}^2$ and (6.45). The algorithm terminates as soon as the absolute error of convergence ε_{err} can be neglected:

$$|\hat{\sigma}_{V,j}^2 - \hat{\sigma}_{V,(j-1)}^2| < \varepsilon_{err} \quad \text{for } j = 1, 2, \dots \quad (6.49)$$

with j Index of the iteration loop

This iterative algorithm results in a locally minimum mean-square estimation of the image signal whereby the corresponding variance σ_V^2 is expected as a measure for intensity fluctuations.

With regard to the implementation of the adaptive Wiener filter by a software, attention should be paid to the computational efficiency. Thus, it is recommended to calculate the

values of the local average $m_{F,local}$ and the local variance $\sigma_{F,local}^2$ using the following convolution:

$$m_{F,local}(n_2) = h_{region}(n_2) \otimes y(n_2) / N_{local} \quad (6.50)$$

$$\sigma_{X,local}^2(n_2) = h_{region}(n_2) \otimes y^2(n_2) / N_{local} - m_{X,local}^2(n_2) - \sigma_V^2 \quad (6.51)$$

where h_{region} Convolution kernel of local image region. This is a vector with N_{local} elements consisting of ones in each element

This procedure is advantageous since the convolution can be performed using the algorithm of the Fast Fourier transform (FFT).

6.3.5 Conclusions and outlook

The presented approach applies the adaptive Wiener filter to estimate both the filtered image signal and the variance σ_V^2 which is used in further calculations to determine the intensity fluctuations and the inner scale l_0 as described in section 4.4.2. Hereby, σ_V^2 is a parameter of the model S_V which describes the power spectrum density of the additive noise and which the Wiener filter requires for the calculation of the filter function (cf. (6.32) and (6.41)). Therefore, the estimation of parameters necessary to determine the intensity fluctuations is related to the estimation of an appropriate filter function.

Although the presented algorithm of the adapted Wiener filter satisfied in evaluating the measurements as presented in section 7.2, some questions remain which should be investigated in further research work:

- The used model for S_V is an approximation only. Further investigations should seek for terms which correspond to the $\kappa^{-11/3}$ -law of the refractive index spectrum and which describe the spectrum of the intensity fluctuations more accurately.
- If further spectral analysis determines a function S_V which is more sophisticated than (6.38), the filter function (6.41) of the adapted Wiener filter still can be used but the inverse Fourier transform (6.42) becomes more difficult. In this case, the algorithm of the adapted Wiener filter must be modified: Instead of estimating the filtered image signal in the time domain as given in (6.43), the filtered image signal F must be estimated in the frequency domain and, in a next step, transformed into the time domain by means of the inverse Fast Fourier transform.
- The presented algorithm of the adapted Wiener filter is computationally expensive. As revealed by the field experiments, the floating of image structures as illustrated in Figure 6.12 is considerably smaller in reality than it was assumed at the time when this algorithm was designed. Therefore, the question may arise how the algorithm can be optimized to decrease the computational effort without affecting adversely the estimation of the desired parameters.

6.4 Edge detection for determination of angle-of-arrival fluctuation

6.4.1 Introduction

Angle-of-arrival fluctuations of the incoming light waves slightly shift image patterns when monitoring a distant target such as a coded levelling rod as described in section 4.3 and 5.5. The displacement of the pattern is perceived as edges changing their position in the image. In order to determine angle-of-arrival fluctuations and the structure constant of refractive index C_n^2 with use of image processing techniques and equation (4.31), the time-dependent position of edges in the grabbed image has to be evaluated and the variance σ_x^2 (fluctuation) of these edges must be determined.

Edges are intensity discontinuities in the progression of the undisturbed image signal $f(x)$ (gray value function). Assuming images which are acquired from line scan sensors, a one-dimensional edge is modelled as a ramp or a step, i.e., a decrease in image amplitude level from a high to a low level or vice versa.

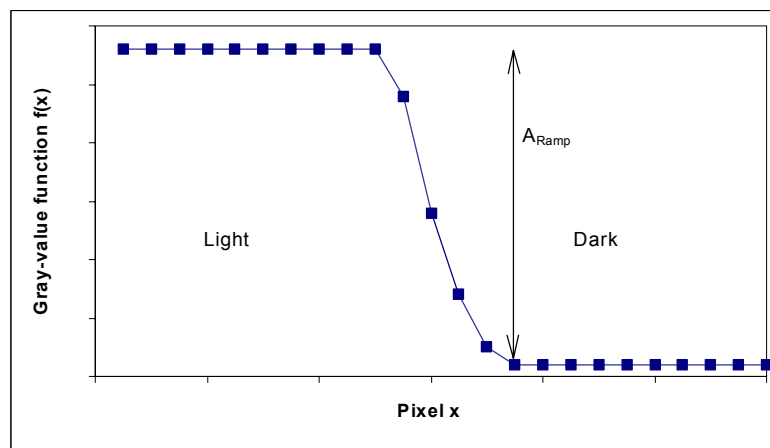


Figure 6.14: Model for edges in one-dimensional images: Ramp
Dots: Sampled values of the image signal

An edge exists if the slope of the ramp and, therefore, the difference of image amplitude level exceeds a specified threshold. To detect edges, places in the image must be found, where the intensity changes rapidly, using one of these criteria (cf. Figure 6.16):

- Places where the first derivative of $f(x)$ is larger in magnitude than a threshold
- Places where the second derivative of $f(x)$ has a zero crossing (cf. Figure 6.16)
- Places where a given template of an edge matches optimally with the gray levels of the image (template matching, cf. Figure 6.18)

When dealing with edge detection in images of natural scenes, the amount of noise must be taken into account. Unfortunately, noisy signals normally consist of similar high frequencies like signals which contain edges. Thus, a crucial step in edge detection is that, on the one hand, edges which occur in the image should be detected despite of noise and, on the other hand, noisy signals must not produce fictitious edges.

Nowadays, a wide variety of edge detection algorithms exists. A classification of the most known algorithms is presented in Figure 6.15.

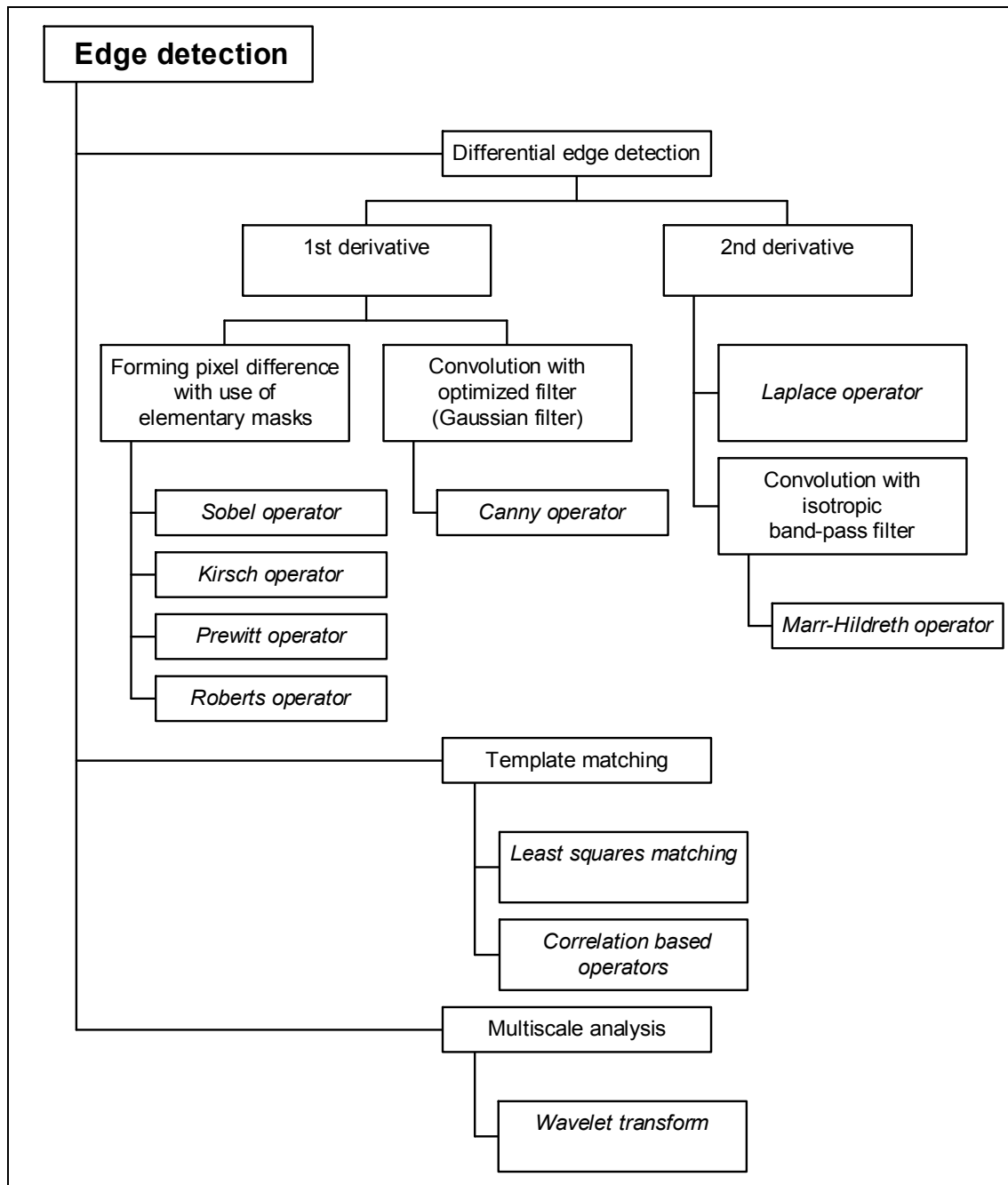


Figure 6.15: Classification of edge detection algorithms.

The Canny operator and the least squares matching are chosen for further investigations concerning refraction influences.

In section 6.4.2, the principles and drawbacks of the presented algorithms are discussed briefly. Section 6.4.3 presents a comparison and evaluation of edge detection algorithms in order to select the appropriate algorithm for refraction analysis. The applied algorithms are explained in more detail in section 6.4.4 and 6.4.5. Section 6.4.6 provides considerations about the accuracy of the applied algorithms.

6.4.2 Edge operators

As shown in Figure 6.15, the investigated edge operators can be classified into differential edge detection, template matching techniques and multiscale analysis. In the case of multiscale analysis, the wavelet transform as a representative for this technique has already been discussed in section 6.2.4 in context of spectral analysis. The template matching techniques are explained at the end of this section since these techniques using reference image patches work completely different from the other edge operators.

The basic concept of differential edge detection is to differentiate the image function $f(x)$ as follows:

$$g(x) = f(x) \otimes h(x) \quad (6.52)$$

Equation (2.4) expresses a convolution between the image signal $f(x)$ and a specific mask or filter function $h(x)$. Since the image function is a discrete function, the differentiation must be approximated using the filter function $h(x)$ whereby several approaches are known for $h(x)$ (cf. Table 6.1). A simple approach is to subtract the gray value of the preceding pixel from the gray value of the subsequent pixel. Thus, the filter function is

$$h(x) = (-1 \quad 1 \quad 0) \quad (6.53)$$

The convolution of (2.4) provides the discrete differentiation $g(x)$, in other words, the amount of the gradient of the image signal, e.g., [PRATT, 1991]. Places of an edge are detected, if the local maximums of the first derivative $g(x)$ exceed a specified threshold. In the last step, the standard deviation of the positions of the edges has to be calculated in order to determine σ_x^2 and the angle-of-arrival fluctuations using (4.31).

The simple approach of (6.53) is not applicable because noisy signals can easily produce fictitious edges and real edge cannot be detected if the specified threshold of the amount of gradient is incorrect. Thus, more sophisticated algorithms are required which are presented in the following sections.

a) *Elementary masks*

The direct subtraction of gray values which was presented in (2.4) is normally not used in practice, since the least perturbation between neighboring pixels will change the amount of the gradient $g(x)$. To overcome this insufficiency, various types of masks have been investigated and documented as shown in Table 6.1.

For applying the convolution kernel of the Sobel, Kirsch, and Roberts operator as presented in Table 6.1, the image must be a two-dimensional signal $f(x, y)$. In the case of line scan camera, this restriction is easily fulfilled when a couple of line scans are grabbed one after another, so that a frame of subsequent lines forms the two-dimensional signal.

Operator	Mask (convolution kernel)	Comments
Prewitt	$h(x) = (-1 \ 0 \ 1)$	The pixel difference is formed with the next but one pixel which is assumed as undisturbed
Roberts	$h(n_1, n_2) = \begin{pmatrix} -1 & 0 & 0 \\ 0 & 1 & 0 \\ 0 & 0 & 0 \end{pmatrix}$	Diagonal-crossing edges are easier to be detected, but no improvement in images containing rectangular structures
Sobel	$h(n_1, n_2) = \begin{pmatrix} -1 & 0 & 1 \\ -2 & 0 & 2 \\ -1 & 0 & 1 \end{pmatrix}$	Smoothing effects in direction of the edge are achieved by use of three lines which are weighted (weights: determined with the binomial distribution which approximates the Gaussian distribution.)
Kirsch	$h(n_1, n_2) = \begin{pmatrix} -3 & 5 & 5 \\ -3 & 0 & 5 \\ -3 & -3 & -3 \end{pmatrix}$	Each edge direction uses its own convolution kernel. Smoothing effects in direction of the edge like the Sobel operator.

Table 6.1: Elementary masks of edge detection operators

The mentioned elementary masks have in common, that edges are detected with relatively small computational efforts. The structure of this elementary masks reduces the influences of noise to a certain degree.

In order to detect edges in one-dimensional images, the Sobel is preferred to the Roberts, Prewitt, and the Kirsch method, since the Prewitt operator is more sensitive to noise and because the Roberts and the Kirsch operator offer advantages which are only useful in two-dimensional images with diagonal structures. The results of the comparison are presented in section 6.4.3.

b) Laplacian operator

The Laplacian operator is based on the second derivative of the image function $f(x)$:

$$g'(x) = \nabla^2 f(x) \tag{6.54}$$

As shown in Figure 6.16, the zero-crossings of $g'(x)$ are places of edges. This is equivalent to other methods using the first derivative where the positions of edge are at places with a local maximum of the first derivative $g(x)$.

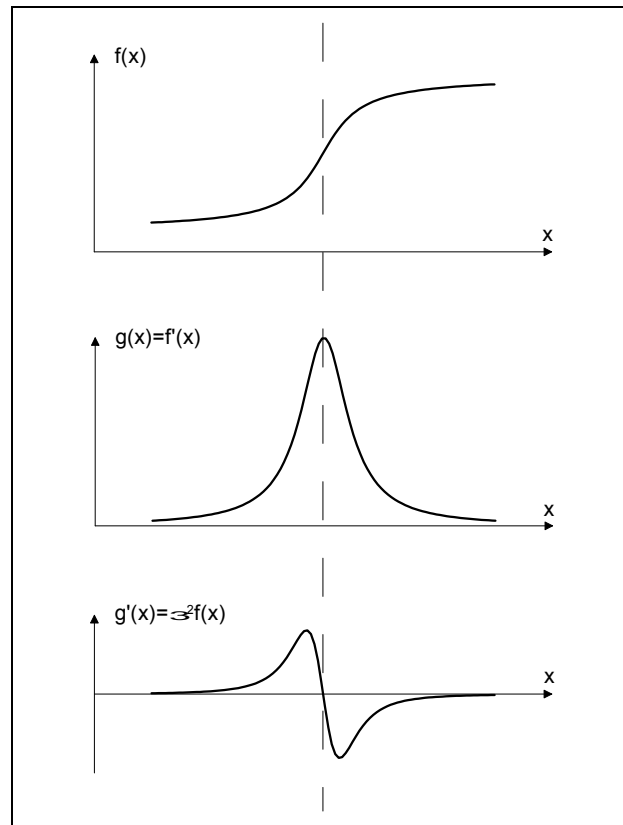


Figure 6.16: Localization of edges

The Laplacian operator is even more sensitive to high-frequency noise signals than the methods based on the first derivative. This influence will be made clear in the following where a sinusoidal noise signal $v(x)$ with frequency ω and amplitude v_0 is investigated:

$$v(x) = v_0 \sin(\omega x) \quad (6.55)$$

The second derivative of (6.55) is

$$\frac{d^2}{dx^2} v(x) = -v_0 \omega^2 \sin(\omega x) \quad (6.56)$$

(6.56) demonstrates that the influence of the noise becomes stronger with the second derivation (amplification factor ω^2). To limit the interfering influence of noise, an appropriate lowpass filter (e.g., Gaussian filter) has to filter the image signal before differentiation [MARR *et. al.* 1980].

This method is almost identical with the Canny operator (see section 6.4.2c) because the maximum in the output of a first derivative operator like the Canny operator corresponds to zero-crossings in the Laplacian operator.

c) Canny operator

The differential edge operators presented in 6.4.2a) have been heuristically derived. However, CANNY [1986] has taken a mathematical approach to edge detection. The Canny operator is based on a one-dimensional, continuous model for a step edge which is disturbed by additive white Gaussian noise with standard deviation σ_V .

The basic strategy of the Canny operator is the convolution of the given noisy edge signal $f(x)$ with an anti-symmetric convolution kernel $h(x)$, which is an impulse response function with zero amplitude outside the range $[-w_c, w_c]$ (Figure 6.17).

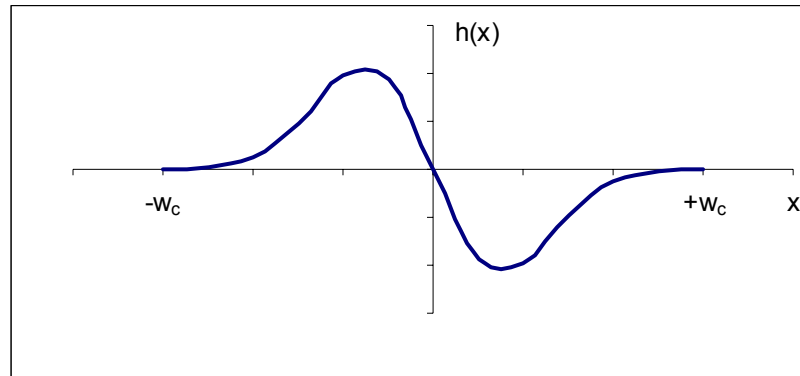


Figure 6.17: Example of asymmetric convolution kernel $h(x)$:
First derivative of the Gaussian function as used by the Canny operator

The impulse response function must fulfill the following three criteria:

1. Good detection: The probability of failing to detect true edge points and the probability of falsely marking nonedge points should be low.
2. Good localization: The detected edges should be as close as possible to the true edge points.
3. Single response: The operator should mark only one place to the same edge. This requirement is implicitly captured in the first criterion. But this criterion must be stated explicitly for mathematical reasons.

In order to mould the first criterion into mathematical terms, the signal-to-noise ratio $SNR(h)$ can be used which is defined as [CANNY, 1986]:

$$SNR(h) = \frac{A_{Ramp} \cdot \int_{-w_c}^0 h(x) dx}{n_0 \int_{-w_c}^{w_c} [h(x)]^2 dx} \quad (6.57)$$

with n_0 Mean-squared noise amplitude per unit length

If a filter h is found which maximizes $SNR(h)$, this high signal-to-noise ratio means good detection. As an assumption of (6.57), the function $f(x)$ assigns the image region which contains an edge, thus $f(x)$ is modelled by a ramp function of the amplitude A_{Ramp} as shown in Figure 6.14.

Referring to the second criterion, a localization factor $Loc(h)$ must be defined which models the quality of the localization of edges [CANNY, 1986], [PRATT, 1991]:

$$Loc(h) = \frac{A_{Ramp}}{n_0} \cdot \frac{h'(0)}{\int_{-w_c}^{w_c} [h'(x)]^2 dx} \quad (6.58)$$

where $h'(x)$ is the first derivative of $h(x)$. $Loc(h)$ increases if the result of the operator is as close to the edge as possible.

With these terms, the design of the optimal impulse response function for the Canny-operator reduces to the maximization of the product $SNR(h) \cdot Loc(h)$:

$$SNR(h) \cdot Loc(h) \rightarrow \max \quad (6.59)$$

In general it is impossible to find analytically a closed form for the optimal impulse response function $h(x)$ which maximizes (6.59). But CANNY [1986] showed that the first derivative of a Gaussian function $G'(x)$

$$G'(x) = \frac{-x}{\sqrt{2\pi\sigma_c^6}} \exp\left(-\frac{x^2}{2\sigma_c^2}\right) \approx h(x) \quad (6.60)$$

with σ_c Standard deviation of Canny operator

is a suitable approximation for the optimal impulse response $h(x)$, especially for large w_c . The standard deviation of the Canny operator σ_c is given by the requirement that

- $h(x)$ is non-zero within the range $[-w_c; +w_c]$ as defined in Figure 6.17
- $h(x)$ is zero outside of the $[-w_c; +w_c]$

The range parameter w_c and, consequently, the standard deviation of Canny operator σ_c are given by the minimal distance which is required for neighboring edges: Within the range $[-w_c; +w_c]$ the Canny operator detects at the most one single edge only. Practical investigations showed that a range defined by $w_c = 7$ is suitable for edge detection in the scope of the used instrumental setup for refraction analysis. If w_c is chosen smaller, the approximation of (6.60) will be deteriorated. If w_c is chosen larger, the used code of the levelling rod involves, that more than one single edge is mapped in the range $[-w_c; +w_c]$.

Thus, $G'(x)$ inserted as filter function $h(x)$ into (2.4) yields:

$$g(x) = f(x) \otimes \frac{-x}{\sqrt{2\pi\sigma_c^6}} \exp\left(-\frac{x^2}{2\sigma_c^2}\right) \quad (6.61)$$

Using equation (6.61), the Canny operator marks an edge at the local maximum of the convolved gradient $g(x)$. Under the assumption that minimal distance of neighboring

edges is not too small (see the remarks to (6.60) above), the Canny operator provides a reliable edge detection as shown in section 6.4.3. The derivation of the desired standard deviation by means of the Canny operator is presented in section 6.4.5f).

d) *Template matching*

Edge detection using template matching uses synthetically generated or measured image patches (or templates) which contains an edge. Template matching can be performed with several techniques whereas least squares template matching is first presented in the following. Least squares template matching used for edge detection and tracking is based on the least squares image matching technique as described in [FÖRSTNER, 1982], [ACKERMANN, 1984], and [GRÜN, 1985]. To extend the least squares template matching algorithm for high accuracy measurement of edge positions, a real feature pattern is introduced as the reference template and is subsequently matched with image patches containing actual edge segments. Thus, the local direction, shape and gray value distribution of the edge point are specified in the template. The extracted edge point is fully determined using transformation parameters which provide a relation between the initial position and the final position of the template in the measured image (Figure 6.18).

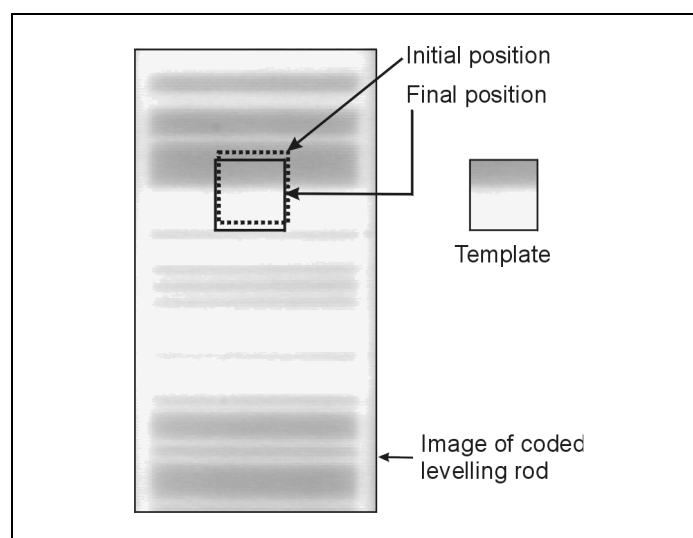


Figure 6.18: Visualization of least squares matching for coded levelling rod

The user gives an approximate position for the edge and the matching procedures locates the precision position. The subsequent approximate position for the next patch containing the edge can be derived from the result of the previously matched point.

Due to the redundancy in the estimation process, a covariance matrix containing information on standard deviations of the parameters and correlations between parameters is determined simultaneously; this allows for an analysis of the determinability and precision of the transformation parameters. Former investigations show that edge positions can be detected with a standard deviation of 0.02 pixel if the image quality (contrast in particular) is good enough [MAAS *et al.*, 1994].

Besides least squares template matching, correlation techniques are also suitable for template matching. This technique marks edges at positions where the coefficient of correlation r_{corr} of the image and the template containing the edge has a local maximum.

With regard for reduction of computational effort, the coefficient of correlation r_{corr} can be calculated using the Fast Fourier transform as follows:

$$r_{corr}(x, y) = \text{DFT}^{-1}[F_1^*(\omega_1, \omega_2) \cdot F_2(\omega_1, \omega_2)] \quad (6.62)$$

with F_1^* Complex conjugate of Fourier transform of the image
 F_2 Fourier transform of the template

Whereas least squares template yield directly to the position of the edge with sub-pixel accuracy, the correlation technique requires an additional interpolation algorithm to obtain results with accuracy in the sub-pixel range. For this purpose, the correlation technique must be modified as reported in [CASOTT, PRENTING, 1999].

6.4.3 Comparison and evaluation

Among the presented techniques, least squares template matching is the only technique which yields not only the positions of edges but also an estimation for the accuracy of the parameters and for the standard deviation of noise overlaying the image signal.

In Figure 6.19, the standard deviation σ_V of noise estimated from the residuals of the least squares template matching (cf. section 6.4.4) is compared with the corresponding standard deviation of noise calculated by use of the adaptive Wiener filter (section 6.3.4). The correlation between these two methods is 0.98 and is quite promising. Therefore, the least squares template matching is implemented for refraction analysis as described in section 6.4.4.

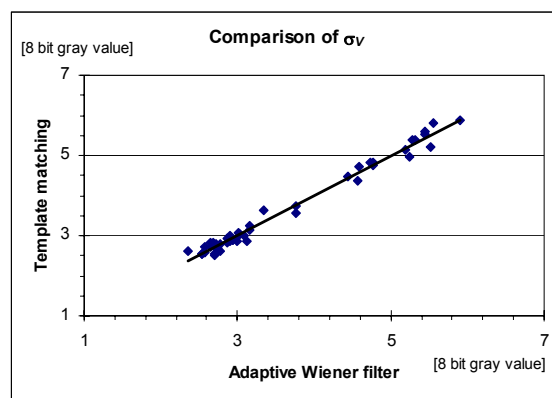


Figure 6.19: Comparison of least squares matching and Wiener filter. Data: Measurements using videotheodolite (1999, Dietlikon, Switzerland)

But a drawback of least squares matching is the need of approximate coordinates which are required to assign the position of the template in the measured image.

In order to compare the performance of the other edge operators (as presented section 6.4.2) and in order to select an appropriate operator for the edge detection of the measured line scan images (section 7.2), the operators of section 6.4.2 are applied to the same image which was grabbed by a line scan sensor.

Table 6.2 presents the recognition rate which is the percentage of correctly detected edges.

Prewitt	52%	Laplacian operator	80%
Roberts	9%		
Sobel	51%	Canny	96%

Table 6.2: Recognition rate of edge operators

The results of this comparison are visualized in Table 6.3.

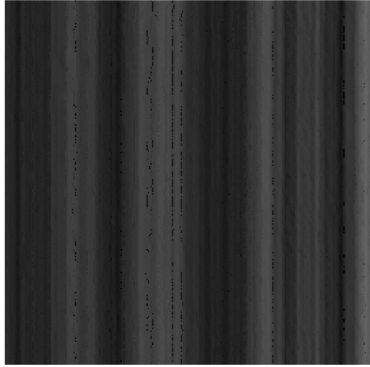
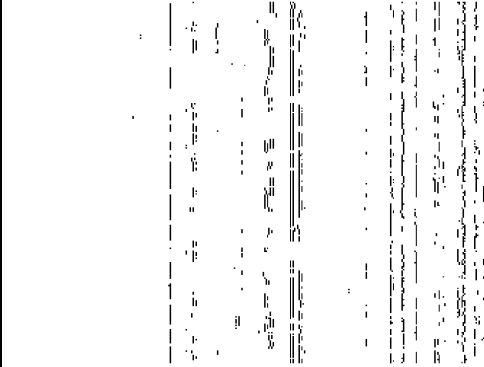
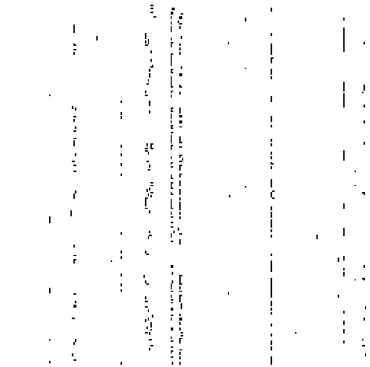
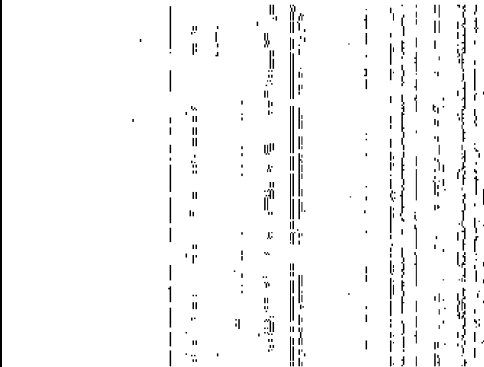
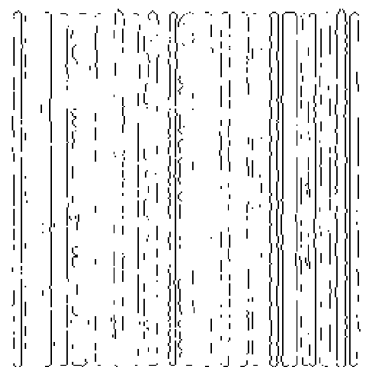
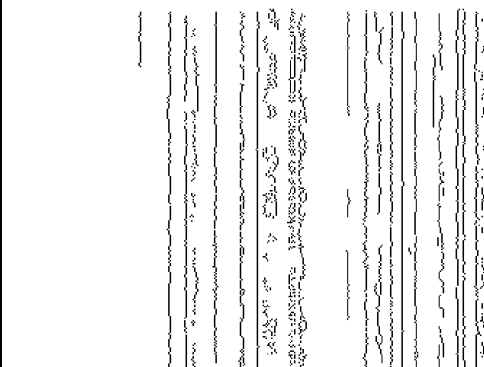
	
a) Original image	b) Prewitt operator
	
c) Roberts operator	d) Sobel operator
	
e) Laplacian operator with lowpass filter	f) Canny operator

Table 6.3: Comparison of edge operators

Obviously, the Canny operator is especially suited for edge detection when using images for refraction analysis. Hence the Canny operator is used for the determination of the angle-of-arrival fluctuations. Section 6.4.5 describes the implementation of the Canny operator which is combined with the Wiener filter to provide both the angle-of-arrival fluctuation and the intensity fluctuation.

6.4.4 Implementation of least squares template matching (LSM)

a) *Determination of angle-of-arrival fluctuations using LSM*

Least squares template matching uses coefficients of an affine transformation (six parameters) for a chosen patch in one image to its transformed counterpart in another image (Figure 6.18). Hereby, the procedure applied in the scope of refraction analysis as discussed in the following was presented in [FLACH, MAAS, 1999].

If the target consists of a one-dimensional signal structure such as coded levelling rods, the analysis can be reduced to a one-dimensional problem due to the characteristics of the phenomenon and the shape of the image signal. As a vertical scale parameter is very unlikely to be determinable over the small size of a patch, the analysis can be further reduced to the determination of one shift parameter Δx in vertical image direction. Hence, the model is given by:

$$f_2(x_j) = f_1(x_j - \Delta x) + v(x_j), \quad j = 1, \dots, M_P \quad (6.63)$$

with	f_1	Reference image signal (one-dimensional feature pattern)
	f_2	Function of the image signal at the corresponding position in the subsequent image
	x	Position of the edge in a one-dimensional signal
	Δx	Shift parameter
	v	Noise signal (error signal)
	j	Index variable
	M_P	Number of pixels of the pattern

Equation (6.63) assumes that the noise of the template is independent of the image noise. Figure 6.14 shows two image signals with a length of $M_P = 45$ pixels obtained by measurements with a video-theodolite with a resolution of 8bit gray values (0...255). This makes it clear that the image signals are not linear and, therefore, the functions f_1 and f_2 must be linearized.

$$f_2(x_j) = f_1(x_j - \Delta x_0) - f_{x,i} d\Delta x + v(x_j) \quad (6.64)$$

with	Δx_0	Approximate shift parameter
	$d\Delta x$	Unknown correction of the shift

$$f_{x,j} = \left. \frac{df_1(x)}{dx} \right|_{x=x_j - \Delta x_0} \quad (6.65)$$

The approximate shift parameter must be provided by the user or derived from previous calculations. In (6.64) the second order terms are assumed to be negligible. The lineari-

zation yields the following system of observation equations concerning one pair of corresponding patches:

$$\Delta f(x_j) = -f_{x,1} d\Delta x + v(x_j), \quad j = 1, \dots, M_p \quad (6.66)$$

with
$$\Delta f(x_j) = f_2(x_j) - f_1(x_j - \Delta x) \quad (6.67)$$

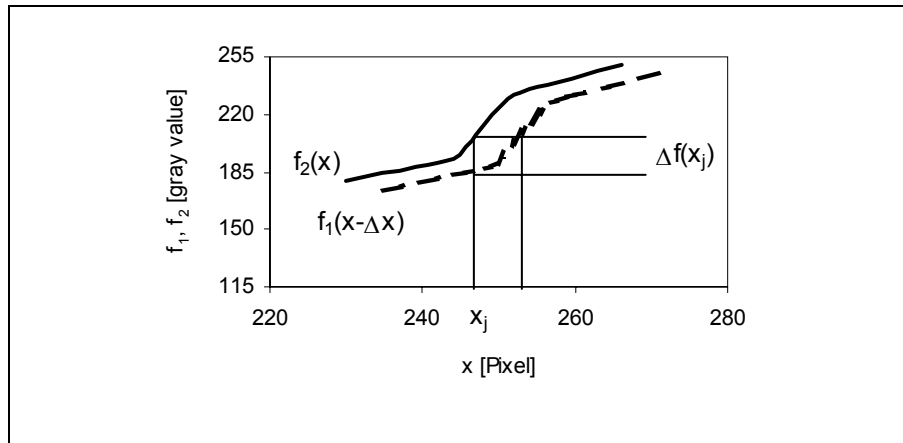


Figure 6.20: Template matching of one-dimensional signals

Using the least squares method, the unknown correction $d\Delta x$ of the shift Δx can be estimated by

$$d\Delta x = \frac{-\sum_{j=1}^{M_p} f_{x,j} \Delta f(x_j)}{\sum_{j=1}^{M_p} f_{x,j}^2} \quad (6.68)$$

and the estimated shift is

$$\Delta x_i = \Delta x_0 + d\Delta x_i \quad i = 1 \dots N_L \quad (6.69)$$

N_L Number of images of a series

The equations from (6.63) to (6.69) are evaluated for each grabbed image of a time series which are indicated by the index i in equation (6.69). In each image of the series, the template matching uses the same template and the corresponding patch. Thus, the variance σ_x^2 can be estimated from the shift of the template within each image as follows:

$$\hat{\sigma}_x^2 = \frac{1}{N_L - 1} \sum_{i=1}^{N_L} [\Delta x_i - \overline{\Delta x}]^2 \quad (6.70)$$

with $\overline{\Delta x}$ Estimated average of the shift

The variance σ_x^2 is an appropriate measure for the angle-of-arrival fluctuation temporal changes of the angle-of arrival of incoming waves influences directly the variance σ_x^2 . In order to improve the reliability and accuracy of σ_x^2 several patches per image are evaluated. Practical investigations show that up to 40 patches can be utilized whereby this number can slightly change depending on the structure of the target, the imaging system and the experimental setup.

The size of the patches can be chosen by the user. For computational reasons, the length of the sides of the patches must consist of an odd number of pixels. If the size of the patches is too small, the redundancy decreases and the determination of σ_V^2 and other parameters (cf. the following section) becomes unstable. But also patches being very large are not suitable because of the increase of computational effort and because of disturbing influences of exposure which can deteriorate the template matching. Practical experiments shows good results with a patch size of $M_p = 45 \times 45$ pixels. Minor deviations (up to 20 %) of M_p do not significantly change the results.

An alternate procedure for determination of angle-of-arrival fluctuations using LSM has been published in [HENNES, FLACH, 1998]. This procedure uses the difference $d_{Patch} = (x_{Ref} - x_{Meas})$ derived from the known coordinate x_{Ref} of the patch in the reference image and the corresponding patch's coordinate x_{Meas} in the measurement image, where x_{Meas} is calculated by LSM for each pattern. Using n_{Patch} patches in one measurement image, the spatial standard deviation $\sigma_{x,spatial}$ is given as

$$\hat{\sigma}_{x,spatial} = \sqrt{\frac{1}{n_{Patch} - 1} \sum_{i=1}^{n_{Patch}} [d_{Patch} - \overline{d_{Patch}}]^2} \quad (6.71)$$

As discussed in [HENNES, FLACH, 1998], $\sigma_{x,spatial}$ can also be used as a measure for the turbulence-related disturbance of the phase front of the light bundle emerging from the target (angle-of-arrival fluctuations). Referring to Taylor's theory of frozen turbulence (section 3.2.1), the standard deviation $\sigma_{x,spatial}$ of (6.71) can be considered as equivalent to σ_x .

b) Determination of intensity fluctuations using LSM

Additionally to the determination of angle-of-arrival fluctuations, least squares template matching enables also the determination of intensity fluctuations. Under the condition that the one-dimensional model really holds and the number of observations (i.e., the pattern size) is large enough, the noise variance σ_V^2 as an additional parameter can be estimated from the residuals of the least squares fit as follows:

$$\hat{\sigma}_{V,i}^2 = \frac{1}{M_p - 1} \sum_{j=1}^{M_p} [f_2(x_j) - f_1(x_j - \Delta x_i)]^2 \quad i = 1 \dots N_L \quad (6.72)$$

$$\hat{\sigma}_V^2 = \frac{1}{N_L} \sum_{i=1}^{N_L} \hat{\sigma}_{V,i}^2 \quad (6.73)$$

On the one hand, the noise variance σ_V^2 indicates the accuracy of the observations (pixel intensities) used for the parameter estimation. On the other hand, σ_V^2 can also be used as a measure for intensity fluctuations of the incoming light ray as introduced in section 4.4. Hereby, this heuristic model assumes that intensity fluctuations which are caused by optical turbulence influence the image signal of the patches and, therefore, increase also the difference $f_2(x_j) - f_1(x_j - \Delta x)$ between the patch of the reference image and the one of the subsequence image. Thus, least squares template matching is also promising for refraction analysis as already mentioned in section 6.4.3 above.

6.4.5 Implementation of Canny operator

The implementation of the Canny operator in combination with the Wiener filter is embedded into an all-embracing proceeding which yields the noise variance σ_V^2 and the fluctuation of the position of an edge σ_x^2 necessary to determine the turbulence parameters C_n^2 and l_0 by means of (4.31) and (4.45). Figure 6.21 presents a comprehensive overview of the applied image processing techniques which are connected with the Canny operator.

The procedure of Figure 6.21 is principally valid for both images grabbed by line scan cameras or images grabbed by area scan cameras (e.g., video theodolites). In the following, the essential elements of the procedure Figure 6.21 are explained with regard to images grabbed by line scan cameras such as presented in Figure 6.2 since images of this type were grabbed in the field experiments using a line scan camera (section 7.2).

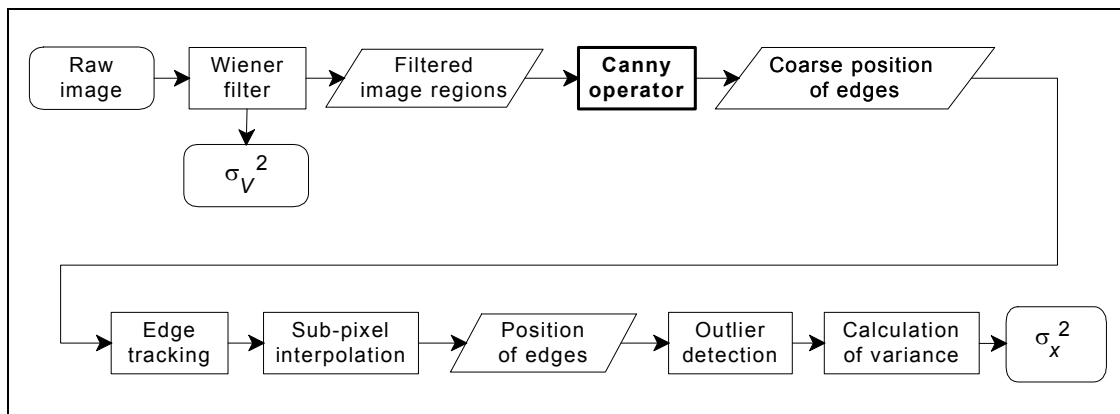


Figure 6.21: Determination of σ_V^2 and σ_x^2 using Wiener Filter and Canny operator

a) Wiener filter

The implementation of the Wiener filter has already been explained in section 6.3. In the following, the application of Wiener filter in connection with the Canny operator is discussed. Assuming a raw image obtained from a line scan sensor, the Wiener filter is only applied to a limited range of the image as shown in Figure 6.22 in order to reduce computational effort.

Herein, the 1024 pixel of the x -axis represent the elements of the line scan sensor and the 3000 pixel of the y -axis consist of the 3000 line readouts which are produced by the line scan sensor. The limitation of the range of the Wiener filter as shown in Figure 6.22 is possible because all line readouts are included and, thus, the temporal intensity fluctuation can be measured.

In order to determine the edges, the Canny operator is applied to a sub-range within the range of the Wiener filter. Figure 6.22 illustrates these ranges: The Canny sub-range is depicted as dark gray and lays within the range of the Wiener filter (light gray). Herein, the user should chose the parameter x_1 and x_2 as shown in Figure 6.22. Although the processing of one single column by the adaptive Wiener filter would be sufficient to determine the intensity fluctuations, the evaluation of the measured image data shows that a width of 100 pixel for the range of the Wiener filter (light gray) can be recommended since the redundancy enables the user to detect outliers. A larger sub-range is also possible but it must be made sure that the sub-range thoroughly maps a part of the target (rod), i.e. there are no disturbing influences (e.g. grass).

The minimal size of the range of the Canny operator (dark gray) depends on the length w_c (cf. Figure 6.17) of the filter function (6.60). Based on practical investigations a length of $w_c = 7$ and a width of 25 pixel for the Canny sub-range was found adequate. The parameter x_1 and x_2 must be chosen in such a way that the approximate position x_n of an edge is situated approximately in the middle of the sub-ranges of Wiener filter and Canny operator.

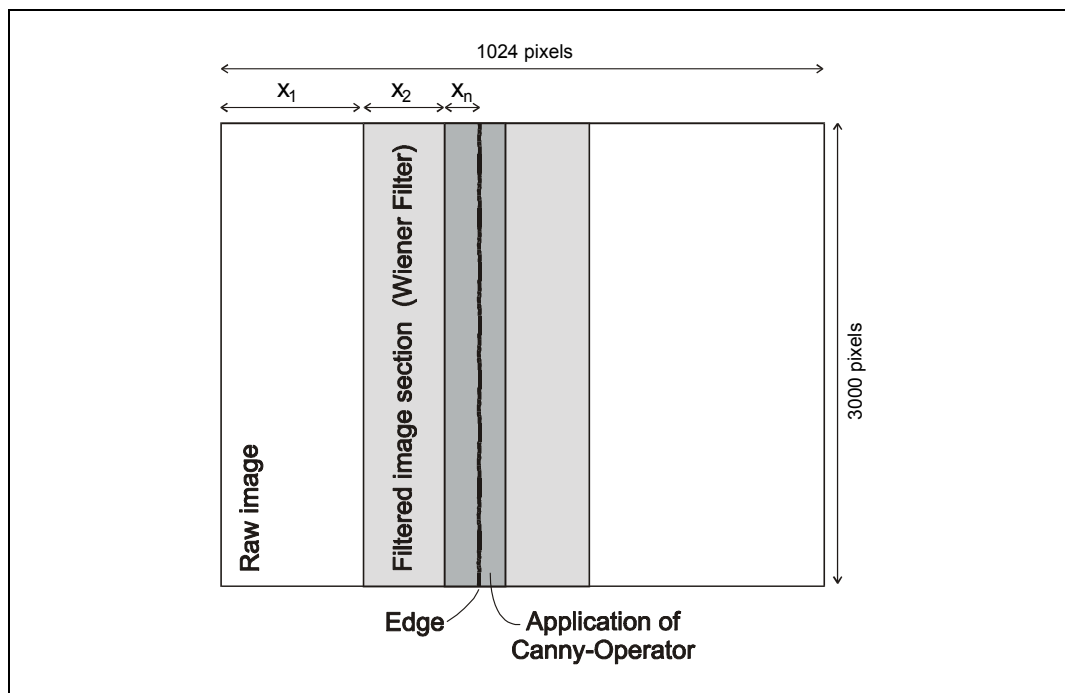


Figure 6.22: Application of Wiener filter and Canny operator in an image grabbed by a line scan camera

b) Canny operator

The implementation of the Canny operator follows the explanations presented in section 6.4.2. Attention should be paid to the threshold parameter because edges are detected at positions where the gradient function $g(x)$ of equation (6.61) is larger than the threshold. Figure 6.23 may illustrate this difficulty: On the one hand, spurious edges are detected if the threshold is chosen too small (e.g., threshold = 0.02), but on the other hand, edges can be omitted if the threshold is too large (e.g., threshold = 0.5).

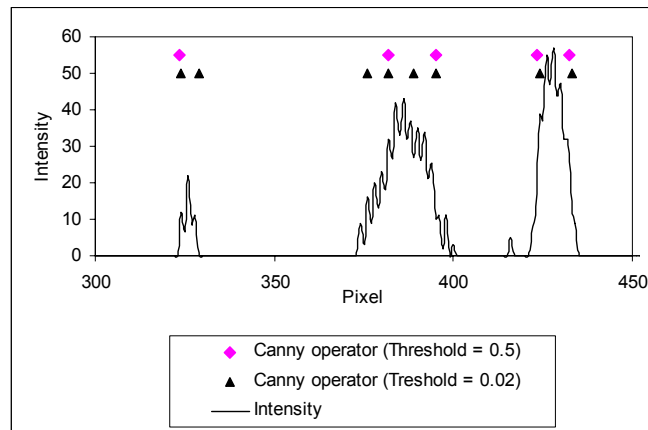


Figure 6.23: Canny operator: Influence of threshold

The threshold can be determined automatically, e.g., if the quotient of number of edges and of length of line is assumed to be known (e.g. if the target structure, the focal length and the distance R are given). Practical investigations using line scan images showed an appropriate threshold in the range of 0.1 to 0.3. This threshold is valid for edges with a good contrast (> 10 dB, cf. section 6.4.6).

The Canny operator implemented as described in section 6.4.2 produces binary images wherein 0 means "no edge" and 1 means "edge detected". These binary images have two difficulties:

1. The resolution of the position of edges is only 1 pixel
2. If an edge is found in a line readout, the position of same edge must be found in the subsequent line readout in order to analyze the slight displacement of an edge. Thus, attention should be paid to edges neighboring in vertical (temporal) direction because edges which occur in a line readout normally should reappear in the subsequent line readout (Figure 6.24).

The first problem can be solved using interpolation as explained in section 6.4.5d). The solution of the second problem can be provided by use of a histogram as shown in Figure 6.25. An edge and its approximate position x_n are identified if the corresponding counts exceed a specified threshold (e.g., 50% of the number of line readouts). Moreover, edge tracking techniques as explained in the following sections are required for the proper detection of temporal displacements of edges caused by turbulence effects.

c) Edge Tracking

In the following context, edge tracking means the assignment of pixels which are marked by ones in the binary image to edges which runs in vertical (temporal) direction (Figure 6.24). An assumption for edge tracking is that the approximate position x_n of the

edge is known or determined as described above (Figure 6.25). In doing this, the use of thresholds and histograms is required. The histogram provides the approximate position x_n of the edge.

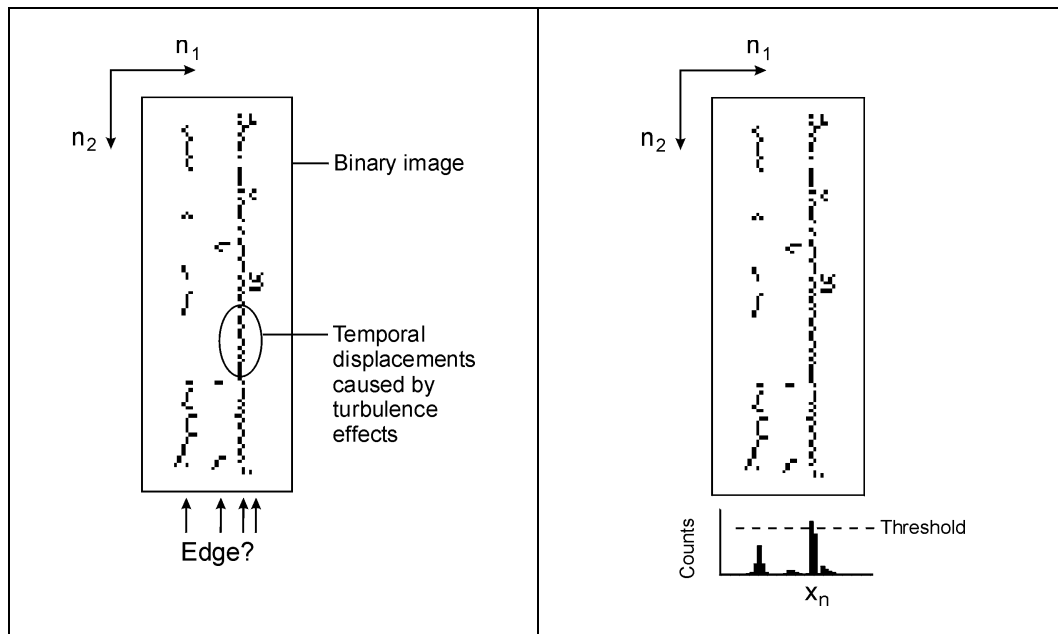


Figure 6.24: Ambiguous edges in binary image. The n_1 -axis contains the coarse positions of edges of one line readout

Figure 6.25: Edge detection using threshold and histogram

When the approximate position x_n is given, the algorithm seeks each row n_2 of the binary image whereby the appropriate coarse positions of the edge x_{edge} are the positions of ones x_{Ones, n_2} located at the closest to the approximate position x_n of the edge:

$$x_{edge, n_2} = \{x_{Ones, n_2} | \min(x_{Ones, n_2} - x_n)^2\} \quad n_2 = 1 \dots N_L \quad (6.74)$$

with x_{edge, n_2} Coarse position of the edge located in the row n_2 corresponding to the approximate position x_n of the edge

x_{Ones, n_2} Position of an edged marked by "1" in the row n_2 of the binary image generated by the Canny operator

N_L Number of rows (Number of line readouts)

This algorithm works satisfactorily under the condition that no gaps occur in the edge of the binary image. However, if a gap occurs as shown in Figure 6.26, the assignment can be deteriorated since confusions with neighboring edges may arise. In this case, outliers emerge by including a pixel from the neighboring edge as depicted in Figure 6.26.

In order to avoid this wrong assignment, a morphological operator should be applied to the binary image which is provided by the Canny operator. Hereby, it can be recom-

mended to use the so-called "bridge"-operator which can be implemented efficiently and, therefore, is described in the following.

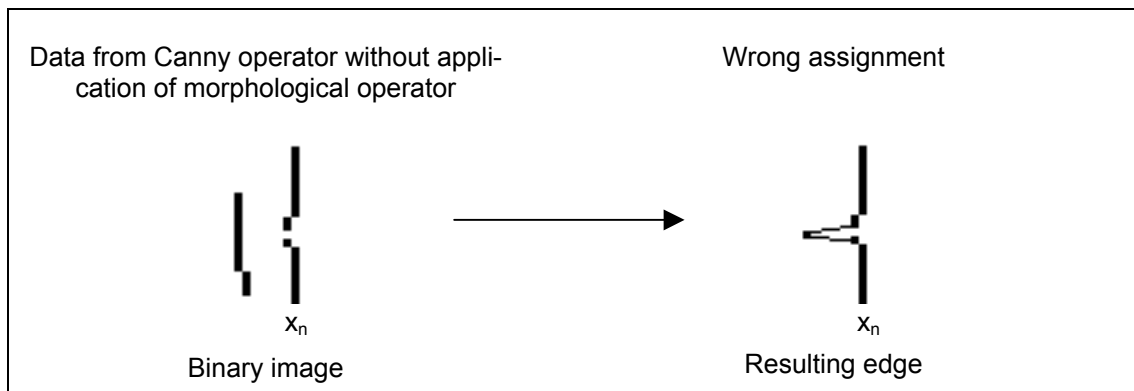
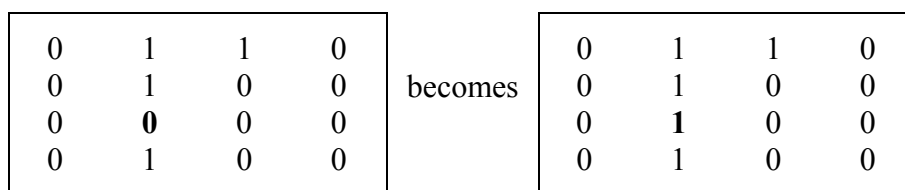


Figure 6.26: Wrong assignment caused by gaps in edge of the binary image

The "bridge"-operator bridges previously unconnected pixels as presented in the following example:



Using this morphological operator, the quality of assignment can be improved considerably as shown in Figure 6.27.

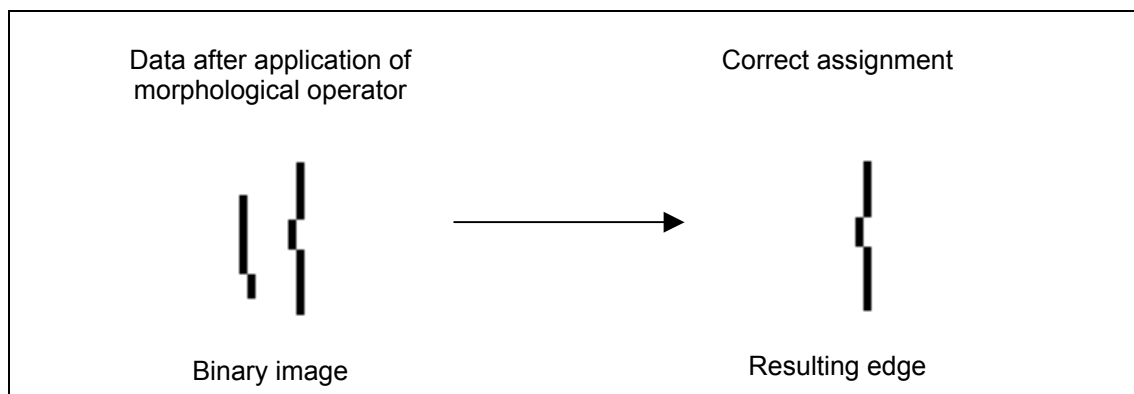


Figure 6.27: Improved assignment after application of morphological operator

The application of the morphological operator is followed by the application of equation (6.74), thus, the position of the relevant edges are known for each line readout (i.e., row in the raw image). However, the resolution of the position is still only one pixel. In order to increase the resolution, interpolation methods are required as introduced in the following section.

d) Interpolation

Interpolation methods enable the detection of edges with sub-pixel accuracy. In doing so, the gradient function $g(x)$ according to (6.61) is calculated in the region of the coarse position x_{edge} . Within a range of 5 pixel, a polynomial approximation can be estimated by use of the least squares method. Thus, the gradient function can be approximated by

$$g(x) = a_2x^2 + a_1x + a_0 \quad (6.75)$$

with a_0, a_1, a_2 Estimated parameters of the regression

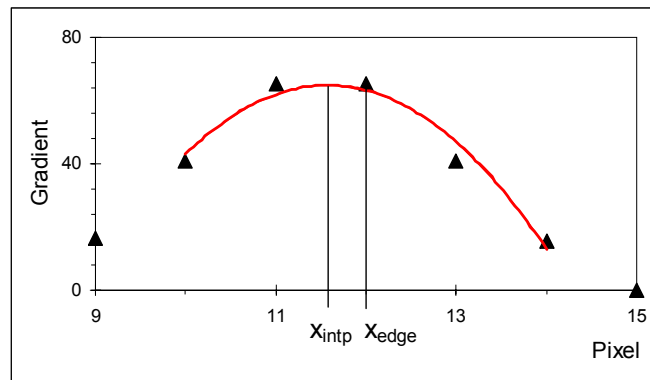


Figure 6.28: Sub-pixel interpolation using polynomial approximation

Determining the maximum of the function of (6.75), the interpolated position x_{intp} of the edge becomes:

$$x_{intp} = -\frac{a_1}{2a_2} \quad (6.76)$$

This procedure yields the position of the edge with sub-pixel accuracy for each row using least squares estimation.

e) Outlier detection

As a property of least squares estimation, outliers may affect the resulting x_{intp} . In order to eliminate or at least to reduce the effects of outliers, robust estimation methods are required. In the application discussed in section d), the median estimator is suitable and easily applicable as robust estimation method. Hence, the median of all the interpolated positions x_{intp} of the same edge are calculated and, then, the deviation of the interpolated positions and the median must be determined. If the amount of the deviation exceeds a specified threshold, the corresponding interpolated position x_{intp} is an outlier, therefore, must be eliminated. The results from field measurements shows that the percentage of outliers is in the range of 0.1% to 1% under normal conditions.

f) Calculation of standard deviation

Once the outliers are removed from the results, the variance σ_x^2 of the edge positions is given by

$$\hat{\sigma}_x^2 = \frac{1}{N_L - 1} \sum_{j=1}^{N_L} [x_{interp,j} - \overline{x_{interp}}]^2 \quad (6.77)$$

with $\overline{x_{interp}}$ Average of the interpolated edge positions

The variance σ_x^2 of (6.77) is equivalent to the variance of (6.70) obtained by template matching. Both variances can be interpreted as a measure for the angle-of-arrival fluctuation. Since the algorithm using the Canny operator only provides the positions x_{interp} of the edge, the noise variance σ_V^2 must be determined by means of the Wiener filter to achieve the full information necessary to determine the parameter C_n^2 and l_0 for the turbulence model as is illustrated in Figure 6.21.

6.4.6 Accuracy of edge detection

The edge detection demands high accuracy as is shown in the following numerical example: For $R = 75$ m, $a = 65$ mm, $\lambda = 550$ nm, and $C_n^2 = 0.5 \cdot 10^{-12} \text{ m}^{-2/3}$, the angle-of-arrival fluctuation is $\sigma_\alpha^2 = 1.05 \cdot 10^{-10} \text{ rad}^2$. Assuming a focal length $f = 300$ mm and a size $p_e = 10^{-5}$ m of pixel elements, the fluctuation of the edges σ_x^2 is 0.09 pixel^2 . Therefore, the required standard deviation for edge detection is $\sigma_{\sigma_x^2} = 0.009 \text{ pixel}^2$ if a relative standard deviation of C_n^2 must not exceed 10 %.

The accuracy of the edge detection depends mainly on the resolution of the gray value and the contrast. The contrast of an edge can be expressed by the ratio of the length x_{Ramp} of the ramp and the amplitude A_{Ramp} of the edge as shown in Figure 6.29.

These parameters define the minimal resolution d_{res} within which the position of an edge can be solved:

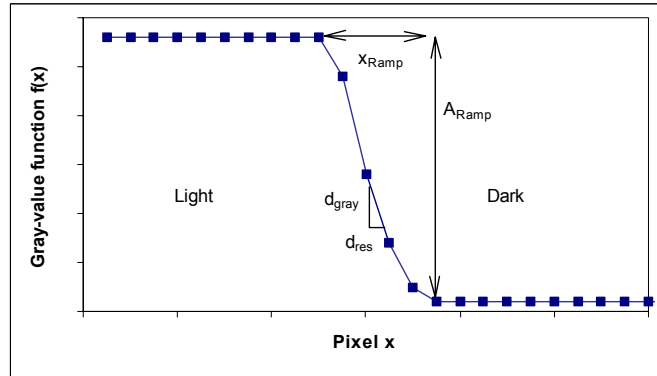


Figure 6.29: Slope of edge as a measure of image contrast

$$d_{res} = \frac{x_{Ramp}}{A_{Ramp}} d_{gray} \quad [\text{Pixel}] \quad (6.78)$$

with d_{gray} Minimal resolution of gray value: $d_{gray} = 1$ [8 bit gray value].

For example, referring to measured images, edges with an excellent contrast typically have a ratio of $x_{Ramp} / A_{Ramp} = 0.04$ [pixel/ 8-bit gray value] (14 dB). This contrast is equivalent, e.g., for width of the edge $x_{Ramp} = 2$ pixel and a dark-to-bright difference $A_{Ramp} = 50$ [8 bit gray value]. From (6.78) follows that the resolution of the position of an edge is limited to 0.04 pixel. Although, it is important to point out that the standard deviation of a single edge is not of interest but the standard deviation $\sigma_{\sigma_x^2}$ of the stan-

standard deviation σ_x which is given by (6.77). Using the law of propagation of variances, it follows:

$$\sigma_{\sigma_x^2} = \frac{2\sigma_x}{\sqrt{N_L}} \sigma_{single} \quad (6.79)$$

with N_L Number of readouts (number of edges)

Supposing $N_L = 24$, $\sigma_x^2 = 0.09 \text{ pixel}^2$, and assuming a standard deviation of the position of one edge $\sigma_{single} = 0.06 \text{ pixel}$ (see below), the standard deviation $\sigma_{\sigma_x^2}$ is 0.007 pixel^2 whereby this value is smaller than the required standard deviation $\sigma_{\sigma_x^2} = 0.009 \text{ pixel}^2$.

Hence, the application of the Canny operator and template matching as described in section 6.4.4 and 6.4.5 can provide results which are accurate enough for determination of angle-of-arrival fluctuation if the assumption $\sigma_{single} = 0.06 \text{ pixel}$ holds. In order to validate this accuracy, a series consisting of 24 images is evaluated by means of both the Canny method (section 6.4.5) and the least squares template matching (section 6.4.4).

The comparison plotted in Figure 6.30 reveals a good correlation between both methods ($r_{corr} = 0.98$). The standard deviation obtained by this comparison amounts to $\hat{\sigma}_{single} = 0.05 \text{ pixel}$ which is in the order of the assumed value of $\sigma_{single} = 0.06 \text{ pixel}$.

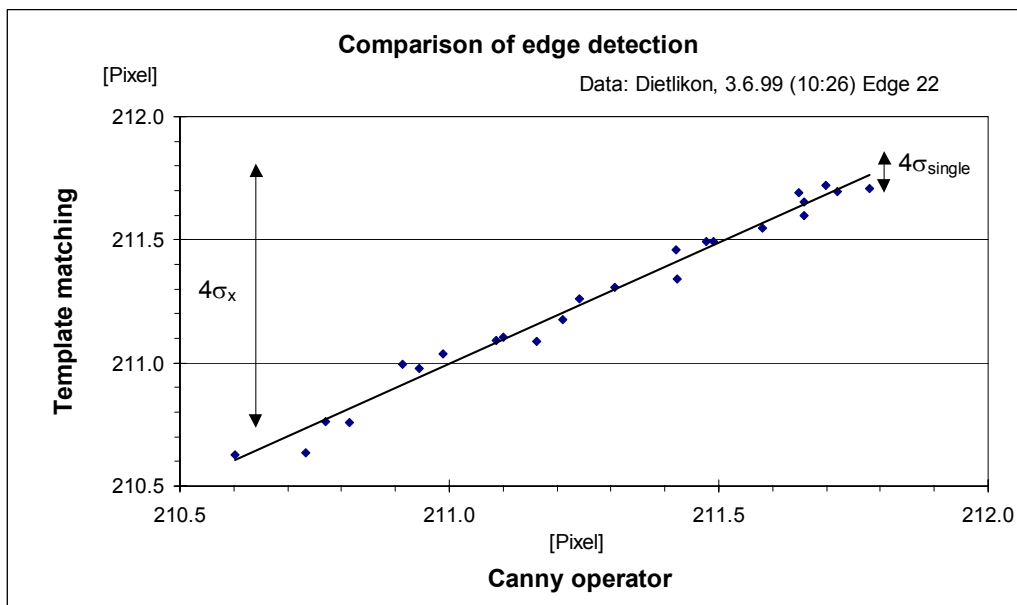


Figure 6.30: Positions of an edge in a series of 24 images. The arrows indicate the 95 % confidence intervals with $\sigma_{single} = 0.05 \text{ pixel}$ and $\sigma_x = 0.35 \text{ pixel}$, respectively

6.4.7 Conclusions

Edge detection which is necessary to determine the angle-of-arrival fluctuations can be performed by using various edge operators in principle. Basically, the presence of strong angle-of-arrival fluctuations can deteriorate the accuracy of the edge detection as

shown in (6.79) and (6.56). Practical investigations presented in section 6.4.3 show that the Canny operator and least squares matching provide accurate results present although the accuracy decreases in the higher range of C_n^2 .

The comparison of these two methods shows that the standard deviation of one single edge is about 0.05 pixel if a good contrast is provided (Figure 6.30). In order to improve the redundancy, it is recommended to detect the position and the standard deviation of more than one edge in the same image. This enables to check the plausibility and reproducibility of the results.

In contrast to the Canny operator, least squares template matching is a semi-automated technique, i.e., the user has to identify the coarse position of edges. But as an advantage, least squares template matching offers the option to determine the noise variance and the variance of the position of edges simultaneously. But the application of the least squares matching as discussed in section 6.4.4 is limited since it provides only the variance of the noise.

If the intensity fluctuations are described by a more sophisticated function $S_V(\omega_2)$ than $S_V(\omega_2) = \sigma_V^2$ as given in (6.38), the template matching cannot determine the intensity fluctuations. But, in contrast to the template matching, the adaptive Wiener filter is able to process also more sophisticated spectral models S_V , as mentioned in section 6.2.4.

The method using the Canny operator as described in 6.4.5 has the potential of fully automated edge detection. Hereby, attention should be paid to the assignment of edges within subsequent line readouts.

If the assignment is not done correctly, outliers may occur with detrimental influences on the quality of the results. But these difficulties can be overcome with use of robust estimation methods and morphological operators as discussed in section 6.4.5c) and 6.4.5e).

As shown, e.g., in Figure 6.19, the results for the intensity fluctuations obtained by least squares matching are equivalent to the results calculated by means of Canny operator in combination with the adaptive Wiener filter. For this reason, the measurements described in the section 7 are evaluated with these two different image processing techniques:

- Least squares template matching is applied to measurements grabbed by two-dimensional image sensors such as video-theodolites and
- the Canny operator evaluates measurements obtained by one-dimensional image sensors such as line scan cameras.

7 Measurements and results

7.1 Video theodolite

7.1.1 Field experiment

The following field experiment was carried out by means of the video theodolite which is a representative of a modern geodetic instrument. The experiment was carried out on 3rd June 1999 in a grassy field (cf. Figure 7.1 and Figure 7.5). The agriculturally used area is approximately flat for the part where the measurements were performed (cf. Figure 7.5). Isolated houses and a slight hill in the background are the most relevant elevations which are about 100 to 500 meters away from the place of the experiment.



Figure 7.1: Area of field experiment (at the corner: emitter unit of scintillometer)

The experimental setup consists of the video theodolite Leica TM3000V and the scintillometer (see also sections 5.2.3 and 5.3.1). The setup of the scintillometer is presented schematically in Figure 7.2. Hereby, the portable computer stores the data of the scintillometer which are averaged using an integration time of 1 minute.

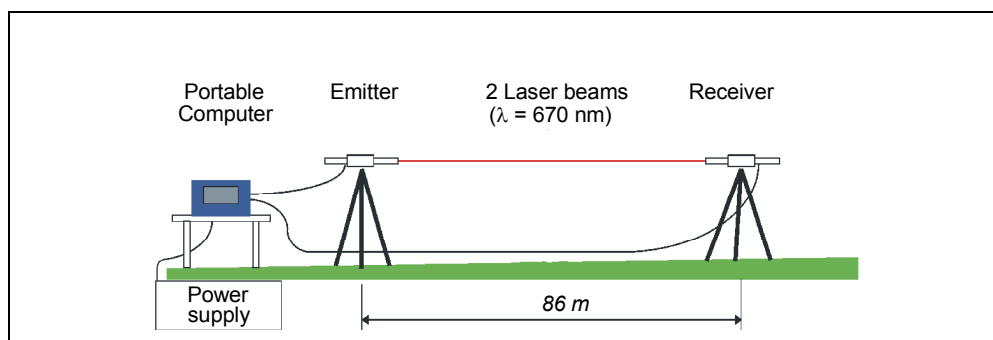


Figure 7.2: Scintillometer

The lines of vision of both instruments are parallel and run horizontally over a distance of 86 m (Figure 7.3).



Figure 7.3: Parallel measurements of scintillometer (left) and video theodolite (right)

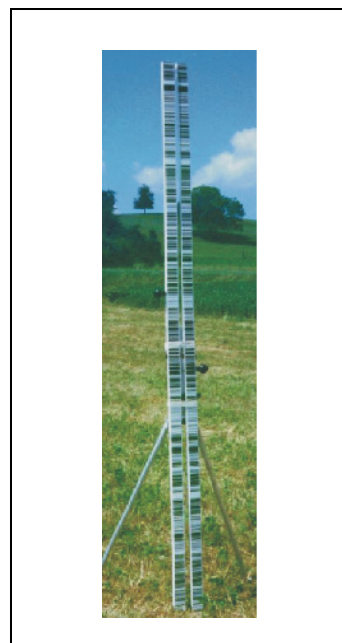


Figure 7.4: Levelling staff

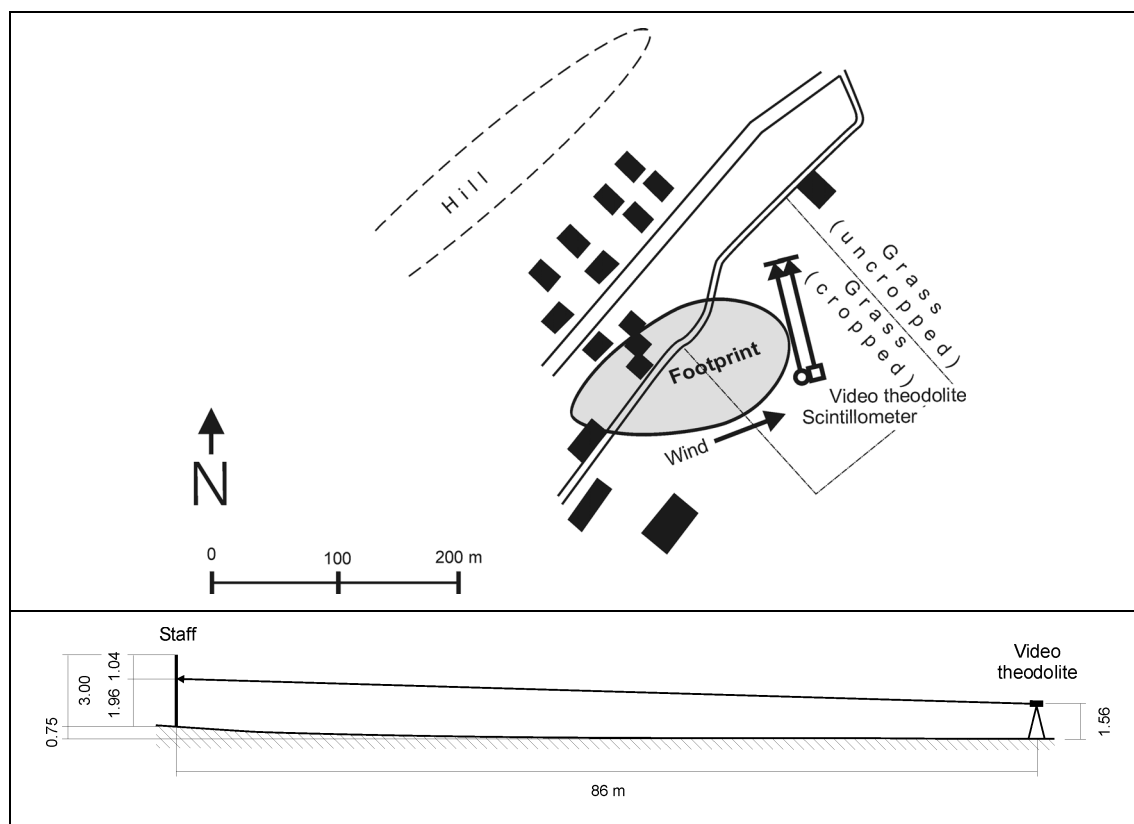


Figure 7.5: Map and profile of the field experiment of 3 June 1999. Hereby, the footprint model of section 3.5 is applied

The video theodolite situated next to the scintillometer (Figure 7.3) aims at two vertical coded levelling staffs (Figure 7.4) positioned at 86 meters away.

The use of two levelling staffs instead of one is advantageous since they provide more edges which can be evaluated and, therefore, increases the redundancy. The structure of the image data of these two staffs is illustrated by the image presented in Figure 7.6. Each measurement of video theodolite consists of 25 images grabbed within 1 second. The measurements are repeated at intervals of about 1 to 2 minutes. The weather was sunny and the temperature was in the range from 20 °C to 27 °C (cf. Figure 7.12).

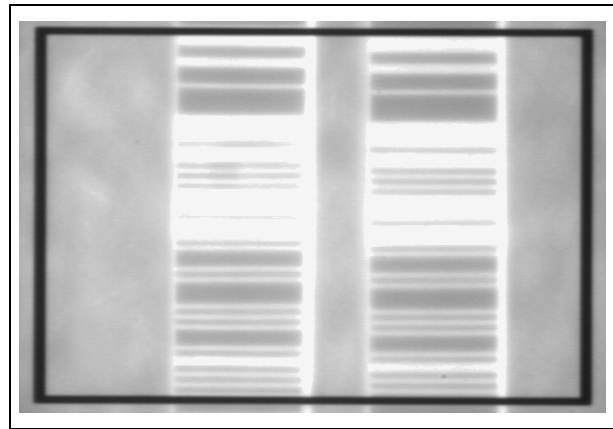


Figure 7.6: Image seen by video theodolite

The wind speed did not exceed 2.9 m/s (median of wind speed: 2.1 m/s). The total measuring period took 6 hours 30 minutes and was interrupted two times for technical problems.

7.1.2 Results and conclusions

The structure constant C_n^2 and the inner scale l_0 are plotted in Figure 7.7 up to Figure 7.10. The results of the video theodolite are combined with those of the scintillometer which can be regarded as a reference instrument. The image data of the video theodolite were processed using least squares template matching according to (6.70). The structure constant C_n^2 is calculated using (4.31).

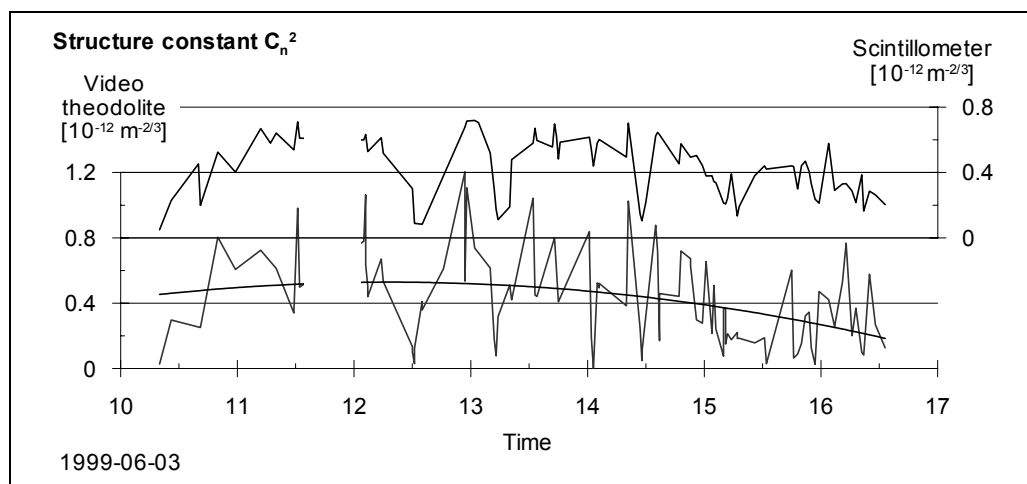


Figure 7.7: Time series of structure constant C_n^2 (Place: Dietlikon / CH)

The structure constant of refractive index as shown in Figure 7.7 tends to increase during the first hours with a maximum at noon (13:00 h in summer-time). Although, C_n^2 is subject to enormous changes which are caused, e.g., by small clouds covering the sun during some minutes. The structure constant of refractive index determined using the

video theodolite is rather volatile whereas the run of the time series of C_n^2 obtained by the scintillometer is more smooth.

The reason for this may be the measuring time of the video theodolite being 1 second only which is considerably shorter than the measuring time of the scintillometer (1 min).

The differences between the results of scintillometer and video theodolite are in the range of $0.2 \cdot 10^{-12} \text{ m}^{-2/3}$ (standard deviation) but do not reveal a systematic behavior. In addition, the correlation coefficient between scintillometer and video theodolite in the time series of C_n^2 is relatively low and only amounts to $r_{corr} = 0.57$. The correlation plot is given in Figure 7.8.

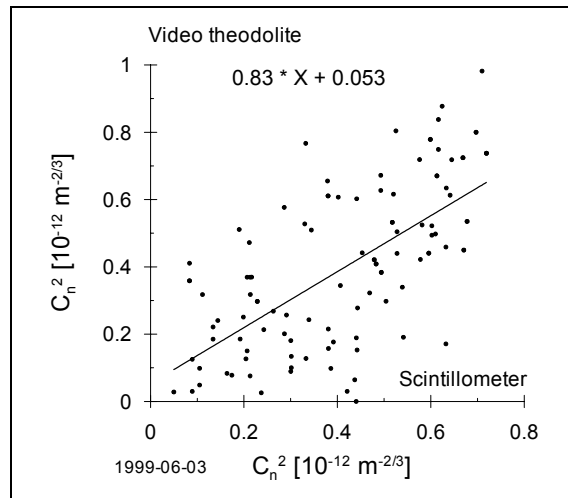


Figure 7.8: Correlation of C_n^2
(Place: Dietlikon / CH)

If the structure constant is calculated the inner scale l_0 can be derived from (4.33) and (4.45) with use of the noise variance σ_V^2 modelled by (6.73). These results of the video theodolite are compared with the inner scale obtained by the scintillometer as shown in Figure 7.9.

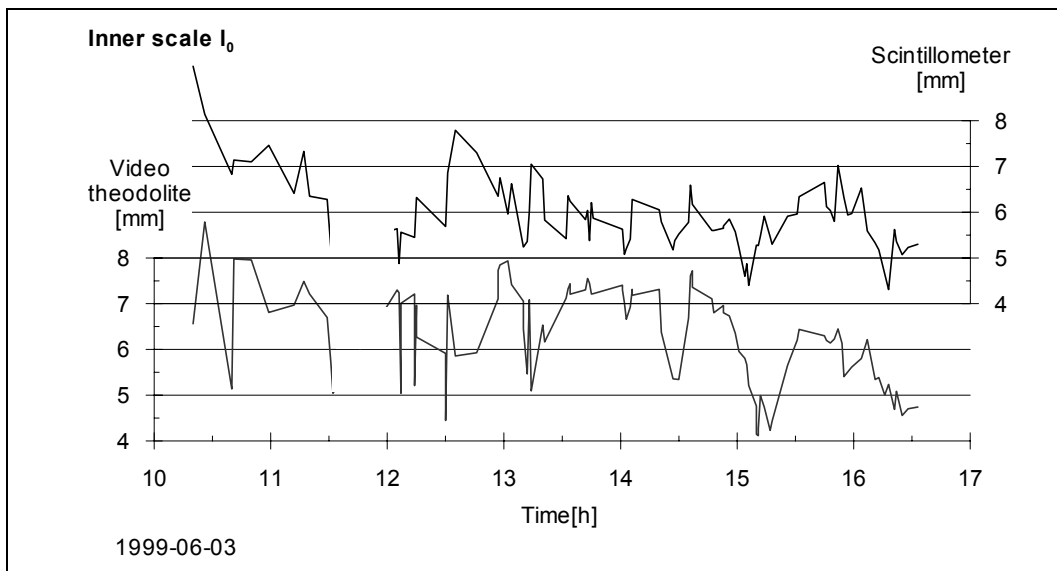


Figure 7.9: Inner scale l_0 (Place: Dietlikon / CH)

The inner scale determined using the video theodolite has an offset of about 1.5 mm in the period from 13:30 h to 15:00. This offset is possibly caused by the intensive sun radiation during this period which can decrease the sensitivity of the video theodolite for intensity fluctuation.

The correlation between the measurements of the scintillometer and the ones of the video theodolite is plotted in Figure 7.10. The correlation coefficient is $r_{corr} = 0.45$. Thus, the correlation of l_0 is lower than the one of C_n^2 . This is an expected result since the algorithms used for determination of l_0 depends also on C_n^2 . This means the deviations of C_n^2 deteriorates also the determination of l_0 . Thus, the determination of l_0 is more demanding than the one of C_n^2 . The inner scale l_0 determined using the video theodolite has a standard deviation of about 1.3 mm whereby the standard deviation is calculated using the differences between the measurements of video theodolite and scintillometer.

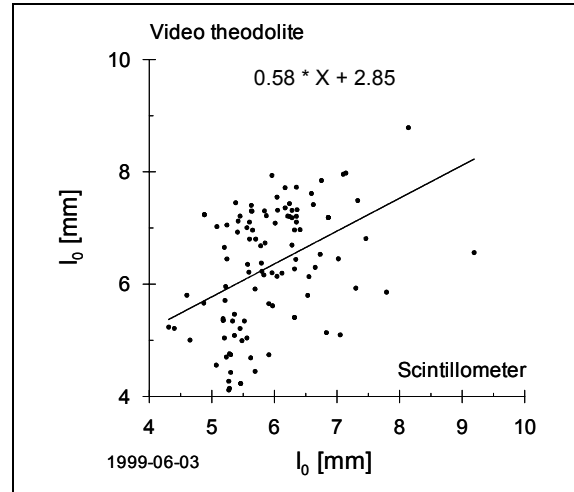


Figure 7.10: Correlation of l_0
(Place: Dietlikon / CH)

With respect of the interpretation of l_0 , it is useful to compare the time series of l_0 with the measured wind speed and temperature as shown in Figure 7.11 and Figure 7.12. In Figure 7.11, the correlation between wind speed and the inner scale is remarkable ($r_{corr} = -0.50$). Generally speaking, an increase of the wind speed leads to a decrease of the inner scale and vice versa. This relationship is also confirmed in section 7.2.2 when the results of the line scan camera are discussed. Those experiments (19 and 25 August 1999) revealed a correlation (about 0.84 to 0.95) which is even better than the correlation in the experiment of 3 June 1999. This relation between wind speed and inner scale can be used to derive the inner scale such as investigated in [DEUSSEN, 2000].

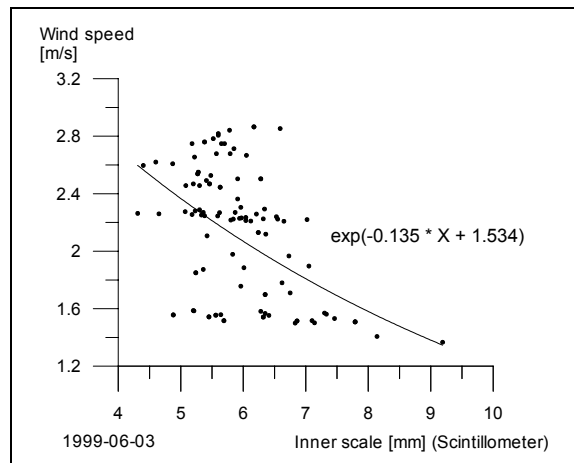


Figure 7.11: Correlation between
inner scale l_0 and wind

The temperature gradients presented in Figure 7.12 are derived from the measured C_n^2 and l_0 using Monin-Obukhov similarity and the algorithm explained in section 3.4. Hereby, the profile function (3.56) of HÖGSTRÖM [1988] is applied. Hereby, the averaged difference between the temperature gradients derived from the scintillometer measurements and the ones of the video theodolite is -0.03 K/m. This means that the refractive angle calculated from the measurements of the video theodolite is about 0.07 mgon smaller than the corresponding refractive angle based on scintillometer measurements. Because no temperature gradient measurement system was available on 3 June, these gradients cannot be verified using temperature differences.

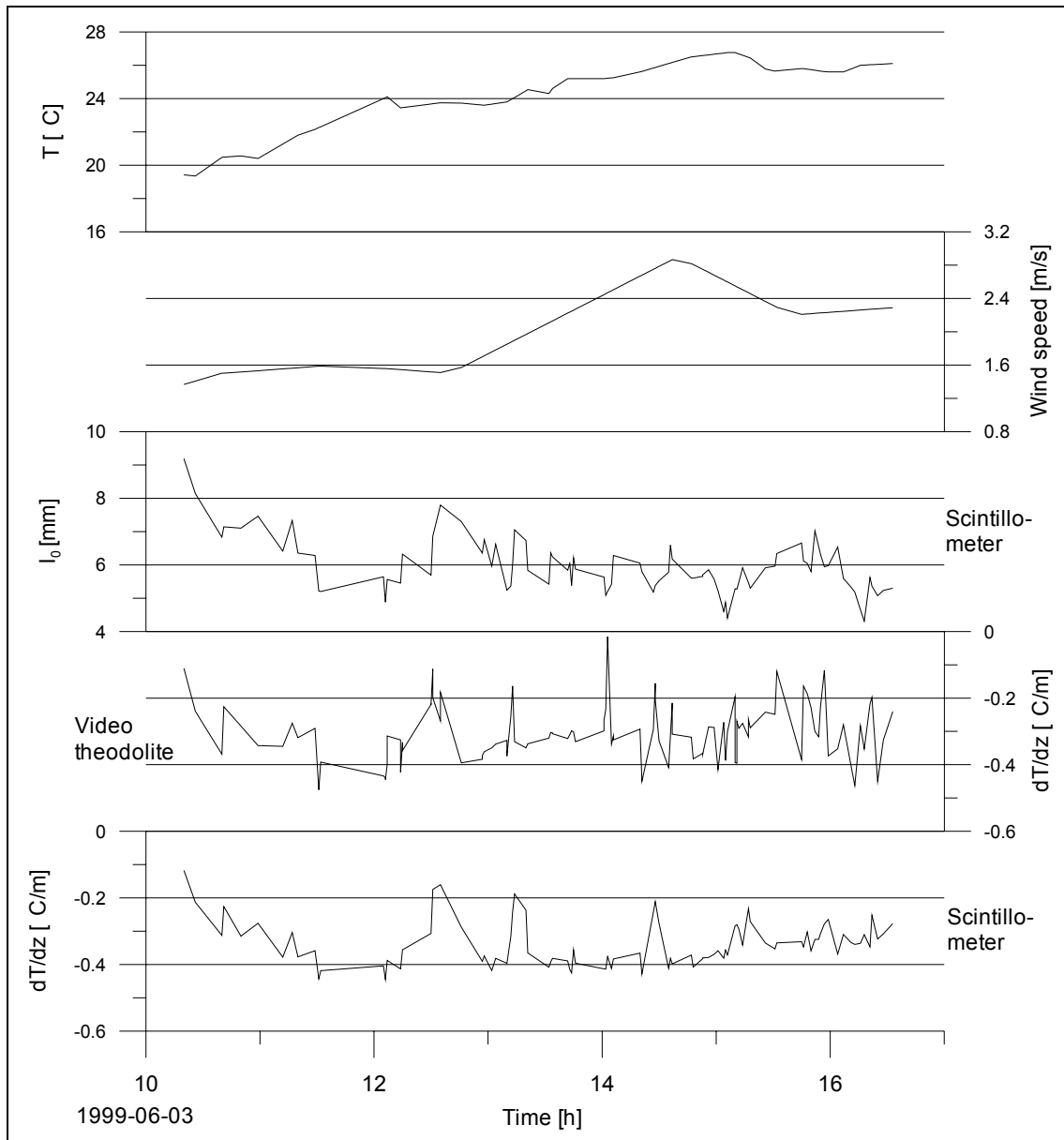


Figure 7.12: Comparison of temperature gradients with other meteorological quantities (Temperature gradient calculated using the dimensionless profile function of Höögström)

Finally, the relation between C_n^2 and the mean intensity of the measurement images is investigated in Figure 7.13. Principally, an image sensor can also be used as "cloud meter" based on the effect that arising clouds in the sky decrease the intensity of the light rays and, therefore, lower the gray values of the pixels.

At the same time, the clouds influence also the optical turbulence which is modelled by C_n^2 . The agreement between these two quantities is shown in Figure 7.13.

The practical experiment of 3rd June 99 reveals that the relationship between mean intensity and C_n^2 is more sophisticated and should be modelled using additional parameters, for example the sunset which is a function of time and the exposure of the target (shadows caused by obstacles, etc.).

Hence, further investigations are necessary to model the "cloud meter" capabilities of the video theodolite and its relation to atmospheric turbulence

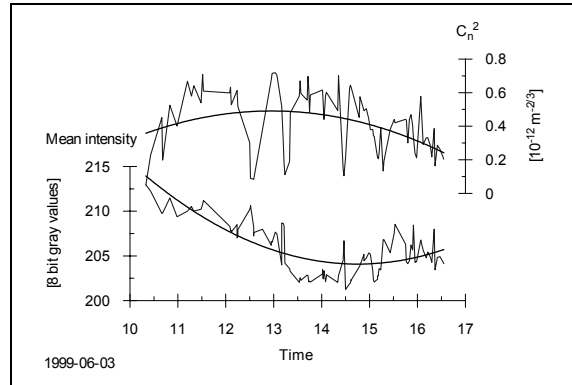


Figure 7.13: Correlation of l_0
(Place: Dietlikon / CH)

This experiment using the video theodolite shows that commercially available geodetic instruments with CCD sensors can provide information about the structure parameters C_n^2 and l_0 of atmospheric turbulence. However, the accuracy is not good enough to determine the refraction angle reliably (cf. section 7.5).

7.2 Line scan camera

7.2.1 Field experiment

a) Location

The field experiments using the line scan camera (type: BASLER L120, cf. section 5.2.4) took place on 19 and 26 August 1999 at two different places in Claro (Switzerland). The experiments were embedded in the Mesoscale Alpine Program (MAP) which is an international research initiative devoted to the study of atmospheric and hydrological processes over mountainous terrain. The areas of both experiments were flat grass fields as shown in Figure 7.14 and Figure 7.15. As depicted in the maps of Figure 7.16 and Figure 7.17 the measuring places are both surrounded by grass fields, wood and corn fields.



Figure 7.14: Area of first field experiment in Claro, 19 August 1999



Figure 7.15: Area of second field experiment in Claro, 25 August 1999

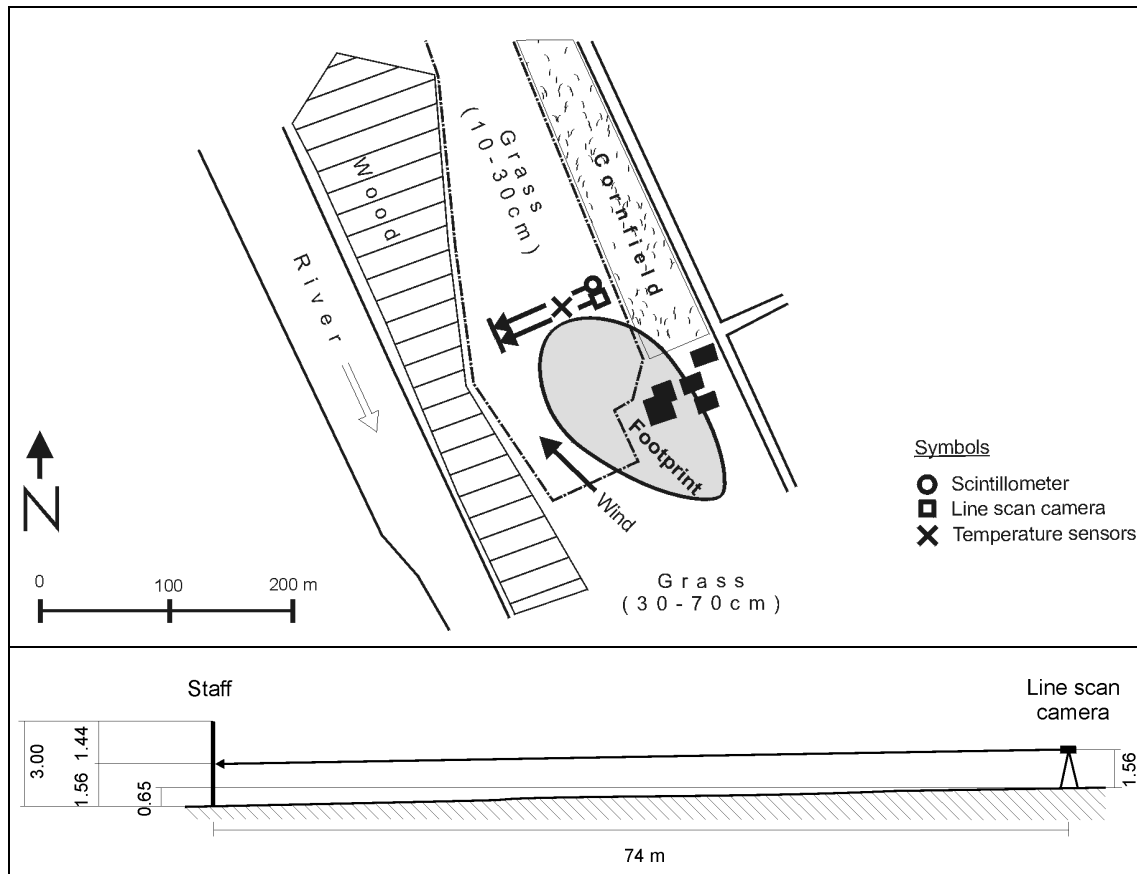


Figure 7.16: Map and profile for the field experiment of 19 August 1999

Similar to Figure 7.5 and Figure 7.17, the gray area of Figure 7.16 indicates the footprint of the measurements, i.e., the area which is assumed to be mainly responsible for the amount of the measured values (section 3.5).

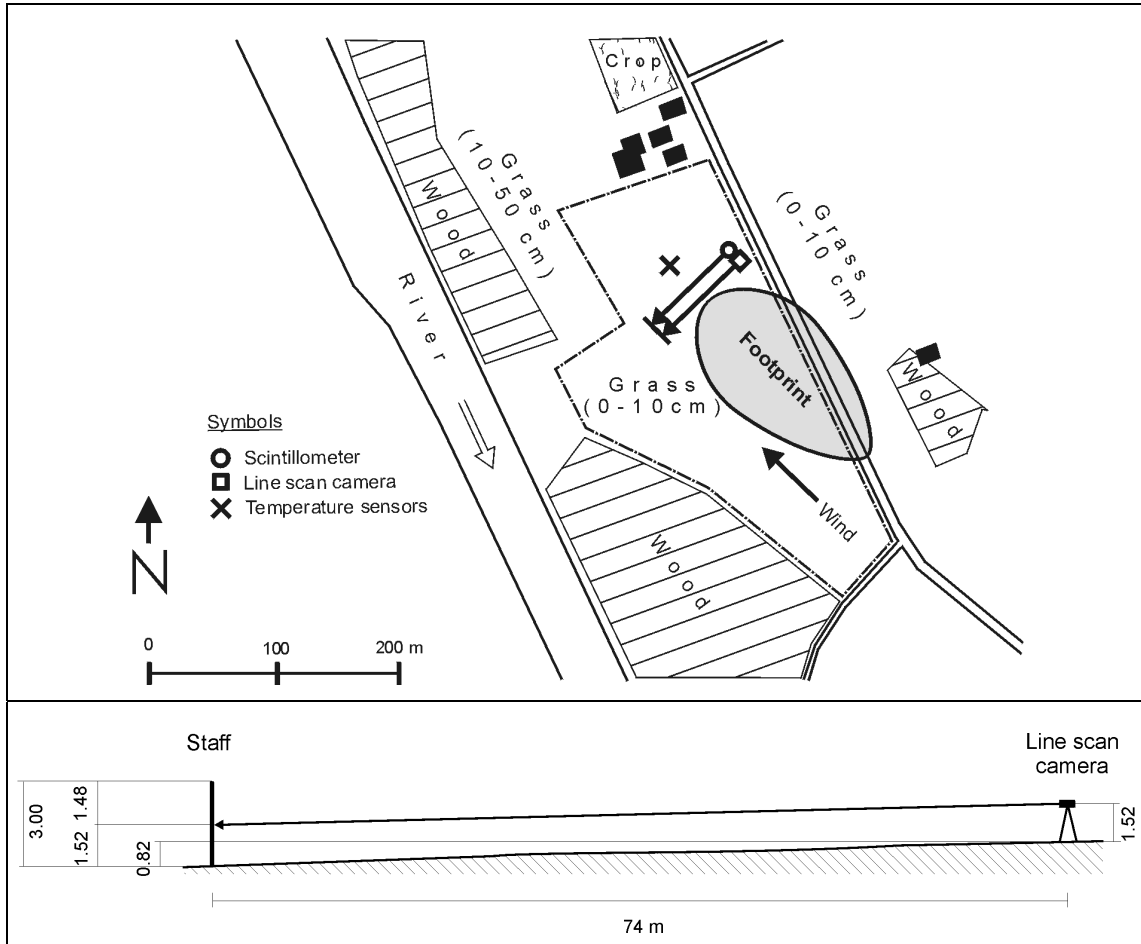


Figure 7.17: Map and profile for the field experiment of 25 August 1999

In general, the wind was rather calm on both measuring days. On 19 August 1999, the wind speed did not exceed 1.9 m/s (median of wind speed: 0.38 m/s). On 25 August, the maximum of wind speed was 1.5 m/s (median of wind speed: 0.35 m/s).

The wind speed is displayed in Figure 7.31 where the wind speed is compared with the inner scale. Both days can be characterized as summer days with temperatures up to 27 degrees on 19 August and 30 degrees on 25 August, respectively (Figure 7.35 and Figure 7.37).

Since the areas of both experiments are located in a broad valley (about 5 km), the direction of wind does not change considerably. As shown in Figure 7.16 and Figure 7.17, the predominant wind direction was approximately perpendicular to the line of vision of the measuring systems.

b) Measuring systems

Like the experiment using the video theodolite, also the following field experiments are based on parallel measurements of the scintillometer and the investigated imaging sensor, i.e., the line scan camera. Figure 7.19 illustrates the parallel measurements where the distance between laser beam emitter of the scintillometer and coded levelling staff was about 3 m. White sun shades as shown in Figure 7.14 to Figure 7.18 were installed

in order to minimize the temperature influences on the instruments and to protect the electronic devices.

In addition to the experiments of the video theodolite, the following field experiments also include temperature gradient measurements by means of the sensor system described in section 5.3.2 where the mast of the temperature sensors is positioned between the line scan sensor and the target (section 7.3).

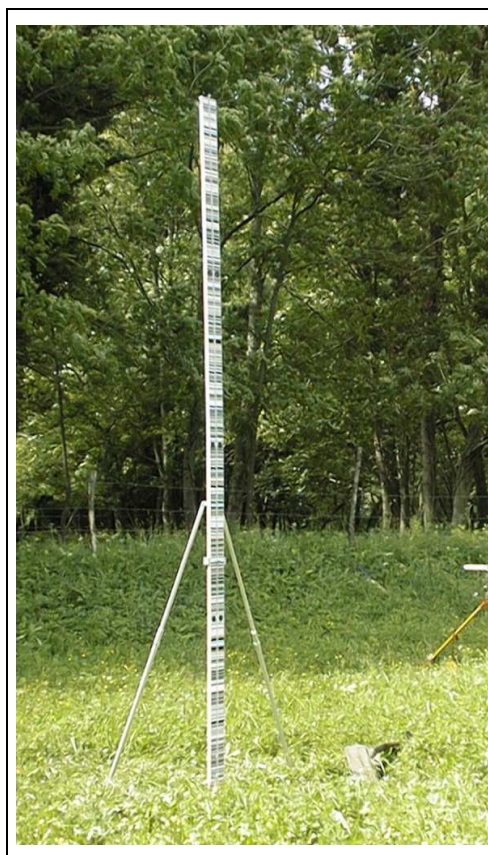


Figure 7.19: Levelling staff (left) and laser emitter of scintillometer (right)

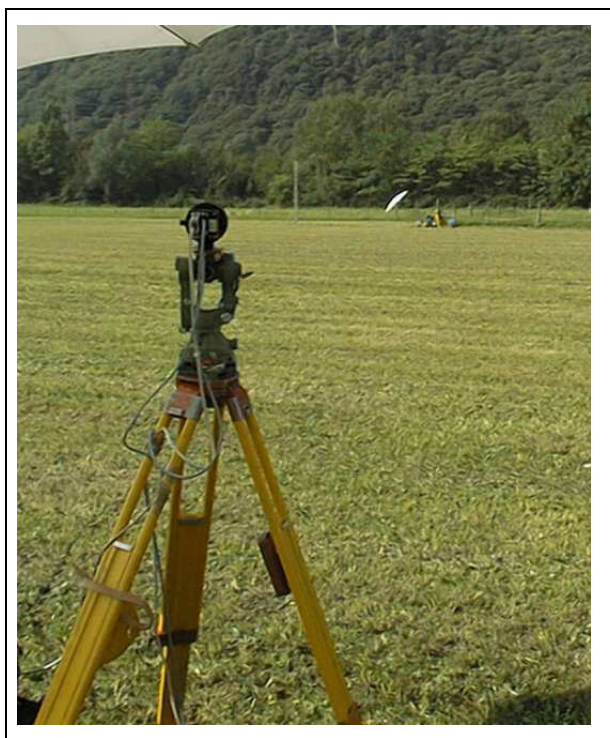


Figure 7.18: Line scan sensor pointing to the target

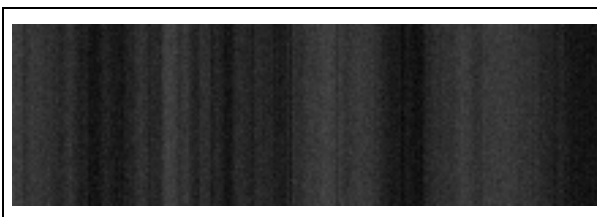


Figure 7.20: Image grabbed by line scan sensor (vertical stripes = code elements of levelling staff)

The measuring process of the line scan camera takes about 9 seconds. Hereby, 333 line readouts per second are grabbed by the line scan camera. The lines readouts are compiled to images containing 3000 lines per one measurement. For illustration, a section of such an image is given in Figure 7.20. Hereby, the vertical white stripes represent the horizontal white code elements of the levelling staff (cf. section 6.2.1).

7.2.2 Results and conclusions

In order to calculate the structure constant C_n^2 , the edge positions of the one-dimensional code patterns are calculated using the Canny operator as an appropriate edge detection operator (section 6.4.5). Hence, C_n^2 follows from the angle-of-arrival fluctuations as modelled by (4.31) whereby the standard deviations of the edge positions (6.77) is a measure for the angle-of-arrival fluctuations.

Besides the edge positions, the intensity fluctuations must be derived from the image data since they are a required quantity for the determination of the inner scale l_0 . In doing so, the variance σ_V^2 (cf. 6.35) is determined using the adaptive Wiener filter as given by (6.48). This variance is a measure for the intensity fluctuations which can be used to estimate the inner scale l_0 by (4.33) and (4.45). The results of C_n^2 and l_0 are plotted in Figure 7.21 up to Figure 7.28.

a) Measurements of 19 August 1999

The first field experiment in Claro (CH) took about five hours and provided time series of the structure parameter C_n^2 and l_0 which are discussed in the following. Figure 7.21 shows the results of the structure constant of refractive index C_n^2 (upper line: line scan camera; higher line: scintillometer).

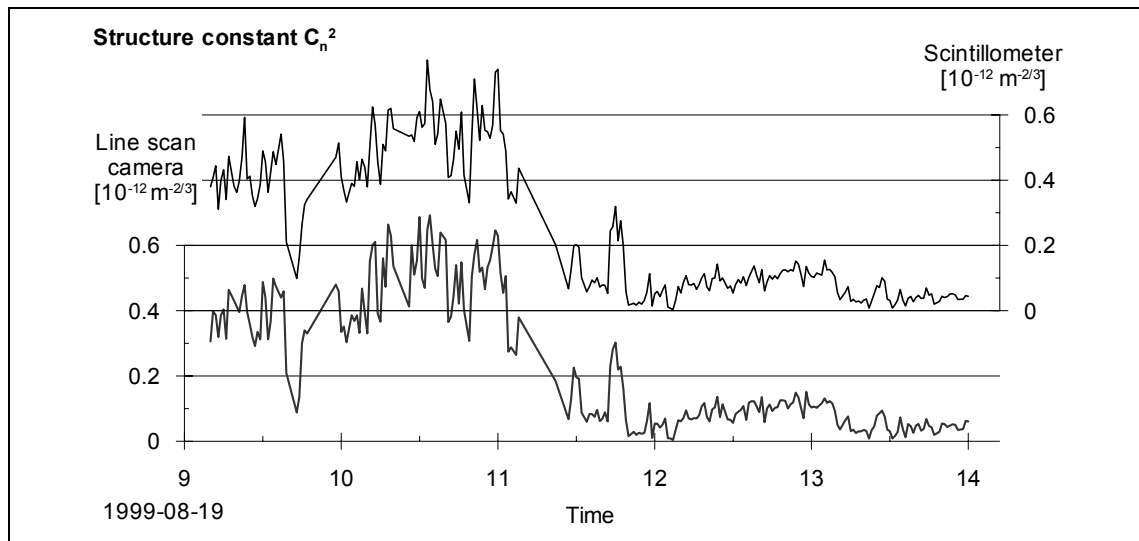


Figure 7.21: Structure constant C_n^2 (Place: Claro / CH)

The time series of C_n^2 shows an broken increase until 11:00 h whereby this increase is caused by solar heating of the soil during the morning. From 11:00 h clouds began to gather which led to a decrease of radiation and heat flux and, therefore, C_n^2 decreased.

The structure constant remained on a relatively low level until the end of the measurements. The results derived from the line scan sensor reveal a good agreement with the results obtained by the scintillometer, whereby the correlation coefficient is $r_{corr} = 0.97$ (Figure 7.22). Although, one should remember the a small range in which the structure constant C_n^2 has varied since 12:00 h. From this time, the measurements lacked of adequate information for comparison because the structure constant C_n^2 was always on a similar level, thus, the sensitivity and measuring range of the instruments cannot be described very well.

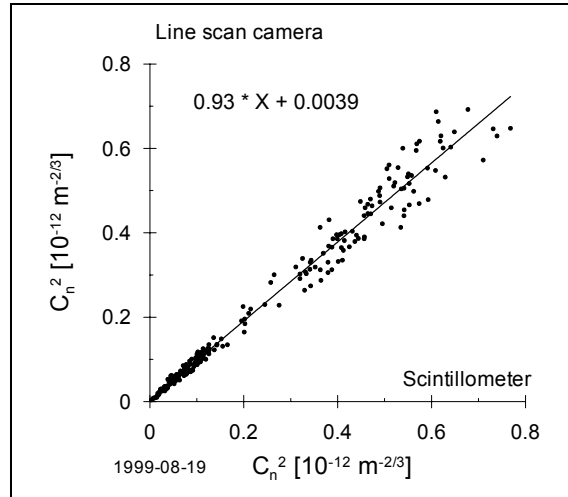


Figure 7.22: Correlation of structure constant C_n^2 (Place: Claro / CH)

The standard deviation of C_n^2 can be estimated by means of the differences between scintillometer and line scan camera and yields about $0.05 \cdot 10^{-12} \text{ m}^{-2/3}$. Thus, the accuracy of the line scan camera is about 4 times better than the one of the video theodolite.

The following diagrams (Figure 7.23 and Figure 7.24) show the inner scale l_0 which was determined together with the structure constant during the same experiment.

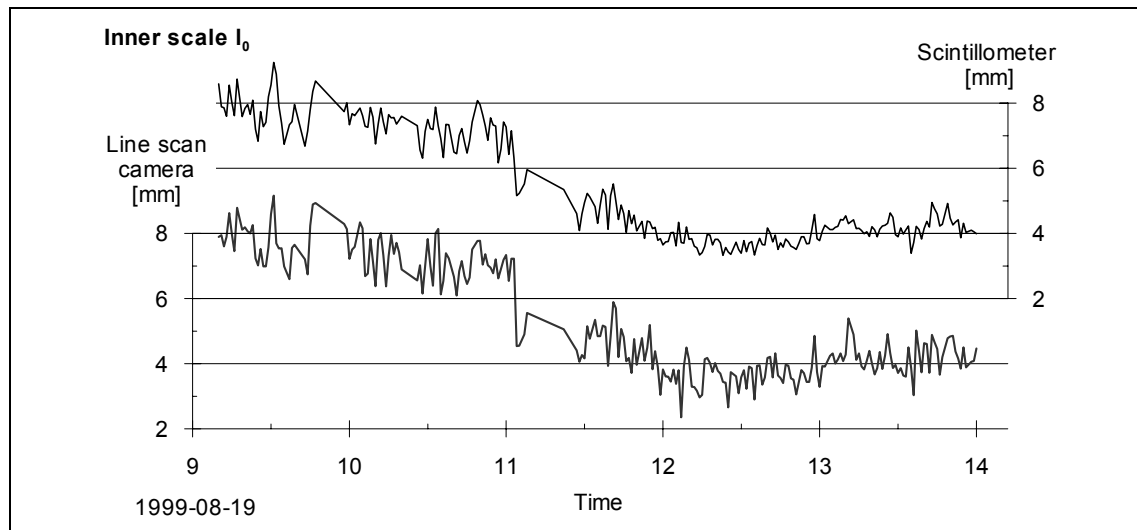


Figure 7.23: Inner scale l_0 (Place: Claro / CH)

As in the case of the video theodolite, the inner scale l_0 is related to the wind speed. High values of l_0 can be found in time periods where the wind velocity was relatively low. For example, the wind speed was only about 0.5 m/s in the period from 9:00 h to 11:00 h wherein the values of l_0 reach local maxima of about 9 mm, see Figure 7.31.

The correlation of the inner scale obtained by the scintillometer and the line scan camera amounts $r_{corr} = 0.95$. The scattering plot of Figure 7.24 illustrates this correlation.

The accuracy of the determination of the inner scale is about 0.5 mm (standard deviation) which is significantly better than the results of the video theodolite (standard deviation: 1.3 mm).

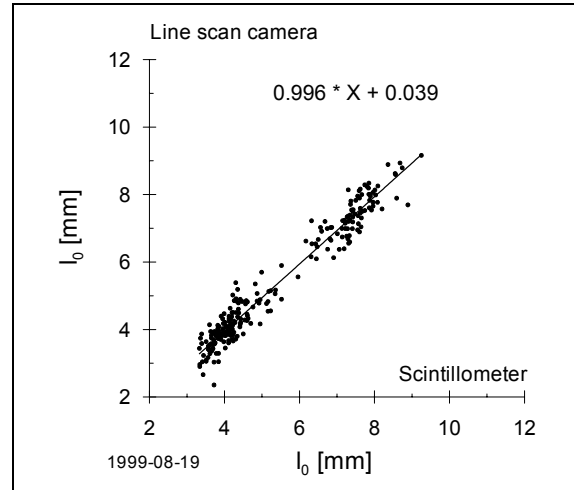


Figure 7.24: Correlation of inner scale l_0 (Place: Claro / CH)

b) Measurements of 25 August 1999

The field experiment of 25 August again investigated the agreement of the results achieved by use of the line scan camera with those of the scintillometer. The measurements were located on an other field in Claro as described in section 7.2.1 (Figure 7.15 and Figure 7.17). Although the experiment took place on a different test area, the length of the line of sight was again about 74 m and the environmental conditions (grass, topography) were very similar to the ones of 19 August.

The measured time series of the structure constant C_n^2 are given in Figure 7.25 and Figure 7.26. From the beginning at 8:30 h the structure constant increased since the sun heating produced increasing fluxes of sensible heat. At about 11:30, a maximum of C_n^2 had been reached. C_n^2 remained on this level until, at 13:30 h, clouds covered the sun for about 10 minutes leading to a sudden fall of C_n^2 .

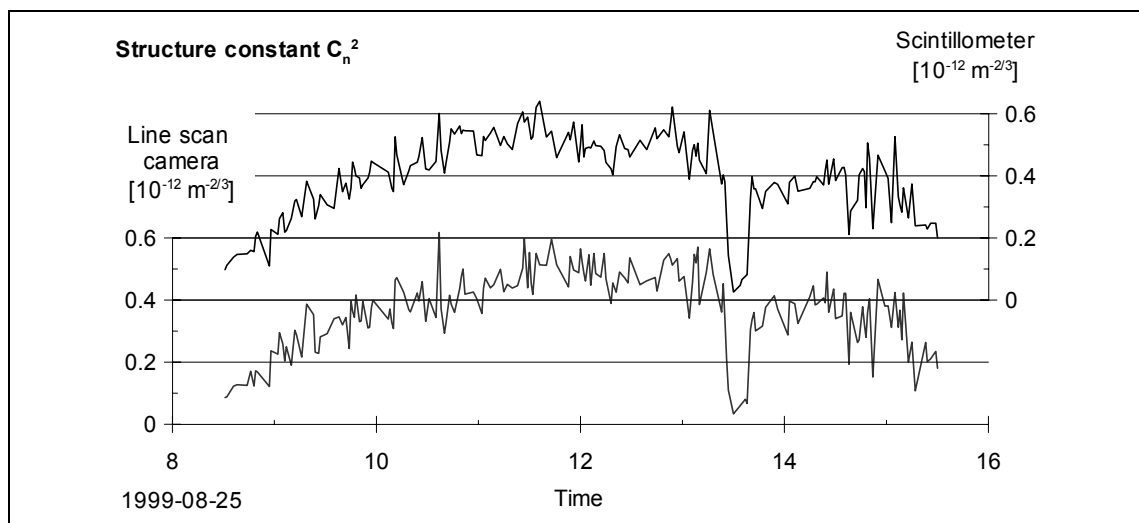


Figure 7.25: Structure constant C_n^2 (Place: Claro / CH)

In comparison to the experiment of 19 August, the structure constant was higher during the afternoon of 25 August. This is understandable since the sky was cloudless for most part on 25 August and therefore, the sun radiation and sensible heat fluxes were stronger. These circumstances are also manifest by a higher maximum of temperature on 25 August.

The results obtained by the line scan camera again revealed a good agreement with the reference represented by the results of the scintillometer and the correlation coefficient is $r_{corr} = 0.91$ (Figure 7.26). Based on this experiment, the estimated accuracy (standard deviation) of the structure constant C_n^2 is $0.06 \cdot 10^{-12} \text{ m}^{-2/3}$. This means the accuracy and correlation coefficient of the experiment of 25 August are marginally worse than the one of 19 August but the accuracy of the line scan camera is still better than the one of the video theodolite.

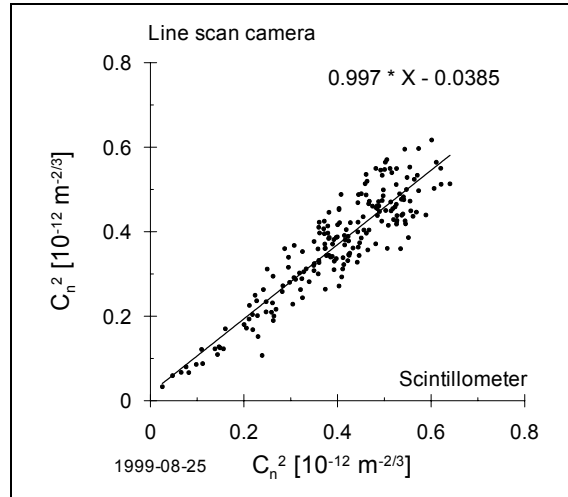


Figure 7.26: Correlation of structure constant C_n^2 (Place: Claro / CH)

The inner scale l_0 measured in the field experiment of 25 August is displayed in Figure 7.27.

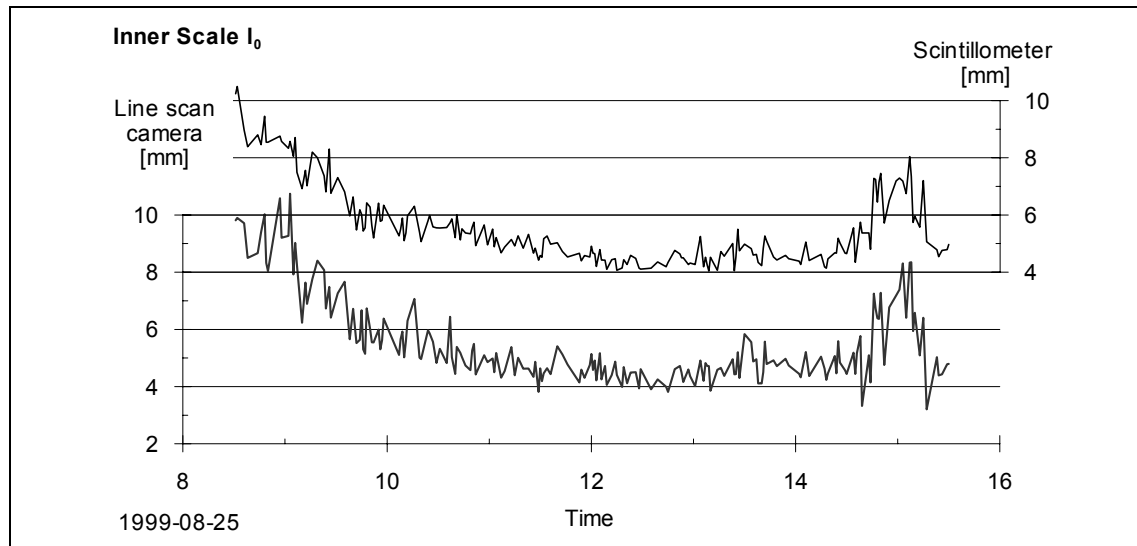


Figure 7.27: Inner scale l_0 (Place: Claro / CH)

At the beginning, the inner scale l_0 had reached the maximal level and decreased whereby short-time fluctuations of l_0 occurred in the order of magnitude of about 0.5 to 1 mm. The inner scale decreases down to a level of about 4.5 mm which is slightly higher than the values of 19 August. This seems plausible since the wind speed of 25 August was modestly smaller than on 19 August (0.3 m/s about 13:30 h on 25 August) which results in a larger size of small eddies and, therefore, in a larger inner scale. This relation is discussed below in Figure 7.31.

Figure 7.28 compares the inner scale l_0 measured using the scintillometer with l_0 derived from the image data of the line scan sensor. Also this correlation coefficient is quite good and amounts to $r_{corr} = 0.89$ which is insignificantly lower than the corresponding correlation coefficient of 19 August.

The accuracy of the inner scale, derived from the differences between scintillometer and line scan camera, is estimated to 0.6 mm (standard deviation). This means both experiments revealed approximately the same accuracy of the inner scale obtained by line scan camera. The influence of the standard deviation on the refraction angle is presented in section 7.5

As mentioned above, the wind speed can be assumed to influence the inner scale l_0 significantly. This influence is investigated empirically using the plots of Figure 7.29 to Figure 7.31 where the empirical functions are fitted using a logarithmic approach.

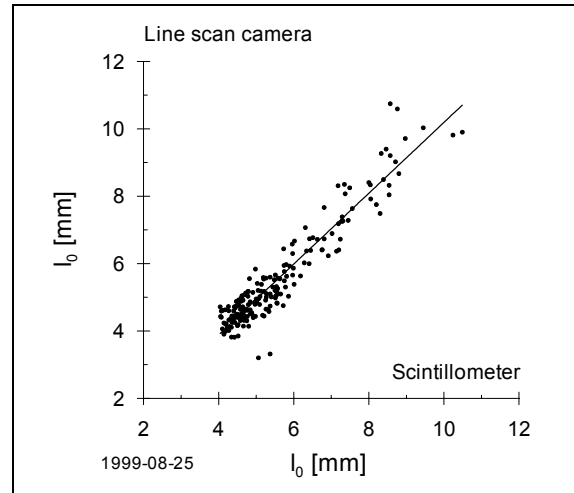


Figure 7.28: Correlation of inner scale l_0 (Place: Claro / CH)

Although the measurements of the inner scale are subject to minor deviations and the measurements of the wind speed are limited in spatial resolution, the correlation of the wind speed with the inner scale is rather high and amounts to $r_{corr} = 0.95$ (19 August 1999) and $r_{corr} = 0.84$ (25 August 1999).

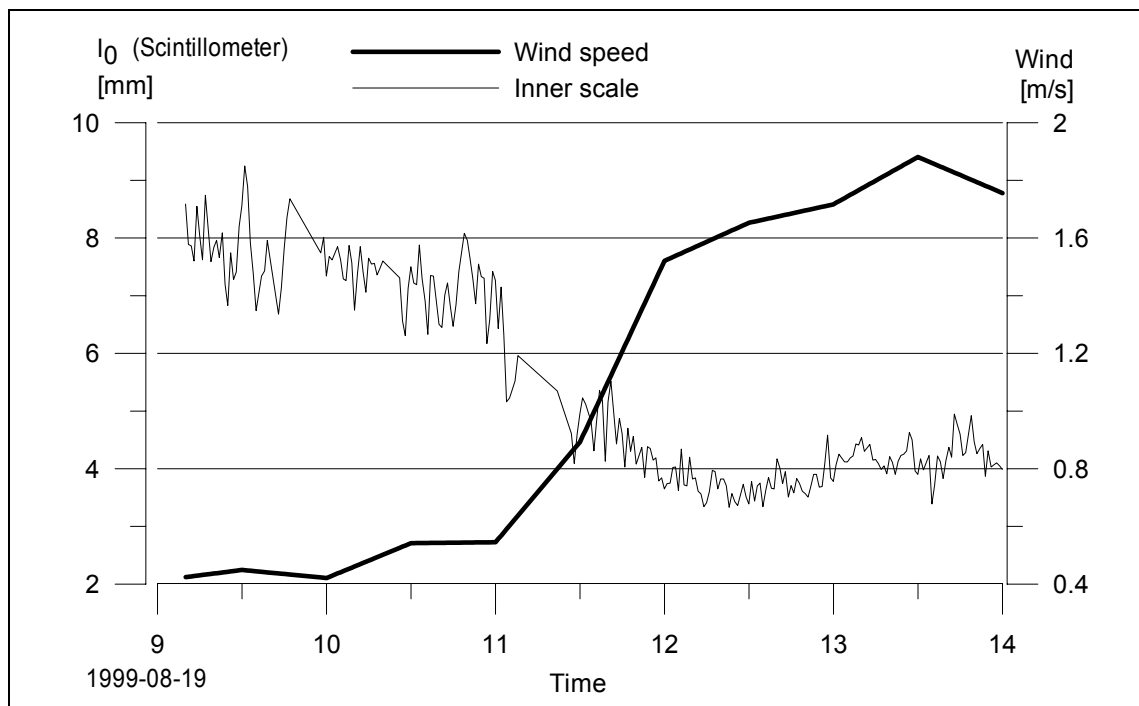


Figure 7.29: Wind speed and inner scale (Place: Claro / CH; 19 August 1999)

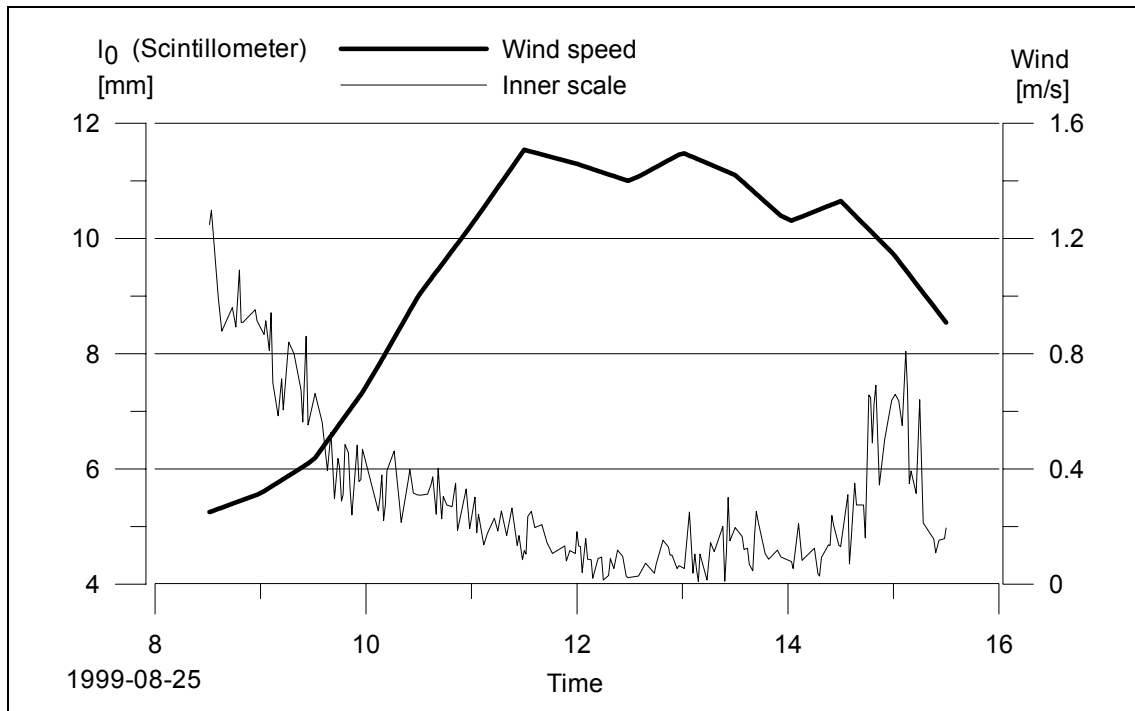


Figure 7.30: Wind speed and inner scale (Place: Claro / CH; 25 August 1999)

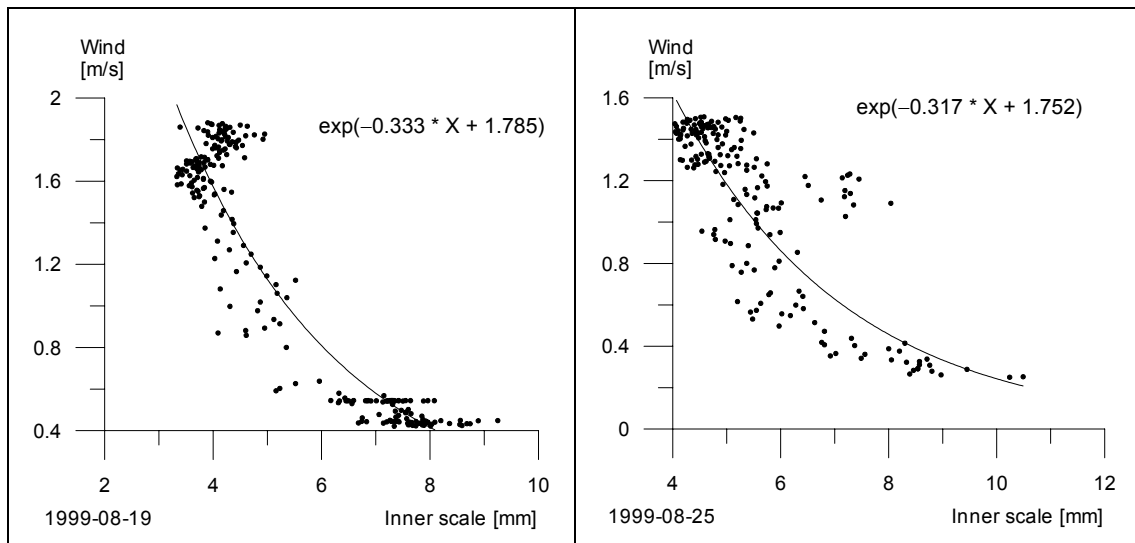


Figure 7.31: Correlation of wind speed and inner scale l_0 (Place: Claro / CH)

Similar to section 7.1.2, the relation between structure constant C_n^2 and the mean intensity of the measurement image can be investigated. This relation is based on the assumption that the mean intensity of the pixels of the line scan sensor coincidences with the structure constant C_n^2 .

As an example, the time series of the experiment of 25 August are displayed in Figure 7.32. The correlation is rather poor ($r_{corr} = 0.31$) but the trend functions reveal a slight relationship between C_n^2 and the mean intensity.

Obviously, the relationship between C_n^2 and the mean intensity is significantly different than the one detected in the experiment of 3 June 1999 (Video theodolite).

Thus, as mentioned in 7.1.2, the mean intensity can only be used for the determination of C_n^2 if further parameter model the influence of the illumination such as the sunset and shadows over the target. Herein, additional quantities must be measured to determine the (non-turbulent) part of the illumination and other systematic effects.

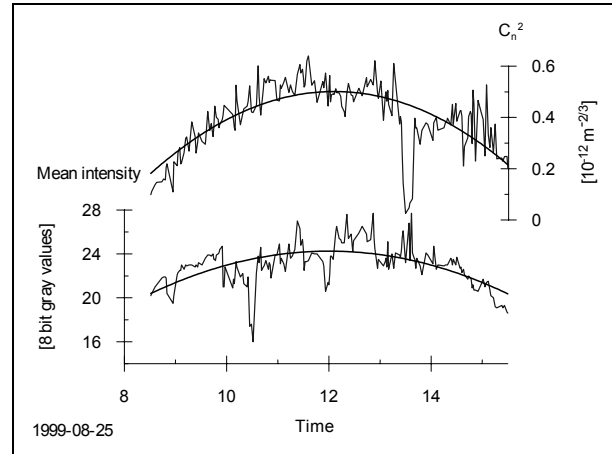


Figure 7.32: Mean gray value vs. C_n^2
(Place: Claro / CH)

7.3 Temperature measurements

As described in section 7.2.1, temperature measurements were performed during the field experiments of 19 August 1999 and 25 August 1999 simultaneously with the measurements using scintillometer and line scan camera. The temperature sensors were mounted on a mast with the geometrical dimensions as described in section 5.3.2 (Figure 7.33).

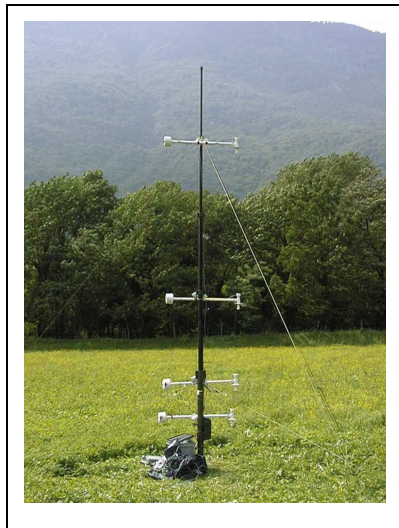


Figure 7.33: Mast of temperature sensors

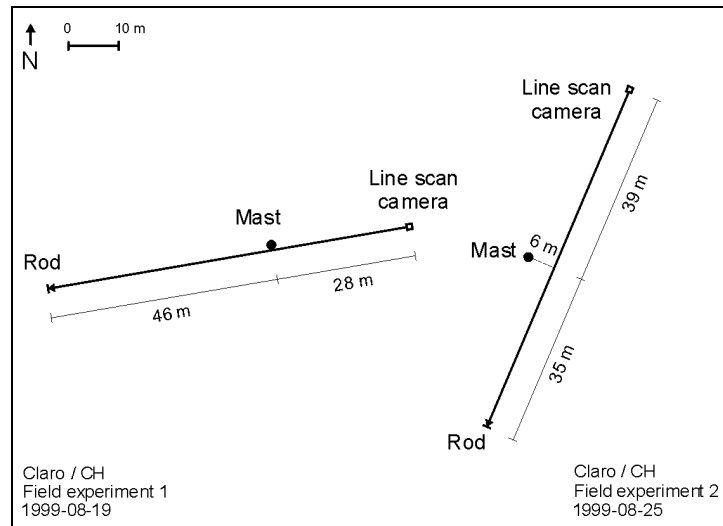


Figure 7.34: Mast in relation to the experimental setup of line scan camera

During the experiment of 19 August 1999, the mast was positioned close to the line of sight. The mast was placed somewhat eccentrically owing to further field experiments taking place at the same time [TROLLER 2000]. On 25 August 1999, the mast was about 6 meters away from the line of sight and situated fairly in the middle of the dis-

tance between instruments and target (Figure 7.34). In both cases, a position of the temperature gradient measuring system was chosen which can be assumed to be representative for the temperature field as far as possible.

The measured temperature gradients as plotted in Figure 7.35 up to Figure 7.38 are determined between the heights of 1.25 m and 2.43 m above ground since this range is also the height in which the line of vision runs above the ground. For comparison, the temperature gradients are calculated using the parameters of optical turbulence (C_n^2 and l_0) derived from the image data of the line scan camera using .

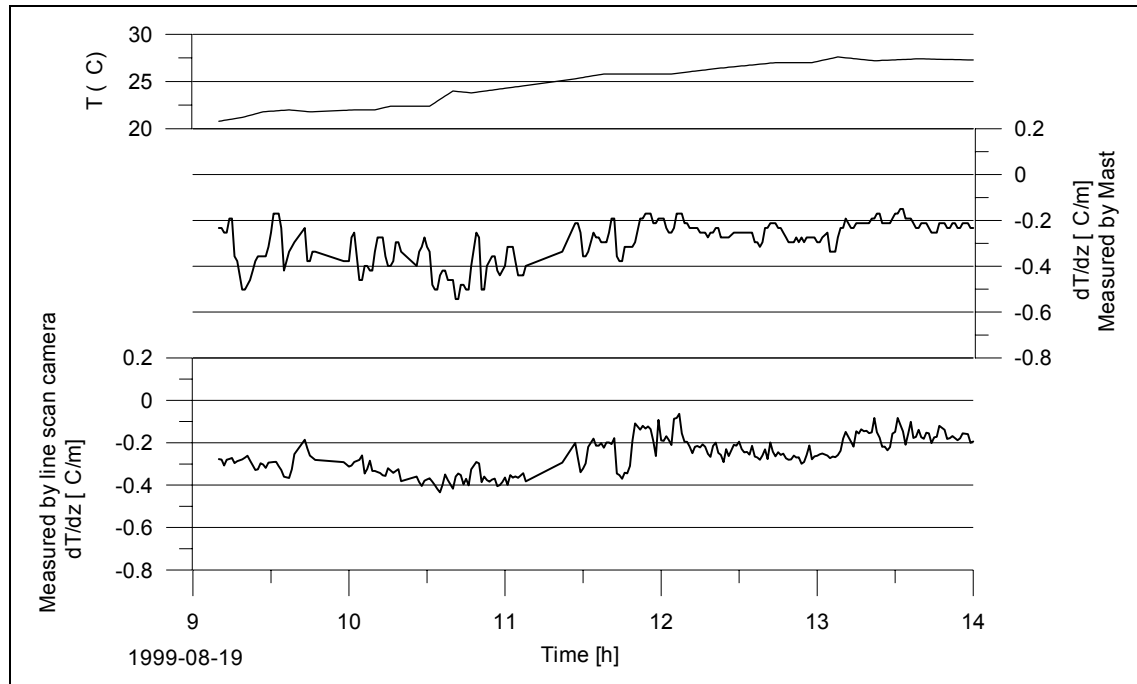


Figure 7.35: Measured temperature gradient vs. modelled gradients (Model: Högström) (first experiment in Claro, 19 Aug 1999)

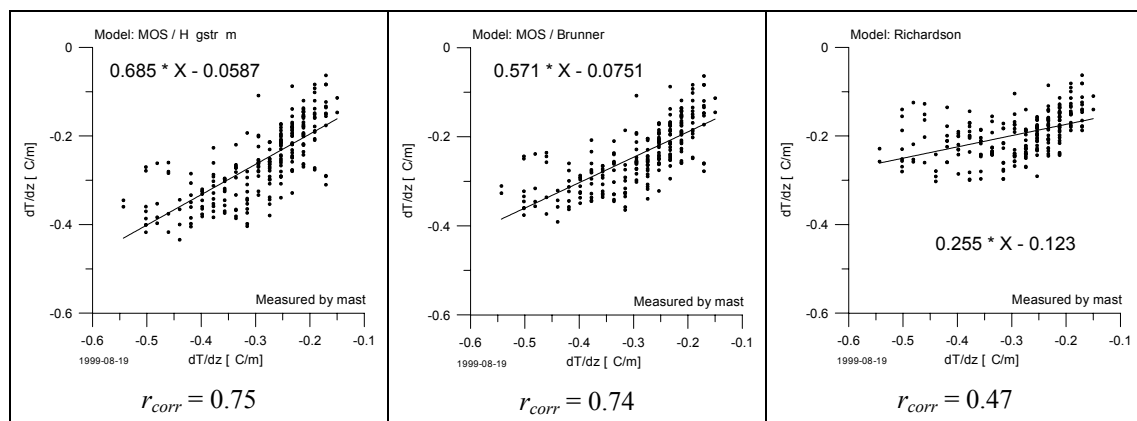


Figure 7.36: Measured temperature gradient vs. modelled gradients

In order to determine the temperature gradient modelled by Monin-Obukhov similarity, the calculation follows the algorithm explained in section 3.4 using (3.57), (3.58), (3.59), (3.61), (3.64), (3.65), (3.66), (4.1) and the profile function (3.56) of HÖGSTRÖM [1988]. In doing so, the obtained results are displayed in Figure 7.35. and Figure 7.36 for the experiment of 19 August 1999.

The standard deviation of the temperature gradient (based on the differences between line scan camera and mast) is 0.05 K/m.

The correlation coefficient between the measured temperature gradients and the modelled results (Monin-Obukhov similarity) amounts to $r_{corr} = 0.74$. As shown in Figure 7.36, the use of other profile functions does not significantly improve the correlation as shown by the application of the profile function (3.55) of BRUNNER [1979]. The profile functions (3.56) of HÖGSTRÖM and BRUNNER utilize the dimensionless quantity ζ defined by (3.50) as presented in section 3.4. Moreover, the refinement of the Monin-Obukhov theory using the flux-Richardson number R_f (section 3.6) is investigated too, whereby the modified dimensionless ratio ζ' is defined by (3.67). The results obtained by means of (3.67) and (3.56) are plotted in Figure 7.36. With respect to the measured temperature gradients, the correlation coefficient between the flux-Richardson-modelled temperature gradients and the measurements is only $r_{corr} = 0.47$, this means the agreement is worse than the results obtained with use of ζ .

In an analogous manner, the following plots (Figure 7.37 and Figure 7.38) compare the modelled temperature gradients obtained by image processing with the temperature gradients measured by the mast during the experiment of 25 August 1999 in Claro.

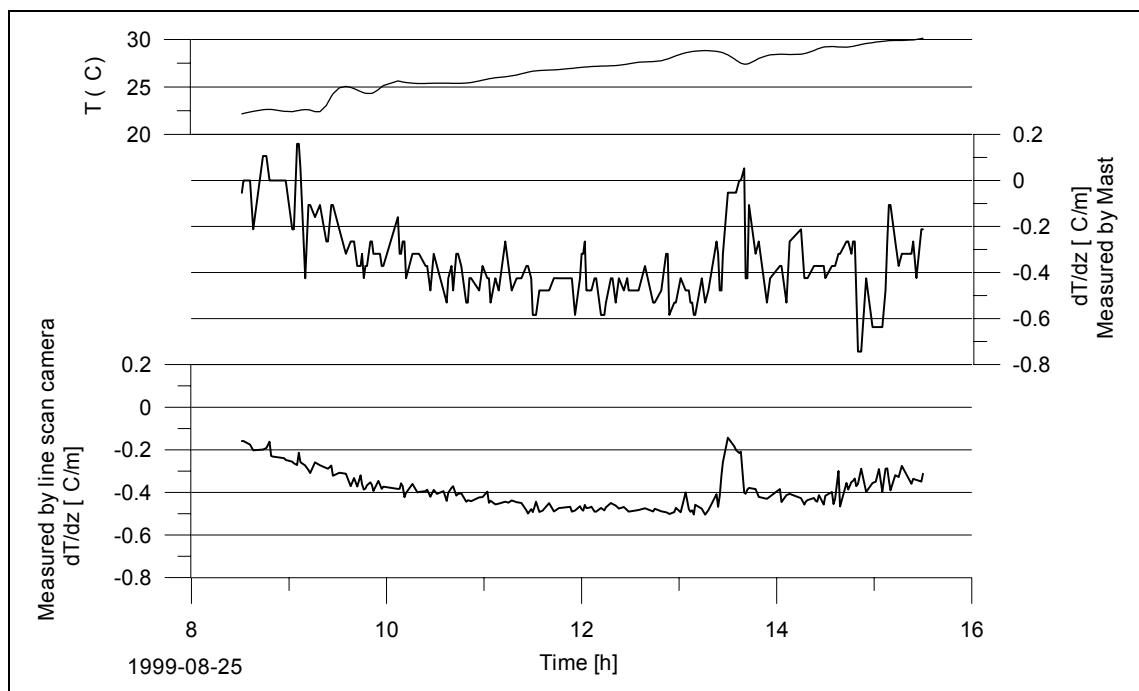


Figure 7.37: Measured temperature gradient vs. modelled gradient (Model: Högström; second experiment in Claro)

Obviously, the measured temperature gradients were subject to considerable fluctuations (up to 0.2 K/m during 5 minutes) on 25 August 1999. The standard deviation calculated using the differences is 0.10 K/m which is considerably worse than the results obtained on 19 August 1999. In general, the deviations seem to be randomly distributed as shown in the scatter plots of Figure 7.38. But the deviations are especially large (up to 0.3 K/m) in the first hour of the measuring time (8:30 h to 9:30 h).

Possibly, the transition from stable ($dT/dz > \approx 0$) to unstable ($dT/dz < \approx 0$) stratification can cause these deviations, since different profile functions must be applied for each type of stratification (cf., e.g., (3.56)) and, therefore, uncertainties of the current stratification can cause significant deviations.

In Figure 7.38, when using the models of HÖGSTRÖM and BRUNNER ($r_{corr} = 0.70$), the correlation coefficients of the scatter plots are slightly lower than the ones of 19 August 1999, but the difference seems not be very significant. Thus, these models can still be applied. It is remarkable that the model using the Richardson number yields better results based on the measurements of 25 August 1999 than on the ones of 19 August 1999. This can be interpreted as follows: On 19 Aug, the deviations of the temperature profile from the adiabatic case are lower than on 25 Aug, therefore, the contradictions of the Monin-Obukhov similarity using the Obukhov length do not cause difficulties since the deviations can be neglected. On 25 Aug, the temperatures are higher and the buoyancy is stronger and re-enforces the turbulence caused by friction production. In this case, the application of the Richardson flux number is more justified, although this model does not yield the same quality such as the models of HÖGSTRÖM and BRUNNER.

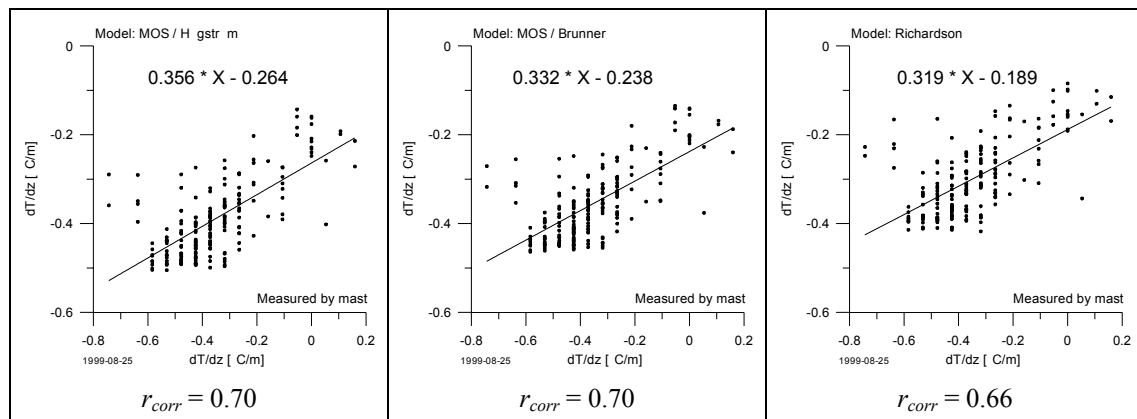


Figure 7.38: Measured temperature gradient and its moving average vs. modelled gradient (second experiment in Claro, continued)

The comparison of the results as shown in the diagrams above illustrates that the modelled temperature gradients are in the order of magnitude of the measured temperature gradients, principally. Nevertheless, depending on the time, considerable deviations between the measured and the modelled gradients may occur.

Under adverse conditions characterized by strong fluctuations of dT/dz such as shown in Figure 7.37 (08:30 h to 09:30 h), the standard deviation of the temperature gradient is about 0.10 K/m. If the conditions are favorable as depicted, e.g., in Figure 7.36, the standard deviation of the temperature gradient is about two times smaller and only amounts to 0.05 K/m.

In respect of the estimation of accuracy as presented above, it should be pointed out that the temperature gradient measurement system only provides temperature gradients for a discrete position in the area, whereas the modelled temperature gradient is an averaged value which is integrally valid for the whole path of propagation. In order to validate the

results, the achieved accuracy of the temperature gradient will be compared with the accuracy of the temperature gradient as derived in section 7.5.

7.4 Temperature gradient profile

The contemplation in section 7.3 is only valid for the vertical temperature gradients at the height of the instrument (about 1.5 m). In this section, the results of investigations which take the entire vertical temperature gradient profile into account are presented. Hereby, the profiles are determined using the temperatures measured by all sensors attached at the mast. The temperature gradient profile was approximated by (2.31) where the parameters a_T and b_T must be estimated. Thus, the temperature gradient profiles can be compared with the ones obtained by the HÖGSTRÖM model. The comparison of the gradients at different heights is presented in Figure 7.39.

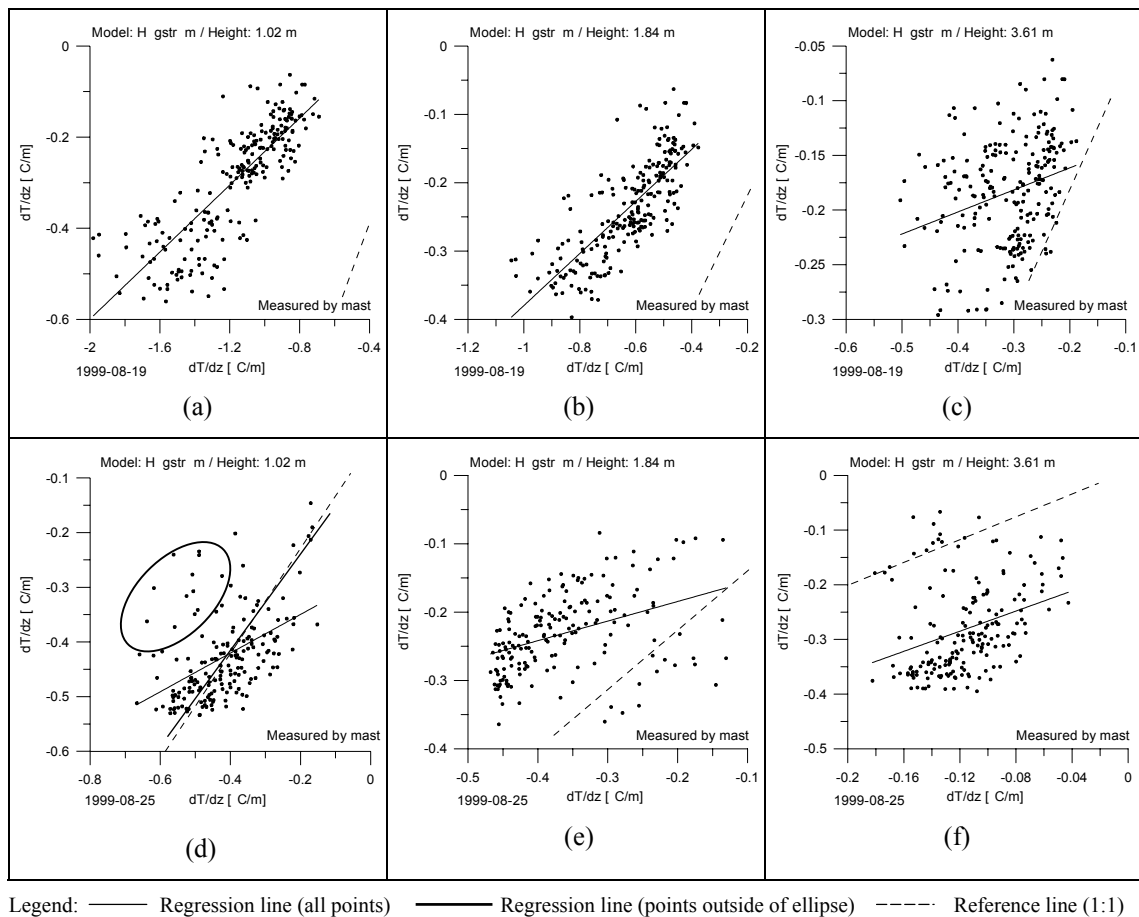


Figure 7.39: Temperature gradients at different heights

The dotted line in Figure 7.39 marks the one-to-one reference line. Diagram d) shows that the gradients of the HÖGRSTRÖM model agree quite well with the ones obtained by the temperature gradient profile modelled using (2.31) except for the values in the ellipse (Figure 7.39d). These outliers refer to the measurements which were performed at about 9:00 PM. At that time, the stratification changed from stable to unstable. That means the HÖGSTRÖM model can be uncertain during the time of the transition. Furthermore, the measured temperatures of the mast can only be fitted properly using the parameters a_T and b_T of (2.31) if the stratification is strictly unstable.

Referring to the remaining diagrams, systematic deviations in the order of 0.1 to 1.4 °C/m may occur. In order to provide more general explanations for these deviations, additional measurements are recommended. Currently, further investigations about the temperature profile are still in process at the Swiss Federal Institute of Technology [WEISS *et al.*, 2000].

7.5 Accuracy of temperature gradient and refraction angle

7.5.1 Derivation

In the following, the accuracy of the temperature gradient and refraction angle is estimated to support the interpretation of the results presented in the previous sections. To estimate the accuracy of the temperature gradient and the refraction angle, the relevant measurands (temperature, pressure, distance, C_n^2 , l_0 , β_1) denoted by the index j , their accuracy σ_j (standard deviation) and their influence coefficients P_j must be given or calculated. Assuming stochastically independent measurands, the accuracy of refraction angle σ_δ (standard deviation) follows from the law of propagation of variances and is given by:

$$\sigma_\delta^2 = \sum_j \sigma_{\delta,j}^2 = \sum_j P_j^2 \sigma_j^2 \quad (7.1)$$

To obtain the influence coefficients P_j for the refraction angle, the refraction angle is modelled by the refraction index gradient n of (2.3) which yields:

$$\delta = -\frac{1}{2n} \frac{78.83 \cdot 10^{-6} p}{T^2} \left(0.0342 + \frac{dT}{dz} \right) R \quad (7.2)$$

Thus, the influence coefficients are given by the correspondent partial derivation:

$$T: \quad P_1 = \frac{\partial \delta}{\partial T} = \frac{1}{n} \frac{78.83 \cdot 10^{-6} p}{T^3} \left(0.0342 + \frac{dT}{dz} \right) R \quad (7.3)$$

$$p: \quad P_2 = \frac{\partial \delta}{\partial p} = -\frac{1}{2n} \frac{78.83 \cdot 10^{-6}}{T^2} \left(0.0342 + \frac{dT}{dz} \right) R \quad (7.4)$$

$$R: \quad P_3 = \frac{\partial \delta}{\partial R} = -\frac{1}{2n} \frac{78.83 \cdot 10^{-6} p}{T^2} \left(0.0342 + \frac{dT}{dz} \right) \quad (7.5)$$

Therefore, the influence coefficients P_j can be calculated under the condition that the amounts of measurands are given such as presented in the third column of Table 7.1. Since the amounts are assumed with use of the results obtained in the previous sections, the influence coefficients can be determined, principally.

This determination may be complicated if the temperature gradient is not given and, therefore, must be derived from C_n^2 and l_0 by means of (3.56), (3.57), (3.58), (3.59), (3.61), (3.64), (3.65), (3.66), and (4.1).

Referring to the conditions of the experiment of 19 August at about 11:45 PM, the gradient yields $dT/dz = -0.39$ K/m derived $C_n^2 = 0.32 \cdot 10^{-12} \text{ m}^{-2/3}$, $R = 74$ m, $l_0 = 4.6$ mm, $\beta_1 = 0.86$, $(n-1) = 261 \cdot 10^{-6}$, $T = 25.8$ °C, $p = 989$ hPa, and a height of instrument $z_i = 1.56$ m (cf. Table 7.1). A more general analysis of the accuracy considering various amounts of the measurands is presented Table 7.3 and, e.g., in [DEUSSEN, 2000].

Likewise, the calculation of the influence coefficients for the parameters of optical turbulence C_n^2 and l_0 is complicated, since the refraction angle (7.2) directly depends on the temperature gradient dT/dz and, indirectly, on C_n^2 and l_0 which are given. However, by means of the Monin-Obukhov similarity, a relation between dT/dz and C_n^2 and l_0 is available as described in section 3.4 and, therefore, can be implemented in a software.

Since the mathematical dependence of C_n^2 and l_0 on the refraction angle cannot be elementarily differentiated, the influence coefficients must be determined by means of the discrete differentiation which is applied as follows:

$$C_n^2: \quad P_4 = \frac{\partial \delta}{\partial C_n^2} \approx \frac{\delta(C_n^2 + \Delta C_n^2, l_0, R, z_i, p, T, \beta_1) - \delta(C_n^2, l_0, R, z_i, p, T, \beta_1)}{\Delta C_n^2} \quad (7.6)$$

$$l_0: \quad P_5 = \frac{\partial \delta}{\partial l_0} \approx \frac{\delta(C_n^2, l_0 + \Delta l_0, R, z_i, p, T, \beta_1) - \delta(C_n^2, l_0, R, z_i, p, T, \beta_1)}{\Delta l_0} \quad (7.7)$$

$$\beta_1: \quad P_6 = \frac{\partial \delta}{\partial \beta_1} \approx \frac{\delta(C_n^2, l_0, R, z_i, p, T, \beta_1 + \Delta \beta_1) - \delta(C_n^2, l_0, R, z_i, p, T, \beta_1)}{\Delta \beta_1} \quad (7.8)$$

Hereby, the expression $\delta(\cdot)$ denotes the refraction angle provided by the software using the algorithm of section 3.4. and provided by the input parameters given in the brackets. The increments of the differentiation ΔC_n^2 , $\Delta \beta_1$, and Δl_0 are to be chosen by the user. On the one hand, the increments of the discrete differentiation ΔC_n^2 , $\Delta \beta_1$, and Δl_0 must be chosen small enough to fulfill the assumption of linearization and, on the other hand, ΔC_n^2 and Δl_0 must be large enough in order to avoid numerical problems (effacement of digits). In Table 7.1, the increments are chosen as 1 % of the amount.

j	Measurand	Amount	Unit	Accuracy σ_j	Influence coefficient P_j	Influence σ_{δ_j} [mgon]
1	T	25.8	°C	1	0.0060	0.006
2	p	989	mbar	1	0.000902	0.001
3	R	74	m	0.01	0.0121	0.000
$\frac{dT}{dz}$	4	C_n^2	$10^{-12} \text{ m}^{-2/3}$	0.05	1.04	0.052
	5	l_0	mm	0.5	0.0601	0.030
	6	β_1	--	0.09	0.36	0.033

Table 7.1: Influences on the accuracy of refraction angle
Total standard deviation = 0.07 mgon

The Obukhov-Corrsin constant can usually be assumed to be about $\beta_1 = 0.86$ but investigations such as [HILL, 1982] show that uncertainties in the value of β_1 are about 10 %.

Therefore, the standard deviation of 0.009 for β_1 is introduced into Table 7.1 since measuring methods for the standard deviation of β_1 were not available.

Thus, the influences of each relevant measurand on the accuracy of refraction angle can be determined and are presented in the rightmost column of Table 7.1. Using (7.1), the total standard deviation of the refractive angle is about 0.07 mgon.

The standard deviation of the refraction angle depends on the length of the propagation path R as shown, e.g., in (2.23). In order to reach an accuracy analysis which is independent of R , the analysis of the influence of T , p , C_n^2 , l_0 and β_1 on the temperature gradient is more meaningful. The influences of each relevant measurand on the temperature gradient can be determined in an analogous manner to the refraction angle. Thus, the accuracy of the temperature gradient can be calculated using Table 7.2 from which follows the total standard deviation of the temperature gradient = 0.03 K/m.

j	Measurand	Amount	Unit	Accuracy σ_j	Influence coefficient P_j	Influence $\sigma_{dTdz,i}$ [K/m]
1	T	25.8	°C	1	0.0029	0.003
2	p	989	mbar	1	0.0004	0.000
4	C_n^2	0.32	$10^{-12} \text{ m}^{-2/3}$	0.05	0.507	0.025
5	l_0	4.6	mm	0.5	0.0293	0.015
6	β_1	0.86	--	0.09	0.1889	0.017

Table 7.2: Influences on the accuracy of temperature gradient
Total standard deviation = 0.03 K/m

Depending on the amount of C_n^2 and l_0 , the influence coefficients of C_n^2 and l_0 on the accuracy of the temperature gradient vary as presented in Table 7.3. The figures in italics correspond to the coefficients of Table 7.2.

		Inner scale l_0			
		4.6 mm	7.6 mm	4.6 mm	7.6 mm
C_n^2	0.11 $10^{-12} \text{ m}^{-2/3}$	0.945 K/m/($10^{-12} \text{ m}^{-2/3}$)	0.738 K/m/($10^{-12} \text{ m}^{-2/3}$)	0.0159 K/m/mm	0.0116 K/m/mm
	0.32 $10^{-12} \text{ m}^{-2/3}$	0.507 K/m/($10^{-12} \text{ m}^{-2/3}$)	0.314 K/m/($10^{-12} \text{ m}^{-2/3}$)	0.0293 K/m/mm	0.0335 K/m/mm

Table 7.3: Variation of C_n^2 and l_0 : Changes of influence coefficients P_j for dT/dz

Summarizing the influences displayed in Table 7.1 and Table 7.2, it follows that the refraction angle and the temperature gradient are sensitive to errors in l_0 and C_n^2 . But also the influence of the uncertainties of the Obukhov-Corrsin constant β_1 cannot be neglected.

7.5.2 Conclusions

As illustrated in Table 7.1, the accuracy of refraction angle mainly depends on the accuracy of the parameters of optical turbulence C_n^2 , l_0 , and β_1 whereas the influences of temperature and pressure on the accuracy of refraction angle are negligible. Under the assumption of a propagation distance $R = 74$ m (case of the field experiments in Claro) the accuracy of refraction angle calculated by (7.1) is about 0.07 mgon (standard devia-

tion) and the corresponding standard deviation of the temperature gradient of $\sigma_{dT/dz}$ is 0.03 K/m.

At first, the accuracy of $\sigma_\delta = 0.07$ mgon derived from Table 7.1 is based on an accuracy of C_n^2 and l_0 (standard deviation of $C_n^2 = 0.05 \cdot 10^{-12} \text{ m}^{-2/3}$ and standard deviation of $l_0 = 0.5$ mm) which has been confirmed by the field experiments. Hereby, the standard deviations are calculated using the differences between line scan camera and scintillometer. With respect to the accuracy of $\sigma_\delta = 0.07$ mgon, the accuracy of the measuring system (line scan camera) seems to be sufficient.

But it should be taken into consideration that the estimation of the accuracy as presented in section 7.5.1 deals with stochastic deviations only and neglects systematic deviations. To form an opinion about the systematic deviations, it is reasonable to interpret the results of the temperature gradient measurements in a more detailed matter. For example, it is possible that the choice of location of the mast or the texture of the footprint (section 3.5) can cause systematic deviations of the temperature gradient measurements.

As shown in Figure 7.36, the temperature gradient measurements of 19 August 1999 ($\sigma_{dT/dz} = 0.05$ K/m) almost achieved the standard deviation of the temperature gradient $\sigma_{dT/dz} = 0.03$ K/m derived from Table 7.2. But, on the contrary, the measurements of 25 August 1999 with $\sigma_{dT/dz} = 0.10$ K/m (Figure 7.37 and Figure 7.38) do not confirm the standard deviation of $\sigma_{dT/dz} = 0.03$ K/m derived from Table 7.2.

In other words, the measurements of 25 August 1999 reveal a standard deviation of about $\sigma_{dT/dz} = 0.10$ K/m which corresponds to an accuracy of refraction angle of about $\sigma_\delta = 0.20$ mgon and which is about 3 times higher than the standard deviation derived from Table 7.1 and Table 7.2, respectively. An accuracy of the refraction angle of about $\sigma_\delta = 0.20$ mgon is not accurate enough since the refraction angle is 0.72 mgon (assuming the amounts of Table 7.2) and, thus, the uncertainty is about 30 %.

Various reasons can be given for these differences:

- Systematic errors are principally possible if the assumptions of the Monin-Obukhov similarity do not hold, e.g., if the fluxes are not stationary and the environment of the area of the field experiment is not homogeneous.
- The shape of the temperature gradient profile function φ_h also systematically influences the quality of the modelled temperature gradient. The temperature gradient profile functions are usually obtained by previous field experiments in a semi-empirical way. Depending on the conditions, the current temperature gradient profile function φ_h is slightly different.
- The transition from stable to unstable stratification can cause uncertainties in the calculation of the temperature gradients using dimensionless profile functions since both types of stratification have their own profile function.

8 Conclusions and outlook

The increasing relevance of imaging sensors in applications of geodesy enables also to make progress in refraction detection using image processing and turbulence models. The basis of these models are presented in section 3 and 4. It is conceivable that turbulence models continuously become more and more important, such as in the design of air crafts and combustion engines using computers without experimental setups.

In geodesy, the application of turbulence models and spectral analysis is promising to characterize turbulent exchange processes in the atmospheric boundary layer as shown by the theoretical considerations in section 3 and 4. In doing so, these exchange processes are modelled by turbulent eddies (section 3.2.1) whereby the turbulent-eddy model postulated by Kolmogorov (section 3.2.3) is the base of the refractive index spectrum (section 4.2.1). Relevant properties of the refractive index spectrum are described by the inner scale l_0 (section 3.2.6) and the structure constant of refractive index C_n^2 (section 4.1). In combination with appropriate models for the temperature profile (section 3.4), these two structure parameters can be used to determine the temperature gradient and, thus, to provide corrections for the refraction influence in geodetic applications. In doing so, the structure parameters C_n^2 and l_0 must be estimated during the field measurements, whereby the presented investigations are concentrated on the determination of C_n^2 and l_0 using image sensors and image processing techniques.

8.1 Determination of C_n^2

As shown in section 4.3 and 6.4, the structure constant C_n^2 can be determined if the time-dependent positions of a single edge in the grabbed images are detected and the variance σ_x^2 of detected positions is calculated. As shown in section 6.4.6, the accuracy of the single detected edge must be about $\sigma_{single} = 0.06$ pixel in order to provide the determination of the structure constant C_n^2 with an accuracy of about 10%. This statement is valid if the chosen imaging system fulfills the criteria presented in section 5.2.1 (Size of the pixel elements $\approx 10 \mu\text{m}$, focal length in the range from 300 mm to 500 mm, and aperture between 34 mm and 65 mm).

In order to achieve these high demands on accuracy, the edge operators which come into question must be investigated in respect of precision and reliability (section 6.4). The Canny operator and the least squares template matching are proved to be suitable image processing algorithms within the scope of this research work but it is still possible that other algorithms can be suitable as well.

When applying edge operators in series of images for the determination of σ_x^2 , it is essential to "track" the edges correctly. This means the edge of an image structure in one image must be related confidentially to the correspondent edge in the subsequent image. If this requirement is not fulfilled, outliers may occur which considerably falsify the calculation of the standard deviation of the edge position and, thus, deteriorate the estimation of C_n^2 .

To avoid outliers and to increase the reliability of edge detection, the following safety measures can be recommended:

- Semi-automatic edge detection: The approximate position of the edge must be provided in each image by the user and is applied as input value for the edge operator. For example, least squares template matching needs these values to linearize the gray value function using the partial differentiation of each unknowns (section 6.4.4).
- Fully automatic edge detection: Edge operators such as Canny operator only detect edges at positions where the gradient or an other related quantity exceeds a predefined threshold (section 6.4.5)
- Tracking of edges in subsequent images: Assuming that the coarse position of edges is given in each image, appropriate algorithms such as the morphological "bridge"-operator (section 6.4.5) ensure that edges are assigned correctly to the edges in the subsequent images and, therefore, fictitious edges can be detected and eliminated.
- Robust estimation: The determination of standard deviation σ_x^2 is based on the estimation of the average \bar{x} of the position of an edge. In a first step, the median of the position of an edge is estimated instead of the average since the median is a robust estimator. Thus, outliers which are still oblique can be detected in the second step and the definitive standard deviation of the position of the edges is calculated in the third step.
- Determination of the variance σ_x^2 using edge detection of several edges in the same image instead of a single one.

These measures and combinations of them lead to a reliable detection of the edges and, thus, to plausible results for the structure constant of refractive index C_n^2 as demonstrated in the field experiments.

8.2 Inner scale

Besides the structure constant C_n^2 , the inner scale l_0 must also be estimated by appropriate image processing algorithms. The theoretical investigations as presented in section 4.4 reveal that the inner scale l_0 can be determined if a measure for the intensity fluctuation is given and the other parameters such as C_n^2 , R , and λ are known as well. In order to investigate these relations, theoretical simulations are performed which are based on the theory of weak turbulence (section 4.5.2a). This theory is valid up to a length of propagation path $R = 200$ m or more, if the scintillation is not saturated (section 4.5.2a). These simulations yield to the functional model presented in section 4.4.2 which allows the determination of the inner scale l_0 under the assumption that appropriate measures for the intensity fluctuations can be derived from the image data.

In order to find these measures for the intensity fluctuations, the image data are analyzed by means of the (temporal) power spectral density. Basically, referring to the refractive index spectrum $\Phi_n = \Phi_n(\kappa^{11/3})$, the temporal spectrum of the intensity of the pixels S_Y (6.35) is expected to depend on the spatial spectrum in an analogous manner, i.e., $S_Y = S_Y(\omega_2^{11/3}, \sigma_V^2)$, whereby the variance of noise σ_V^2 is a parameter of this spectrum. Based on investigations in section 6.3.3, S_Y can be approximated by neglecting the $\omega_2^{11/3}$ -term. This approximation facilitates the estimation of the noise variance σ_V^2 by means of image processing techniques such as the adaptive Wiener filter (section 6.3.4) and template matching (section 6.4.4). These image processing techniques provide the

noise variance σ_V^2 which is assumed to determine the inner scale as described in section 4.4.2. In doing so, the sensitivity of the image sensors must reach at least a signal-to-noise ratio of about 9 dB (4.47) whereby this demand can be easily fulfilled using the sensors presented in section 5 (video theodolite: 46 dB, line scan camera: 75 dB). Although, the accuracy of the determination of the inner scale l_0 can be deteriorated by random deviations of the structure constant C_n^2 (4.47). This statement is confirmed by practical experiments where the correlation of the inner scale l_0 is systematically lower than the one of the structure constant C_n^2 .

8.3 Field experiments

The experiment using the video theodolite shows that the standard deviation of C_n^2 determined with use of the two-dimensional image data is about $0.2 \cdot 10^{-12} \text{ m}^{-2/3}$ and the standard deviation of l_0 is about 1.3 mm. In order to improve the accuracy of C_n^2 and l_0 the following relevant considerations and improvements are achieved:

- Theoretical considerations and field experiments using two-dimensional images, e.g., [TROLLER, 2000] proved that the angle-of-arrival fluctuations (section 4.3.1) in vertical direction are approximately equivalent to the ones in horizontal direction (cf. 4.23). This means the use of line scan sensors applied, e.g., for digital levelling in geodesy, is principally feasible for the determination of C_n^2 and l_0 as well as two-dimensional sensors.
- The line scan sensor enables a higher sampling frequency (333 Hz and more) whereas the data packages of the acquired image data are considerably smaller than in the case of the video theodolite and, therefore, the use of line scan sensors allows a longer measuring time (9 seconds instead of 1 second as in the case of the video theodolite).

The extension of the measuring time in combination with a higher sampling frequency provides an image data sample which is assumed to be more representative for the current turbulent regime.

Therefore, the line scan camera is applied in further field experiments wherein the comparison with the scintillometer shows that the results for C_n^2 (achieved standard deviation = $0.05 \cdot 10^{-12} \text{ m}^{-2/3}$) and the inner scale (achieved standard deviation = 0.5mm) are considerably better. Based on these results, a standard deviation for the refraction angle of 0.07 mgon can be expected (based on $R = 74 \text{ m}$ and a standard deviation of $dT/dz = 0.03 \text{ K/m}$, cf. Table 7.1 and Table 7.2).

However, this expected accuracy depends significantly on the quality of the dimensionless profile functions and the validity of the Monin-Obukhov similarity which are used to model the temperature gradient. As the comparison of the temperature gradients obtained by the image processing with the measured temperature gradients reveals in section 7.3, major deviations still can occur which are not acceptable (standard deviation of dT/dz amounts up to 0.1 K/m instead of 0.03 K/m). Therefore, improvements of the micrometeorological models are necessary.

For this reason, appropriate models are still investigated at the Swiss federal institute of technology [WEISS *et al.*, 2000].

8.4 *Disturbing influences on imaging systems*

The quality of the estimation of C_n^2 and l_0 using image processing techniques can be affected by various disturbing influences. When using imaging systems, disturbing influences are typically caused by the improper illumination which falsifies the measured gray values. These influences must be treated carefully because they can deteriorate the estimation of intensity fluctuations, on the one hand, and weaken the accuracy of edge detection, on the other hand.

Optical filters can be an appropriate mean to reduce disturbing intensity fluctuations which are caused by troublesome sources of (infrared) light. Since most of the field experiments took place on grass fields emitting infrared radiation, the application of an optical infrared cut-off filter can be strongly recommended (section 5.2.4).

Moreover, aperture averaging makes also the determination of l_0 difficult. Theoretical simulations as illustrated in Figure 4.18 demonstrate that the relation between intensity fluctuations and l_0 is influenced by the effective diameter d_e of the detector (Figure 4.17). The results of the field experiments indicate that the assumption of $d_e = 0$ (i.e., point detector, section 4.5.2b) leads to the most plausible results, especially for the line scan camera. With regard to further research work, it is possible that the aperture averaging must be modelled using (4.51) an other diameter d_e when applying other imaging systems.

8.5 *Outlook*

The investigated image processing techniques in combination with the imaging sensors are suitable to derive the parameters of optical turbulence C_n^2 and l_0 . When designing a system for commercial use, attention should be paid to the following aspects:

- The influence on the measuring range (maximal distance, measuring range of C_n^2 and l_0) should be investigated in more detail.
- Further investigations about the measuring time are also recommended. The measuring time in the field experiments of the line scan camera was about 9 seconds. A shortening of the measuring time may be possible, but the risk increases that the refractive index spectrum cannot be measured correctly because a shortage of measuring time lowers the quality of the spectral analysis.
- The derivation of temperature gradients from C_n^2 and l_0 presumes the stratification of the atmospheric boundary layer (stable, unstable) to be given. In the normal case, the stratification of the atmospheric boundary layer is unstable during day-time but deviations from this assumption produce systematic errors on the estimation of the temperature gradient. For this reason, a device for geodetic instruments should be developed which determines the stratification of the atmospheric boundary layer easily and reliably.
- Considerable importance must be attached to the dimensionless profile functions and to the turbulence model in general which are the base of the determination of the temperature gradient and refraction angle.

- As shown, e.g., in Figure 7.31, the wind speed measurements are highly correlated with the inner scale l_0 . These results confirm the investigations which have already been made in [DEUSSEN, 2000]. Therefore, the use of wind speed measurements for estimation of atmospheric turbulence and temperature gradients can be recommended but, of course, this would require additional measuring instruments.
- Correlations between the structure constant C_n^2 and mean gray value of an image section seem to exist. But the estimation of the structure constant C_n^2 by use of the mean value of the pixel intensities is only possible if other parameters such as sunset and shadows lying over the target are also included into the model. Moreover, additional calibration procedures for the CCD sensors are required to control the relationship between the solar radiation and the gray values of the pixel.

At present, the accuracy and reliability of the model of the atmospheric boundary layer is crucial and further investigations are strongly recommended. In doing so, the installation of a calibration line for which the height difference is known exactly could be useful for long-term measurements which reveal more information about the temporal variation of the observed refraction angle in comparison to the refraction angle derived from the structure parameters C_n^2 and l_0 . Moreover, in future, the dimensionless profile functions and turbulence model should be investigated in more detail because they are not valid with respect to special geodetic applications such as tunnel measurements.

Under the assumption that further investigations will refine the turbulence models, the measurement of optical turbulence with the use of image processing techniques will become noticeably more important in geodetic applications.

Appendix A: Fractals

Turbulence and fractal theory

The perturbations of the turbulent flow have a transient chaotic behavior and therefore cannot be described in a deterministic way. The theory of fractals expresses that turbulence is a scaling phenomenon. In the context of this (phenomenological) theory, there is a universal function that characterizes this extremely convoluted organization of turbulence. In other words, fractal theory shows that turbulent flows can be equated to self-similar structures such as fractals. Fractals are self-similar on all scales and, thus, can be modelled mathematically. The concept of self-similar relation of fractals is illustrated in Figure A.1: Turbulent flows need not exhibit exactly the same structure at all scales, but, at least, the same "type" of structures must appear on all scales

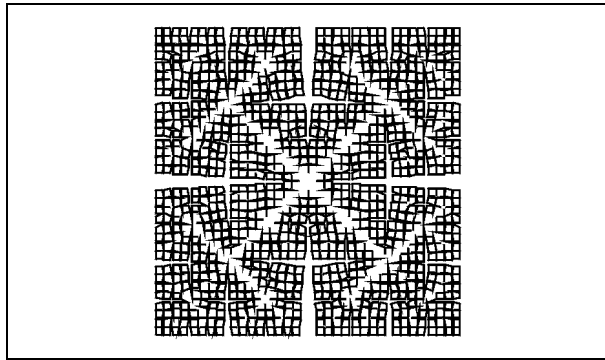


Figure A.1: Example of a fractal: Caesàro-Curve, e.g. [HERRMANN, 1994]

Since self-similarity means that an object looks the same on any scale and, therefore, has the same structure on any scale, too. This relation can be expressed mathematically by, e.g. [GROSSMANN, 1990]:

$$D_{F, n_F+1} = \Lambda^{d_F} D_{F, n_F} \quad (\text{A.1})$$

with D_F Fractal structure function
 Λ Scale factor
 d_F Fractal dimension
 n_F Index of recursion

Equation (A.1) allows the building of fractal structures using the following procedure:

1. An appropriate structure function D_F must be chosen.
2. An appropriate measure must be selected in order to be used as scale factor Λ .
3. The fractal dimension d_F can be derived from the scale factor and the structure function.

The algorithms of fractal theory produce an object or quantity which displays self-similarity. Hence, fractals are suitable as a mathematical tool to describe turbulence. To illustrate these procedures, the steps mentioned above are applied to the calculation of the Caesàro fractal shown in Figure A.1.

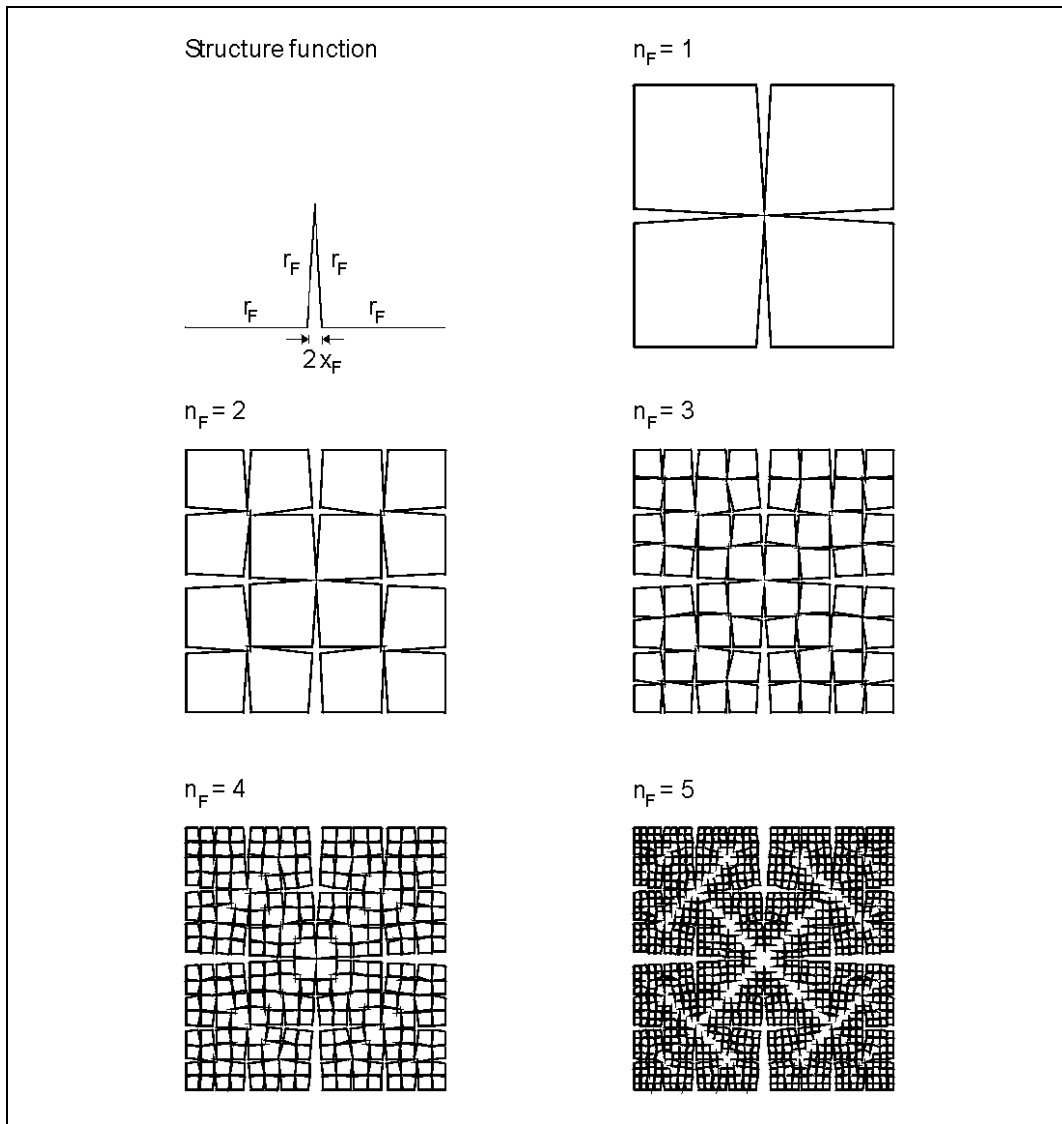


Figure A.2: Example of a Fractal (Caesàro curve): Structure function and 5 iterations

In the first step, the structure function D_F of the Caesàro curve is defined by the triangular structure function shown in Figure A.2. The base angle α_F is given by

$$\cos \alpha_F = \frac{x_F}{r_F} \quad (\text{A.2})$$

The base angle is known since it can be derived from Figure A.2 of the structure function.

In the second step, an appropriate scale factor can be selected as follows:

$$\Lambda = \frac{1}{r_F} \quad (\text{A.3})$$

Since the structure function D_F is applied to a line of the length 1 (standardization), it follows

$$2x_F + 2r_F = 1 \quad (\text{A.4})$$

$$\text{and } \Lambda = 2(1 + \cos \alpha_F). \quad (\text{A.5})$$

In the third step, the fractal dimension has to be calculated as defined by MANDELBROT [1977]:

$$d_F = \frac{\ln(M_F)}{\ln(\Lambda)} = \frac{\ln(M_F)}{2(1 + \cos \alpha_F)} \quad (\text{A.6})$$

with M_F Number of lines of which the fractal consists (Caesàro curve: $M_F = 4$)

If the parameters D_F , Λ and d_F of (A.1) are known, the fractal can be built using recursions which are given by (A.1). These parameters are also used to describe the self-similarity property of structure functions as introduced below in (A.9).

As shown in Figure A.2, the curve of iteration $n_F = 1$ and the curve of iteration 5 have the same shape but the fractal with $n_F = 5$ shows more details. Thus, fractal theory provides efficient tools to model complicated structures as, e.g., turbulence effects, in a realistic manner.

There is a direct relationship between turbulence and fractals. GROSSMANN [1990] showed that the Navier-Stokes equation generates a fractal structure D_F which can be assigned to the structure function of the velocity field u defined by the Navier-Stokes equation.

$$D_F = D_u(\mathbf{r}) \quad (\text{A.7})$$

Herein, the structure function of the velocity field $D_u(r)$ is defined by

$$D_u(\mathbf{r}) = \left\langle |u(\mathbf{x} + \mathbf{r}) - u(\mathbf{x})|^2 \right\rangle \quad [\text{m}^2/\text{s}^2] \quad (\text{A.8})$$

with \mathbf{r} Displacement vector between two points of the turbulent flow

The structure function describes the time variation of the velocities of two points in space separated by a displacement vector \mathbf{r} where the angle brackets indicate an ensemble average.

The structure function as defined in (A.8) implies that the velocity field is locally homogenous, i.e., the structure function only depends on the displacement vector. Moreover, if the velocity field is locally isotropic, the structure function only depends on the magnitude of the displacement vector r .

From (A.7) follows that self-similarity is a property of the structure function and can be expressed by:

$$D(\Lambda r) = \Lambda^{d_F} D(r) \quad (\text{A.9})$$

with Λ Scale factor
 d_F Fractal dimension

The index u has been omitted in (A.9) because this relation is valid for all quantities the structure function can be applied to. For example, in the case of optical turbulence as investigated in section 4, the structure function of refractive index is given by

$$D_n(r) = \left\langle |n(x+r) - n(x)|^2 \right\rangle \quad (\text{A.10})$$

with n Refractive index.

As the example of the Caesàro curve showed, fractals can calculate complicated phenomena of nature based on structure functions and scale factors. The scale factor must be selected with regard to the phenomena of nature. In the case of atmospheric turbulence, the dissipation rate of turbulent kinetic energy ε can be used as scale factor Λ to describe atmospheric turbulence. The definition and application of the dissipation rate ε of turbulent kinetic energy is explained in detail in section 3.2. The use of the dissipation rate as scale factor can be derived from the Navier-Stokes equation, too [GROSSMANN, 1990]:

$$\Lambda = \varepsilon \quad (\text{A.11})$$

Besides the dissipation rate and the structure function given by (A.8), the fractal dimension d_F still remains unknown and must be determined whereby the equation (A.9) gives the relation between the scale factor, structure function, and fractal dimension. Using dimensional analysis as shown in section 3.2, the fractal dimension of turbulence is $d_F = 2/3$. At this point, all parameters of (A.9) are given and, therefore, the structure function can be modelled using self-similarity as follows:

$$D_u(\varepsilon r) = \varepsilon^{2/3} D_u(r) \quad \text{for } L_0 > r > l_0 \quad (\text{A.12})$$

This means that, in the inertial subrange ($L_0 > r > l_0$), the turbulent velocity field is (statistically) self-similar. If the scale factor (dissipation rate ε) changes and the velocity differences D_u are scaled, the resulting velocity field is the same. Therefore, the turbulent flow is scale-invariant in the inertial subrange. By means of experiments, the measured inner scale l_0 determines the dissipation rate using (3.61), i.e., the scale factor of the velocity field is determined. Using (3.59) and ε , the Obukhov length L_{MO} can be calculated which is the scale factor of further dimensionless profile functions and which allows the calculation of the temperature gradient profile.

Appendix B: List of symbols

Roman symbols

A	Amplitude
a	Aperture
a_0, a_1, a_2	Parameters of a regression
A_{DC}	DC-value of power spectral density
A_f	Area of footprint
a_f	Distance between near end of footprint and sensor
A_{Ramp}	Amplitude of a ramp in an intensity function of an image
a_T	Parameter of temperature gradient model (factor)
a_w	Scale parameter of wavelet transform
a_ω	Scale parameter of power spectral density
B	Bowen ratio
b	Image distance
b_f	Distance between far end of footprint and sensor
b_T	Parameter of temperature gradient model (exponent)
b_w	Shift parameter of wavelet transform
c_f	Lateral half-width of footprint
c_L	Influence coefficient for outer scale
C_n^2	Structure constant of refractive index
c_p	Constant-pressure heat capacity of air
C_T^2	Structure constant of temperature
D	Structure function
d	Diameter
d_F	Fractal dimension
D_F	Fractal structure function
D_n	Structure function of refractive index
d_{patch}	Difference of the position of two corresponding patches
d_q	Deviation in transverse direction
d_{res}	Resolution
D_S	Structure function of phase
D_u	Structure function of velocity
\mathbf{E}	Electric field vector
e	Base of the Natural Logarithm (Euler number)
E_{kin}	Total kinetic energy
E'	Turbulent kinetic energy
$E[\cdot]$	Expected value
e_c	Eccentricity
E_{Norm}	Normalized estimation error
f	Focal length
F	Gray value function of an image (stochastic process)
$f(\cdot)$	Gray value function of an image
F_1	Fourier Transform of the gray value function f_1 of an image
F_1^*	Complex conjugate Fourier Transform of the gray value function f_1
$f_r(\cdot)$	Signal section (sub-signal)

f_s	Sampling rate
$f_{\Phi}(\kappa)$	Decay of turbulent spectrum
g	Gravitation constant
$g(x)$	Gradient function
G_S	Geothermal flux
H	Sensible heat flux
$H(\cdot)$	Fourier transformed filter function
$h(\cdot)$	Convolution kernel, filter function
h_{caus}	Causal filter
i	Imaginary unit
i, j	Index variable
k	Wave number
K_S	Number of windowed signal sections
k_1, k_2	Index variable of image signal
k_k	Von Kàrmàn constant
k_r	Refraction induced deviation between foresight and backsight readings in height levelling
L	Characteristic length
ℓ	Diameter of eddy
l_0	Inner scale
L_0	Outer scale
L_{ET}	Latent heat flux
L_{MO}	Obukhov length
Loc	Localization factor
l_{Pr}	Prandtl mixing length
L_{reg}	Set of pixels in a local region of image
L_s	Signal length
M_P	Number of pixels
$m_{F, local}$	Average of signal f in a local image region
n	Refractive index
n_0	Mean-squared noise amplitude per unit length (used for Canny operator)
n_1, n_2	Image coordinates
N_1, N_2	Number of sampling points of a discrete signal (rows, columns)
$N(0,1)$	Random variable with standardized Gaussian distribution
N_{Filt}	Length of the filter
N_L	Number of lines or number of read-outs
N_{local}	Length of local image region
n_{Patch}	Number of patches in one measurement image
p	Pressure
P	Influence coefficient
p_e	Size of quadratic pixel element
p_{res}	Resolution defined by diffraction effects
Pr	Prandtl's number
q	Specific humidity
Q_l	Influential quantity of inner scale on log-amplitude variance
R	Propagation path length
r	Integration variable for propagation path
r_{corr}	Coefficient of correlation
r_{χ}	Correlation of the log-amplitude

R_{Down}	Incoming radiation (short-wave)
R_n	Net radiation
R_{Up}	Radiation emitted by the ground (long-wave)
r_{corr}	Coefficient of correlation
R_E	Radius of earth
R_f	Flux-Richardson number
r_F, x_F, α_F	Parameters of Caesàro fractal
R_n	Net radiation
$R_n(\cdot)$	Autocorrelation function of refractive index
$R_F(\cdot)$	Autocorrelation function of stochastic signal F
$R_{FY}(\cdot)$	Cross-correlation function of stochastic signals F and Y
$R_u(\cdot)$	Autocorrelation function of velocity
S	Phase
SNR	Signal-to-noise ratio
$S_F(\cdot)$	Power spectrum density of stochastic signal F
$S_{FY}(\cdot)$	Cross power spectrum density of stochastic signals F and Y
T	Temperature
T^*	Temperature scale factor
t	Time
t_k	Lag
U	Characteristic velocity
u	Velocity
u^*	Friction velocity
u_q	Velocity of crosswind
v	Noise signal
V	Noise (stochastic process)
w	Vertical component of wind
$w(\cdot)$	Windowing function
w_c	Limiting value of windowing function of Canny operator
x	Coordinate; pixel coordinate
x_{edge, n_2}	Coarse position of the edge located in the row n_2
x_f	Upwind distance of maximum source weight of footprint
x_{Ones, n_2}	Position of the edge located in the row n_2 determined by Canny operator
x_{Ramp}	Length of a ramp of an edge
y	Noisy image signal
z	Height
z_i	Height of instrument

Greek symbols

α	Angle-of-arrival
α_{Alb}	Albedo
α_λ	Dry-air wavelength-dependence function for wavelength λ
α_1, α_2	Exponents of equation of Pi-Theorem
β	Angle of incidence
β_1	Obukhov-Corrsin constant
β_0^2	Rytov variance

χ	Log-amplitude
δ	Refraction angle
$\delta(\cdot)$	Delta function (Dirac pulse)
$\Delta\beta$	Deviation of vertical angle
Δx	Shift parameter of least squares template matching
ε	Dissipation rate
ε_{err}	Absolute error of convergence
$\Phi_n(\kappa)$	Refractive index spectrum (Hill spectrum)
$\Phi_K(\kappa)$	Refractive index spectrum of Kolmogorov
γ_n	Angle between refractive index gradient and vertical axis z
Γ	Gamma function
Γ_d	Dry-adiabatic temperature gradient
η	Kolmogorov microscale
φ_g	Gravitation potential
φ_h	Dimensionless profile function of sensible heat flux gradient
φ_{CT}	Dimensionless profile function of temperature structure constant
φ_m	Dimensionless profile function of momentum
φ_ε	Dimensionless profile function of dissipation rate
ϑ	Angle between refraction index gradient and propagation path
κ	Spatial frequency of the fluctuation
κ_l	Limiting spatial frequency
κ_{ref}	Curvature of propagation path
κ_{ref}'	Coefficient of refraction
λ	Optical wavelength
Λ	Scale factor
ν	Kinematic Viscosity
Π	Dimensionless numerical coefficient of Pi-Theorem
θ	Potential temperature
ρ	Density
σ_c	Standard deviation of Canny operator
$\sigma_{F, local}$	Standard deviation of the signal f in a local image region
σ_n^2	Fluctuation of refractive index
σ_S^2	Fluctuation of phase
σ_{single}	Standard deviation of the position of a single edge
σ_V^2	Variance of noise
σ_x^2	Fluctuation of the position of an edge
$\sigma_{x, spatial}^2$	Spatial standard deviation of the position of an edge
σ_α^2	Fluctuation of angle-of-arrival
σ_χ^2	Fluctuation of log-amplitude
σ_δ	Standard deviation of refraction angle
τ_s	Shearing stress or momentum flux
ω	Angular frequency
ψ	Complex phase perturbation
Ψ	Wavelet function
ζ	Dimensionless ratio between height and Obukhov length
ζ'	Modified dimensionless ratio between height and Obukhov length

References

- ACKERMANN, F. [1984]: *Digital image correlation: Performance and potential application in photogrammetry*. Photogrammetric Record, Vol. 11 No. 64, pp. 429-439.
- ANDREAS, E. L. [1990]: *Selected Papers on Turbulence in a Refractive Medium*. SPIE Milestone Series, Vol. 25, Society of Photo-Optical Instrumentation Engineers, Bellingham, WA.
- ANDREWS, H.C.; HUNT, B.R. [1977]: *Digital Image Restoration*. Prentice-Hall, New Jersey.
- ANDREWS, L. C. [1992]: *Aperture-averaging factor for optical scintillations of plane and spherical waves in the atmosphere*. J. Opt. Soc. Am. A 9, pp. 597-600.
- ANDREWS, L. C.; PHILLIPS, R. L. [1998]: *Laser beam propagation through random media*. SPIE Bellingham, Washington, pp. 125-128, 136-137, 403-409.
- ANDREWS, L.C. [1992]: *An analytical model for the refractive index power spectrum and its application to optical scintillations in the atmosphere*. J. mod. Opt. Vol. 39, pp. 1849-1853.
- AZOULAY, E.; THIERMANN, V.; JETTER, A.; AZAR, Z. [1988]: *Optical measurement of the inner scale of turbulence*. J. of Physics D: Applied Physics, Vol. 21, pp. 41-44.
- BAHNERT, G. [1986]: *Refraktion und Refraktionskoeffizient*. VT, Vol. 34 pp. 276-279.
- BASLER VISION TECHNOLOGIES [1998]: *User manual of line scan camera Basler L120*.
- BATCHELOR, G. K. [1993]: *The theory of homogenous turbulence*. Cambridge University Press, Ed. 1.
- BAYER, G. [1992]: *Zur hochgenauen automatischen Führung langsam bewegter Objekte mit Zielverfolgungssystemen im Nahbereich*. DGK Diss., Reihe C, Heft Nr. 398.
- BELAND, R. R. [1993]: *Propagation through Atmospheric Optical Turbulence*. In: Smith, F. G. (ed.): *The Infrared & Electro-Optical Systems Handbook, Vol. 2: Atmospheric Propagation of Radiation*, SPIE, Bellingham, Washington USA, pp. 157-232.
- BETH, S.; CASOTT, N.; DEUSSEN, D.; FREEDEN, W.; WITTE, B [1997]: *Wavelet Methods in Edge Detection and Refraction*. In: Grün, A.; Kahmen, H.: *4th Conference on Optical 3-D Measurement Techniques, Zurich 1997*, Wichmann Verlag, Karlsruhe, pp. 76-85.
- BEYNON, J.D.E.; LAMB, D.R. [1980]: *Charge-coupled devices and their applications*. McGraw-Hill, London.
- BLACKADAR, A. K. [1996]: *Turbulence and Diffusion in the Atmosphere: Lectures in Environmental Sciences*. Springer-Verlag Heidelberg, p 87.

- BÖCKEM, B. [2000]: *Technologische Aspekte und Systemtests des Dispersometer-Theodoliten für Anwendungen in der Ingenieurgeodäsie*. Paper to XIII Kurs f. Ingenieurvermessung, München, 13.-17.3.2000, In: Schnädelbach, K.; Schilcher, M. (eds.): *Ingenieurvermessung 2000*, Wittwer Verlag, Stuttgart, pp. 178-189.
- BÖCKEM, B.; FLACH, P.; WEISS, A.; HENNES, M. [2000]: *Refraction influence analysis and investigations on automated elimination of refraction effects on geodetic measurements*. Paper to XVI IMEKO World Congress 2000, 25-28 Sept. 2000, Vienna.
- BORN, M., WOLF, E. [1959]: *Principles of Optics: Electromagnetic Theory of Propagation, Interference and Diffraction of Light*. 1th. Edition, Pergamon Press, Oxford, pp. 479-489.
- BOYLE, W.S.; SMITH, G.E. [1980]: *Charge coupled semiconductor devices*. Bell System Technical Journal Vol. 49.
- BRANDSTAETTER, G. [1989]: *Das analytische Modell der videogestützten räumlichen Zielerfassung mit panfokalen Fernrohren*. In: Grün, A.; Kahmen, H.: *Optical 3-D Measurement Techniques*, Wien 1989, ISBN 3-87907-200-0.
- BREMER, M. [1999]: *Millimeter Interferometry: Atmospheric Fluctuations*. In: Guillo-teau, pp. (ed.): *Proc. of the IRAM Millimeter Interferometry Summer School*, Grenoble, 14 to 18 Sept. 1998, Chapter 9.
- BROCKS, K. [1948]: *Über den täglichen und jährlichen Gang der Höhenabhängigkeit der Temperatur in den unteren 300 Metern der Atmosphäre und ihren Zusammenhang mit der Konvektion*. Bericht des Deutschen Wetterdienstes in der US-Zone Nr. 5, Bad Kissingen.
- BRUNNER, F.K. [1992]: *Refraction, refractive index and dispersion: some relevant history*. In: DeMunck, J.C., Spoelstra, T.A. (Eds.), *Proc. Refr. Transatmos. Signals in Geodesy*. Netherlands Geod. Commission, 36:3-9.
- BRUNNER, F.K. [1984]: *Modelling of Atmospheric Effects on Terrestrial Geodetic Measurements*. In: Brunner, F.K. (Ed.): *Geodetic Refraction, Effects of Electromagnetic Wave Propagation Through the Atmosphere*. Springer Verlag, Berlin, Heidelberg, New York, Tokio, 1984, pp. 143-161.
- BRUNNER, F.K. [1982]: *On the Correction for Humidity in Two Colour Refraction Measurement*. *ZfV*, pp. 108-118.
- BRUNNER, F.K. [1980]: *Systematic and Random Atmospheric Refraction Effects in Geodetic Levelling*. *Proc. of Second International Symposium on Problems Related to the Redefinition of North American Vertical Geodetic Networks*, Ottawa (Canada), pp. 691-703.
- BRUNNER, F.K. [1979]: *Vertical Refraction Angle Derived from the Variance of the Angle-of-Arrival Fluctuations*. In: E. Tengström und G. Teleki (Ed.), *Refraction Influences in Astrometry and Geodesy*, Reidel Publ. pp. 227-238.
- BRUNNER, F.K.; FRASER, C.S. [1977]: *Application of the Atmospheric Turbulent Transfer Model (TTM) for the Reduction of Microwave EDM*. *Unisurv G, Austral. J. Geodesy, Photogrammetry & Surveying*, No. 27 (Dec. 1977), pp. 3-26.

- BUSINGER, J. A., J. C. WYNGAARD, Y. IZUMI, E. F. BRANDLEY [1971]: *Flux-Profile Relationships in the Atmospheric Surface Layer*. J. Atmos. Sci., Vol. 28, pp. 181-189.
- BUSINGER, J. A.; YAGLOM, A. M. [1971]: *Introduction to Obukhov's Paper on 'Turbulence in an Atmosphere with a Non-uniform Temperature'*. Boundary-Layer Meteorology, Kluwer Academic Publishers, Vol. 2, pp. 3-6.
- CANNY, J. F. [1986]: *A Computational Approach to Edge Detection*. IEEE Transactions on Pattern Analysis and Machine Intelligence, Vol. 8, No. 6, pp. 679-698.
- CASOTT, N. [1999]: *Erfassung des Einflusses der turbulenten Refraktion auf optische Richtungsmessungen mit CCD-Sensoren*. Diss., Mitteilungen aus den Geodätischen Instituten der Rheinischen Friedrich-Wilhelms-Universität Bonn, Heft Nr. 86.
- CASOTT, N.; PRENTING, J. [1999]: *Genauigkeitssteigerung beim Korrelationsverfahren in der digitalen Bildverarbeitung*. Photogrammetrie, Fernerkundung, Geoinformation 2/1999 pp. 101-112.
- CCIR [1990]: *CCIR Rec. 601-2: Encoding parameters of digital television for studios*. International Telecommunication Union, General Secretariat, Geneva (CH).
- CHUI, C.K. [1992]: *An introduction to wavelets*. Academic Press.
- CHURNSIDE, J. H. [1990]: *A spectrum of refractive-index turbulence in the turbulent atmosphere*. J. Mod. Opt. Vol. 37, pp. 13-16.
- CLIFFORD, S. F., G. R. OCHS, R. S. LAWRENCE [1973]: *Saturation of optical scintillation by strong turbulence*. J. Opt. Soc. Am., Vol. 64, No. 2, pp. 148-154.
- CLIFFORD, S.F. [1978]: *The Classical Theory of Wave Propagation in a Turbulent Medium*. In: J.W. Strohbehn (Ed.), *Laser Beam Propagation in the Atmosphere*, Topics in Applied Physics. Springer Verlag, Berlin, Heidelberg, New York.
- CORRSIN, S. [1951]: *On the Spectrum of Isotropic Temperature Fluctuations in an Isotropic Turbulence*. J. of Applied Physics, Vol. 22, No.4, pp. 469-473.
- COULTER, R. L. AND M. L. WESELY [1980]: *Estimates of Surface and Heat Flux from Sodar and Laser Scintillation Measurements in the Unstable Boundary Layer*. J. Appl. Meteorol., Vol. 19, No.10, pp. 1209-1222.
- DEUSSEN, D. [2000]: *Messverfahren zur Erfassung der Vertikalrefraktion unter Nutzung der atmosphärischen Turbulenz*. Shaker-Verlag, Aachen.
- DEUSSEN, D.; WITTE, B. [1997]: *Detecting 'image dancing' for determination of vertical refraction using a digital camera*. Second Turkish-German Joint Geodetic Days, Berlin, May 28-30, 1997.
- DORMAND, J. R.; PRINCE, P. J. [1980]: *A family of embedded Runge-Kutta formulae*. J. Comp. Appl. Math., Vol. 6, 1980, pp. 19-26.
- DRACOS, T. [1990]: *Hydraulik*. Verlag der Fachvereine, Zürich, 3. Aufl., p. 4-6.
- DYER, A. J. [1974]: *A review of flux-profile relationships*. Boundary-Layer Meteorol., Vol. 7, pp. 363-372.
- DYER, A.J.; BRADLEY [1982]: *An Alternative Analysis of Flux-Gradient Relationships at the 1976 ITCE*. Boundary-Layer Meteorology Vol. 22, pp. 3-19.

- ELMIGER, A.; WUNDERLIN, N. [1983]: *Dreidimensionale Berechnung von geodätischen Netzen : Methoden und Erfahrungen*. ETH Zürich, IGP; Bericht Nr. 73, p. 8.
- FANTE, R. L. [1983]: *Inner-Scale Size Effect on the Scintillations of Light in the Turbulent Atmosphere*. J. Opt. Soc. Am. 73 (1983). p 277.
- FAVRE, C.; FLACH, PH. [1999]: *Stations totales motorisées: Etat de la technique et perspectives d'avenir*. VPK 3/99, pp. 96-100.
- FAVRE, C.; HENNES, M. [2000]: *Zum Einfluss der geometrischen Ausrichtung von 360°-Reflektoren bei Messungen mit automatischer Zielerfassung*. VPK 2/00, pp. 72-78.
- FEFFERMAN, C. L. [2000]: *Existence and smoothness of the Navier-Stokes equation*. Princeton University Department of Mathematics, Princeton, to appear.
- FEIST, W.; GÜRTLER, K.; MAROLD, T., ROSENKRANZ, H. [1995]: *Die neuen Digitalnivelliere DiNi 10 und DiNi 20*. VR 57/2 April 1995 pp. 65-77.
- FLACH, PH.; HENNES, M. [1998]: *Die optische Turbulenz - wirklich nur ein limitierender Faktor für geodätische Messungen?*. In: Freedden W. (ed.): Progress in Geodetic Science, Proc. to Geodätische Woche Kaiserslautern 1998, pp. 65-72.
- FLACH, PH.; MAAS, H.-G. [1999]: *Vision-based Techniques for Refraction Analysis in Applications of Terrestrial Geodesy*. IAPRS, Onuma, Vol. XXXII, Part. 5-3W12, pp. 195-201.
- FLACH, PH.; NATEROP, D. [1999]: *Neue Analysetechniken für Deformationsmessungen in permanenten Robotertachymeter-Netzen*. AVN, 8-9/1999, pp. 284-291.
- FÖRSTNER, W. [1984]: *Quality Assessment of Object Location and Point Transfer using Digital Image Correlation Techniques*. ISPRS, Vol. 25 Part A3a, pp. 197-217.
- FRIED, D. L. [1967]: *Aperture averaging of scintillation*. J. Opt. Soc. Am., Vol. 68, pp.169-175.
- GARDNER, C. S.; PLONUS, M. A. [1975]: *The effects of atmospheric turbulence on the propagation of pulsed laser beams*. Radio Science, Vol. 10 No. 1 pp. 129-137.
- GEIGER, A. [1988]: *Der Lichtstrahl in differentialgeometrischer Formulierung*. IGP, Bericht Nr. 140, ETH Zürich.
- GEIGER, R.; ARON, R.H.; TODHUNTER, P. [1995]: *The climate near the ground*. 5th Ed.; Vieweg, Braunschweig, pp. 8-27.
- GOTTWALD, R. [1985]: *Zur Genauigkeitssteigerung und Erstellung eines automatisierten Datenflusses beim trigonometrischen Nivellement mit kurzen Zielweiten*. Diss., RWTH Aachen, Veröff. des Geodätischen Instituts der RWTH Aachen, Nr. 37.
- GRAY, D. A., A. T. WATERMAN, JR. [1970]: *Measurment of fine-scale atmospheric structure using an optical propagation technique*. JGR, Vol. 75, No. 6, pp. 1077-1082.
- GROSSMANN, S. [1990]: *Turbulenz*. Phys. Bl. 46 (1990) No 1 pp. 2-7.

- GRÜN, A. [1985]: *Adaptive Least Square Correlation: A Powerful Image Matching Technique*. South African Journal of Photogrammetry, Remote Sensing and Cartography, Vol. 14, No. 3, pp. 175-187.
- GÜLCH, E. [1984]: *Geometric Calibration of two CCD-cameras used for digital image correlation on the planicomp C100*. IAPRS, Vol. XXV, Part A3a, Rio de Janeiro, pp. 159-168.
- GURVICH, A. S. [1997]: *A heuristic model of three-dimensional spectra of temperature inhomogeneities in the stably stratified atmosphere*. Ann. Geophysicae 15 (1997), pp. 856-869.
- GURVICH, A. S., N. S. TIME, L. S. TUROVTSEVA, V. F. TURCHIN [1974]: *Reconstruction of the temperature fluctuation spectrum of the atmosphere from optical measurements*. Izvestiya, Atmospheric and Oceanic Physics, Vol. 10, No. 5, pp. 292-297.
- GURVICH, A.S.; KALLISTRATOVA, M. A.; TIME, N. S. [1968]: *Fluctuations of the parameters of a laser light wave propagating in the atmosphere*. Radiofizika, Vol. 11, pp. 1360-1370.
- HENNES, M. [1995]: *Entwicklung eines Meßsystems zur Ermittlung von Turbulenzparametern der Atmosphäre für Anwendungen in der Geodäsie*. Diss., GIUB, DGK, Reihe C, Heft 438
- HENNES, M., DÖNICKE, R. CHRIST, H. [1999]: *Zur Bestimmung der temperaturgradienteninduzierten Richtungsverschwenkung beim Tunnelvortrieb*. VPK, 8/99, pp. 418-426.
- HENNES, M.; FLACH, P. [1998]: *Techniken zur Ermittlung von Refraktionskorrekturen aus Videobildern von geodätischen Messinstrumenten*. AVN 1998, pp. 41-49.
- HERRMANN, D. [1994]: *Algorithmen für Chaos und Fraktale*. Addison-Wesley, Bonn, p. 159.
- HERTZSPRUNG, E. [1912]: *Photographische Messung der atmosphärischen Dispersion*. Astron. Nachr., Vol. 192, pp. 308-319.
- HILL, R. J. [1992]: *Atmospheric Propagation*. In: Tatarskii, V. I.; Ishimaru, A.; Zavorotny, V. U. (eds.): *Wave Propagation in Random Media*, Seattle, Aug. 1992, pp.22-31.
- HILL, R. J. [1982]: *Theory of measuring the path-averaged inner scale of turbulence by spatial filtering of optical scintillation*. J. Appl. Opt., Vol. 21, No. 7, pp. 1201-1211.
- HILL, R. J. [1978]: *Models of the scalar spectrum for turbulent advection*. J. Fluid Mech., Vol. 88, pp. 541-562.
- HILL, R. J., G. R. OCHS [1978]: *Fine calibration of large-aperture optical scintillometers and an optical estimate of inner scale turbulence*. J. Appl. Opt., Vol. 17, No. 22, pp. 3608-3612.
- HILL, R. J., G. R. OCHS, J. J. WILSON [1992]: *Measuring Surface-Layer Fluxes of Heat and Momentum using Optical Scintillation*. Boundary-Layer Meteorol., Vol. 58, pp. 391-408.

- HILL, R. J.; BOHLANDER, R. A.; CLIFFORD, S. F.; MCMILLAN, R. W.; PRIESTLEY, J. T., SCHOENFELD, W. P. [1988]: *Turbulence-Induced Millimeter-Wave Scintillation Compared with Micrometeorological Measurements*. IEEE Transactions on Geoscience and Remote Sensing, Vol. 26 No. 3, pp. 330-342
- HILL, R. J.; CLIFFORD, S. F.; LAWRENCE, R. S. [1980]: *Refractive-index and absorption fluctuations in the infrared caused by temperature, humidity, and pressure fluctuations*. J. Opt. Soc. Am., Vol. 70 No. 10, pp. 1192-1205
- HILL, R. J; CLIFFORD, S. F. [1978]: *Modified spectrum of atmospheric temperature fluctuations and its application to optical propagation*. J. Opt. Soc. Am., Vol. 68 No. 7, pp. 892-899
- HÖGSTRÖM, U. [1988]: *Non-Dimensional Wind and Temperature Profiles in the Atmospheric Surface Layer: A Re-Evaluation*. Boundary-Layer Meteorol., Vol. 42, pp. 55-78.
- HUFNAGEL, R. E. [1978]: *Propagation through Atmospheric Turbulence*. In: Wolfe, W. L.; Zissis, G. J. (eds.), *The Infrared Handbook*, Office of Naval Research, Washington DC, Chapter 6, p. 9.
- HUFNAGEL, R. E.; STANLEY, N. R. [1964]: *Modulation Transfer Function Associated with Image Transmission through Turbulent Media*. J. Opt. Soc. Am., Vol. 54(1), pp. 52-61.
- HUISER, A.M.J.; GÄCHTER, B.F. [1989]: *A solution to atmospherically induced problems in very high-accuracy alignment and levelling*. Applied Physics, Vol. 22, pp.1630-1638.
- INGENSAND, H. [1995]: *Neue digitale Nivelliertechniken und ihre Anwendungen*. VPK 4/95 pp. 221-226.
- INGENSAND, H. [1990a]: *Das Rapid Precisions Levelling Projekt*. VR 52/2+3 (April 1990), pp. 105-114.
- INGENSAND, H. [1990b]: *Das Wild NA 2000. Das erste digitale Nivellier der Welt*. AVN 6/1990 pp. 201-210.
- INGENSAND, H.; BÖCKEM, B. [1997]: *Automatic Location and Pointing Techniques in Local Positioning Systems*. In: Grün, A.; Kahmen, H.(eds.): 4th Conference on Optical 3-D Measurement Techniques, Zürich 1997, pp. 329-338.
- INGENSAND, H.; MEISSL A. [1995]: *Digital Levels on the Way to 3-D-Measurement*. In: Grün, A.; Kahmen, H. (eds.): *Optical 3-D Measurement Techniques III*, Wichmann Verlag, Heidelberg.
- ISHIMARU, A. [1978]: *Wave Propagation and Scattering in Random Media*. Vol. 1+2, Academic Press, New York.
- JORDAN, W.; EGGERT, O.; KNEISSL, KNEISSL, M. [1956]: *Handbuch der Vermessungskunde*. Vol. III, p 410-429.
- KANTHA, L.H.; BLUMBERG, A. F.; MELLOR, G. L. [1990]: *Computing phase speeds at open boundary*. J. Hydraulic Engineering, Vol. 116, pp. 592-597.

- KATOWSKI, O. [1996]: *Setzungsmessungen mit automatischen Theodolitsystemen*. In: Brandstätter, Brunner, Schelling (eds.): *Ingenieurvermessung '96*, Beiträge zum XII. Internationalen Kurs für Ingenieurvermessung, Graz 1996.
- KOCH, K.-R.; SCHMIDT, M. [1994]: *Deterministische und stochastische Signale*. Dümmler Verlag, Bonn, pp. 220-231.
- KOLMOGOROW, A. N [1941]: *Rasseyanie energii pri lokal'no izotropnoi turbulentnosti (Energy Dissipation with locally Isotropic Turbulence)*. Dokl. Akad. Nauk. SSSR, Vol. 32 No. 1, p 19.
- KROSCHEL, K. [1996]: *Statistische Nachrichtentheorie*, Springer Verlag, Berlin, pp. 288-318.
- KUKKAMÄKI, T. J. [1950]: *Über das Flimmern und Schweben des Zielbildes*. Geofisica pura e applicata, Vol. 18, pp. 120-127.
- LAWRENCE, R. S.; STROHBEHN, J. W. [1970]: *A Survey of Clear-Air Propagation Effects Relevant to Optical Communications*. Proc. of the IEEE, Vol. 58 No 10/1970 pp. 1523-1545.
- LEICA LTD [1989]: *User manual of video theodolite TM3000V*.
- LENZ, R. [1991]: *Gewinnung von Bilddaten mit CCD-Flächensensoren*. In: Welsch, W., Schlemmer, H., Lang, M.: *Geodätische Messverfahren im Maschinenbau*, 26. DVW Seminar, München 1991.
- LIM, J. S. [1990]: *Two-Dimensional Signal and Image Processing*. Englewood Cliffs, NJ: Prentice Hall, pp. 536-540.
- LUND, T. S. [1996]: *Large-eddy simulation of a concave wall boundary layer*. Int. J. Heat and Fluid Flow, Vol. 17, pp. 290-295.
- LUND, T. S.; CHASNOV, J. R.; MENEVEAU, C.; JIMENEZ, J. [1998]: *On the local nature of the energy cascade, part II: Spectral evolution of a sudden increase in low wavenumber energy*. Center for Turbulence research, Stanford University, Stanford CA, (unpubl.).
- MAAS, H.-G. [1993]: *Destriping of digital images*. ISPRS Com. I, Workshop on digital sensors and systems, Trento (I), 21-25 June 1993, pp. 290-299.
- MAAS, H.-G.; STEFANIDIS, A.; GRÜN, A. [1994]: *From Pixels to Voxels - Tracking volume elements in sequences of 3-D digital images*. IAPRS, Vol. 30, Part 3/2.
- MALLAT, S. [1989]: *A theory for multiresolution signal decomposition: the wavelet representation*. IEEE Pattern Anal. and Machine Intell., Vol. 11, no. 7, pp. 674-693.
- MANDELBROT, B. [1977]: *Fractals: Form, Chance, & Dimension*. San Francisco, CA: W. H. Freeman.
- MANNEVILLE, P. [1991]: *Structures dissipatives, chaos et turbulence*. Gif-sur-Yvette: Commissariat à l'Energie Atomique.
- MATROX [1996]: *Pulsar hardware and installation manual*. Matrox electronic systems.

- MAURER, W. [1982]: *Ein interferometrisches Messverfahren zur Bestimmung von Strichverbesserungen an eingebauten Theodolitteilkreisen*. Diss., TU München, pp. 26-29.
- MONIN, A.S., A.M. OBUKHOV [1954]: *Basic laws of turbulent mixing in the atmosphere near the ground*. Trudy, Akademiia Nauk. SSSR, Geofizicheskogo Instituta. Vol. 24, No. 151, pp. 163-187.
- MONIN, A.S., YAGLOM, A.M. [1975]: *Statistical fluid mechanics: Mechanics of turbulence*. MIT press, Cambridge, London, Vol. 2, p. 485.
- MORITZ, H. [1962]: *Zur Geometrie der Refraktion*. OeZfV, pp. 3-13.
- NIKON [2000]: *Personal communication*.
- OBUKHOV, A. M. [1949]: *Structure of the temperature field in a turbulent current*. Izvestiya, Akademiia Nauk SSSR, Series Geograficheskaya, Vol. 13, No. 1, pp. 58-69.
- OHMURA, A.; ROTACH, M. [1997]: *Mikroklimatologie*. Institut für Klimaforschung, ETHZ, pp. 64-86.
- OPPENHEIM, A. V.; SCHAFFER, R. W. [1992]: *Zeitdiskrete Signalverarbeitung*. R. Oldenbourg Verlag, München Wien.
- ORLONSKI, I. [1976]: *A simple boundary condition for unbounded hyperbolic flows*. J. Comp. Phys., Vol. 21, pp. 251-269.
- OWENS, J. C. [1967]: *Optical Refractive Index of Air: Dependence on Pressure, Temperature and Composition*. J. Appl. Opt., Vol. 6, No.1, pp. 51-60.
- PANOFSKY, H. A. [1977]: *Wind Structure in Strong Winds below 150 m*. Wind Engineering Vol.1 No. 2, 1977.
- PANOFSKY, H.A.; DUTTON, J.A. [1984]: *Atmospheric turbulence: models and methods for engineering applications*. Wiley, New York.
- PAO, Y.-H. [1965]: *Structure of turbulent velocity and scalar fields at large wavenumbers*. Phys. Fluids, Vol. 8, pp. 1063-1075.
- POWELL, D.C.; ELDERKIN, C.E. [1974]: *An investigation of the application of Taylor's hypothesis to atmospheric boundary layer turbulence*. J. Atmos. Sci., 31, pp. 990-1002.
- PRANDTL, L [1932]: *Meteorologische Anwendungen der Strömungslehre*. Beitr. Phys. Atm., 19, 188-202.
- PRATT, W. K. [1991]: *Digital Image Processing*. Wiley and Sons, New York.
- PRIESTLEY, J. T., R. J. HILL [1985]: *Measuring High-Frequency Humidity, Temperature and Radio Refractive Index in the Surface Layer*. Journal of atmospheric and oceanic technology, Vol. 2, No. 2, pp. 233-251.
- PRUPPACHER, H. R.; KLETT, J. D. [1978]: *Microphysics of Clouds and Precipitation*. D. Reidel Publishing Company, Dordrecht.
- RICHARDSON, L.F. [1920]: *The supply of energy from and to atmospheric eddies*. Proc. Roy. Soc., A, 97, pp. 354-373.

- RYTOV, S. M., KRAVTSOV YU. A.; TATARSKII, V. I. [1978]: *Principles of Statistical Radiophysics Vol. 4: Wave Propagation Through Random Media*. Springer-Verlag.
- RYTOV, S. M.; KRAVTSOV, YU. A.; TATARSKII, V. I. [1987]: *Principles of statistical radiophysics Vol. 1: Elements of Random Process Theory*. 2. Aufl., Springer-Verlag Berlin Heidelberg New York.
- SALEH, B. E. A., TEICH, M. C. [1991]: *Fundamentals of Photonics*. John Wiley & Sons, Inc.
- SCHMID, H. P. [1994]: *Source Areas For Scalars and Scalar Fluxes*. *Boundary-Layer Meteorol.* Vol. 67, pp. 293-318.
- SCHNURER, G. [1993]: *Moderne PC-Bussysteme, Aktueller Entwicklungsstand bei MCA, EISA, VL-Bus und PCI*. C't, Vol. 10/1993, p.110.
- SCHOTANUS, P., F.T. M. NIEUWSTADT, H. A. R. DE BRUIN [1983]: *Temperature Measurements with a Sonic Anemometer and its Application to Heat and Moisture Fluxes*. *Boundary-Layer Meteorol.*, Vol. 26, pp. 81-93.
- SCHWIZER, P.; STÄHLI, D. [1998]: *Bestimmung von vertikalen Temperaturprofilen mit dem Scintillometer SLS 20*. Diploma thesis, IGP, ETH Zürich, unpubl.
- SEQUIN, C. H.; TOMPSETT, M. F. [1975]: *Charge transfer devices*. Academic Press, New York.
- SREENIVASAN, K.R.; MENEVEAU, C. [1996]: *The fractal facets of turbulence*. *J. Fluid Mech.* Vol. 173 (1996), p. 357.
- STROHBEHN, J. W. [1978]: *Modern Theories in the Propagation of Optical Waves in a Turbulent Medium*. In: J.W. Strohbehn (Ed.), *Laser Beam Propagation in the Atmosphere*, Topics in Applied Physics. Springer Verlag, Berlin, Heidelberg, New York.
- STROHBEHN, J. W. [1968]: *Line-of-Sight Wave Propagation Through the Turbulent Atmosphere*. *Proc. of the IEEE*. Vol. 56(8). 1301-1318 (August 1968) and Vol. 57(4), 703-704 (April 1969).
- STULL, R. B. [1991]: *An Introduction to Boundary Layer Meteorology*. Kluwer Academic Publishers.
- TATARSKII, V. I. [1992]: *Review of Scintillation Phenomena*. In: Tatarskii, V. I.; Ishimaru, A.; Zavorotny, V. U. (ed.): *Wave Propagation in Random Media*, Seattle, Aug. 1992, pp. 2-15.
- TATARSKII, V. I. [1971]: *The effects of the Turbulent Atmosphere on Wave Propagation*. Keter Press, Jerusalem, pp. 50-59.
- TATARSKII, V. I. [1961]: *Wave propagation in a turbulent Medium*. Dover Publications, New York.
- THIERMANN [1997]: *Surface Layer Scintillometer*. User's Manual, Scintec Atmosphärenmesstechnik GmbH, Germany.
- THIERMANN, V. [1992]: *A displaced-beam scintillometer for line-averaged measurements of surface layer turbulence*. Preprint Volume of the 10th Symposium on Turbulence and Diffusion, 29 Sept-2 Oct. 1992, Portland, OR.

- THIERMANN, V. [1990]: *Optische Messung turbulenter Flüsse und Vorhersage der optischen Turbulenz aus einfachen Grenzschichtparametern*. Diss., Universität Hamburg, Fachbereich Geowissenschaften.
- THIERMANN, V., H. GRASSL [1992]: *The measurement of turbulent surface-layer fluxes by use of bichromatic scintillation*. *Boundary-Layer Meteorol.*, Vol. 58, pp. 367-389.
- TRITTON, D. [1977]: *Physical fluid dynamics*. Van Nostrand Reinhold Co., New York, pp. 52-53 and 59-60.
- TROLLER, M. [2000]: *Szintillometrische Refraktionsbeobachtung*. Diploma thesis, IGP, ETHZ, unpubl.
- USGS [1998]: *USGS Digital Spectral Library*. U.S. Geological Survey, Reston, VA, USA, <http://speclab.cr.usgs.gov>.
- VINOGRADOV, V.V.; SUCHOV, G. N.; MEDOVIKOV, A.S. [1985]: *Opređelene refrakeji pri geodeziceskom nivelirovani po rozmytju regularnyh struktur (Determination of Refraction in geodetic levelling with use of blurring of images of regular structures)*. UDK 528.024.4 / 535.3, *Izv. vyss. ucebn. Zav. Geodezija Aerofotos'emka*, 2 (1985), Moskva, pp. 32-39.
- WANG, T., G. R. OCHS, S. F. CLIFFORD [1978]: *A saturation-resistant optical scintillometer to measure Cn²*. *J. Opt. Soc. Am.*, Vol. 68, No. 3, pp. 334-338.
- WEISS, A. [1998]: *Der Brechungsindex in der Grenzschicht der Atmosphäre*. Internal report, IGP, ETH Zürich, unpubl.
- WEISS, A.; HENNES, M.; ROTACH, M. [2000]: *Derivation of refractive index and temperature gradients from optical scintillometry for the correction of atmospherically induced problems in highly precise geodetic measurements*. Paper to EGS 2000, Nizza, 25.-29.4.2000. In: Kluwer Academic Press, Netherlands.
- WEISS, A.; ROTACH, M.; HENNES, M. [1999]: *Comparison of Turbulence Parameters derived from Optical Scintillometry and the Eddy-Correlation Technique over Flat Terrain*. 79th AMS-annual Meeting, 13th Symposium on Boundary Layers and Turbulence, 10.-15.1.1999, Dallas, TX, p. 145-147.
- WELCH, P. H. [1967]: *The Use of Fast Fourier Transform for the Estimation of Power Spectra: A Method Based on Time Averaging Over Short, Modified Periodograms*. *IEEE Transactions on audio and electroacoustics*. Vol. AU-15 (June 1967), pp. 70-73.
- WESELY, M. L.; DERZKO, Z. I. [1975]: *Atmospheric Turbulence Parameters from Visual Resolution*. *Applied Optics*, Vol. 14, pp. 847-853, April 1975.
- WIENER, N. [1950]: *Extrapolation, Interpolation, and Smoothing of Stationary Time Series*. New York, Wiley.
- WILD LEITZ AG [1988]: *Electrical characteristics of (GaAl) As infrared emitting diode*. Internal report, unpubl.
- WILHELM, W. [1993]: *Empirische Bestimmung der Seitenrefraction an 10 Objekten in der Praxis*. IGP Bericht Nr. 219 ETH Zürich.
- WITTE, B. [1990]: *Möglichkeiten und Grenzen des trigonometrischen Nivellements*. VR52/2+3, pp. 86-96.

- WYNGAARD, J. C., CLIFFORD, S. F. [1978]: *Estimating Momentum, Heat and Moisture Fluxes from Structure Parameters*. J. Atmos. Sci, Vol. 35 No. 7, pp. 1207-1211, July 1978.
- WYNGAARD, J. C., Y. IZUMI, S. A. COLLINS; JR. [1971]: *Behavior of the refractive-index-structure parameter near the ground*. J. Opt. Soc. Am., Vol. 61, No. 12, pp. 1646-1650.

Abbreviations

Appl. Opt.	Journal of Applied Optics
Atmos. Sci.	Journal of the Atmospheric Science
AVN	Allgemeine Vermessungsnachrichten
Comp. Appl. Math.	Journal of comparative applied mathematics
Comp. Phys.	Journal of comparative physiology
c't	Magazin für Computer Technik
DGK	Deutsche Geodätische Kommission
Diss	Dissertation
EGS	European Geophysical Society
ETHZ	Eidgenössische Technische Hochschule Zürich
Fluid Mech.	Journal of Fluid Mechanics
GIUB	Geodätisches Institut der Universität Bonn
IAPRS	International Archives of Photogrammetry and Remote Sensing
IEEE	Institute of Electrical and Electronics Engineers (New York)
IGP	Institut für Geodäsie und Photogrammetrie
IMEKO	International Measurement Confederation
ISPRS	International Society of Photogrammetry and Remote Sensing
J.	Journal
JGR	Journal of Geophysical Research
MIT	Massachusetts Institute of Technology
Mod. Opt.	Journal of Modern Optics
NOAA	National Oceanic and Atmospheric Administration
OeZfV	Oesterreich. Zeitschrift für Vermessung und Photogrammetrie
Opt. Soc. Am.	Journal of the Optical Society of America
Phys. Bl.	Physikalische Blätter
Proc.	Proceedings
RWTH	Rheinisch-Westfälische Technische Hochschule Aachen
SPIE	Society of Photo-Optical Instrumentation Engineers
UDK	Universal'naja desjaticnaja klassifikacija
USGS	U.S. Geological Survey
VPK	Vermessung, Photogrammetrie, Kulturtechnik
VR	Vermessungswesen und Raumordnung
VT	Vermessungstechnik
ZfV	Zeitschrift für Vermessungskunde

“Geodätisch-geophysikalische Arbeiten in der Schweiz”

**(Fortsetzung der Publikationsreihe ”Astronomisch-geodätische Arbeiten in der Schweiz”
der Schweizerischen Geodätischen Kommission (ab Bd. 42):**

- 42** 1990 Höhensysteme, Schwerepotentiale und Niveaulächen: Systematische Untersuchungen zur zukünftigen terrestrischen und GPS-gestützten Höhenbestimmung in der Schweiz. B. Wirth. 204 Seiten.
- 43** 1990 Gravimetrisches Geoid der Schweiz: Potentialtheoretische Untersuchungen zum Schwerefeld im Alpenraum. A. Geiger. 231 Seiten.
- 44** 1991 Rapid Differential Positioning with the Global Positioning System (GPS). E. Frei. 178 Seiten.
- 45** 1992 Dreidimensionales Testnetz Turtmann 1985-1990 Teil I. F. Jeanrichard (Hrsg.) Autoren: A.Geiger, H.-G. Kahle, R. Köchle, D. Meier, B. Neiningen, D. Schneider, B. Wirth. 183 Seiten.
- 46** 1993 Orbits of Satellite Systems in Space Geodesy. M. Rothacher. 243 Seiten.
- 47** 1993 NFP 20. Beitrag der Geodäsie zur geologischen Tiefenstruktur und Alpendynamik. H.-G. Kahle (Hrsg.) Autoren: I. Bauersima, G. Beutler, B. Bürki, M. Cocard, A. Geiger, E. Gubler, W. Gurtner, H.-G. Kahle, U. Marti, B. Mattli, M. Rothacher, Th. Schildknecht, D. Schneider, A. Wiget, B. Wirth. 153 Seiten plus 90 Seiten Anhang.
- 48** 1994 Ionosphere and Geodetic Satellite Systems: Permanent GPS Tracking Data for Modelling and Monitoring: Urs Wild, 155 Seiten.
- 49** 1994 Optical Astrometry of Fast Moving Objects using CCD Detectors: Thomas Schildknecht, 200 Seiten.
- 50** 1995 Geodätische Alpen traverse Gotthard: A. Elmiger, R. Köchle, A. Ryf und F. Chaperon. 214 Seiten.
- 51** 1995 Dreidimensionales Testnetz Turtmann 1985-1993, Teil II (GPS-Netz). F. Jeanrichard (Hrsg.) Autoren: G. Beutler, A. Geiger, M. Rothacher, Stefan Schaer, D. Schneider, A. Wiget, 173 Seiten.
- 52** 1995 High Precision GPS Processing in Kinematic Mode: M. Cocard. 139 Seiten.
- 53** 1995 Ambiguity Resolution Techniques in Geodetic and Geodynamic Applications of the Global Positioning System. L. Mervart. 155 Seiten.
- 54** 1997 SG 95: Das neue Schweregrundnetz der Schweiz: F. Arnet und E. Klingelé. 37 Seiten.
- 55** 1997 Combination of Solutions for Geodetic and Geodynamic Applications of the Global Positioning System (GPS). Elmar Brockmann, 211 Seiten.
- 56** 1997 Geoid der Schweiz 1997. Urs Marti, 140 Seiten.
- 57** 1998 Astrometry and Satellite Orbits: Theoretical Considerations and Typical Applications. Urs Hugentobler, 209 Seiten.
- 58** 1998 Systematic Investigations of Error- and System-Modelling of Satellite Based Flight Approaches and Landings in Switzerland. Maurizio Scaramuzza, 165 Seiten.
- 59** 1999 Mapping and Predicting the Earth’s Ionosphere Using the Global Positioning System. Stefan Schaer, 205 Seiten.
- 60** 2000 Modeling and Validating Orbits and Clocks Using the Global Positioning System. Timon Anton Springer, 154 Seiten.
- 61** 2001 Spatial and Temporal Distribution of Atmospheric Water Vapor using Space Geodetic Techniques. Lars Peter Kruse, 128 Seiten.
- 62** 2001 Solar Spectrometry for Determination of Tropospheric Water Vapor. Bernd Sierk, 221 Seiten.
- 63** 2001 Analysis of refraction influences in geodesy using image processing and turbulence models. Philipp Flach, 175 Seiten.